THE ORIENTATION OF ACCRETION DISKS AND JETS IN QUASARS

EMILY DOWN
TRINITY COLLEGE
UNIVERSITY OF OXFORD

A thesis submitted in candidature for the degree of
Doctor of Philosophy

Trinity 2008

Declaration

I declare that no part of this thesis has been accepted, or is in the process of being submitted, for any degree, diploma, certificate or other qualification in this University or elsewhere.

This thesis is the result of my own work unless otherwise stated. The research was carried out in collaboration with my supervisors Professor Steve Rawlings and Dr Joanne Baker, and with Dr Devinder Sivia.

The infrared spectra presented in Chapter 2 were observed by Dr Joanne Baker. The new radio maps in Chapter 4 were reduced at Jodrell Bank, with much assistance from Dr Tom Muxlow and Dr Anita Richards. Other radio maps in Chapter 4 were kindly supplied by Dr Eric de Silva (publication in preparation), and yet others are taken from Kapahi et al. (1998a). The 20 GHz radio flux densities for the Molonglo quasars used in Chapter 5 are preliminary data from the Australia Telescope 20 GHz (AT20G) Survey (publication in preparation), and were generously provided by Dr Elaine Sadler. Radio flux densities for the Molonglo quasars at other frequencies are from various surveys; Tables 5.1 and 5.2 in Chapter 5 state their origins with references.

The orientation of accretion disks and jets in quasars

Emily Down
Trinity College

*A thesis submitted in candidature for the degree of
Doctor of Philosophy*

Trinity 2008

All massive nearby galaxies, including our own, host supermassive black holes. Active galactic nuclei (AGN) are seen when such black holes accrete, and when they produce powerful jets of synchrotron-emitting plasma, they are termed radio-loud AGN. The close correlation between black hole mass and galaxy bulge mass in elliptical galaxies indicates that AGN feedback may be the key to the regulation of galaxy formation. It is thus necessary to fully understand the structure of AGN, the way that they are fuelled, and their duty cycle, in order to study the feedback processes and get a clear picture of galaxy formation.

In this thesis, independent methods are developed to constrain the accretion disk and radio jet angles to the line of sight. $\mathrm{H}\,\alpha$ emission from a sub-sample of high-redshift quasars is measured from near-infrared spectroscopy and modelled as sums of different components, including the characteristic double-peaked profile which results from a thin, rotating accretion disk. Comparing the models using Bayesian evidence, almost all quasars were found to have infrared spectra consistent with the presence of a disk. The jet inclination angles of the same set of quasars were constrained by fitting a model, including the effect of Doppler boosting and the receding torus model for dust obscuration, to the radio spectral energy distribution.

The fitted disk and jet angles correlate strongly, and are consistent with a model in which the radio jets are launched orthogonally to the plane of the accretion disk, as expected if the jet is powered by energy drawn from the spin of the black hole. Both disk and jet angles correlate with the observed linear source size, which is a projection effect; when deprojected using the fitted angles, the distribution of source sizes agrees with a scenario in which the sources expand into the surrounding medium at a constant rate up to ~ 1 Mpc and then shut off, probably as the nuclei become quiescent. The accretion disk angle was found to correlate weakly with the low-frequency radio luminosity, which provides direct, albeit tenuous, evidence for the receding torus model.

The *Contents*

Chapter 1 *Introduction*

Active galactic nuclei (AGN) come in many flavours. The focus of this thesis is radio-loud quasars. These sources are thought to share the same basic structure as most or all other AGN types. There are variations in black hole mass, dimensions and jet power, but the layout of each type is consistent with a central accreting black hole around which may be an accretion disk, and further out a torus of dusty gas; spherically-distributed gas clouds which are dense and fast-moving close to the black hole, but slower-moving and less dense further out; and opposing jets of synchrotron-emitting plasma that can extend up to $\sim$ Mpc scales.

Section 1.1 explains the classification of different types of AGN and the ways in which they are related. Section 1.2 explains the structure of a radio-loud quasar in greater detail, focussing on the accretion disk and radio jets. Section 1.3 discusses the interactions between radio sources and their host galaxies, and puts this research in context.

1.1 *Active Galactic Nuclei Taxonomy*

There is a plethora of different types of AGN. Putting aside the exotic species (for example, the blazars, which are characterised by high variability and lack of emission lines), there are three main ways in which the sources are split up. Divisions are made on the basis of quasar luminosity; radio-loudness, the ratio of radio to optical emission; and the width of optical emission lines (Urry & Padovani 1995; Antonucci 1993). Figure 1.1 shows classes based on this three-parameter scheme, though it should be noted that the borders delineating the classes are often very fluid, and there are many types of AGN which do not fit neatly into this simplified scheme.

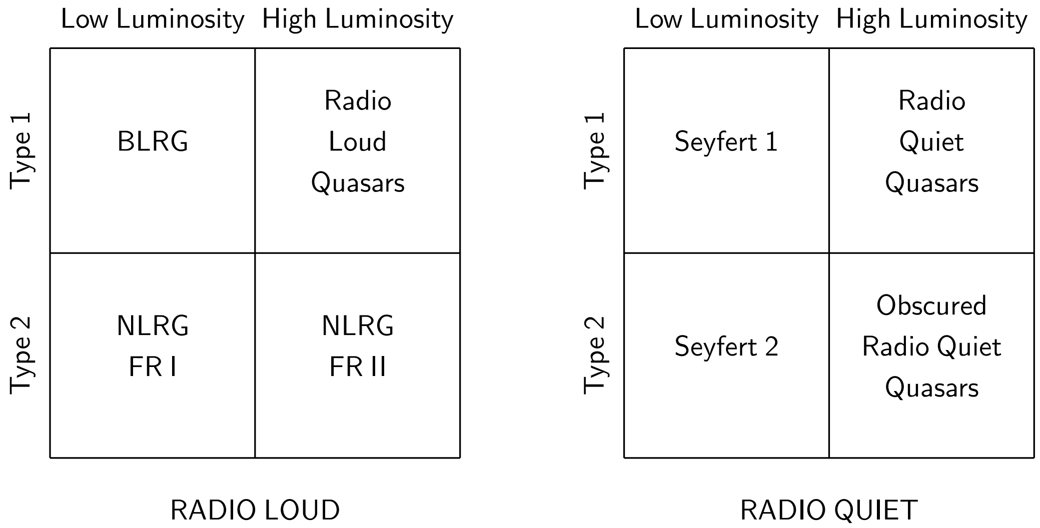

Figure 1.1: A very simplified diagram of various types of AGN, splitting them up by radio-loudness, quasar luminosity (this is optical luminosity for the radio-quiet AGN; in radio-loud AGN, optical and radio luminosity are correlated (Rawlings & Saunders 1991)), and by observation of the optical spectrum, which splits the sample into Type 2 sources (with narrow emission lines and weak non-stellar continuum emission) and Type 1 sources (with broad emission lines in addition to the narrow lines, and strong non-stellar continuum emission). This divide is thought to arise from orientation effects.

1.1.1 *Radio-loudness*

The radio-loud – radio-quiet divide was first discovered by Kellermann et al. (1989) to form a bimodal population between those AGN whose ratio of radio-to-optical flux density was close to or less than unity, and those whose radio flux density greatly exceeded the optical (with the flux ratio $F_{5\mathrm{GHz}}/F_{\mathrm{B}} \gtrsim 10$, where F_{B} is the optical B-band flux density). However, this dichotomy is not clear-cut, and radio-intermediate objects have been discovered (Miller et al. 1993). The difference in host galaxy structure between these two groups was the key to the current best unification theory: radio-loud AGN are found exclusively in massive elliptical galaxies, whereas radio-quiet AGN are found both in elliptical and spiral host galaxies (e.g. Hutchings et al. 1989). Studies of the host galaxies of optically-matched samples of these classes, together with the famous Magorrian et al. (1998) paper linking black hole mass and galaxy spheroid mass, led to the discovery that radio-loudness is a property of black hole mass (McLure et al. 1999; Lacy et al. 2001).

1.1.2 *Quasar luminosity and radio luminosity*

Radio luminosity was found by Fanaroff & Riley (1974) to correlate with the ratio of the distance between the regions of highest radio emission (hot-spots) in the AGN and the extent of the diffuse radio lobe emission. The less luminous sources with $\log[L_{178\mathrm{MHz}}/\mathrm{WHz}^{-1}\mathrm{sr}^{-1}] \lesssim 25.3$, referred to as FRI sources, have zones of highest radio emission closer to the AGN nucleus, whereas the more luminous FRIIs ($\log[L_{178\mathrm{MHz}}/\mathrm{WHz}^{-1}\mathrm{sr}^{-1}] \gtrsim 25.3$) have hot-spots near the ends of the radio lobes. Furthermore, the FRIs often show complex structure and significant curvature in their jets, unlike the FRIIs, which have highly collimated radio jets. These jets may precess: Scheuer (1982) first proposed the "dentist's drill" model in which the movement of the hotspot expands the radio lobe outwards, and recently Steenbrugge & Blundell (2008) discovered precession in the jets of the FRII source Cygnus A.

The divisions between these luminosity classes are blurred, for example, broad-line radio galaxies may either be low-luminosity FRI AGN, or high-luminosity FRII sources in which the central nucleus is highly reddened (Dennett-Thorpe et al. 2000; van Bemmel & Barthel 2001). These latter objects may be as optically luminous as FRII narrow-line radio galaxies.

1.1.3 *Orientation effects*

Differences in the optical emission spectra of AGN matched in radio luminosity are now firmly believed to be due to orientation effects rather than underlying differences in the sources themselves. There are two separate orientation-dependent effects, each with their own unification scheme.

The Type 1/Type 2 classification of AGN is made on the basis of the presence of broad emission lines. Type 2 AGN possess only narrow emission lines, $\lesssim 2000$ km s^{-1} (e.g. Peterson 1997) and weak continuum emission. Type 1 AGN possess, in addition to narrow lines similar to the Type 2 sources, broad emission lines of $\sim 2000 - 20000$ km s^{-1}, and strong non-stellar continuum emission. An explanation for this disparity grew from the discoveries of broad emission lines seen in polarised light from Type 2 Seyfert sources (e.g. Antonucci & Miller 1985), which suggested orientation-dependent obscuration such as a dusty molecular torus (Krolik & Begelman 1986). It has recently become clear that obscuration by dust in starbursting galaxies can also be responsible for hiding Type 1 AGN (e.g. Martínez-Sansigre et al. 2005).

The second orientation-dependent effect arises from the relativistic motion of the plasma in the radio jets. Scheuer & Readhead (1979) first suggested that viewing a radio source with opposing relativistic jets would cause a large contrast in the luminosities of the approaching and receding jets, and that objects with jet axes close to the line of sight would be seen more often due to Doppler boosting of the core. Orr & Browne (1982) were the first to make the connection between Doppler boosting of the core, and a measure of quasar orientation from the core-to-lobe radio flux density ratio; this allowed them to unify the "core-dominated" quasars with flat optical spectra, viewed at angles close to the line of sight, with the "steep-spectrum" quasars viewed at larger angles. Wills & Browne (1986) then linked the radio properties to the optical properties by discovering an anticorrelation between the core-to-lobe radio flux ratio and the width of the H β line, and interpreting this connection as the result of beaming of radio emission from a jet emerging along the rotation axis of an accretion disk, while the broad H β lines arise from the accretion disk with a width correlated with the angle between the line of sight and the disk axis. This crucial result paved the way for the work in this thesis.

The two optical schemes were pulled together by Barthel (1989), who gave a consistent picture in which FRII narrow line radio galaxies (hereafter shortened to "radio galaxies"), steep-spectrum quasars and flat-spectrum quasars are all drawn from the same parent population, but viewed at decreasing jet angles to the line of sight. Figure 1.2 summarises this unification scheme for radio-loud AGN.

1.1.4 *Compact Steep-Spectrum sources*

Another subtlety is that while many of the quasars with small projected sizes are flat-spectrum core-dominated sources, there are another group of these small sources with

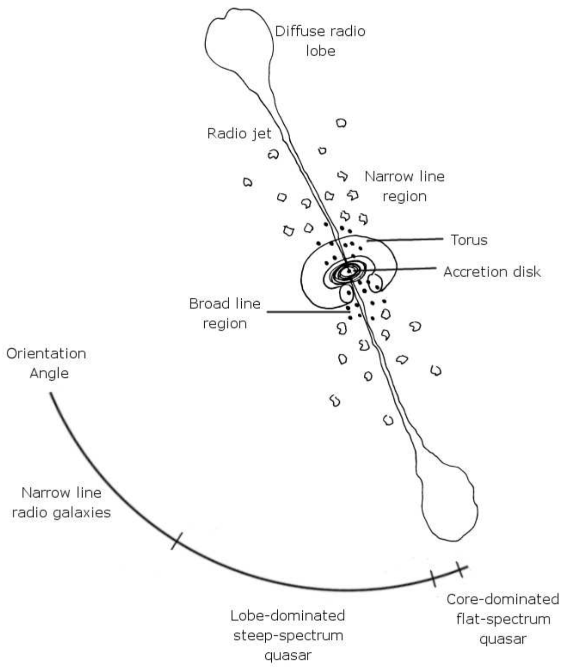

Figure 1.2: Sketch of a luminous, radio-loud AGN, mapping the relative positions of the central black hole accretion disk, the dusty torus, the broad and narrow-line regions, and the radio jets. This diagram indicates how when the AGN is seen with the jet pointing close to the line of sight, it appears as a core-dominated quasar, and at jet angles up to $\sim 45^\circ$, as a lobe-dominated quasar. At jet angles greater than this, the dusty torus shields the broad-line region from view, and only narrow lines are visible; these AGN are then referred to as narrow-line FRII radio galaxies.

steep radio spectra ($\alpha \sim 1$) similar to the lobe-dominated sources. It is thought that at least some of these Compact Steep Spectrum (CSS) sources are young, recently-triggered AGN (Fanti et al. 1995; O'Dea 1998). Submillimetre observations have revealed that the star formation rate appears to be larger in the smaller sources (e.g. Willott et al. 2002), and evidence is stacking up that they may be born in a burst of star formation as galaxies interact or merge. These young sources may be shrouded in dust, which clears from the jet axis as the source expands (Baker et al. 2002), resulting in a dusty torus forming around the nucleus.

1.1.5 *Microquasars*

It is also worth mentioning that whilst AGN are located at cosmological distances, there are laboratories available in the local universe in the form of microquasars. These are X-ray binary systems in which neutron stars or stellar-mass black holes accrete matter from their companion, and may eject a relativistic, synchrotron-emitting jet, which corresponds remarkably closely to an AGN jet (e.g. Fender 2004). Jester et al. (2006) and Körding et al. (2006) showed that the optical/X-ray and radio properties of AGN and microquasars follow similar tracks in a diagram which plots the fraction of non-thermal emission against total emission (thermal and non-thermal); this is strong evidence that accretion proceeds in the same way in both classes of source.

Falcke et al. (2004) postulated that the "hard" or "low" states of microquasars, which arise from black holes accreting at sub-Eddington rates from jet-dominated accretion flows, and give rise to steady jets, correspond to lower-luminosity AGN, such as FRI radio galaxies. The "soft" or "high" microquasar states, which result from near-Eddington accretion from a disk onto the black hole, which launches transient, highly relativistic jets, correspond to radio-loud quasars and to radio-quiet sources. Nipoti et al. (2006) suggest that as microquasars flip between active and steady states, if a parallel is drawn with radio-loud and radio-quiet AGN, these more powerful sources may also have a "duty cycle" in which they cycle through active and steady states.

1.2 *Anatomy of a Quasar*

1.2.1 *The black hole and accretion disk*

There is a growing body of evidence that AGN are powered by accretion of gas and dust onto supermassive black holes, and this is now the accepted paradigm. As the black hole feeds on the surrounding material, it is expected that this will form an accretion disk of infalling matter (Shakura & Sunyaev 1973). Collin-Souffrin et al. (1980) first suggested that a thick inner accretion disk, shielding and reprocessing the hard X-ray emission from the black hole, gives rise to the strong UV and optical [Fe II] emission seen in Type 1 Seyferts.

Filippenko (1988) reviews the different lines of evidence that accretion disks feed the central black hole. Baldwin (1977) recorded the anticorrelation of the UV continuum luminosity with the equivalent widths of broad C IV emission (the "Baldwin Effect"). Both this observation and the "Big Blue Bump" of excess UV continuum emission found by Malkan & Sargent (1982) may be explained by emission from an optically thick, geometrically thin accretion disk (Netzer 1985). However, the strongest direct evidence is in the form of double-peaked optical emission lines arising from the accretion disk itself (Eracleous & Halpern 1994), although these are not much studied.

There is a parallel diagnostic line to the double-peaked Balmer lines which is seen in the X-ray spectrum. The Fe Kα line (Reeves et al. 2001; Pounds et al. 2001) arises from the inner, geometrically thick part of the accretion disk, from similar processes that give rise to the double-peaked optical lines.

There are many different models for AGN accretion disks. The disk model used in this thesis is taken from Chen & Halpern (1989), and consists of a thick, hot, ion-supported torus (Rees et al. 1982), which extends up to $100\,R_{\mathrm{G}}$, where the gravitational radius $R_{\mathrm{G}} = GM/c^2$, from the black hole. Inverse Compton-scattered X-rays from this inner disk illuminate an optically thick, geometrically thin outer disk (Halpern & Chen 1989). This outer disk, which produces the double-peaked emission lines (e.g. Chen & Halpern 1989; Pérez et al. 1988), may extend up to $\sim 10^5\,R_{\mathrm{G}}$ from the central engine. See Figure 1.3 for a diagram of this scheme.

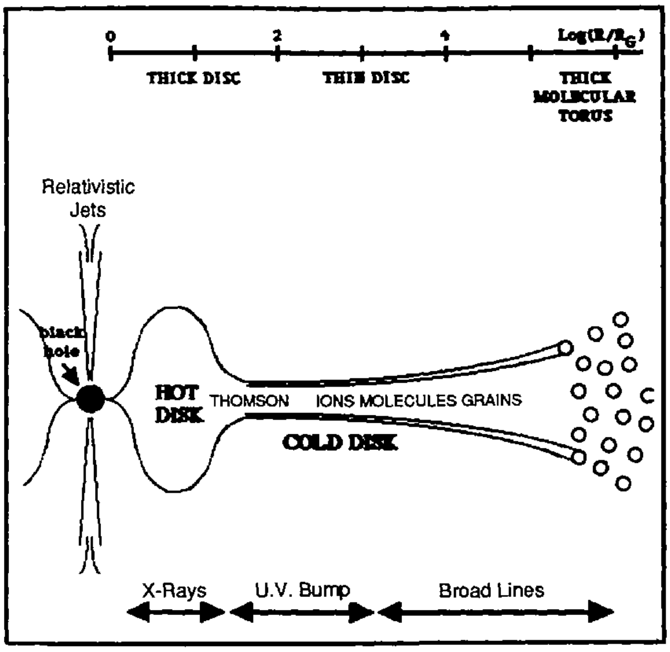

Figure 1.3: A diagram from Collin-Souffrin (1987) showing the different components of an accretion disk, and their extents in gravitational radii.

In a circular, relativistic Keplerian disk, the rotation gives rise to two peaks: a redshifted peak, and a blueshifted peak, which is Doppler boosted and so has higher intensity. There is a small effect from gravitational redshift due to the proximity of the black hole, which affects the wings and centroid of the line (Strateva et al. 2003). This effect is small, as to first order, the gravitational redshift is given by

$$z_{\mathrm{gravitational}} \sim \frac{GM}{c^2 R} = \frac{R_{\mathrm{G}}}{R}. \tag{1.1}$$

The region considered is outside 100 R_{G}, and so $z_{\mathrm{gravitational}} < 0.01$ for these models.

The thin, outer accretion disk is thought to be a different entity from the broad-line region of the AGN, if accretion is the only power source (Collin-Souffrin 1987); however, if the disk was heated by scattered non-thermal continuum, this could then produce the observed line profiles and widths accredited to the broad-line region.

1.2.2 *Broad-line region*

The classical model for the broad-line emitting region of an AGN is a zone of hot, fast-moving clouds of matter which are distributed roughly spherically within the volume bounded by the ion torus. These clouds give rise to collisionally-broadened emission lines of up to $\sim 20,000$ km s^{-1} (e.g. Peterson 1997), the optical diagnostic of a quasar. The emission from these clouds is visible if the AGN is viewed along a sight line within the cone which is not blocked by the torus; viewed edge on, the clouds are obscured by the torus, and the AGN is classified as a radio galaxy.

1.2.3 *Dusty torus*

A torus of molecular material was postulated by early optical unification models (see Section 1.1.3) in order to explain the differences between Seyfert Type 1 objects and Seyfert Type 2s. Since that time, the so called "dusty torus" has been extensively modelled (Pier & Krolik 1992, 1993). One widely-accepted refinement to the original model was put forward by Lawrence (1991) and expanded upon by Simpson (1998), and concerns the opening angle of the torus; this is found to be luminosity-dependent, probably as dust-grains are sublimed at a larger radius from a more luminous nucleus, and hence the opening angle of the torus is larger. Simpson et al. (1999) find qualitative evidence for the receding torus model through detection of a population of heavily-reddened quasar nuclei in the mid-infrared from a sample of radio galaxies, which is statistically consistent with the predictions of this model.

Recent developments in the field of interferometry have allowed direct imaging of the dusty torus in local sources (e.g. Tristram et al. 2007). VLTI observations of several bright nearby Seyferts have revealed clumpy tori which are orthogonal to the jets.

1.2.4 *Narrow-line region*

Outside the torus lie cooler clouds of gas, the emission from which is visible from any angle. This zone gives rise to narrow emission lines with widths < 2000 km s^{-1} (e.g. McLure & Dunlop 2004). The strongest narrow emission line at restframe wavelengths $\sim$

6000 – 7000 Å is Hα, but since the density of this region is low, forbidden lines are also seen. The intensities of these lines are dependent on the electron density and temperature in this region, and so the relative line strengths are linked.

1.2.5 *Radio jets and lobes*

The radio jets in radio-loud quasars are very highly-collimated (Jeyakumar & Saikia 2000) streams of magnetised plasma which can extend for distances of hundreds of kiloparsecs (Bridle & Perley 1984), far outside the reaches of the host galaxy. The jet power is similar to the narrow line luminosity in powerful FRII sources (Rawlings & Saunders 1991), and tends towards the Eddington luminosity (luminosity of 100% efficient accretion) for high jet powers (Willott et al. 1999). This supports the theory that the jets are powered by accretion on to the nucleus of the AGN. Blandford & Znajek (1977) postulated that the jets extract rotational energy from the central black hole (see also Rees et al. (1982) and Begelman et al. (1984)), and hence align with the spin of the black hole.

Radio jets have a steep, featureless power-law spectrum, and are therefore known to arise from a non-thermal process. The spectral indices of the radio lobes at low frequencies are seen to be $\alpha \sim 0.5$, where $S_\nu \propto \nu^{-\alpha}$, in good agreement with the prediction for optically-thin synchrotron emission arising from first order Fermi acceleration across strong shocks (Blandford 1979; Peacock 1981). At higher radio frequencies, the power law steepens due to synchrotron losses and inverse Compton losses (Webb et al. 1984) to a power law of $\alpha \sim 1$ (e.g. Alexander & Leahy 1987).

Superluminal motion was discovered in the early seventies (e.g. Cohen et al. 1971). This paved the way for the unification of steep-spectrum and flat-spectrum quasars as fundamentally similar sources viewed at different angles by Orr & Browne (1982), with the steep-spectrum quasars viewed from the side so that their extended radio emission dominates the spectrum, and the flat-spectrum sources viewed along the axis of their jets, so that the Doppler-boosted base of the jet dominates. The flat ($\alpha \sim 0$) spectrum at the base of the jet arises from synchrotron self-absorption (e.g. Kaiser 2006).

There is independent evidence that radio jets are Doppler boosted, in the form of the Laing-Garrington effect (Laing 1988; Garrington et al. 1988), in which for radio sources with one-sided jets, depolarisation with wavelength is weaker for the lobe with the radio jet. If the depolarisation is caused by an intervening screen of material, then the visible jet is approaching, and the receding jet is not visible, an observation which can be explained by Doppler boosting.

The Doppler factor γ can be constrained by observations of proper motion of the jets, for example (Cohen et al. 1988) found values of $\gamma \sim 9 - 18$ and Vermeulen & Cohen (1994) found a similar range. The Doppler factor has also been modelled by the contrast between cores and jets (Wardle & Aaron 1997; Hardcastle et al. 1999); typical values found are low, $\beta = 0.5 - 0.7c$, where $\gamma = 1/\sqrt{1-\beta^2}$, i.e. $\gamma \sim 1.15 - 1.4$, or $\gamma \sim 2$ from Bridle et al. (1994). These different Doppler factors can be reconciled in a scheme in which jets have velocity structure. Hardcastle (2006) suggests a model in which the outer sheath of the jet has $\gamma \lesssim 5$, while the spine of the jet has $\gamma \gtrsim 15$.

It should be noted that the bulk relativistic motion of the material in the jet which has Doppler factor γ is not equivalent to the speed at which the heads of a source, powered by jets, advance into the intergalactic medium. This pattern speed was given a rigorous upper limit of $\sim 0.2c$ by Longair & Riley (1979) through statistical studies of radio lobe separations. By refining this technique to statistical analysis of the excess of length of the approaching jet over the receding jet, Scheuer (1995) found a maximum hotspot advance speed of less than $0.1c$. Owsianik & Conway (1998) directly constrain the rate at which the heads of the jets move apart through a multi-epoch study of compact sources, and find a rate of $\sim 0.25h^{-1}c$.

1.3 *The Environment of AGN*

McCarthy et al. (1987) discovered that the radio source axes of radio galaxies align with their extranuclear optical emission, which is known as the "alignment effect". This can be explained by several mechanisms, such as shocking of the host galaxy material by the radio jet (De Young 1998), dynamic coupling between the radio and gravitational axes (Eales 1992) or by inverse Compton scattering of cosmic microwave background photons (Daly 1992). The close correlation between black hole mass and galaxy bulge mass in elliptical galaxies (Magorrian et al. 1998) indicates that AGN feedback may be the key to regulation of star-formation (Silk & Rees 1998). There are several possibilities which could explain this link. An intense starburst triggered by the AGN might deplete the gas and dust and starve the black hole (Archibald et al. 2002). The feedback could also occur the other way, with superwinds from the AGN driving this material out of the galaxy and hence quenching star formation (Fabian 1999).

In all but some unusual cases, powerful AGN are found in elliptical galaxies rather than spiral galaxies (see Section 1.1.1). This raises the question as to what difference in elliptical galaxies triggers the radio jets. One possible answer, set out by Scheuer (1992), is that the elliptical galaxies have undergone recent mergers (Barnes & Hernquist 1991) which result in a misalignment between the spin of the black hole and the angular momentum of the accretion disk which reforms after the merger. As powerful radio jets are thought to be powered by the rotational energy of the black hole (see Section 1.2.5), this would result in a situation where the radio jets and accretion disk are not necessarily perpendicular. This misalignment would correct itself as the black hole is spun up by the new accretion disk on timescales of order $10^7 - 10^8$ years. Observational evidence for misalignments between dust disks and jet axes in radio galaxies has been found by Schmitt et al. (2002), so there is an observational precedent for non-orthogonal axes.

This thesis aims to study in detail the inclination of the accretion disk in a sample of radio-loud quasars, by modelling the optical disk emission, and to compare the distribution of disk axis angles to predicted models. The angle of the jet axis to the line of sight is measured in an entirely independent way, using the radio spectral energy distributions of the quasars. The jet angle distribution is compared to the predicted distribution for this sample of radio sources, and a direct comparison is made between the disk axis angles and the jet angles, to investigate whether the jets of the quasars are launched orthogonally to the plane of the accretion disk.

Chapter 2
Infrared Spectroscopy

The selection of a sub-sample of 19 quasars from the Molonglo Quasar Sample (Kapahi et al. 1998a) is discussed in Section 2.1. Near infrared (J, H and K-band) spectra of this sub-sample were obtained prior to this thesis by J. Baker; the reduction of these spectra is detailed in Section 2.2. The spectra are presented in Section 2.3.

2.1 *Sample selection*

2.1.1 *Molonglo quasar sample*

The Molonglo Quasar Sample, from which the objects for this study were selected, has been defined using minimal selection criteria to avoid biases wherever possible (Kapahi et al. 1998a). The Molonglo Quasar Sample includes all quasars with flux densities $S_{408\mathrm{MHz}} > 0.95$ Jy in a 10° strip in the Southern sky, $-20^\circ > \delta > -30^\circ$, excluding sources with low Galactic latitude ($\mid b \mid > 20^\circ$) and also those in the Galactic R.A. range $14^{\mathrm{h}}03^{\mathrm{m}}$–$20^{\mathrm{h}}20^{\mathrm{m}}$ in order to reduce the size of the sample to a manageable level. Quasar samples that are flux-limited at high radio frequencies preferentially select the core-dominated objects; at 408 MHz, there will be some sources included in the sample which have been boosted in to the sample by their strong core emission.

The initial sample of radio sources were selected from the Molonglo Reference Catalog (MRC) Large et al. (1981), and then identified by VLA 1 arcsecond resolution radio images, optical imaging and spectroscopy. The Molonglo Quasar Sample was defined in parallel with a brother sample of radio galaxies (McCarthy et al. 1996; Kapahi et al. 1998b), the quasars being defined as those sources with broad optical emission lines, and so the quasar sample is expected to be more than 97% complete.

The MRC resulted from a 408MHz survey conducted with the Molonglo Synthesis Telescope. The limiting flux density of the catalog is 0.7 Jy, but it is not complete at this level; it is believed to be 99.9% complete at 1 Jy. The survey frequency and beam size (2.5 arcminutes) of the telescope built in some biases in the range of spectral indices and angular sizes sampled, but these have little effect on sources brighter than 0.95 Jy and with angular sizes smaller than 2.5 arcminutes.

2.1.2 *Molonglo quasar sub-sample*

A sub-sample of 19 high-redshift quasars was selected from the Molonglo Quasar Sample, originally in order to use H α to study reddening. The sub-sample was selected on the basis of four criteria: observability during the telescope period applied for; that the H α and H β emission lines fell in the wavelength windows of the filters; that the objects were sufficiently bright to require only a reasonable integration time; and that they were not in the RA range 14h – 3h. One additional source was excluded due to time constraints.

The optical magnitude limitation is the only factor which adds a significant bias in this selection process. The objects were selected to be brighter than $J \sim 18.5$, and this excluded one source from the sample, MRC0418-288. This source is likely to be reddened or dusty, which means that it has a higher chance of being inclined at a large jet angle to the line of sight. MRC1256-243 was excluded on the basis of time-constraints; however, this source is core-dominated, and would have been boosted into the sample by the core component of emission. Two core-dominated sources exist in the sample, MRC0327-241 and MRC0346-279; these are present as the result of a selection effect, which must be kept in mind when analysing the results, and it should be noted that MRC1256-243 would have been included as part of this group.

2.1.3 *Comparison to the 3CRR sample*

Figure 2.1 shows the K-corrected radio luminosity plotted against redshift for the Molonglo samples of quasars (dark red points) and radio galaxies (purple points). The sub-sample of quasars studied in this thesis are plotted in bright red. These can be seen to fall into three redshift bands: $0.8 < z < 1.0$, where the H α emission line falls in J-band; $1.5 < z < 1.65$, where H α falls in H-band; and $2.2 < z < 2.3$, where H α falls in K-band.

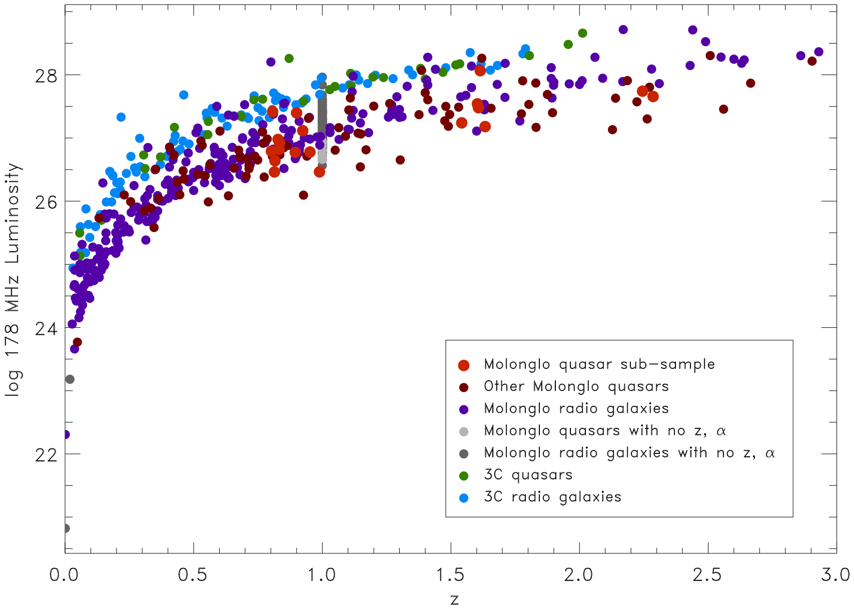

Figure 2.1: Logarithmic, K-corrected 178 MHz luminosity for the Molonglo and 3C samples of radio sources, plotted against redshift. The large red points show the Molonglo sub-sample used in this thesis; the dark red points are Molonglo quasars and the purple points are Molonglo radio galaxies. In cases where no redshift existed for these sources, this was set to $z = 1$, and in cases where there was no radio spectral index, this was set to $\alpha = 1$: these points are marked out by being plotted in pale grey (quasars) and dark grey (radio galaxies). The 3C quasars are plotted in green, and the 3C radio galaxies in blue.

The Molonglo Sample was selected at the relatively high radio frequency of 408 MHz, compared to the 178 MHz-selected 3CRR sample. As the $\log L_{178\mathrm{MHz}} - z$ plot shows, the Molonglo Sample includes fainter and higher-redshift sources than the 3CRR sample. There is a low space density of sources with $\log L_{\mathrm{low-frequency}} \gtrsim 28.3$, so that there is not enough observable volume in the universe to detect examples (e.g. Willott et al. 1998). The penalty for the depth of the Molonglo Sample is paid in terms of uniformity; this sample is not expected to be an entirely representative sample of AGN, as it will include sources which are in the sample by virtue of their strong radio cores alone. The Molonglo Sample therefore contains orientation selection biases, from which the 3CRR sample is expected to be free (e.g. Willott et al. 1998).

2.2 *Data Reduction of Infrared Spectroscopy*

2.2.1 *The infrared data*

Near infrared spectra of the Molonglo quasar sub-sample were taken with the Infrared Spectrometer And Array Camera (ISAAC) spectrograph (Moorwood et al. 1998) at the Very Large Telescope (VLT), part of European Southern Observatory (ESO), between October 2001 and February 2002, prior to this thesis. ISAAC is mounted on the Naysmyth B focus of telescope UT1. The spectra were taken in short wavelength low resolution mode, using a 1 arcsecond wide slit. The observational details, including exposure times, seeing and airmass, are given in Table 2.1.

Quasar (1)	(2)	R.A. J(2000) (3)	Dec. J(2000) (4)	z (5)	b_J (6)	Date obs. (7)	Waveband (8)	Exp. time (s) (9)	Seeing arcseconds (10)	Airmass (11)
1	MRC0222-224	02 25 16.6	-22 15 22	1.603	19.1	2001-10-07	H	180 × 8	0.9	1.015
2	MRC0327-241	03 29 54.1	-23 57 09	0.895	19.4	2001-10-12	J	180 × 8	0.6	1.209
3	MRC0346-279	03 48 38.1	-27 49 14	0.989	20.5	2001-10-12	J	180 × 8	0.7	1.077
4	MRC0413-210	04 16 04.3	-20 56 28	0.807	18.4	2001-10-12	J	180 × 8	0.9	1.053
5	MRC0413-296	04 15 08.7	-29 29 03	1.614	18.6	2001-10-12	H	180 × 8	0.7	1.004
6	MRC0430-278	04 32 17.7	-27 46 24	1.633	21.3	2001-12-23	H	180 × 10	1.2	1.138
7	MRC0437-244	04 39 09.2	-24 22 08	0.834	17.5	2001-10-06	J	180 × 8	0.6	1.012
8	MRC0450-221	04 52 44.7	-22 01 19	0.900	17.8	2001-11-20	J	180 × 8	0.5	1.214
9	MRC0549-213	05 51 58.3	-21 19 49	2.245	19.1	2001-12-22	K	100 × 28	0.5	1.075
10	MRC1019-227	10 21 27.6	-23 01 54	1.542	21.1	2001-12-25	H	180 × 10	0.7	1.144
11	MRC1114-220	11 16 54.5	-22 16 53	2.286	20.2	2002-01-01	K	100 × 28	0.7	1.137
12	MRC1208-277	12 10 43.6	-27 58 55	0.828	18.8	2002-01-27	J	180 × 8	0.5	1.034
13	MRC1217-209	12 20 22.3	-21 13 09	0.814	20.2	2002-02-05	J	180 × 8	1.1	1.106
14	MRC1222-293	12 25 01.2	-29 38 17	0.816	18.5	2002-01-27	J	180 × 8	0.6	1.006
15	MRC1301-251	13 04 14.7	-25 24 37	0.952	21.0	2002-02-12	J	180 × 8	0.4	1.011
16	MRC1349-265	13 52 10.3	-26 49 28	0.924	18.4	2002-02-11	J	180 × 8	0.5	1.051
17	MRC1355-215	13 58 38.2	-21 48 54	1.607	19.9	2002-02-13	H	180 × 8	0.5	1.002
18	MRC1355-236	13 58 32.7	-23 52 20	0.832	17.8	2002-02-11	J	180 × 8	0.4	1.013
19	MRC1359-281	14 02 02.4	-28 22 25	0.802	18.7	2002-02-14	J	180 × 16	0.6	1.048

Table 2.1: Observational details:
Columns 1 and 2 : Index and name of the quasars.
Columns 3 and 4 : J(2000) right ascension (in hours, minutes and seconds) and declination in degrees, minutes and seconds.
Column 5 : Redshift of the quasar.
Column 6 : Optical b_J magnitude from the UK Schmidt IIaJ plates, where $b_J = B - 0.23(B - V)$ (Bahcall & Soneira 1980)
Column 7 : Date of the observations.
Column 8 : Waveband of the observations.
Column 9 : Exposure time in seconds for each exposure, and the total number of exposures in the observation, i.e. 180 × 8 indicates a total integration time of 1440s, split into 8 frames.
Column 10 : Seeing of the observation in arcseconds, measured from the images.
Column 11 : Airmass of the observation.

2.2.2 *Pre-reduction and detector effects*

The first stage of the data reduction process was to clean the raw images to remove cosmic rays and systematic detector effects. Cosmic rays were removed from the object frames in a two-stage process. Firstly, *crmedian* in *IRAF*[*] (Tody 1986, 1993) was used to automatically remove the most obvious cosmic rays, which fell more than 10σ below or 3σ above the median value, replacing these pixels with the median value. The regions of the image including the spectrum and the sky subtraction zone were then cleaned by hand using *credit* in *IRAF*, comparing sets of images to identify bad pixels and cosmic rays, and replacing these with local sky values.

The detector used with ISAAC was a Hawaii Rockwell 1024 × 1024 array (with a scale of 0.147 arcsecond/pixel), which had four quadrants which were read out separately. The detector had a number of known reproducible image effects (Amico et al. 2002): "electrical ghosts" and the "odd-even column effect" were found to have the highest impact on the images, and the other effects were neglected. The "electrical ghosts" consist of an additional signal, which on each spectral row is proportional to the sum of the intensity on the row itself, and the row 512 rows away. This was corrected for using the dedicated *eclipse* (Devillard 1997) recipe *ghost*. This algorithm collapses the image in the spectral direction, summing over all points, and adds to each spatial point in the 1-D array the counts from the spatial point 512 pixels away. This array is then multiplied by 1.35×10^{-5} according to the empirical value given in the *ISAAC Data Reduction Guide* (Amico et al. 2002) and subtracted from each column in the image.

The "odd-even column effect" is an offset between the odd and even columns in the array, creating a low-intensity peak-trough pattern with intensity of $\sim 5\%$ of the pixel value, repeating every two pixels in the spectral direction. It is a function of the flux detected, and of the quadrant of the detector. This issue disappeared and reappeared over the period during which these data were taken, and checks were made by eye as to whether this effect was important for each set of observations by collapsing flatfield images from each night along the spatial direction and examining them by eye.

---

[*] *IRAF* is distributed by the National Optical Astronomy Observatories, which are operated by the Association of Universities for Research in Astronomy, Inc., under cooperative agreement with the National Science Foundation.

The "odd-even effect" was corrected for using an *IDL* script which divided the image into quadrants, took the forward Fourier transform of each quadrant, masked the two pixels corresponding to the highest frequency spatial variations, and then performed the inverse Fourier transform and reassembled the quadrants. The number of pixels to mask in order to remove the effect without degrading the data was found by experimentation; the worst-affected spectra had the effect reduced to $\lesssim 1\%$ by the correcting algorithm.

The images were then divided with a flatfield frame, to remove pixel-to-pixel variations due to the detector from the image. The flatfield was made by taking pairs of images, one in which the detector was illuminated by a lamp, and one in which it was not, and subtracting these from each other. This frame was then normalised by dividing each pixel in the frame by the mean value, calculated from the central region of the CCD. The result was an image which convolved the pixel-to-pixel variations of the CCD with the spectral shape of the lamp and the illumination function of the lamp in the spatial direction. This frame was created with a routine written in *IDL*. The illumination function of the lamp in the spatial direction was then removed by fitting a polynomial in this direction, and dividing the flatfield image by the polynomial using the *IRAF* task *response*. The spectral shape of the lamp was not removed at this point in the reduction, but was divided out when the quasar spectrum was divided by the standard star spectrum, since they were both corrected using the same flatfield.

2.2.3 *Distortion correction and wavelength calibration*

Each image was corrected to remove the curvature of the spectrum along the spatial direction (the distortion correction). Since the quasars are faint, this correction was made by fitting a function to the standard stars closest in time and position on the slit. The peaks of the stellar spectra were marked in the spatial direction using the *identify* and *reidentify* tasks in *IRAF*, and fitted with a 3^{rd}-order (3-term) Legendre function using *fitcoords* in *IRAF*. The residuals for this are of the order of 0.03 – 0.15 pixels for J-band and H-band, and 0.1 – 0.4 pixels for K-band.

The dispersion correction accounts for the variations in wavelength scale along the spectrum. Two separate dispersion solutions were found: the arc frames have easily identifiable, non-blended lines which give a solid wavelength scale, but since the grating can move between observations, the night-sky OH lines were used to apply a small shift correction to this scale. Selecting the arc frames based on the strongest, least blended lines, the argon lamp frames were chosen for the K-band spectroscopy, and the xenon lamp frames for the J- and H-band spectroscopy. The wavelength solution was found using *identify* and *reidentify* in *IRAF* to attach laboratory-measured vacuum wavelengths to the strong lines, tracing them spatially across the CCD so the lines were mapped in two dimensions. The same procedure was carried out to identify the OH lines, using the atlas of Rousselot et al. (2000). Some of the H-band sky lines were rejected from the fitting process as they were saturated.

The *IRAF* routine *fitcoords* was used to fit a 4th-order (4-term) Legendre function to the spectral direction (except in the case of the sky lines in J-band, which were better fit with a 3rd-order (3-term) Legendre function) and a 3rd-order (3-term) Legendre function in the spatial direction (see Table 2.2 for orders of fit and residuals). The images were then mapped to a linear wavelength scale. This wavelength scale was chosen to match the average wavelength scale per pixel in the images before the distortion correction.

Waveband	Source of correction	Spectral order	Spatial order	Typical residuals (Å)
J	Arc lamp	4	3	1 – 2
J	Sky lines	3	3	2 – 3
H	Arc lamp	4	3	2 – 3
H	Sky lines	4	3	2 – 3
K	Arc lamp	4	3	3 – 4
K	Sky lines	4	3	3 – 5

Table 2.2: The orders of fit and residuals from performing the dispersion correction using *fitcoords* in *IRAF*.

The distortion correction and dispersion correction were applied simultaneously in the *IRAF* routine *transform*, to remove the spectral curvature and map the dispersion to a linear scale, while conserving the flux. This procedure was performed twice, creating two separate images, one with the arc lamp dispersion correction and one with the OH line dispersion correction. The cross-correlation between these images was performed with an *IDL* script which called the *c_correlate* routine. The image corrected with the arc lines was shifted to a zero point found from the sky-line corrected image.

2.2.4 *Spectrum combination and extraction*

In the infrared, the sky background is strong (for MRC0222-224, the sky lines per frame were estimated as 100 times brighter than the $H\alpha$ emission line, and 300 times brighter than the quasar continuum emission), and so good sky subtraction is imperative. This is accomplished by nodding and jittering along the slit; every two image frames, the telescope is nodded so that the target moves by a distance of $\sim$ 60 arcseconds along the slit, between two positions A and B such that the images form a sequence ABBAABBA for example, where the frames marked A are taken in one nod position, and the frames B are taken in the other nod position. On top of this, a small extra offset within a box size of 15 arcseconds is added, such that the spectrum does not fall on exactly the same pixels of the CCD each time: this acts as insurance against dead pixels or other CCD artifacts. The sequence is then $A_1B_2B_2A_3A_3B_4B_4A_5$, where the subscripts denote different jitter positions.

The procedure to coadd the spectra in these image frames with sky subtraction is to first subtract the images in pairs, i.e. $A_1 - B_2$, $B_2 - A_3$, etc, which removes the sky lines from each image using the image closest in time. Each of the resultant images is then inverted, shifted, and added back to the un-inverted image, such that the two spectra are added. This was performed for all pairs of images, and all the spectra were then stacked.

This process was performed using a script written in *IDL*, which used the approximate position of the spectrum in each image to search for the spectrum and fit a Gaussian, hence finding the spectrum position in fractional pixels. The spectra were then shifted along the spatial direction to coadd them, since the spectral curvature and variation in spectral scale were removed by the dispersion and distortion corrections.

The spectrum was extracted using *apall* in *IRAF* which fitted an aperture to the spectrum and summed the fractional pixels, collapsing them in the spatial direction. The aperture width was found by summing together 200 pixels across the spatial direction to get a strong fix on the position of the spectrum, and determining the full width half maximum of the spectrum, which gives an optimal signal to noise spectrum when the pixel values are summed across this aperture. The spectrum was assumed to be straight, since a correction for spatial curvature had already been made. The spectrum was then scaled for exposure time, and the gain was used to convert the spectrum into units of electrons. The standard star spectra were extracted in an analogous way.

The official ESO measurement of gain for the ISAAC spectrograph in short wavelength mode is 4.5 electrons per ADU. This was checked from the data by taking a section of a flatfield frame comparable in dimensions to the extracted spectrum, and creating a histogram of the pixel values. The gain was calculated as the square of the histogram width, since the noise is expected to be Poisson. The results were found to be consistent with the given value, and the ESO value was therefore used.

2.2.5 *Flux calibration*

The flux calibration was made by comparing the spectrum of the standard star with a model flux standard star. Hot stars are relatively featureless, and so these were approximated by a blackbody of the correct temperature, created using the *planck* function from the *IDL* Astronomy User's Library (Landsman 1993). Temperatures were taken from the Tycho-2 Spectral Type Catalog (Wright et al. 2003) which converts spectral types into temperatures. Since using spectral types to estimate temperatures is not ideal, Geneva-Copenhagen catalogue values were used where these existed (5 of the 18 standard stars). Solar-type stars (F and G spectral types) in the H and K wavebands are also featureless enough to approximate as blackbodies. The cool stars observed in J-band were modelled by the composite standard star templates of Pickles (1998). These models were normalised at the central wavelength of the waveband using 2MASS magnitudes[†]. Zero-points from Zombeck (1990) were used to convert the magnitudes to fluxes.

The flux standards were also used as "telluric standards", to remove atmospheric absorption lines from the quasar spectra. The intrinsic features of the standard star were therefore removed to leave only these telluric absorption lines. For solar-type stars, this was accomplished using a solar spectrum[‡] normalised to unity, degraded with *gauss* in *IRAF* to the resolution of the standard star spectrum by matching the FWHM of the absorption lines. This was then divided into the spectrum. This was not a perfect process,

---

[†] This thesis makes use of data products from the Two Micron All Sky Survey, which is a joint project of the University of Massachusetts and the Infrared Processing and Analysis Center/California Institute of Technology, funded by the National Aeronautics and Space Administration and the National Science Foundation

[‡] NSO/Kitt Peak FTS data used here were produced by NSF/NOAO.

and minor adjustments were made by eye, shifting the template solar spectrum by up to two pixels. The hot stars have strong Paschen and Brackett absorption lines in their spectra, which were modelled using the relative fluxes of these lines normalised by scaling the intensity of the strongest absorption line to the observed intensity of this line in the telluric standard spectrum. Any of the intrinsic lines which were not cleanly removed were neatened up by interpolating up to 10 pixels across the artifacts; this method was used with care, referencing the theoretical atmospheric transmission curves[§] to check that only spurious features were removed.

To make the calibration, the quasar spectrum was divided by the cleaned standard star spectrum, and multiplied by the model standard star spectrum. The division of the quasar spectrum by the standard star removed the spectral distribution of the flatfield lamp; the transmission of the instrument; and the telluric absorption lines. The ratio of the standard spectrum to the model spectrum for a standard star of the same type applied the flux calibration.

Two further small corrections were made during the flux calibration process. The first is that a small correction was made to compensate for reddening of the spectrum due to dust in the Milky Way. The corrections of between 0.01 – 0.14 magnitudes were taken from the Schlegel et al. (1998) maps of Galactic dust emission. The second was to correct the spectra to the heliocentric rest frame [¶].

2.2.6 *Redshifts*

New redshift measurements were made where appropriate, from the ISAAC spectra including [O III] lines where available, or from the latest optical spectra from EFOSC2 on the ESO 3.5 m telescope (in preparation). If no recent spectra including narrow lines were available, the most recent redshift values were taken. Table 2.3 lists these updated redshifts and their origins. The only exception to this was MRC1349-265, whose redshift was given as $z = 0.934$ in Baker et al. (1999), but for which $z = 0.924$ was a solid measurement, even in the absence of narrow [O III]; a change of this size is likely to result from a typing

---

[§] NSO/Kitt Peak FTS data used here were produced by NSF/NOAO.

[¶] The correction was calculated using ephemerides from the Markwardt IDL library.

error in the original paper.

Quasar		Redshift	Source of redshift
1	MRC0222-224	1.603	EDS
2	MRC0327-241	0.895	JCB
3	MRC0346-279	0.989	EDS/JCB
4	MRC0413-210	0.807	EDS/JCB
5	MRC0413-296	1.614	NEW
6	MRC0430-278	1.633	NEW
7	MRC0437-244	0.834	EDS
8	MRC0450-221	0.900	EDS
9	MRC0549-213	2.245	EDS/JCB
10	MRC1019-227	1.542	NEW
11	MRC1114-220	2.286	NEW
12	MRC1208-277	0.828	JCB
13	MRC1217-209	0.814	EDS/JCB
14	MRC1222-293	0.816	JCB
15	MRC1301-251	0.952	JCB
16	MRC1349-265	0.924	NEW
17	MRC1355-215	1.607	NEW
18	MRC1355-236	0.832	JCB
19	MRC1359-281	0.802	EDS/JCB

Table 2.3: The sources of the redshifts are as follows:
JCB: Baker et al. (1999)
EDS: de Silva et al. (in preparation, a)
NEW: New measurement.
MRC0346-279 and MRC1217-209 have questionable redshifts, but the available data was not sufficient to make a better measurement.

2.2.7 *Creating error spectra*

Error spectra were created for the Bayesian optimisation process used in Chapter 3. The greatest source of error in these spectra arises from the strong sky lines. A Poisson error is therefore created by extracting a sky spectrum in an analogous way to the quasar spectrum and taking the square root of this, accounting for the instrumental gain.

The sky spectra were created from single images which were corrected for distortion effects and wavelength corrected. Spectra were extracted from the first image in each set of observations using exactly the same aperture as was used to extract the quasar spectrum from the combined frame. In order to apply the flux calibration to these spectra such that they were in units of electrons, they were corrected by a frame made from the model star spectrum divided by the standard star spectrum, normalised to match a multiplication of the transmission curve for the correct instrumental setup with an atmospheric absorption spectrum. The heliocentric correction was applied, but the Galactic extinction correction was not applied to these spectra, as the sky emission lines are formed locally.

The square root of the sky spectrum, in units of electrons, was taken to find the Poisson error for a single image frame, and this was then multiplied by the number of exposures to find the overall error spectrum. Finally, this spectrum was converted back to real flux units, to match the quasar spectrum.

The ISAAC CCD is 99% linear to 10,000 ADU and saturates at 40,000 ADU, for the short wavelength spectroscopy mode. No lines were found to be saturated, except at the very long-wavelength edge of K-band, but some of the strongest sky lines were found to be non-linear: these lines are listed in Table 2.4.

2.3 *Reduced IR Spectra*

The reduced spectra are presented in Figure 2.2. These have been slightly smoothed, in order to more clearly display the true features.

2.3.1 *Notes on infrared spectra*

MRC0222-224 : Broad and narrow H α lines are visible. The sky subtraction is poor.

MRC0327-241 : There is some visible H α structure, but it is not clearly defined, and H α has a low equivalent width. The continuum slopes with an index of $\alpha \sim 1.7$, where $F_{\nu} \propto \nu^{-\alpha}$. This is a BL-Lac type continuum, as these have spectral indices of $\alpha > 1$ (Brown et al. 1989).

MRC0346-279 : There is some visible H α structure, but it is not clearly defined, and H α has a low equivalent width. The continuum is strongly sloped, with $\alpha \sim 2.7$; this is a BL-Lac type continuum.

MRC0413-210 : A clean spectrum with narrow H α and [S II] visible.

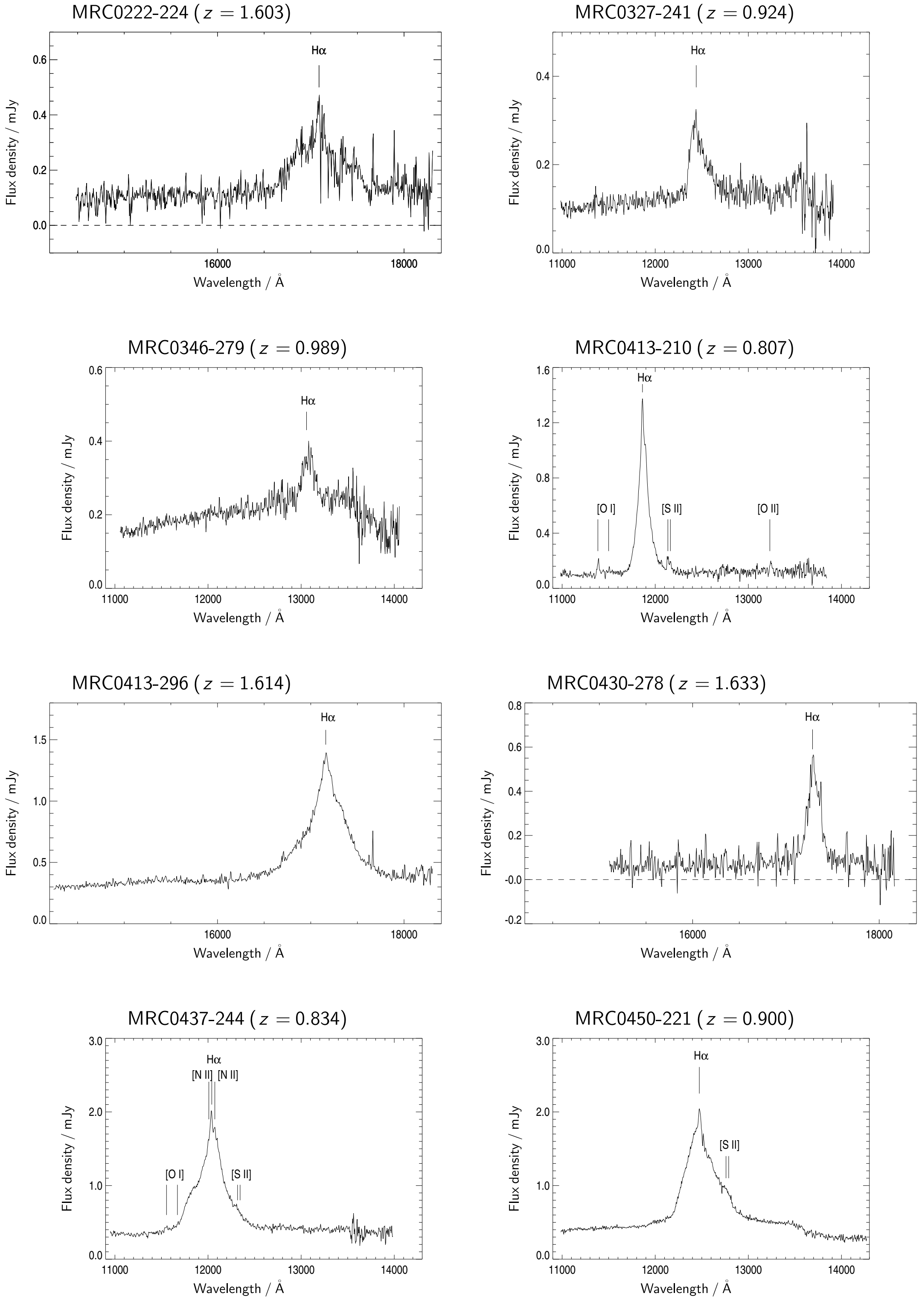

MRC0222-224 ($z = 1.603$)

MRC0327-241 ($z = 0.924$)

MRC0346-279 ($z = 0.989$)

MRC0413-210 ($z = 0.807$)

MRC0413-296 ($z = 1.614$)

MRC0430-278 ($z = 1.633$)

MRC0437-244 ($z = 0.834$)

MRC0450-221 ($z = 0.900$)

Figure 2.2: Observed near-infrared spectra, including the H α emission lines, for the Molonglo sub-sample quasars, observed with ISAAC on ESO's VLT UT1. The observed wavelength is in Å, and the flux density scale is in mJy. The spectra have been slightly smoothed.

MRC0549-213 ($z = 2.245$)

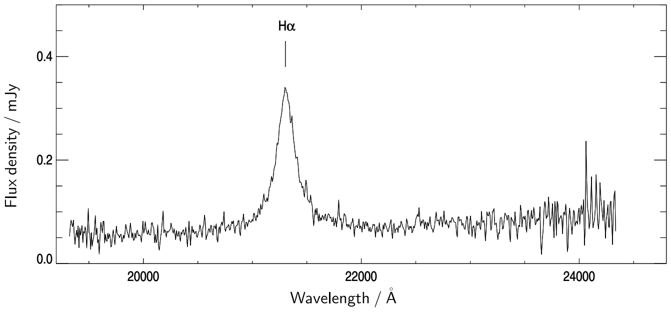

MRC1019-227 ($z = 1.542$)

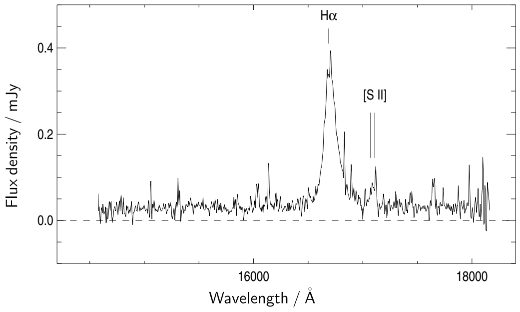

MRC1114-220 ($z = 2.286$)

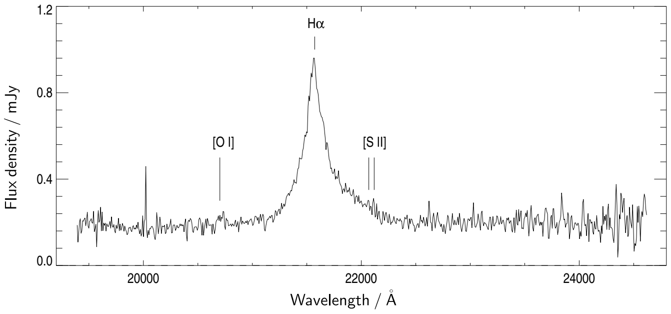

MRC1208-277 ($z = 0.828$)

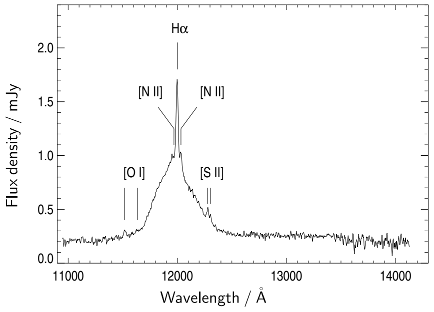

MRC1217-209 ($z = 0.814$)

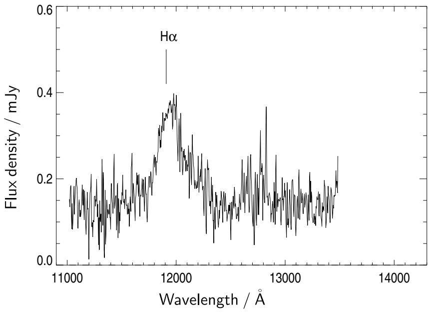

MRC1222-293 ($z = 0.816$)

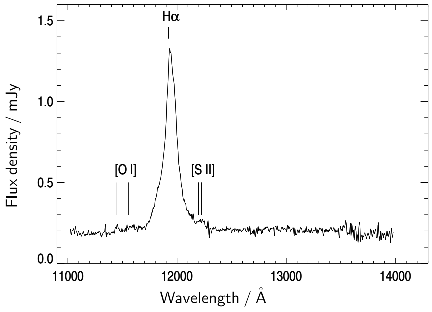

MRC1301-251 ($z = 0.952$)

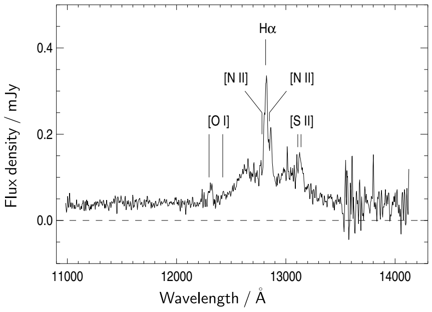

MRC1349-265 ($z = 0.924$)

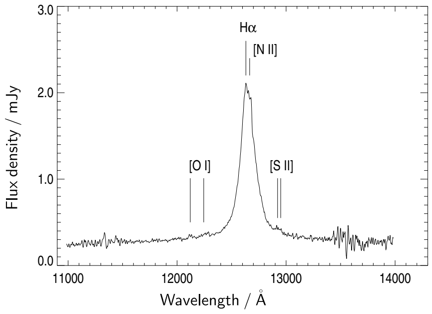

MRC1355-215 ($z = 1.607$)

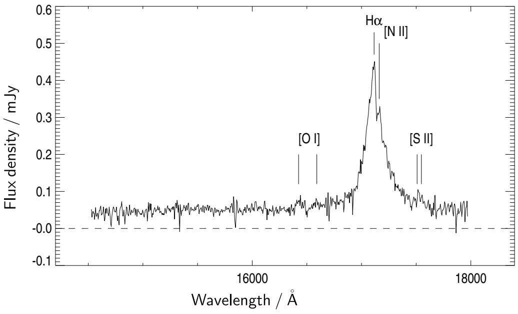

MRC1355-236 ($z = 0.832$)

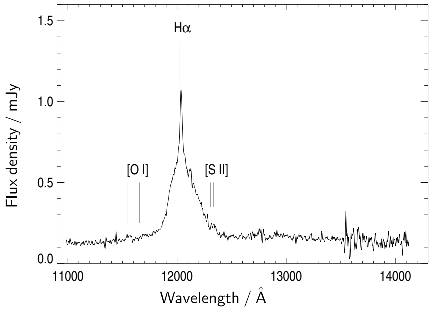

MRC1359-281 ($z = 0.802$)

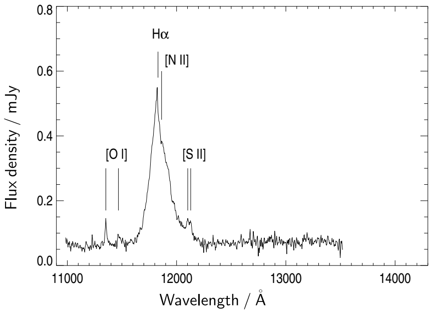

Quasar		Waveband	Observed wavelength of non-linear lines (Å)	Notes
1	MRC0222-224	H	15055.5, 15833.2, 16692.1, 17653.2, 16128.6	
2	MRC0327-241	J	None	
3	MRC0346-279	J	None	
4	MRC0413-210	J	None	
5	MRC0413-296	H	15055.5, 15833.2, 16692.1, 17653.2	
6	MRC0430-278	H	15055.5, 15833.2, 16692.1, 17653.2	
7	MRC0437-244	J	None	
8	MRC0450-221	J	None	
9	MRC0549-213	K	> 23300	Saturated at > 24300 Å
10	MRC1019-227	H	15055.5, 15833.2, 16692.1, 17653.2, 15332.4, 16030.8, 16128.6	
11	MRC1114-220	K	> 23300	Saturated at > 24300 Å
12	MRC1208-277	J	None	
13	MRC1217-209	J	None	
14	MRC1222-293	J	None	
15	MRC1301-251	J	None	
16	MRC1349-265	J	None	
17	MRC1355-215	J	None	
18	MRC1355-236	J	None	
19	MRC1359-281	J	None	

Table 2.4: OH lines which were bright enough to be non-linear, and around which the spectrum was considered to be non-usable for Bayesian fitting purposes.

MRC0413-296 : The $H\alpha$ line has a triangular profile with no clear broad and narrow components visible. The sky subtraction is poor.

MRC0430-278 : There are no separate broad and narrow components visible. The sky subtraction is very poor.

MRC0437-244 : The $H\alpha$ line has complex broad structure and a narrow component.

MRC0450-221 : The $H\alpha$ line has complex broad structure and a narrow component.

MRC0549-213 : The $H\alpha$ line has a triangular profile with no clear broad and narrow components visible.

MRC1019-227 : The sky subtraction is poor. The apparent narrow $H\alpha$ line is a sky line defect, and is not fit in the Bayesian optimisation.

MRC1114-220 : The H α line has a triangular profile with no clear broad and narrow components visible.

MRC1208-277 : The H α line has complex broad structure and the narrow lines are very strong.

MRC1217-209 : This spectrum is very noisy due to poor seeing. The structure of H α is not readily apparent.

MRC1222-293 : A clean spectrum.

MRC1301-251 : The narrow lines are very strong, dominating the spectrum.

MRC1349-265 : Narrow H α and [S II] are visible.

MRC1355-215 : Narrow H α is visible. The sky subtraction is poor.

MRC1355-236 : There is a strong narrow H α line.

MRC1359-281 : The H α profile is very triangular, such that it is not easy to distinguish the broad and narrow lines.

2.4 *Conclusions*

High quality infrared spectra including the H α emission line and corresponding error spectra have been generated for a sub-sample of Molonglo quasars at $0.8 < z < 2.3$. There is complex structure visible in many of the H α lines.

Chapter 3

Disk Axis Inclination Angles

3.1 *Introduction*

Optical emission from the sub-sample of Molonglo quasars in the region of H α was emulated using a range of multi-component models. Two sets of the models included a component of emission from a Keplerian accretion disk surrounding the black hole at the heart of the quasar. This component of the emission had free parameters which included the inclination angle of the disk axis to the line of sight.

These models were fitted to the observed infrared spectra of the quasars, which included the redshifted H α line, using a Bayesian statistical Monte Carlo routine. For each model, the best-fit parameters and the Bayesian evidence and information were obtained. The Bayesian evidence was used to discriminate between the models, with the aim of discovering whether there is evidence for accretion disks in these quasars, and if there are accretion disks present, determining the angles of their axes to the line of light.

Section 3.2 describes the theoretical model used for the emission from an accretion disk, and in Section 3.3 the multi-component model for the emission region surrounding H α is described. Section 3.4 describes the Bayesian Monte Carlo techniques to make the fits to the data. Section 3.5 discusses how the best model for the data is selected and the stability of the results. Section 3.6 presents the fits to the data, and discusses the results, and some brief conclusions are drawn in Section 3.7.

3.2 *Accretion Disk Emission*

3.2.1 *The equation for emission from an accretion disk*

The equation used in fitting the disk emission is taken from Chen & Halpern (1989), which is a refinement of the equations presented in Chen et al. (1989) to include the effects of local Doppler broadening of the emission. The largest assumption in this derivation is the assumption of a circular, Keplerian disk. Allowing the disk to be elliptical allows a greater variety of line shapes (Strateva et al. 2003). The Schwarzchild metric and the weak field approximation (a linear perturbation to the Special Relativity metric) are assumed. The surface emissivity of the disk is assumed to vary as a power law with radius, and the disk is assumed to be optically thick. The specific intensity of a line in the emitting frame is represented by this emissivity multiplied by a Gaussian function in frequency.

Taking the equation for emission from a geometrically-thin, optically-thick Keplerian disk from Chen & Halpern (1989):

$$F_{\nu} = K \int_{R_{\text{inner}}}^{R_{\text{outer}}} \int_{-\frac{\pi}{2}}^{\frac{\pi}{2}} \exp - \frac{(\frac{\nu}{\nu_0} - D)^2}{2D^2 \Delta v^2} D^3 R^{1-q} g(D) \mathrm{d}R \mathrm{d}\phi \tag{3.1}$$

where

$$K = \frac{G^2}{\nu_0 c^4} \frac{2\epsilon_0 M^2 \cos\theta_{\text{disk}}}{4\pi d^2} \frac{\Delta v}{(2\pi)^{\frac{1}{2}}} \tag{3.2}$$

and

$$g(D) = 1 + \frac{1}{R} \left\{ \frac{2D^2}{D^2 \cos^2\theta_{\text{disk}} + R(D - (1 - \frac{3}{R})^{\frac{1}{2}})^2} - 1 \right\} \tag{3.3}$$

and G is the gravitational constant, c is the speed of light, M is the black hole mass; ϵ_0 is the normalisation and q is the radial exponent of the disk emissivity, defined by $\epsilon = (\epsilon_0/4\pi)R^{-q}$; d is the distance to the quasar; θ_{disk} is the angle of the disk axis to the line of sight; ν_0 is the characteristic frequency; Δv is the dimensionless local velocity dispersion of the disk material in units of c; R is the dimensionless disk radius in units of the gravitational radius, R_{G}, integrated between characteristic inner and outer radii of R_{inner} and R_{outer}; ϕ is the angle of the disk axis to be integrated over; ν_0 is the rest frequency and ν is the observed frequency; and $D = \frac{\nu}{\nu_e}$, the Doppler factor, where ν_e is the emission frequency.

In the weak field approximation, the Doppler factor is

$$D = \frac{(1 - \frac{3}{R})^{\frac{1}{2}}}{(1 + R^{-1} \sin\theta_{\text{disk}} \sin\phi)}. \tag{3.4}$$

To simplify these equations, multiply $g(D)$ by R

$$Rg(D) = R - 1 + \left\{ \frac{2D^2}{D^2 \cos^2\theta_{\text{disk}} + R(D - (1 - \frac{3}{R})^{\frac{1}{2}})^2} \right\} \tag{3.5}$$

$$Rg(D) = R - 1 + \left\{ \frac{2}{\cos^2\theta_{\text{disk}} + R(1 - \frac{1}{D}(1 - \frac{3}{R})^{\frac{1}{2}})^2} \right\}. \tag{3.6}$$

Substituting for D

$$Rg(D) = R - 1 + \left\{ \frac{2}{\cos^2\theta_{\text{disk}} + R(1 - (1 + R^{-\frac{1}{2}} \sin\theta_{\text{disk}} \sin\phi))^2} \right\} \tag{3.7}$$

$$Rg(D) = R - 1 + \frac{2}{(\cos^2 i + \sin^2\theta_{\text{disk}} \sin^2\phi)^2} \tag{3.8}$$

$$Rg(D) = R - 1 + \frac{2}{(1 - \sin^2\theta_{\text{disk}} \cos^2\phi)^2}. \tag{3.9}$$

Now, the equation reduces to

$$\begin{aligned} F_\nu \quad = \quad & K \int_{R_{\text{inner}}}^{R_{\text{outer}}} \int_{-\frac{\pi}{2}}^{\frac{\pi}{2}} \exp - \frac{(\frac{\nu}{\nu_0} - D)^2}{2D^2 \Delta v^2} D^3 R^{-q} \\ & \left[R - 1 + \frac{2}{(1 - \sin^2\theta_{\text{disk}} \cos^2\phi)^2} \right] \mathrm{d}R \mathrm{d}\phi. \end{aligned} \tag{3.10}$$

Finally, using the substitution $\frac{\nu}{\nu_0} = \frac{\lambda_0}{\lambda}$ then

$$\begin{aligned} F_\nu \quad = \quad & K \int_{R_{\text{inner}}}^{R_{\text{outer}}} \int_{-\frac{\pi}{2}}^{\frac{\pi}{2}} \exp - \frac{(\frac{\lambda_0}{\lambda D} - 1)^2}{2 \Delta v^2} D^3 R^{-q} \\ & \left[R - 1 + \frac{2}{(1 - \sin^2\theta_{\text{disk}} \cos^2\phi)^2} \right] \mathrm{d}R \mathrm{d}\phi. \end{aligned} \tag{3.11}$$

When fitting to an observed line shape, the parameters R_{inner}, R_{outer}, θ_{disk} and Δv can be found from the line shape, while the normalisation fixes $\epsilon_0 M^2$. The radial exponent of the disk emissivity q can also be fitted from the line shape; however, to reduce the number of free parameters and simplify the model, this parameter was fixed at a fiducial value of $q = 3$ for H α (Eracelous & Halpern 2003). This is a reasonable approximation to make, since the emission line flux re-radiated by the disk is proportional to the illuminating flux, which is predicted to vary as R^{-3}, for a wide range of radii.

3.2.2 *Integrating the disk emission*

Finding a model of accretion disk emission by integrating Equation 3.11 is computationally time-consuming, and therefore it is not practical to calculate this emission from within the Bayesian Monte Carlo routine. The disk emission is therefore calculated for a grid of input parameters, shown in Table 3.1. These models were written to a binary file, which was designed to be small enough that it could be read into the memory of the machines that the Bayesian fitting of the disk emission was run on. The integration of Equation 3.11 was performed with a multi-dimensional Monte Carlo integration routine, *gsl_monte_vegas*, from the GNU Scientific Library (GSL).

Parameter	Range	Number of points	Log?
Wavelength	6064 – 7064 Å	101	No
Sine of the disk axis inclination angle	0 – 0.9994	21	No
Local velocity dispersion of disk material	$10^{-3} - 10^{-2}c$	21	Yes
Inner disk radius	100 – 1000 R_G	21	Yes
Multiplication factor for disk outer radius	2 – 100	26	Yes

Table 3.1: Ranges of input parameters for the accretion disk model. The outer radius of the accretion disk is defined in terms of a multiplication factor for the inner radius. Column 2 gives the range covered by the parameter values, Column 3 gives the number of points in the array covering these values, and Column 4 states whether the coverage of the parameter space is logarithmic or not.

The wavelength coverage of the disk models is 6064 – 7064 Å, which was chosen because for all quasars in the sub-sample, the line emission was observed to be negligible outside this region. There are some disk emission models at the outer edges of the parameter space which have significant intensity at the boundaries of this region, but these models would simply be selected against during the fitting process. The emission models are calculated at a resolution of 10 Å, which is adequate, as the resolution of the spectra themselves is 12 – 16 Å, and the accretion disk emission is smooth and broadband.

The sine of the disk axis angle is allowed to vary across almost all of the possible parameter range, stopping just short of a value of unity (an exactly edge-on disk), which is an extremely unlikely case; values of exactly unity caused errors in the integration routine.

The local velocity dispersion of the material in the disk covers the range 10^{-3} to $10^{-2}c$, where c is the speed of light; these values are similar to those used by Strateva et al. (2003). This assumes that the local velocity dispersion in the disk is of similar order to that in the classical broad-line region, which is located at a similar distance from the black hole.

The inner and outer disk radii are defined in terms of gravitational radii. The inner disk radius has a logarithmic range, and the outer disk radius is defined in terms of a logarithmic multiplication factor for the inner radius. These ranges were chosen to agree with those used in similar studies: Strateva et al. (2003) find that the inner radii of the disks are $\sim$ 200 – 800 R_{G}, and the outer radii are $\sim$ 700 – 4000 R_{G}, mostly in the range $\gtrsim$ 2000 R_{G}. Bon (2005) finds inner radii from $100 - 600 R_{\mathrm{G}}$, and outer radii from 3 – 200 times the inner radius, with the largest disk being 1.24×10^5 R_{G} in diameter.

The initial file of disk emission models, created with 10,000 Monte Carlo steps per integration point, was tested by fitting spline curves to these models and checking for model points which differed from the splines by more than 3 percent. These models were then checked by eye, as they were mostly artifact-free but sharply peaked. The models were also compared to a file of disk emission models that was created with an alternative integration method, Romberg integration from Numerical Recipes in C (Press et al. 1992) altered to work for two-dimensional integration; this method produced a set of models which was found to contain more artifacts, but which was useful as a comparison for the best set of models. On the basis of these tests, large areas of the parameter space where numerous errors were seen in the disk models were chosen to be integrated with 20,000 calls or 50,000 calls to the Monte Carlo optimisation. Any spurious values in the models (these were usually at the extreme edges of the wavelength range) were interpolated over.

The file of disk emission templates was then tested again, and found to contain no extraneous dips or peaks with fluctuations greater than 3 percent of a smoothed spline fit to the model.

During the Bayesian fitting process, the disk parameters (sine of the angle of the disk axis to the line of sight $\sin\theta_{\mathrm{disk}}$, local velocity dispersion of disk material Δv, and the inner and outer radii, R_{inner} and R_{outer}) are allowed to take continuous values over the prior ranges. The model for each set of parameters is calculated by interpolating between the sixteen disk emission templates which bracket the required parameter values. This is a reasonable approximation, since the disk emission varies slowly over each of the parameter ranges.

3.3 *Models of Optical Quasar Emission*

3.3.1 *Continuum emission*

The emission from the quasars is modelled as a sum of different components. A smooth, broadband UV and optical continuum arises from the energy released as the central black hole accretes matter; by the virial theorem, half of the potential energy of the infalling matter is dissipated, by radiation and mass loss (Gaskell 2008). This part of the emission is not fitted by the Bayesian optimisation, since it is dominated by the processes occurring immediately around the black hole, and not the distribution of gas and dust outside the central region which is the focus of this study. Instead, it is subtracted from the spectrum, using either a linear or a quadratic fit made in *DIPSO*[*]. The necessity of the quadratic term was judged by eye.

In order to allow for a small residual component of continuum emission, a constant term was included in each of the models to account for a flat continuum.

---

[*] *DIPSO* is a Starlink program

3.3.2 *Broad emission lines*

Emission from the broad-line regions is modelled as a Lorentzian line, which is collisionally broadened with a width proportional to P/T, where P is the pressure and T the temperature. This line profile was chosen as it has been found observationally to be a good fit to many broad emission lines from quasars.

One set of the models has an additional broad line component, which can represent a range of different physical processes, including two separate broad-line regions with different temperatures, or outflows from the central region. A red wing on the emission line may be caused by an outflow of optically thick clouds, of which only those on the far side of the quasar from the central source would be visible (Krolik, priv. comm.). This broad line is modelled by a Gaussian profile, which arises from Doppler or thermal broadening, and so has a width proportional to $\sqrt{T}$, where T is the temperature. The difference between Lorentzian and Gaussian profiles is minimal near the line centroid, though the Lorentzian has much broader wings; combining the two different lines allows the maximum amount of flexibility in the two-component broad-line region models.

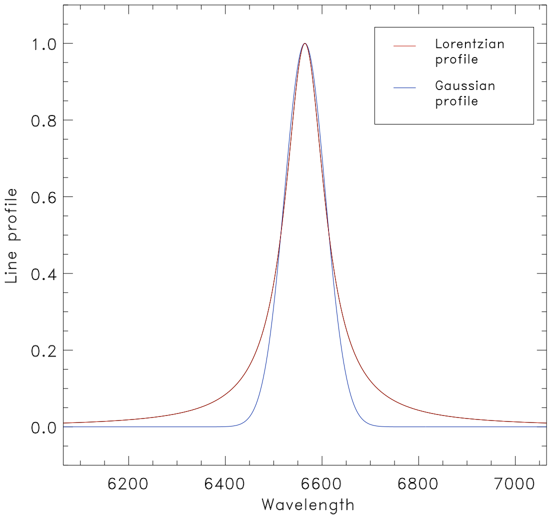

Figure 3.1: A comparison of the Lorentzian and Gaussian line profiles, matched at the full width half maximum, and normalised to the same peak height.

3.3.3 *Narrow emission lines*

All narrow lines are modelled with Gaussian distributions. The relative intensities of some of the forbidden lines are constrained as they depend only on temperature and electron density, which can be assumed to be approximately constant over this region. The [N II] and [O I] emission lines are temperature sensitive. Koski (1978) examined a sample of 28 Seyfert 2 galaxies and narrow line radio galaxies; these had an average [O I] line ratio of $[\mathrm{O\,I}]_{6300}/[\mathrm{O\,I}]_{6364} = 3.13$ and an average [N II] line ratio of $[\mathrm{N\,II}]_{6583}/[\mathrm{N\,II}]_{6548} = 3.01$. These ratios depend on temperature, and other factors such as reddening, and were measured for narrow-line radio galaxies: however, since these emission lines make only a modest contribution to the spectra under consideration, it is sufficient to fix these line ratios at a value of 3.0.

The $[\mathrm{S\,II}]_{6716}/[\mathrm{S\,II}]_{6731}$ ratio depends both on the square root of the temperature and on the electron density (Peterson 1997). Ratios varying between around 0.44 and 1.5 are measured, as the electron density varies from 10^{-5} m^{-3} to 0.1 m^{-3}. Reasonable prior ranges of 0.003 - 10 for the relative intensities of [N II] and [S II] with respect to narrow H α were found from Veilleux & Osterbrock (1987).

The widths of the observed narrow lines depend upon the effective spectral resolution. The intrinsic line width due to Doppler broadening of narrow H α is left as a free parameter in the model, and assumed to be the same for all narrow lines, since they are all low-ionisation lines formed in approximately the same region. This intrinsic width is convolved with the line width due to the spectral resolution, which is in general a wavelength-dependent quantity, so that

$$\text{Line width}^2 = (\text{Doppler broadened line width})^2 + \left(\frac{\lambda}{\text{Resolution}}\right)^2 \tag{3.12}$$

whenever the quasar light fills the spectrograph slit due to seeing, intrinsic spatial size, or a convolution of the two. The resolution of each waveband was found by measuring the velocity widths of the sky lines, which are effectively delta functions broadened only by the spectral resolution, observed across the entire slit width. The spectral resolution was found to be approximately constant across the spectral range of each waveband: these resolutions are given in Table 3.2.

Waveband	Measured resolution ($\Delta\lambda/\lambda$)
J	543.8
H	563.8
K	408.7

Table 3.2: The spectral resolution of different ISAAC wavebands, measured from the widths of the sky emission lines. Note that this assumes the quasar light is distributed uniformly across the spectrographic slit.

Since these high-redshift quasars are point sources, they will fill the slit if the seeing (measured in arcseconds) is greater than or equal to the slit width, and if they are properly centred on the slit. If the seeing is smaller than the slit width, then the resolution width should be scaled down by the ratio of the seeing to the slit width, and Equation 3.12 should be replaced by

$$\begin{aligned}\text{Line width}^2 &= (\text{Doppler broadened line width})^2 \\ &\quad + \left(\frac{\lambda}{\text{Resolution}} \times \frac{\text{Seeing in arcsec}}{\text{Slit width in arcsec}}\right)^2 \end{aligned} \tag{3.13}$$

The seeing at the time that each spectrum was observed was measured by taking a spatial cut across the spectrum, binning in the spectral direction, and finding the full width half maximum of the spectrum in arcseconds. This method assumes constant seeing over the period of the observations, and that the contribution of narrow lines (which may be spatially extended rather than a pure point source) is negligible.

3.3.4 *Array of models*

Twelve different models consisting of combinations of these components were fit to the emission lines of the quasars. These are divided into four sets of models, which have different broad emission contributions. One set of models has a single Lorentzian line from the classical broad-line region; one set has a Lorentzian and a Gaussian line, to account for the two broad-line regions, or a broad line region plus an outflow. There are two sets of

	No narrow lines	Narrow Hα only	All narrow lines
Lorentzian plus disk emission	5	3	1
Lorentzian plus Gaussian line	9	8	7
Disk emission only	12	11	10
Single Lorentzian	6	4	2

Figure 3.2: An illustration of the components included in each of the models, labelled with index numbers 1 to 12.

models including accretion disks: one set has the accretion disk plus the Lorentzian line to model the broad-line region, while the other set has disk emission only. Each of the sets have three models, one with all the narrow lines included, one with narrow H α only and none of the forbidden lines, and one with no narrow components of emission. The parameters included in each of the models are detailed in Table 3.3. The standard prior ranges, and any changes to the prior ranges for each of the models, are shown in Tables 3.4 and 3.5. It should be noted that in Bayesian statistics, the definition of a model includes the prior values for the parameters.

It is important to note that whilst changes were made to the standard set of priors for the fits to some spectra, these changes were made uniformly across the entire set of models used to fit each spectrum. This means that the process of comparing the evidence values to select the best model to fit the emission of each quasar is unaffected; however, it does mean that it does not make sense to compare the model evidence values between different quasars.

There was usually a physically obvious reason to change the priors; for example, some spectra had higher intensity lines than the norm, and the prior range had to be expanded to allow for this. An example of a less clear-cut case is the tightening of a prior range on the centroid of narrow H α: this was used in several cases to prevent narrow H α

from fitting spurious noise spikes. With enough computer time and resources, the ideal would be to rerun all models with the maximum prior ranges necessary for each and every object.

Parameter		Model											
		1	2	3	4	5	6	7	8	9	10	11	12
1	Flat continuum	●	●	●	●	●	●	●	●	●	●	●	●
2	Broad H α shift with respect to narrow H α	●	●	●	●			●	●				
3	Broad H α central wavelength					●	●			●			
4	Broad H α Lorentzian width	●	●	●	●	●	●	●	●	●			
5	Broad H α intensity	●	●	●	●	●	●	●	●	●			
6	Narrow H α central wavelength	●	●	●	●			●	●		●	●	
7	Narrow H α Gaussian width	●	●	●	●			●	●		●	●	
8	Narrow H α intensity	●	●	●	●			●	●		●	●	
9	[N II]$_{6550}$/Narrow H α intensity ratio	●	●					●			●		
10	[S II]$_{6718}$/[S II]$_{6732}$ intensity ratio	●	●					●			●		
11	[S II]$_{6732}$/Narrow H α intensity ratio	●	●					●			●		
12	[O I]$_{6302}$/Narrow H α intensity ratio	●	●					●			●		
13	Second broad H α component shift with respect to narrow H α							●	●	●			
14	Second broad H α component Gaussian width							●	●	●			
15	Second broad H α component intensity							●	●	●			
16	Disk intensity normalisation	●		●		●					●	●	●
17	Disk shift with respect to 6564.61 Å	●		●		●					●	●	●
18	Sine of the disk axis angle	●		●		●					●	●	●
19	Local velocity dispersion of the disk material	●		●		●					●	●	●
20	Inner disk radius	●		●		●					●	●	●
21	Multiplication factor for disk outer radius	●		●		●					●	●	●
Number of free parameters		17	11	13	7	10	4	14	10	7	14	10	7

Table 3.3: Summary of the parameters included in each model.

	Parameter	Range	Log?
1	Flat continuum	$-0.5 – 0.5 \times 10^{-9}\,\mathrm{Wm}^{-3}$	No
2	Broad H α shift with respect to narrow H α	0.985 – 1.015	No
3	Broad H α central wavelength	6540 – 6590 Å	No
4	Broad H α Lorentzian width	30 – 500 Å	Yes
5	Broad H α intensity	$0.05 – 20 \times 10^{-9}\,\mathrm{Wm}^{-3}$	Yes
6	Narrow H α central wavelength	6540 – 6590 Å	No
7	Narrow H α Gaussian width	1 – 30 Å	Yes
8	Narrow H α intensity	$0.01 – 10 \times 10^{-9}\,\mathrm{Wm}^{-3}$	Yes
9	$[\mathrm{N\,II}]_{6550}$ / Narrow H α intensity ratio	0.003 – 10	Yes
10	$[\mathrm{S\,II}]_{6718}$ / $[\mathrm{S\,II}]_{6732}$ intensity ratio	0.2 – 3.0	No
11	$[\mathrm{S\,II}]_{6732}$ / Narrow H α intensity ratio	0.003 – 10	Yes
12	$[\mathrm{O\,I}]_{6302}$ / Narrow H α intensity ratio	0.003 – 10	Yes
13	Second broad H α component shift with respect to narrow H α	0.985 – 1.015	No
14	Second broad H α component Gaussian width	30 – 500 Å	Yes
15	Second broad H α component intensity	$0.05 – 20 \times 10^{-9}\,\mathrm{Wm}^{-3}$	Yes
16	Disk intensity normalisation	$10 – 10^4$	Yes
17	Disk shift with respect to 6564.61 Å	$-100 – 100$ Å	No
18	Sine of the disk axis angle	0 – 0.9994	No
19	Local velocity dispersion of the disk material	$10^{-3} – 10^{-2} c$	Yes
20	Inner disk radius (R_{in})	100 – 1000 R_G	Yes
21	Multiplication factor for disk outer radius	$2 – 100 R_{\mathrm{in}}$	Yes

Table 3.4: Standard prior ranges of input parameters for the emission models. Column 2 gives the prior ranges of the parameter values, and Column 3 states whether the coverage of the parameter space is logarithmic or not.

Quasar	Alterations to the standard prior ranges
MRC0222-224	Wider shift allowed in broad components, 0.97 – 1.03, or -200 Å – 200 Å for the disk shift Maximum disk intensity increased to 10^5 (arbitrary units)
MRC0327-241	Smaller prior on the centroid of the reference line, 6550 – 6580 Å Width of broad components allowed to vary from 30 – 150 Å
MRC0346-279	No changes
MRC0413-210	Smaller prior on the centroid of the reference line, 6550 – 6580 Å
MRC0413-296	Width of narrow components allowed to vary from 1 – 80 Å Maximum intensity of [N II] lines limited to match maximum narrow Hα intensity
MRC0430-278	No changes
MRC0437-244	Smaller prior on the centroid of the reference line, 6550 – 6580 Å
MRC0450-221	Wider shift allowed in broad components, 0.97 – 1.03, or -200 Å – 200 Å for the disk shift Width of broad components allowed to vary from 20 – 500 Å Width of narrow components allowed to vary from 1 – 50 Å
MRC0549-213	No changes
MRC1019-227	Width of broad components allowed to vary from 20 – 500 Å
MRC1114-220	Wider shift allowed in broad components, 0.97 – 1.03, or -200 Å - 200 Å for the disk shift
MRC1208-277	Wider shift allowed in broad components, 0.97 – 1.03, or -200 Å - 200 Å for the disk shift Width of broad components allowed to vary from 10 – 500 Å
MRC1217-209	No changes
MRC1222-293	Width of broad components allowed to vary from 20 – 500 Å Width of narrow components allowed to vary from 1 – 50 Å
MRC1301-251	Wider shift allowed in broad components, 0.97 – 1.03, or -200 Å - 200 Å for the disk shift Width of broad components allowed to vary from 30 – 1000 Å Width of narrow components allowed to vary from 1 – 40 Å
MRC1349-265	No changes
MRC1355-215	No changes
MRC1355-236	Wider shift allowed in broad components, 0.97 – 1.03, or -200 Å – 200 Å for the disk shift Maximum intensity of [N II] lines limited to match maximum narrow Hα intensity
MRC1359-281	No changes

Table 3.5: Priors which were changed during the fitting process. Where changes were made, these were made consistently across the full range of models for each quasar, to allow the evidence values to be compared on an even footing.

3.4 *Bayesian Optimisation*

3.4.1 *The Bayesian method*

Bayes' Theorem provides a method of calculating the probability of a certain hypothesis, such as the values of a set of parameters of a given model, when presented with a set of data. To achieve this, the problem is inverted, and the probability of the data set arising given the parameters and the model is calculated first, which is called the likelihood function. This is modified by the prior probability, which is used to encode any initial knowledge of the parameters. This can be written

$$\mathrm{Prob}(\mathrm{X}|\mathrm{D},\mathrm{M}) = \frac{\mathrm{Prob}(\mathrm{D}|\mathrm{X},\mathrm{M})\mathrm{Prob}(\mathrm{X}|\mathrm{M})}{\mathrm{Prob}(\mathrm{D}|\mathrm{M})} \tag{3.14}$$

where X are the parameters of the model M, and D is the data set. The term $\mathrm{Prob}(\mathrm{X}|\mathrm{D},\mathrm{M})$ is the posterior probability or posterior, the probability of the set X of parameters to the model M, given the data D. $\mathrm{Prob}(\mathrm{D}|\mathrm{X},\mathrm{M})$ is the likelihood function, the probability of data set D occurring if model M has parameters X. $\mathrm{Prob}(\mathrm{X}|\mathrm{M})$ is the prior probability or prior, the probability of a certain set of parameters occurring for the given model M, and the evidence $\mathrm{Prob}(\mathrm{D}|\mathrm{M})$ describes the probability of obtaining the data set D given the model M. The evidence term is sometimes ignored in Bayesian statistics, since a proportionality between the two sides of the equation is sufficient if there is only one model being tested. For this analysis, twelve models are used, and so the Bayesian evidence is used to discriminate between these models to find those which provide the best fits to the data.

The Bayesian evidence is given by the equation

$$\mathrm{Prob}(\mathrm{D}|\mathrm{M}) = \int_{\mathrm{all\ parameter\ space}} \mathrm{Prob}(\mathrm{D}|\mathrm{X},\mathrm{M})\mathrm{Prob}(\mathrm{X}|\mathrm{M})\mathrm{dX}\ . \tag{3.15}$$

3.4.2 *Calculating the likelihood function*

The Bayesian fitting is carried out using a "least squares" method. This folds in two important assumptions: first, that the prior is a fixed value over the entire range; second, that the noise on the data is well-approximated by a Gaussian distribution. Since there is little prior knowledge available as to the values of the model parameters, a uniform prior over a reasonable range (prior ranges are given in Tables 3.4 and 3.5) is a sensible assumption to make. The assumption that the noise on the data is Gaussian is a reasonable one; the noise on each data point is assumed to be Poisson-like sky emission noise, and since the data values are much larger than the error bars, this can be approximated as Gaussian noise.

Following Sivia (1996), for a uniform prior Bayes' Theorem, given in Equation 3.14, reduces to

$$\mathrm{Prob}(\mathrm{X}|\mathrm{D},\mathrm{M}) \propto \mathrm{Prob}(\mathrm{D}|\mathrm{X},\mathrm{M}). \tag{3.16}$$

Making the further reasonable assumption that each data point is independent, then for a set of N data points

$$\mathrm{Prob}(\mathrm{D}|\mathrm{X},\mathrm{M}) = \prod_{i=1}^{\mathrm{N}} \mathrm{Prob}(\mathrm{D}_i|\mathrm{X},\mathrm{M}). \tag{3.17}$$

Each data point D with error bar σ is compared to a value F generated from the model M with parameter set X, so that

$$\mathrm{Prob}(\mathrm{D}_i|\mathrm{X},\mathrm{M}) = \frac{1}{\sigma_i\sqrt{2\pi}} e^{-\frac{(\mathrm{F}_i-\mathrm{D}_i)^2}{2\sigma_i^2}} \tag{3.18}$$

and substituting into Equation 3.17 then

$$\mathrm{Prob}(\mathrm{D}|\mathrm{X},\mathrm{M}) = \left(\frac{1}{\sqrt{2\pi}}\right)^{\mathrm{N}} \prod_{i=1}^{\mathrm{N}} \frac{1}{\sigma_i} \times e^{-\frac{1}{2}\sum_{i=1}^{\mathrm{N}} \frac{(\mathrm{F}_i-\mathrm{D}_i)^2}{\sigma_i^2}}. \tag{3.19}$$

Let the chi-squared measure be defined as

$$\chi^2 = \sum_{i=1}^{\mathrm{N}} \frac{(\mathrm{F}_i - \mathrm{D}_i)^2}{\sigma_i^2}, \tag{3.20}$$

then putting this relation into 3.19 and using 3.16

$$\mathrm{Prob}(\mathrm{X}|\mathrm{D},\mathrm{M}) \propto e^{-\frac{1}{2}\sum_{i=1}^{\mathrm{N}} \chi^2}. \tag{3.21}$$

Taking the natural logarithm of this probability

$$\ln[\mathrm{Prob}(\mathrm{X}|\mathrm{D},\mathrm{M})] = \mathrm{K} - \frac{\chi^2}{2} \tag{3.22}$$

where K is a constant. The maximum of the posterior probability occurs where χ^2 is minimised, and therefore when the natural logarithm of the likelihood is maximised.

3.4.3 *Dealing with nuisance parameters*

The error on each data point is not known; however, in infrared spectra, the sky emission dominates the error bars (the sky lines are much brighter than the quasar signal by a factor of ~ 100 and require careful subtraction before the signal is extracted), and so the error on each point can be approximated as Poisson noise with an unknown scaling factor

$$\sigma_i = Q\sqrt{\mathrm{S}_i} \tag{3.23}$$

where Q is the scaling factor, and S_i are the values of the sky spectrum at each data point, calculated in Section 2.2.7 of Chapter 2. The absolute values of the errors are not important to the analysis, and so the scaling factor Q can be marginalised.

Writing Equation 3.18 with the errors substituted in, so that the probability of the parameters X are now explicitly dependent on the scaling parameter Q, then

$$\mathrm{Prob}(\mathrm{D}_i|\mathrm{X},\mathrm{M},Q) = \frac{1}{\sqrt{2\pi}Q\sqrt{\mathrm{S}_i}} e^{-\frac{(\mathrm{F}_i-\mathrm{D}_i)^2}{2Q^2\mathrm{S}_i}} \tag{3.24}$$

so

$$\mathrm{Prob}(\mathrm{D}|\mathrm{X},\mathrm{M},Q) = \prod_{i=1}^{\mathrm{N}} \frac{1}{\sqrt{2\pi}Q\sqrt{\mathrm{S}_i}} e^{-\frac{(\mathrm{F}_i-\mathrm{D}_i)^2}{2Q^2\mathrm{S}_i}}. \tag{3.25}$$

Taking only the terms which depend on the scaling factor Q

$$\mathrm{Prob}(\mathrm{D}|\mathrm{X},\mathrm{M},Q) \propto \frac{1}{Q^{\mathrm{N}}} e^{-\frac{1}{2}\sum_{i=1}^{\mathrm{N}} \frac{(\mathrm{F}_i-\mathrm{D}_i)^2}{Q^2\mathrm{S}_i}}. \tag{3.26}$$

Defining a new χ^2

$$\chi^2 = \sum_{i=1}^{\mathrm{N}} \frac{(\mathrm{F}_i - \mathrm{D}_i)^2}{\mathrm{S}_i} \tag{3.27}$$

and so

$$\mathrm{Prob}(\mathrm{D}|\mathrm{X},\mathrm{M},Q) \propto \frac{1}{Q^{\mathrm{N}}} e^{-\frac{\chi^2}{2Q^2}}. \tag{3.28}$$

The noise scaling factor can then be marginalised. Integrating this probability over all possible values of Q

$$\mathrm{Prob}(\mathrm{D}|\mathrm{X},\mathrm{M}) = \int_0^{\infty} \mathrm{Prob}(\mathrm{D}|\mathrm{X},\mathrm{M},Q)\mathrm{Prob}(Q|\mathrm{X},\mathrm{M})\mathrm{d}Q \tag{3.29}$$

A Jeffreys' prior may be used, which is a statement of complete ignorance about the magnitude of the scaling factor. This prior is uniform in logarithmic space,

$$\mathrm{Prob}(Q|\mathrm{X},\mathrm{M}) = \mathrm{Prob}(Q|\mathrm{M}) \propto \frac{1}{Q}. \tag{3.30}$$

Substituting 3.28 and 3.30 into 3.29, then

$$\mathrm{Prob}(\mathrm{D}|\mathrm{X},\mathrm{M}) \propto \int_0^\infty \frac{1}{Q^{\mathrm{N}+1}} e^{-\frac{\chi^2}{2Q^2}} \mathrm{d}Q. \tag{3.31}$$

Now make a change of variable, $z = \frac{\chi^2}{2Q^2}$, so $Q = (\frac{\chi^2}{2z})^{\frac{1}{2}}$. Then $\mathrm{d}Q = -\frac{Q^3}{\chi^2}\mathrm{d}z$ and

$$\mathrm{Prob}(\mathrm{D}|\mathrm{X},\mathrm{M}) \propto \int_0^\infty -\frac{1}{\chi^2} Q^{2-\mathrm{N}} e^{-z} \mathrm{d}z \tag{3.32}$$

$$\mathrm{Prob}(\mathrm{D}|\mathrm{X},\mathrm{M}) \propto \frac{1}{\chi^{\mathrm{N}}} \int_0^\infty -(2z)^{(\frac{\mathrm{N}}{2}-1)} e^{-z} \mathrm{d}z. \tag{3.33}$$

The integral term is simply equivalent to a constant, and so

$$\mathrm{Prob}(\mathrm{D}|\mathrm{X},\mathrm{M}) = \mathrm{K}\chi^{-\mathrm{N}} \tag{3.34}$$

where K is a constant, and so taking the natural logarithm

$$\ln \mathrm{Prob}(\mathrm{D}|\mathrm{X},\mathrm{M}) = \ln \mathrm{K} - \frac{\mathrm{N}}{2} \ln \chi^2. \tag{3.35}$$

3.4.4 *Input spectra*

The input spectra are created from the emission spectra of the objects, with a linear or quadratic fit to the continuum subtracted from the emission. Certain points were excluded from the fits, such as spectral points with unrealistically small errors due to high noise in the standard star spectra used for flux calibration. This affected only a few data points in seven of the spectra. Strong OH sky lines in H-band spectra, the continuum which dipped in intensity longward of 7150Å in MRC0450-221, an absorption-like artifact in the MRC0222-224 spectrum, and the few pixels of the narrow H α line of MRC1359-281 which are noise were also excluded.

The error spectrum consists of the square root of the sky spectrum, with a normalisation factor which is marginalised in the fitting process. Details of the creation of the sky spectrum are given in Section 2.2.7 of Chapter 2.

3.4.5 *BayeSys3*

The Bayesian optimisation was carried out using *BayeSys3* by Skilling (2004)[†]. A C program was written which called *BayeSys3* through a wrapper written by D. Sivia (priv. comm.), providing a set of prior parameters, and the likelihood function of the observed data given the model and a set of parameters.

BayeSys3 was set up with an ensemble of 20 trial objects, or “walkers”, to explore the parameter space; having a large number of “walkers” exploring the parameter space allows any which get stuck at anomalously low likelihood to be overwritten, and an ensemble of this size was chosen as the largest number with which the program would run in a reasonable time. Initially, an ensemble of 10 “walkers” was used, but this was found to be unstable in several cases. All the Monte Carlo exploration engines available were switched on, which was again a measure to avoid the “walkers” exploring the parameter space getting trapped in local minima. Only when all six exploration engines get stuck is the “walker” truly trapped.

A relatively slow rate of annealing (0.1, though there are no units available as this is a trial-and-error quantity) was chosen, which controls the speed at which the Monte Carlo simulation switches from exploring the entire parameter space to exploring the posterior parameter space. The slower the annealing rate, the more thoroughly the parameter space is explored and the more slowly the “walkers” focus in on the zones of maximum likelihood.

3.4.6 *Comparing evidence*

The Bayesian evidence is compared in order to choose the model which best fits the data for the fewest parameters necessary. The evidence has an unknown scaling, but since the

---

[†] *BayeSys* website: http://www.inference.phy.cam.ac.uk/bayesys/

ratios of evidences for different models are compared, the scaling is unimportant.

The Bayes factor is written

$$B_{\mathrm{AB}} = \frac{\mathrm{Prob}(\mathrm{D}|\mathrm{M_A})}{\mathrm{Prob}(\mathrm{D}|\mathrm{M_B})}, \tag{3.36}$$

and gives a statistical measure of the degree to which Model A has gained or lost support compared to Model B given the data D. The "Jeffreys' scale" (Jeffreys 1939), shown in Table 3.6, gives an empirical scale for translating the relative Bayesian evidence of two models into a more intuitive scale of odds and into four bands of evidence: strong, moderate, weak and inconclusive.

$\lvert\ln \mathrm{B_{AB}}\rvert$	Odds radio	Probability	Strength of evidence
<1.0	$\lesssim$ 3:1	$<$ 0.750	Inconclusive
1.0	$\sim$3:1	0.750	Weak evidence
2.5	$\sim$12:1	0.923	Moderate evidence
5.0	$\sim$150:1	0.993	Strong evidence

Table 3.6: "Jeffreys' scale" for comparing the strength of the evidence for two models (Jeffreys 1939).

The Bayesian information is also a useful criterion for judging a model. The information is the negative entropy, and is approximately a measure of the ratio of the volume of the prior parameter space to the volume of the posterior parameter space. When models have similar Bayesian evidences, a model with a lower Bayesian information might be preferred on the basis that it has a smaller number of effective free parameters (e.g. Trotta 2008). If the posterior parameters are well-constrained, then the information is high, indicating that the application of the model has increased the state of knowledge concerning the parameters.

3.5 *Model Selection*

The observed spectra are plotted in Figure 3.13. The model selection was performed on the basis of Bayesian evidence, using the criterion discussed in section 3.4.6. A quasar is considered to have strong evidence for the presence of a disk if the model with the highest evidence is a disk model, and no other models without disks fall within one Jeffreys' criterion ($\Delta \ln(\text{Evidence}) = 5$) of the preferred model.

Fig 3.3 illustrates this selection procedure, with the natural logarithmic evidence plotted against the natural logarithmic information. The quality of the data is a large factor in the model selection. Broadly speaking, high signal-to-noise spectra have very high ranges of evidence, as the difference between the best and worst fits is more apparent than for the lower signal-to-noise spectra. There is also a correlation between logarithmic evidence and logarithmic information for these high signal-to-noise cases; higher evidence is linked to better fits, which constrain the posterior parameters more tightly. For poor spectra, however, such as those of MRC0346-279 or MRC1217-209, there is no correlation apparent between the evidence and information, and one Jeffreys' criterion can encompass most of the models, so it is impossible to discriminate reliably between them.

Fig 3.4 shows the natural logarithmic evidence for all models for each quasar plotted as a 3-dimensional histogram, with the narrow-line models arranged on the x-axis and the broad-line models arranged on the y-axis. This alternative representation of the model selection process shows which models have fits whose parameters did not properly converge within the bounds of the prior range; this often affects a sub-set of the models, such as those models which include narrow lines in cases where the spectrum has insufficient signal-to-noise ratio to fit the widths of these lines.

3.5.1 *Notes on individual quasars*

MRC0222-224: The full set of narrow lines is present in this spectrum; models with two broad components but less than the full complement of narrow lines have low evidence values and are not well constrained (they have low information), since the broad components attempt to fit to the narrow lines. Note also that the model with the disk component plus narrow H α has low evidence and is unconstrained, since the narrow line attempts to fit a second broad component. There are two reasons for this: the narrow H α component is fitting the [N II] lines in addition to the narrow H α emission; and the disk component does not easily fit a "triangular" profile which has extended wings plus a strongly peaked centroid. There is strong evidence (a Jeffreys' criterion of greater than 5) to select one of

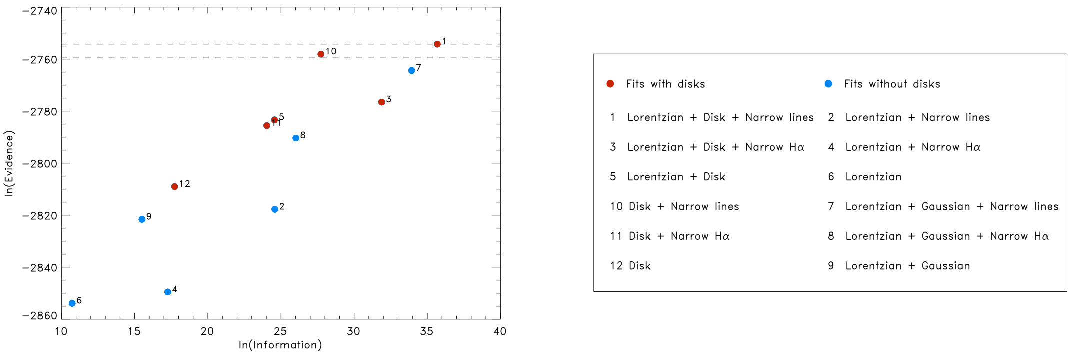

MRC0222-224

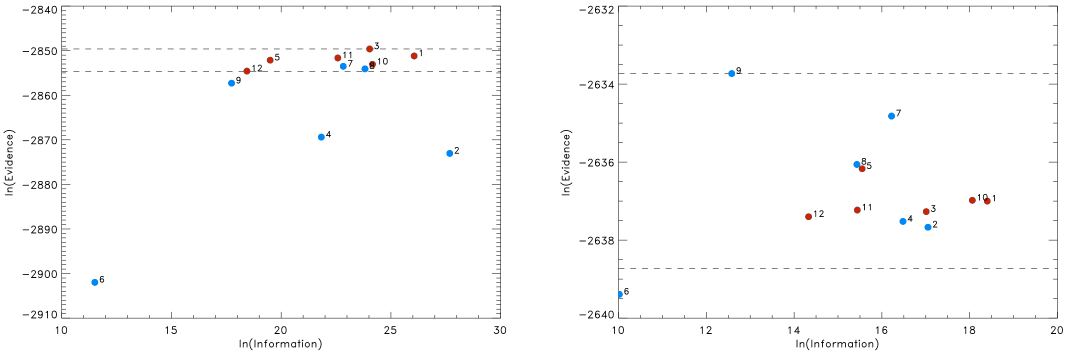

MRC0327-241

MRC0346-279

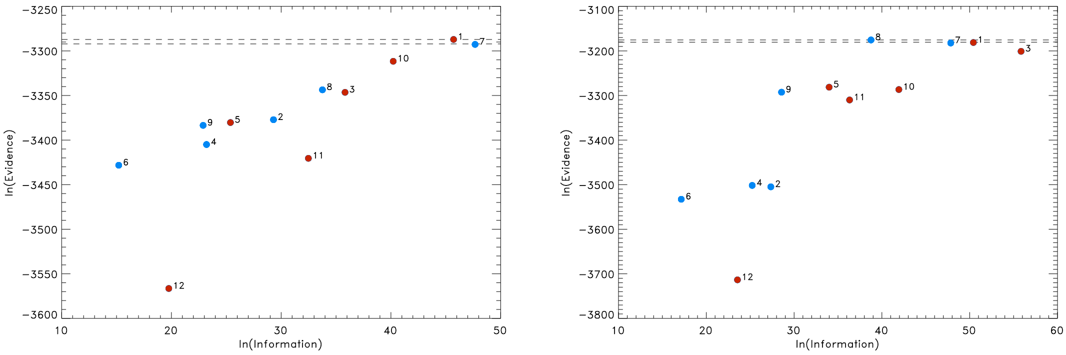

MRC0413-210

MRC0413-296

Figure 3.3: Natural logarithmic evidence plotted against natural logarithmic information for all models applied to each quasar spectrum. The upper dotted line shows the evidence of the preferred model, while the lower dotted line is plotted to show one Jeffreys' criterion, i.e. a difference in ln(Evidence) of 5.

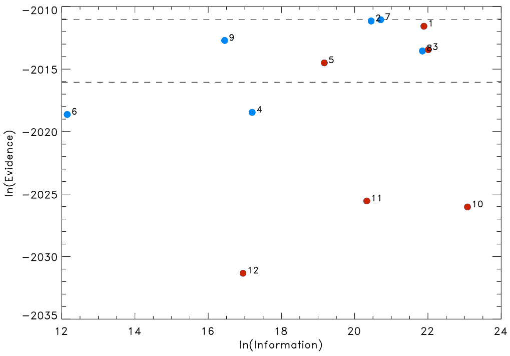

MRC0430-278

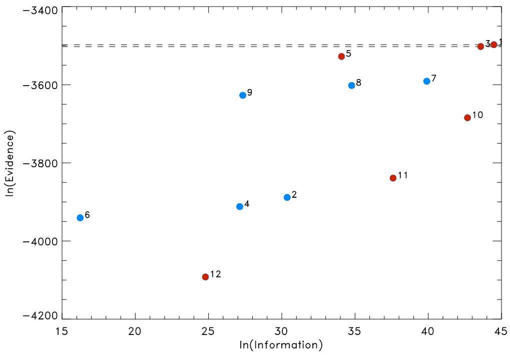

MRC0437-244

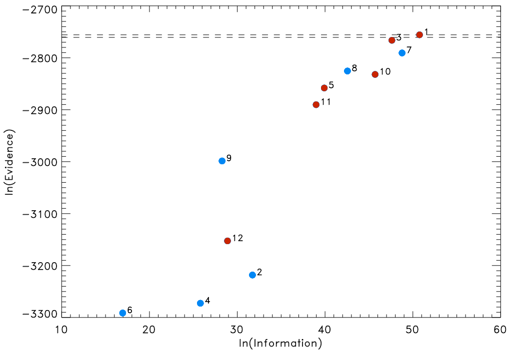

MRC0450-221

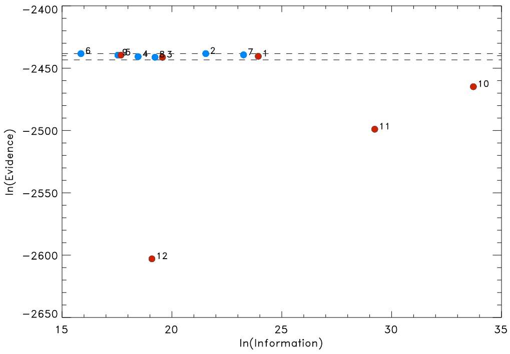

MRC0549-213

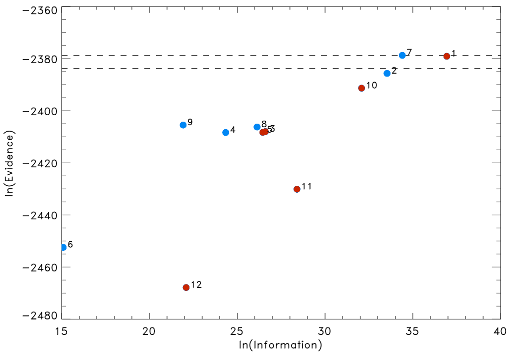

MRC1019-227

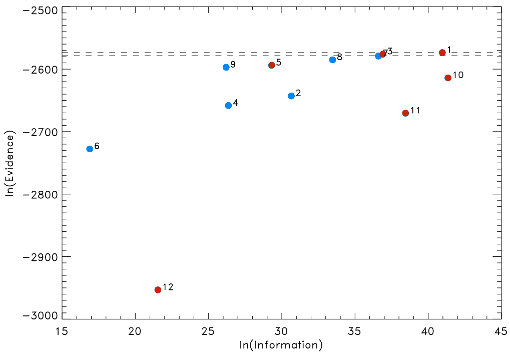

MRC1114-220

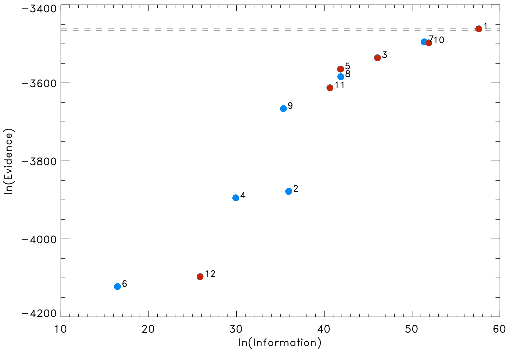

MRC1208-277

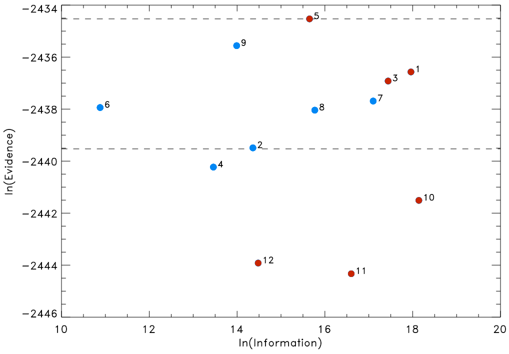

MRC1217-209

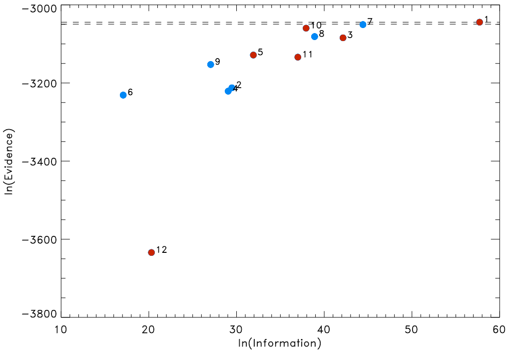

MRC1222-293

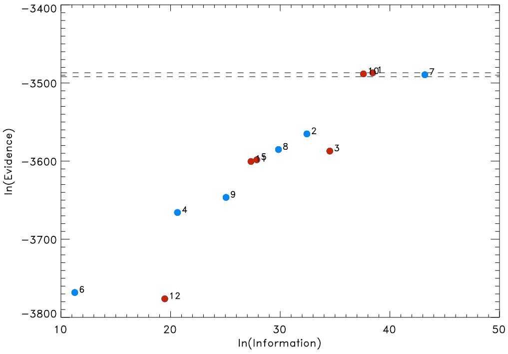

MRC1301-251

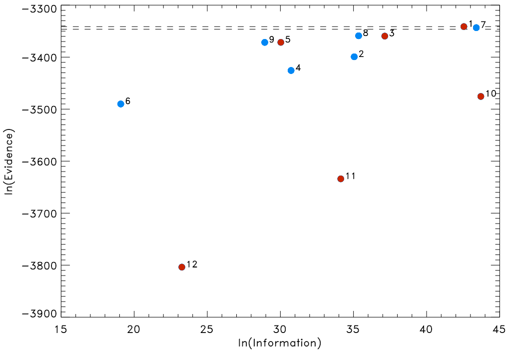

MRC1349-265

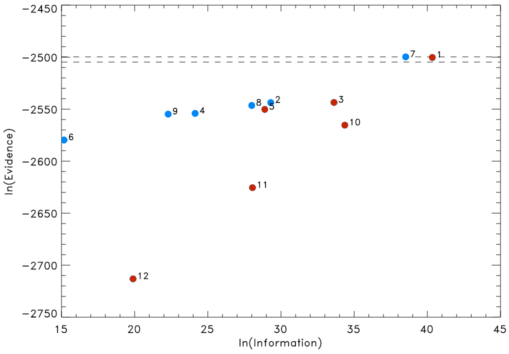

MRC1355-215

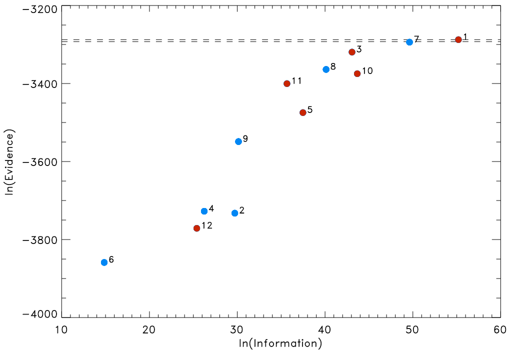

MRC1355-236

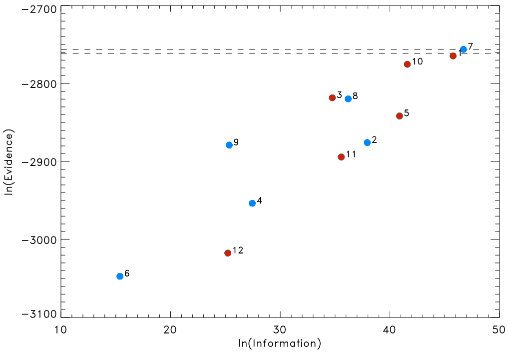

MRC1359-281

the models with the disk over the single Lorentzian or Lorentzian plus Gaussian models. The model with both disk and Lorentzian line has higher evidence of $\Delta \ln(\text{Evidence}) = 3.8$ than the model consisting of a single disk, which means there is moderate evidence that a Lorentzian component is needed, but there is strong evidence for the presence of a disk.

MRC0327-241: This spectrum suffers from comparatively low signal-to-noise, and so in most cases, the narrow lines are not constrained. Models which include disk emission are preferred, but the evidence for this is only moderate ($\Delta \ln(\text{Evidence}) = 3.9$ between best-fit disk model and best-fit non-disk model). The best model has a Lorentzian broad line, a disk, plus all the narrow lines, and it is worth noting that not all the parameters in this fit were properly constrained, so simpler (lower information) models like models 11 and 5 (with $\Delta \ln(\text{Evidence}) = 2.0$ and $\Delta \ln(\text{Evidence}) = 2.5$ from the best-fit model respectively) are also plausible.

MRC0346-279: This spectrum suffers from low signal-to-noise, and so there is little evidence to discriminate between the models: all but one of the models fall within the Jeffreys' criterion for strong evidence. The fit with the broad Lorentzian and the broad Gaussian was selected by the Bayesian evidence, which is the second simplest model after the single Lorentzian. This model has greater evidence by $\Delta \ln(\text{Evidence}) = 1.1$ than the next best fit, as well as lower information.

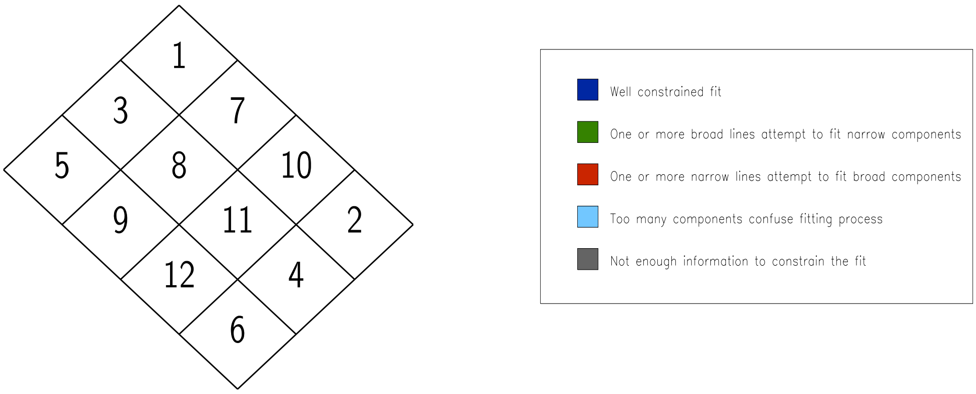

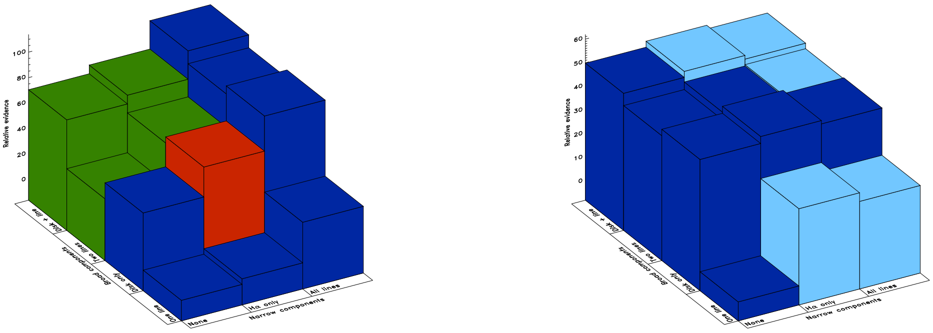

MRC0222-224

MRC0327-241

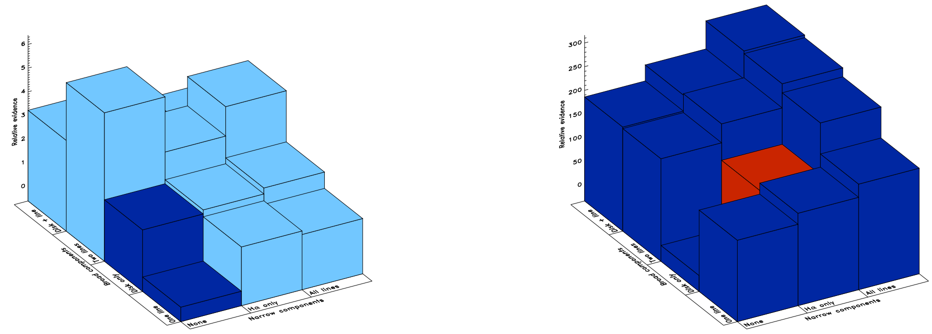

MRC0346-279

MRC0413-210

Figure 3.4: 3-D histograms illustrating aspects of the model selection process. The vertical scale plots $\Delta \ln($Evidence, the relative logarithmic Bayesian evidence. The x-axis plots increasing number of narrow components, while the broad components are arrayed on the y-axis, in order of increasing complexity. A key is given in the top left as to which model corresponds to each bar. The colour-coding gives a qualitative comment on the goodness of fit.

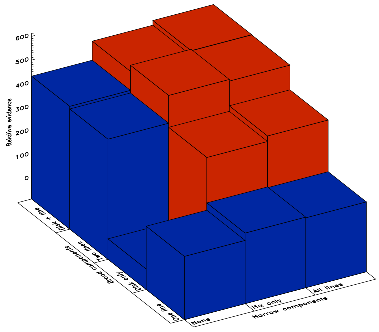

MRC0413-296

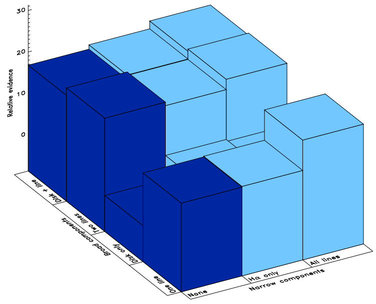

MRC0430-278

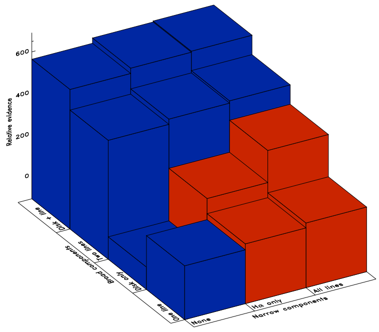

MRC0437-244

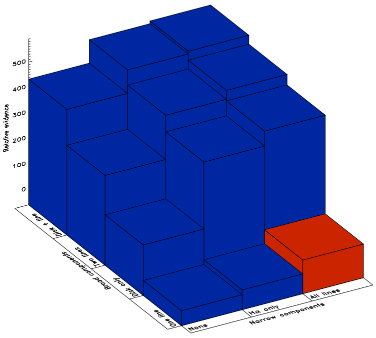

MRC0450-221

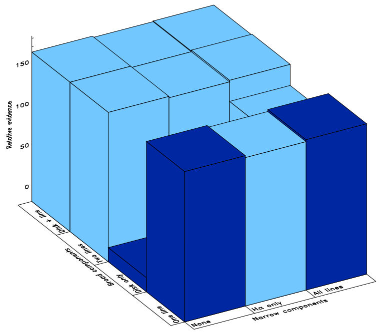

MRC0549-213

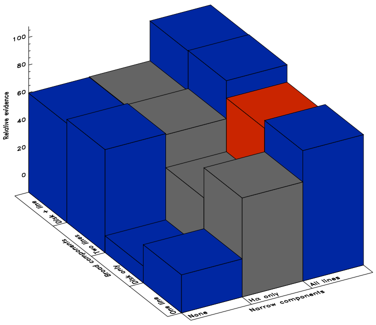

MRC1019-227

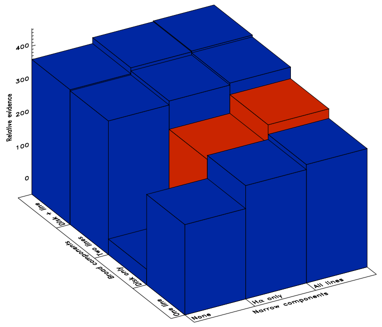

MRC1114-220

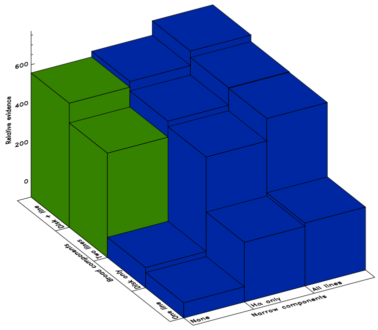

MRC1208-277

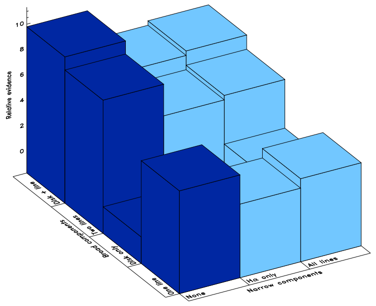

MRC1217-209

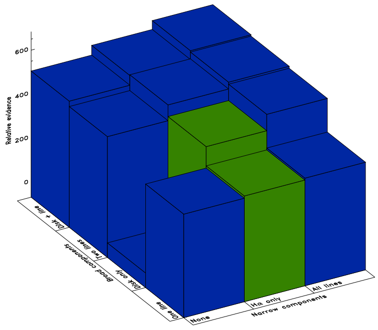

MRC1222-293

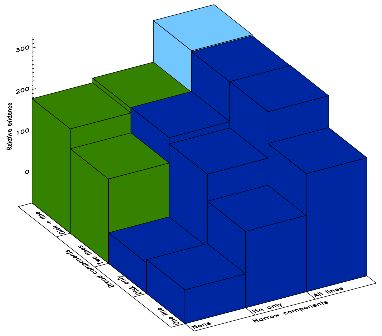

MRC1301-251

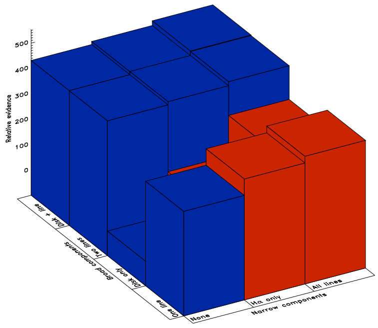

MRC1349-265

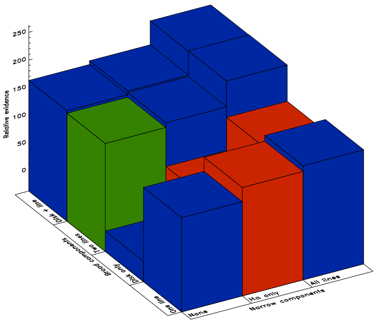

MRC1355-215

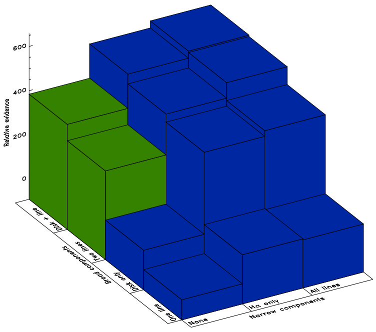

MRC1355-236

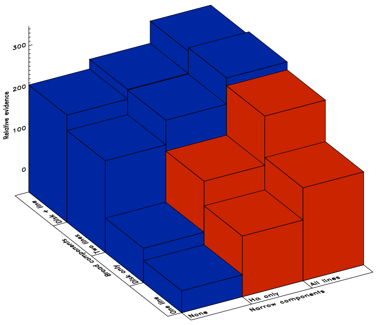

MRC1359-281

MRC0413-210: There is strong evidence ($\Delta \ln(\text{Evidence}) = 5.5$ over the next best-fit) for the model with the disk plus the Lorentzian line and all the narrow lines. Note that the model with the disk emission plus narrow Hα is unconstrained, as the narrow line attempts to fit a broad component: this appears to be due to the disk emission models not fitting "triangular" line profiles effectively (i.e. broad wings with a peaked centroid).

MRC0413-296: This quasar is a special case, since there are obviously narrow lines present in the spectrum but the narrow lines will not constrain properly in the fit as they attempt to fit broad components of emission. There appears to be more than two components of broad emission in this spectrum. From the evidence, the best model is that which has the broad Lorentzian, the broad Gaussian, and narrow Hα, although the narrow Hα is fitting to a third broad component, rather than to the spike obvious in the residuals. $\Delta \ln(\text{Evidence}) = 5.7$ between the best fit, and the best-fit model which includes a disk.

MRC0430-278: This is another spectrum with a reasonably low signal-to-noise ratio. The preferred model is the Lorentzian broad line plus the Gaussian broad line and all the narrow lines, though the margin in logarithmic evidence over the model with the Lorentzian line and the narrow lines is only $\Delta \ln(\text{Evidence}) = 0.1$. Many models fall within the Jeffreys' criterion, including model 1, which is also close in evidence to the selected model (making this quasar a "possible disk" source), though the models with the disk as the only broad component can be excluded. Again, it should be noted that due to the low signal-to-noise, the model with the highest probability did not have all the parameters constrained, so simpler (low information) models such as model 9 should be considered seriously.

MRC0437-244: The models with only one broad component and narrow components present do not constrain well, as the narrow lines model secondary elements of broad emission. There is strong evidence ($\Delta \ln(\text{Evidence}) = 93.6$) for the presence of a disk in addition to the main broad emission, and the preferred model is the disk plus Lorentzian line with the full complement of narrow lines, although this has only moderate evidence for being a better model that the disk plus Lorentzian line with narrow H α emission (though the presence of $[\text{O I}]_{6300}$ is clear from the spectrum).

MRC0450-221: The model with one broad Lorentzian and the full set of narrow lines has low information and is not well constrained, as the narrow lines attempt to fit secondary broad emission. The evidence is strong ($\Delta \ln(\text{Evidence}) = 10.6$) for the model with the disk plus Lorentzian line and the full complement of narrow lines.

MRC0549-213: This spectrum has weak or absent narrow H α emission, but some weak [S II] emission; however, the extra parameters required to fit all the narrow lines mean that there is virtually no difference in evidence between the models with all narrow lines present and the ones which exclude narrow lines. The majority of the models with emission more complex than a single Lorentzian line do not converge. Most of the models fall within the Jeffreys' criterion, including all of the disk plus Lorentzian line models, so this quasar is a "possible disk" source. The models with broad disk emission plus various degrees of narrow line emission are not favoured. The evidence is identical for the two best models, the single Lorentzian line with no narrow lines (model 6), and the single Lorentzian line with all the narrow lines (model 2), and although the former might be preferred on the basis of its simplicity (low information), the clear presence of the [S II] narrow lines should influence the overall fit.

MRC1019-227: This spectrum contains artifacts from poor sky subtraction which were blanked out for the Bayesian fitting process, including the region surrounding narrow H α. This means that the sub-set of models with the narrow H α line only are not constrained, although the models with all narrow lines present can converge, since the narrow H α parameters are fixed with reference to the other narrow lines. Note that the model with the disk plus narrow lines is fitting the [N II] and H α narrow lines to a broad component, since the disk profiles do not fit well to "triangular" profiles such as this, so these models do not fit well. The best fit is the model with the broad Lorentzian, the broad Gaussian and all the narrow lines, though this is only favoured over the model with the Lorentzian, the disk and all the narrow lines by $\Delta \ln(\text{Evidence}) = 0.35$, so this source is a "possible disk" candidate.

MRC1114-220: The single disk models do not fit well, as the disk profiles do not emulate this "triangular" profile. The preferred model is the disk plus Lorentzian line with the full collection of narrow lines, but this has only moderate evidence ($\Delta \ln(\text{Evidence}) = 2.4$) over the model with the same broad components, but narrow H α only. There is strong evidence for a disk ($\Delta \ln(\text{Evidence}) = 5.5$).

MRC1208-277: There is strong evidence supporting the model with all narrow lines and the Lorentzian line plus the disk ($\Delta \ln(\text{Evidence}) = 33.4$). The models with two elements of broad emission but no narrow lines do not fit well, since the narrow H α is so strong that one of the broad components attempts to fit to narrow H α.

MRC1217-209: This spectrum does not have high enough signal-to-noise ratio to constrain any narrow lines, and models with narrow lines have lower evidence than their counterparts without narrow lines. The model with the Lorentzian line plus the disk is preferred, but the evidence for this model over the model with the Lorentzian line and the Gaussian is weak ($\Delta \ln(\text{Evidence}) = 1.0$).

MRC1222-293: Narrow H α is weak in this spectrum, and so for the models with a single broad emission element, narrow H α emission fits an additional broad component if it is not fixed by the other narrow lines. The model with the Lorentzian line plus the disk and the full set of narrow lines is selected as the best model with strong evidence ($\Delta \ln(\text{Evidence}) = 6.1$).

MRC1301-251: This spectrum has strong narrow H α, [N II] and [S II], so models with insufficient narrow lines do not fit well as the broad emission attempts to fit narrow lines. In addition, the model with the disk plus the Lorentzian does not fit well, as there is some confusion between the components. The three models including all narrow lines, plus Lorentzian and disk, Lorentzian and Gaussian, or single disk, have probabilities within the Jeffreys' criterion of each other and are clearly preferred above the other models. The model with Lorentzian plus Gaussian has a shift between these components of $\Delta z \sim 0.03$ or 9,000 km s^{-1}, which is not likely to be physical, so although formally this is a "weak disk", it probably is a clear detection of a disk.

MRC1349-265: The narrow lines are relatively weak in this spectrum, so models with single broad components plus narrow lines do not fit well as the narrow lines attempt to fit secondary broad emission. The preferred fits are those with two broad components plus the full set of narrow lines. Of these, the model with the disk plus broad line is preferred, but only with weak evidence, $\Delta \ln(\text{Evidence}) = 2.0$.

MRC1355-215: The single component models with narrow lines show a tendency for the narrow lines to attempt to fit supplementary broad emission components. The model with the Lorentzian line and the Gaussian line, but an absence of narrow lines, has degeneracy between the components, both of which partially fit narrow H α. The preferred models for this spectrum are overwhelmingly those with two components of broad emission and with all the narrow lines. Of these models, the one with the extra Gaussian line (model 7) has a marginally higher probability than the one with the disk (model 1), but only by $\Delta \ln(\text{Evidence}) = 0.57$, which is inconclusive evidence by the Jeffreys' scheme. In this case, the shift between the two broad lines in model 7 is $\Delta z \sim 0.006$, which is ~ 1800 km s^{-1}, and is physically reasonable.

MRC1355-236: The models with two parts of broad emission but an absence of narrow lines are unconstrained, as one of the broad lines attempt to fit the strong narrow H α.

There is strong evidence ($\Delta \ln(\text{Evidence}) = 6.4$) that the model with the Lorentzian line, the disk emission, and all the narrow lines is preferred over the next best model.

MRC1359-281: The single broad component models including narrow lines are unconstrained, as the narrow lines attempt to fit additional broad emission. The Bayesian evidence indicates that two broad components plus all narrow lines are present in this spectrum. The favoured model in this case is that with the Lorentzian line and the Gaussian line, and there is strong evidence ($\Delta \ln(\text{Evidence}) = 8.4$) that this is preferred over the model with the disk and the Lorentzian line, so this is the only quasar with strong evidence against the existence of an accretion disk. The shift between the two broad lines in model 7 is $\Delta z \sim 0.009$ (~ 2700 km s^{-1}) which is physically reasonable.

3.5.2 *Tests for stability of the fitting*

Detailed tests were run on two of the quasars selected at random, MRC0437-244 and MRC0450-221, to check the Bayesian routines for stability. In the case of MRC0437-244, the parameters all converged to the same posterior parameter space; in the case of MRC0450-221, the local velocity dispersion converged to two slightly different, though directly adjacent, zones. In both cases, the posterior probabilities for the disk converged to one small area of parameter space.

3.5.2.1 *Changes to the Bayesian random seed*

Figure 3.5 shows the convergence of the disk parameters for MRC0437-244 (top figure) and MRC0450-221 (bottom figure), and the correlations between their parameters, when the fitting process was run using ten different Bayesian random seeds to initialise the Monte Carlo process. The posterior probability distributions converge in the same regions for all Bayesian seeds for MRC0437-244. In the case of MRC0450-221, the local velocity dispersion converges in two slightly different areas of parameter space, depending on the Bayesian seed, though these areas are within a reasonable error bound of the original fitted parameter value. The false minima do not have vastly different evidence values in this case ($\Delta \ln(\text{Evidence}) \sim 5$ between the highest and lowest evidence cases); this is due to the fact that the profile of the disk emission varies only weakly with the local velocity dispersion (Strateva et al. 2003).

Figure 3.6 shows the scatter in the sine of the disk axis angle for the best-fit model run with ten different seeds for the two randomly-selected test sources. MRC0437-244 has a very stable disk angle. MRC0450-221 has a small variation in disk angle with the one "bad" seed, though this falls well within the 1-σ error bounds of the fits found from other seeds.

Figure 3.7 shows the scatter in the sine of the disk axis angle of MRC1114-220, for the model chosen by the Bayesian selection run with ten different random seeds. This quasar has one of the largest error bars on the fitted disk axis angle, and was found to be an outlier in the plot of disk axis angle plotted against jet angle (Figures 6.12 and 6.13 in Chapter 6), and was therefore thought to be the source most likely to have an incorrect disk axis angle found from a false minimum in the posterior parameter space. However, the bets-fit model was found to have a very stable disk axis angle, although with a larger error bar.

3.5.2.2 *Changes to the annealing rate*

Figure 3.8 shows the distribution of posterior probabilities for the quasars MRC0437-244 (top) and MRC0450-221 (bottom) for a range of different annealing rates set in *BayeSys3*. The yellow points correspond to an annealing rate of 0.1, which was selected as the annealing rate used in the fitting process. Orange points are fits made using an annealing rate of 0.2, and red points use an annealing rate of 0.5; these points would generally be expected to produce worse fits if this rate was too rapid to allow the probability distribution to converge properly. Green points and blue points use slower annealing rates of 0.08 and 0.05 respectively. For MRC0437-244, the posterior distributions for these different rates are all similar. For MRC0450-221, a false minimum is found as before in the local velocity dispersion for this quasar ($\Delta \ln(\text{Evidence}) \sim 2$ between the highest and lowest evidence cases), but this parameter still constrains reasonably within a sensible error bound of the original measurement. It is interesting that this false minimum is shown by one fit made with a slower rate and one with a faster rate; this shows that it is not the rate which is

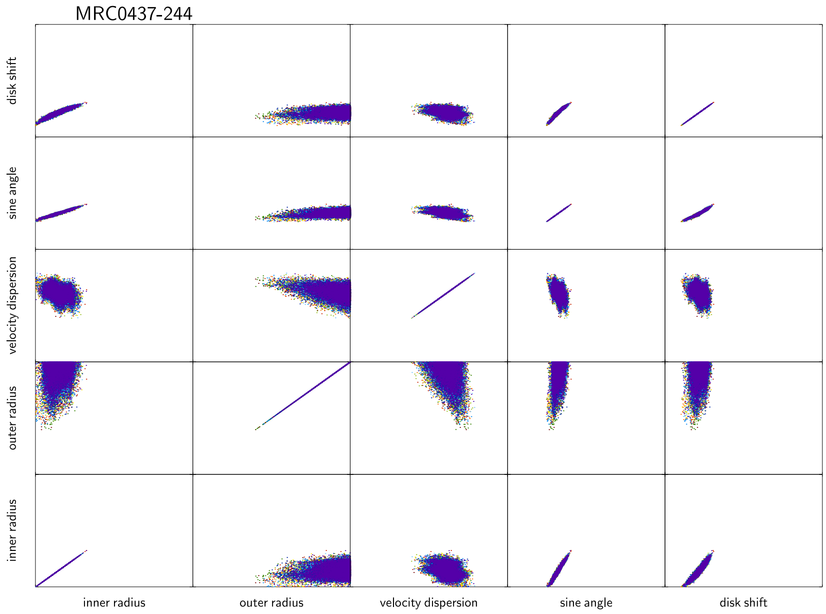

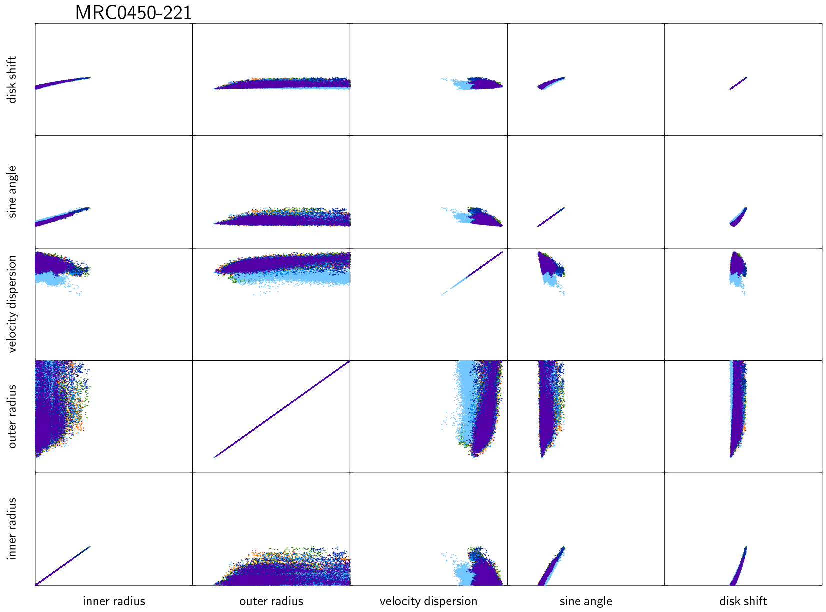

Figure 3.5: A plot of the correlations between the disk parameters for MRC0437-244 (top) and MRC0450-221 (bottom); the inner disk radius (R_{inner}), the outer disk radius (R_{outer}), the local velocity dispersion of the disk material (Δv), the sine of the angle of the disk axis to the line of sight ($\sin \theta_{\mathrm{disk}}$), and the shift of the disk emission with respect to 6564.61 Å (Δx) are plotted against each other to show correlations. Different random seeds for the Bayesian fitting are plotted in different colours. For all 10 different seeds, the probability distributions converge on the same regions.

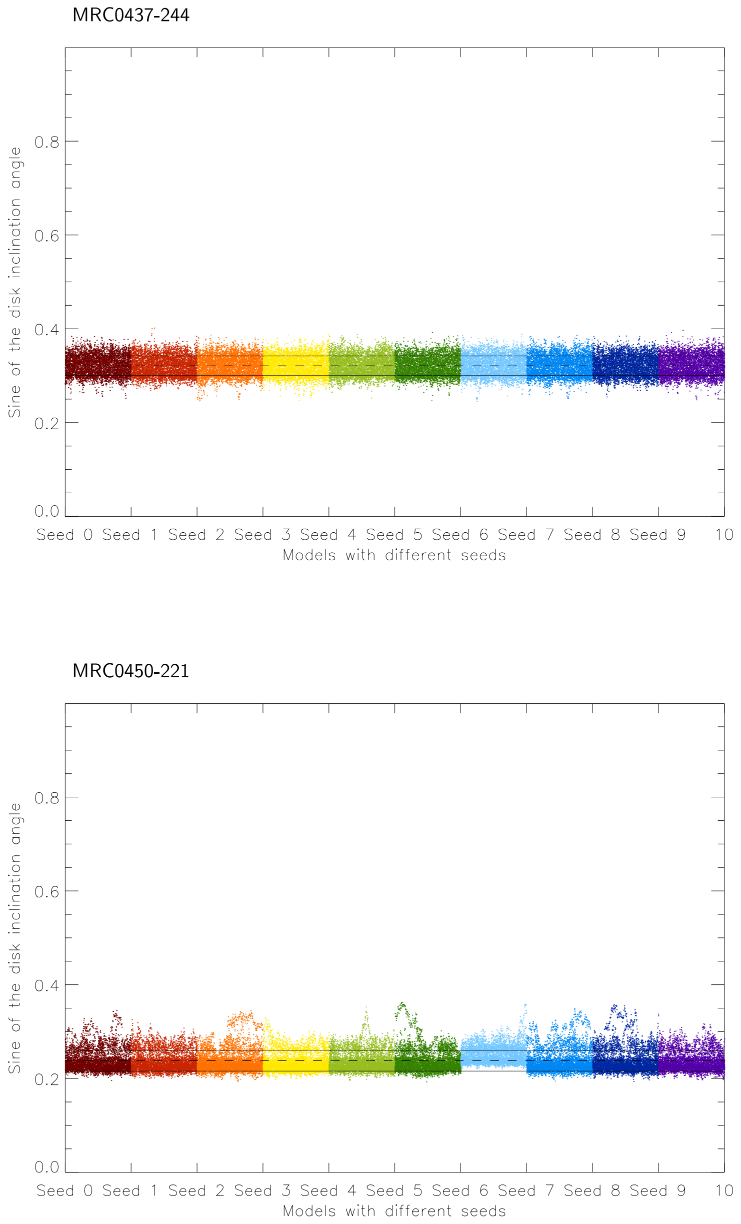

Figure 3.6: Scatter of disk axis angles caused by changes in the seed for MRC0437-244 (top) and MRC0450-221 (bottom). This illustrates the stability of the fitted angles with a change of seed. The dotted black line marks the mean angle across all seeds, and the solid black lines mark the 1-σ error on this angle.

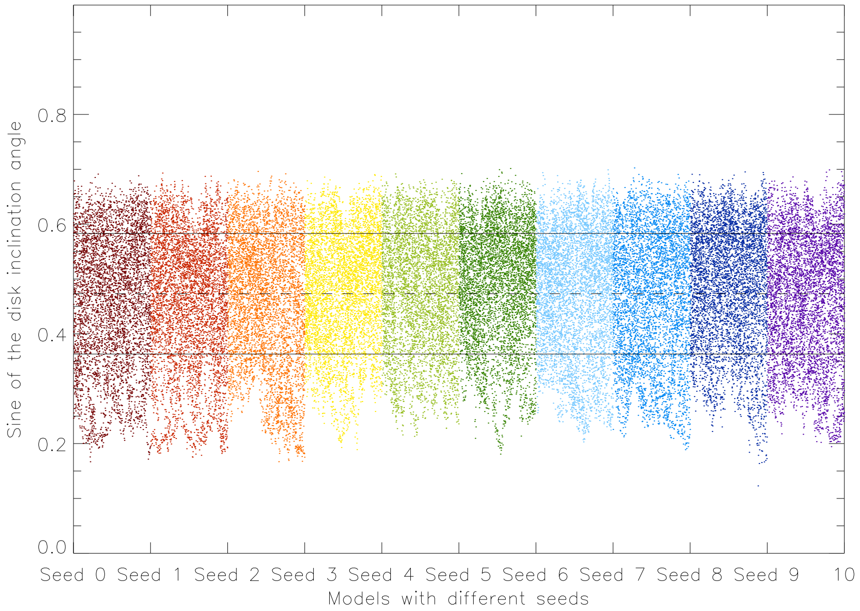

Figure 3.7: Scatter of disk axis angles caused by changes in the seed for MRC1114-220. This source was singled out for an extra test, as it is an outlier in the disk axis angle – jet angle plot, and has one of the largest error bars. The disk axis angle is shown to be still extremely stable in the fit to this spectrum. The dotted black line marks the mean angle across all seeds, and the solid black lines mark the 1-σ error on this angle.

leading to the false minimum.

3.5.2.3 *Changes to the ensemble number*

Figure 3.9 shows the posterior probabilities for MRC0437-244 and MRC0450-221 for fits in which the ensemble number has been allowed to vary in *BayeSys3*. The ensemble is the number of different parallel explorations of the parameter space, and if this number is set too low, the posterior probability may end up localised in a false minimum. Initially, an ensemble of 10 was used in this study, until a previous test showed that this ensemble was insufficient for good fitting; an ensemble of 20 is used for all results presented here. The yellow points show the fits created with an ensemble number of 20. Orange and red points show the results from using ensembles of 10 and 5 respectively, while green and blue show the probability distributions from using ensembles of 30 and 50. For MRC0437-244, all fits constrain to the same regions of the parameter space.

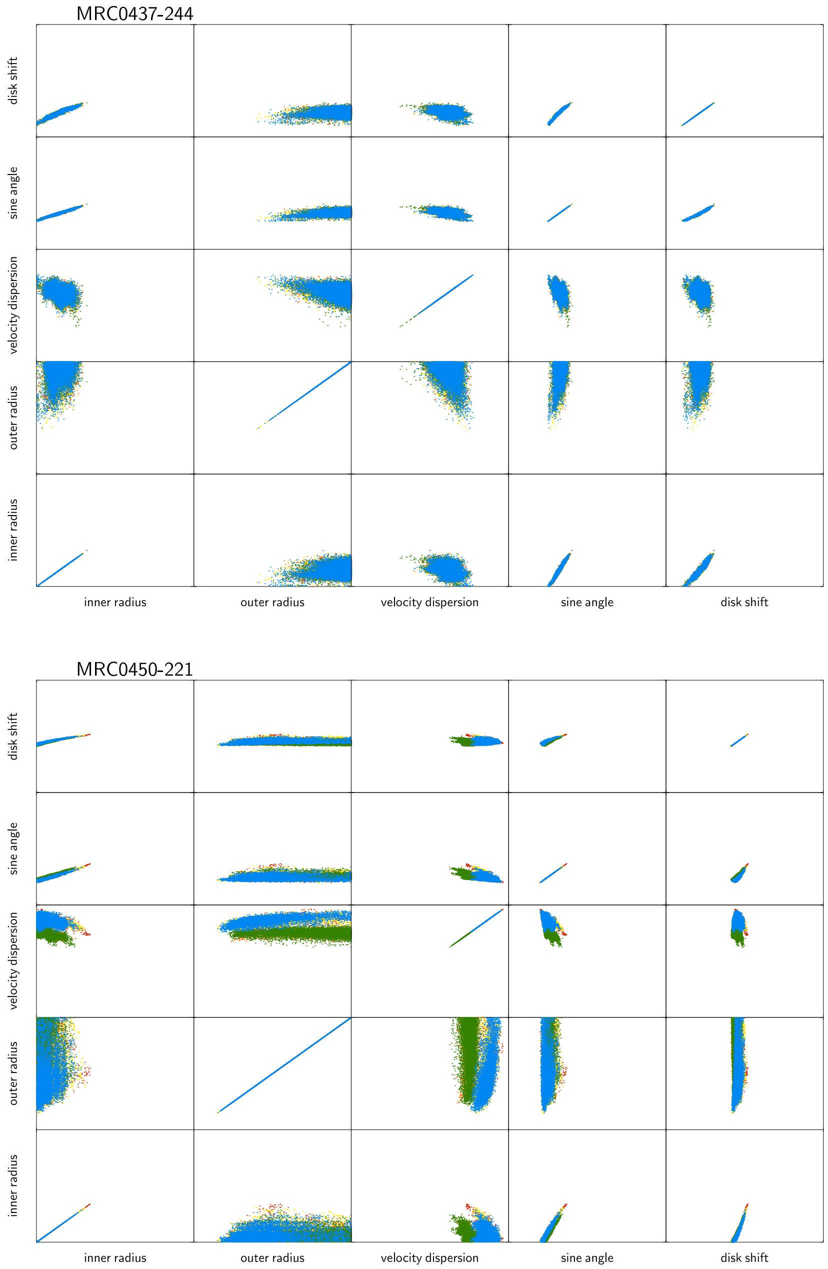

Figure 3.8: A plot of the correlations between the disk parameters for MRC0437-244 (top) and MRC0450-221 (bottom) with different rates for the annealing phase of the Bayesian optimisation plotted in different colours. Red is a rate of 0.5, orange a rate of 0.2, yellow 0.1 (the rate used in the main fitting), green 0.08 and blue is a rate of 0.05.

MRC0450-221 again shows that there is a false minimum found for the local velocity dispersion of the disk, as in Sections 3.5.2.1 and 3.5.2.2, with ensembles of both larger and smaller size constraining to a different values of this parameter; this point indicates that it is not the ensemble size that is causing the posterior distribution to become localised in two different regions. There is a difference of $\Delta \ln(\text{Evidence}) \sim 3$ between the highest and lowest evidence cases.

3.5.2.4 *Adding noise to the spectrum*

Tests were made in which additional Gaussian random noise was added to the spectra, with a FWHM of 5% of the data value. This test is not ideal; the aim is to quantify how greater noise on a spectrum affects the fitting, but in this scenario, noise is being added not to a perfect emission spectrum but to the already noisy spectrum. Figure 3.10 shows the results of this test for the two randomly-selected test quasars. For MRC0437-244, the posterior probability distributions for the parameters are constrained to very similar regions. For MRC0450-221, the probability distributions for the disk parameters are seen to cover a slightly larger range than for the single fits; the posterior parameter space for the local velocity dispersion is covered by a very similar distribution of fits to the overall space occupied by the two adjacent regions seen in the tests in Sections 3.5.2.1, 3.5.2.2 and 3.5.2.3, which seems sensible.

3.5.2.5 *Smoothing the spectrum*

Fits were made to spectra smoothed in *IDL* using boxcar widths of between 3 and 9 pixels, where the pixel scale is ~ 2 Å. Figure 3.11 (bottom) shows the degraded MRC0437-244 spectra, and Figure 3.11 (top) shows the results of the different Bayesian fits for these spectra. The red points show the original fits, and orange, yellow, green and blue points show increasing smoothing. For this quasar, the smoothing allows the fit to constrain to a tighter probability distribution. This shows that the fit is not affected by any minor noise spikes.

Figure 3.12 (bottom) shows the smoothed MRC0450-221 spectra, and Figure 3.12 (top) shows the probability distributions of parameters for this quasar spectrum under

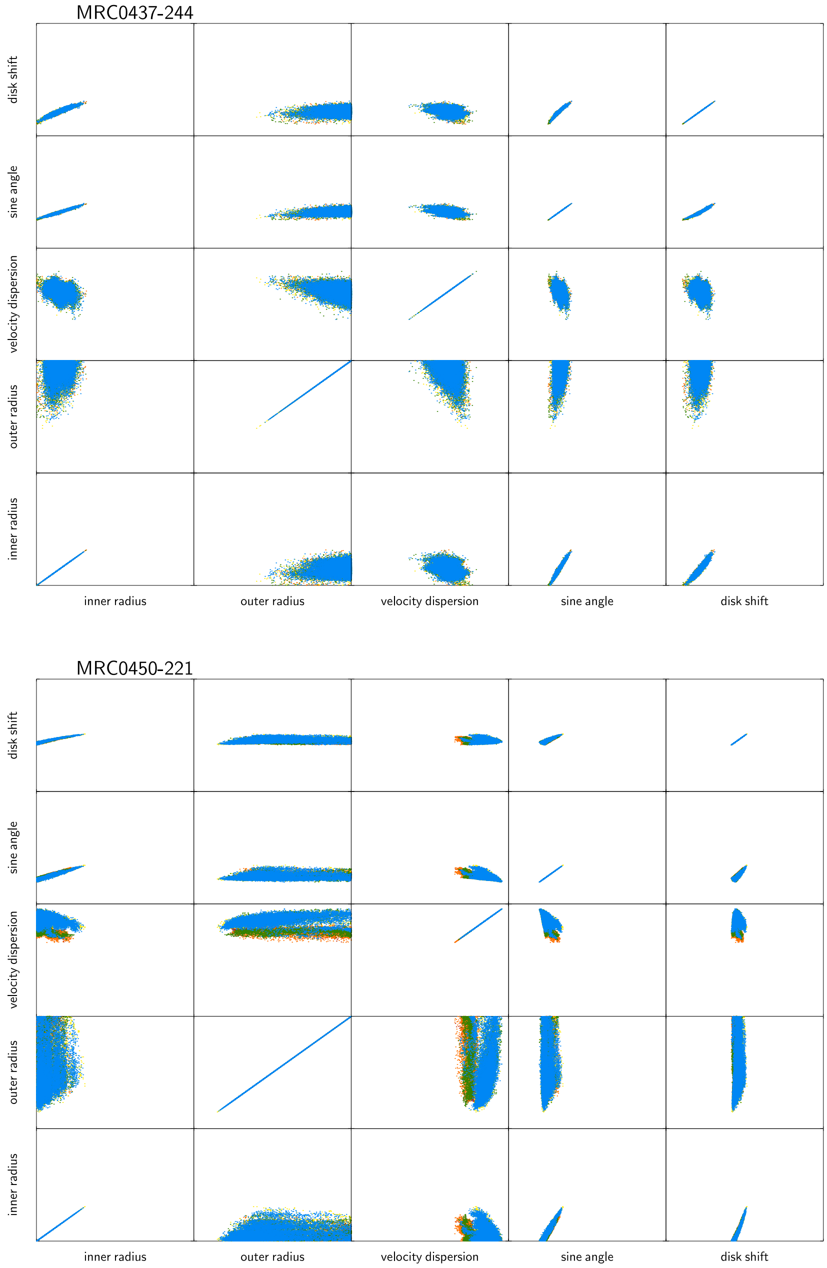

Figure 3.9: A plot of the correlations between the disk parameters from MRC0437-244 (top) and MRC0450-221 (bottom) with different ensemble sizes for the Bayesian Monte Carlo fitting plotted in different colours. Red is an ensemble of 5, orange an ensemble of 10, yellow an ensemble of 20 (the ensemble used in the main fitting), green is 30, and blue is an ensemble of 50.

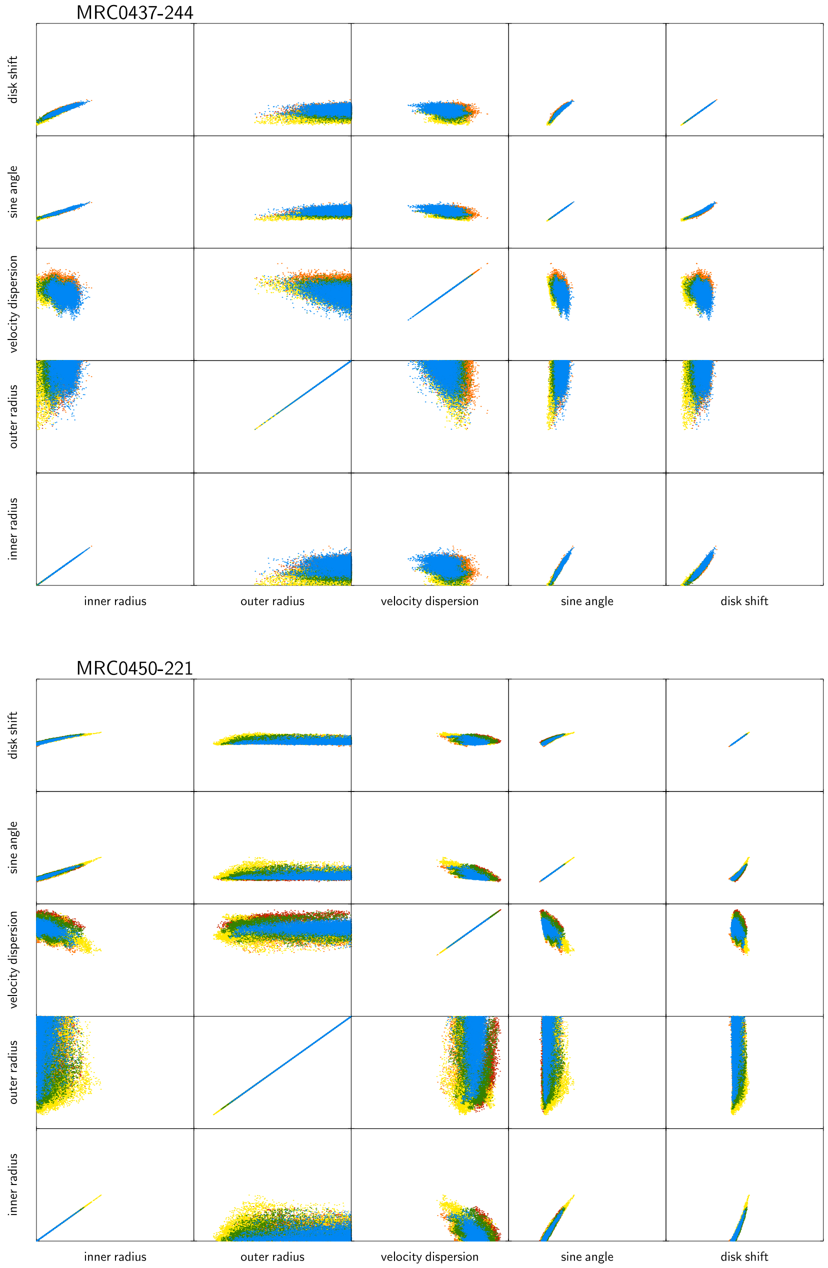

Figure 3.10: A plot of the correlations between the disk parameters from fits to the MRC0437-244 spectrum (top) and the MRC0450-221 spectrum (bottom) with Gaussian noise added to the spectra. The added noise has a FWHM of 5% of the data value. The red points are the fit to the original spectra, all other colours are fits to the spectra with different random noise added.

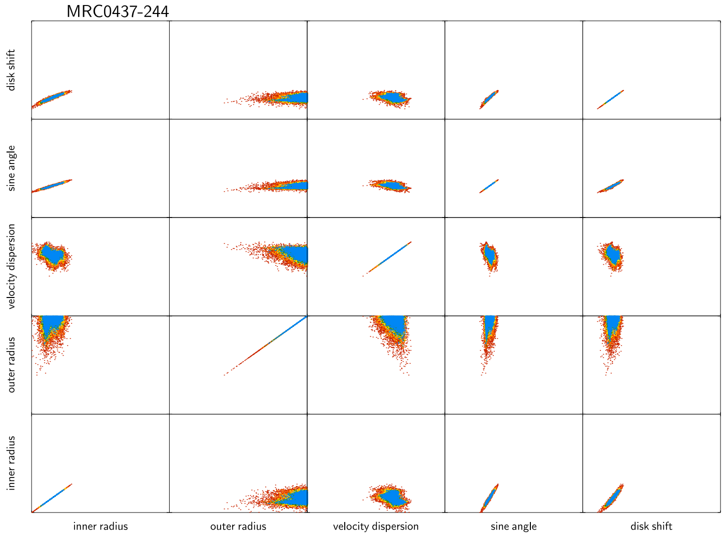

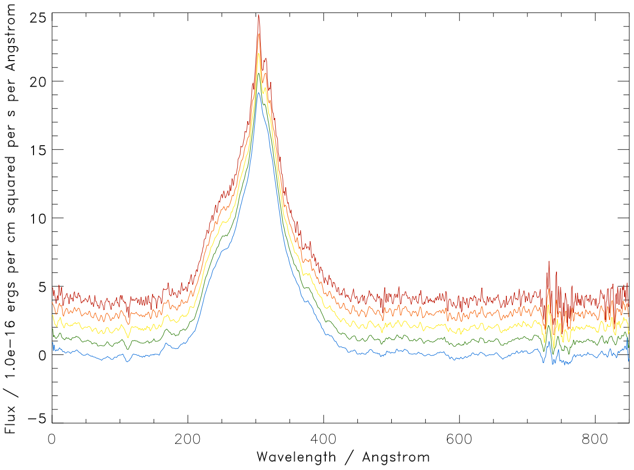

Figure 3.11: Top: A plot of the correlations between the disk parameters from fits to the MRC0437-244 spectrum which has been smoothed using a boxcar smoothing routine in *IDL*. The red points are the fit to the unsmoothed spectrum, other spectra have been smoothed with boxcar widths of 3 pixels (orange points), 5 pixels (yellow points), 7 pixels (green points) and 9 pixels (blue points).
Bottom: The MRC0437-244 spectrum, degraded using a boxcar smoothing routine in *IDL*. The red spectrum is unsmoothed, the orange spectrum has been smoothed with a boxcar width of 3 pixels , the yellow with a width of 5 pixels , the green with a width of 7 pixels, and the blue with a width of 9 pixels.

different degrees of degradation. The orange points, yellow points and green points (representing fits to spectra smoothed with boxcar widths of 3, 5 and 7 pixels respectively) fit to the same regions in probability space (including the slight degeneracy in local velocity dispersion) that the other stability tests show. However, the fit to the spectrum smoothed with the boxcar width of 9 pixels (blue points) show that at this stage, fitted structure has been removed from the spectrum. At this width of smoothing, the degraded features include genuine structure as well as noise (for example, narrow H α has been significantly reduced in intensity), so this is a reasonable point for this test to fail. As with previous tests (see Sections 3.5.2.1, 3.5.2.2 and 3.5.2.3), there are two adjacent minima found for the local velocity dispersion.

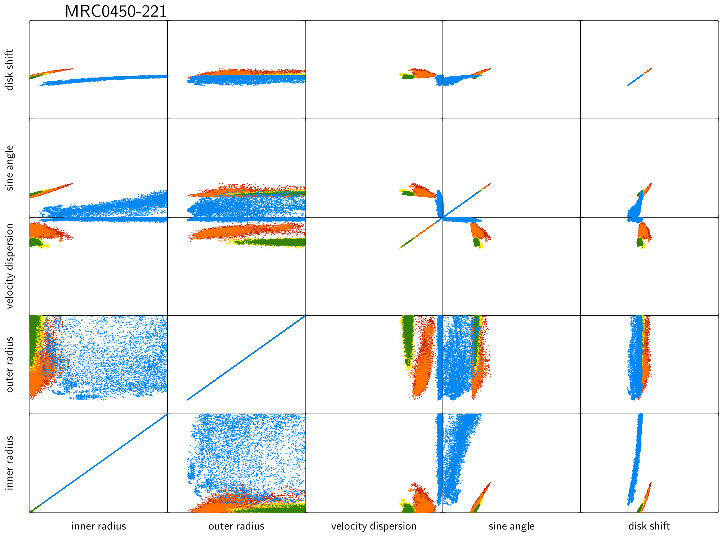

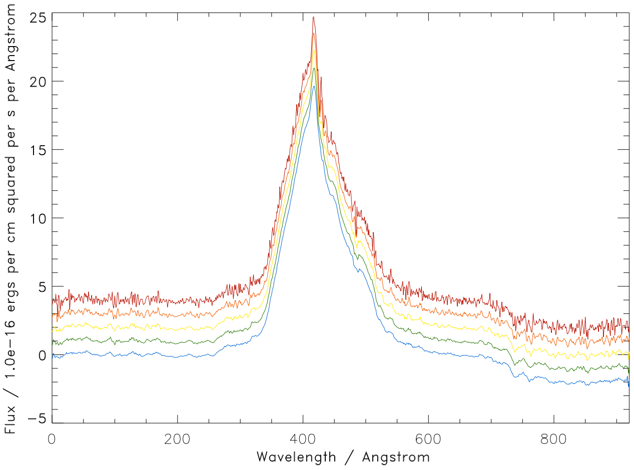

Figure 3.12: Top: A plot of the correlations between the disk parameters from fits to the MRC0450-221 spectrum which has been smoothed using a boxcar smoothing routine in *IDL*. The red points are the fit to the unsmoothed spectrum, other spectra have been smoothed with boxcar widths of 3 pixels (orange points), 5 pixels (yellow points), 7 pixels (green points) and 9 pixels (blue points).
Bottom: The MRC0450-221 spectrum, degraded using a boxcar smoothing routine in *IDL*. The red spectrum is unsmoothed, the orange spectrum has been smoothed with a boxcar width of 3 pixels, the yellow with a width of 5 pixels, the green with a width of 7 pixels, and the blue with a width of 9 pixels.

3.6 *Results*

3.6.1 *Fits to the spectra*

The best-evidence Bayesian fits to spectra and the residuals from these fits are shown in Figure 3.13, with the fit plotted in blue on the spectrum. In cases where disks were fit, the disk fit is plotted in red, and the posterior distribution of the sine of the disk axis angle is shown in a small plot to the right of the spectrum. Each plot is marked with the model with which it was fit, and whether there was strong evidence for a disk according to the Jeffreys' criterion (SD), moderate evidence (MD), weak evidence (WD), whether the results were inconclusive but did not rule out a disk (PD), or whether there was strong or moderate evidence against the presence of a disk (ND).

For completeness, Figure 3.14 shows the best fits including a disk for those quasars whose selected best models did not include an accretion disk.

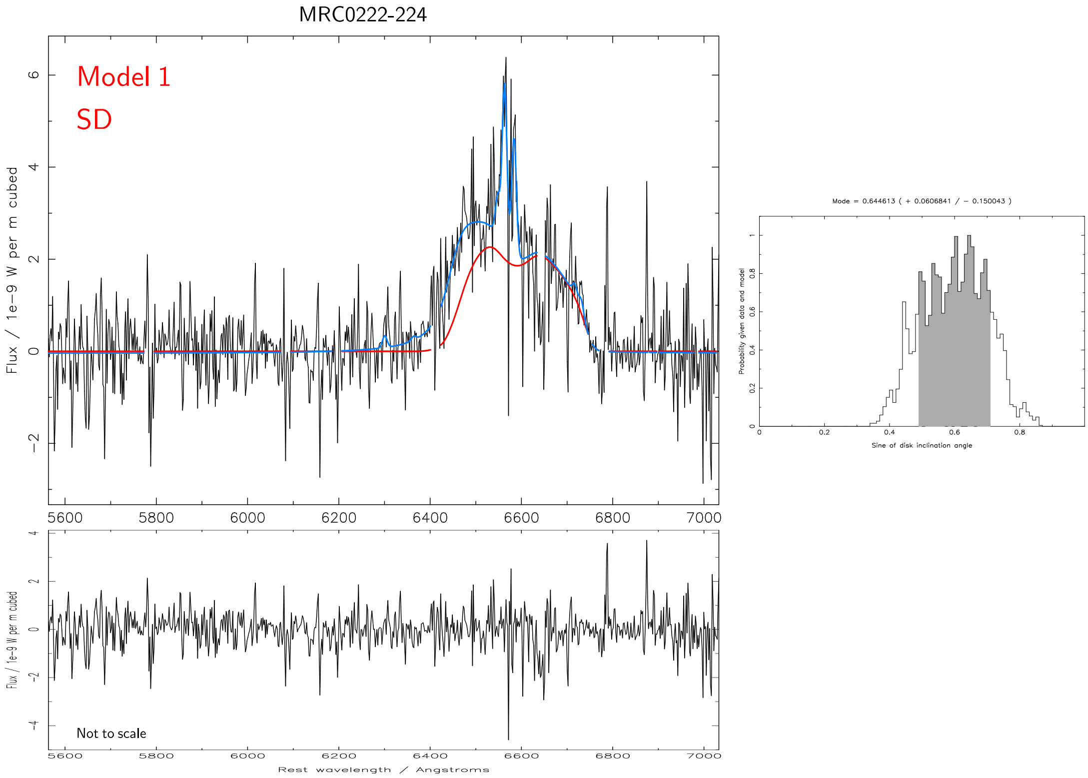

Figure 3.13: The best Bayesian fits for each quasar with residuals plotted below. The flux scale of the residuals is the same as for the spectrum, except in cases specifically marked "Not to scale" in the lower left corner. Wavelengths are rest frame.
The best fit is shown with the blue line. In cases where the disk is present, the disk component is shown with a red line, and the posterior distribution of the sine of the disk axis angle (normalised to unity) is shown plotted against the sine of the disk axis angle (axis from 0 to 1) in a small plot to the right of the spectrum. The shaded area of this plot shows the 1-σ error bounds.
Each plot is labelled with the index of the model with which it was fit, written in red if the model includes a disk, and blue if it does not. It is also labelled with a code according to whether there is evidence for a disk: SD = strong evidence for a disk; MD = moderate evidence for a disk; WD = weak evidence for a disk; PD = a possible disk, i.e. the best fit is a non-disk model, but there is only weak or inconclusive evidence for this; ND = strong evidence against the presence of a disk.

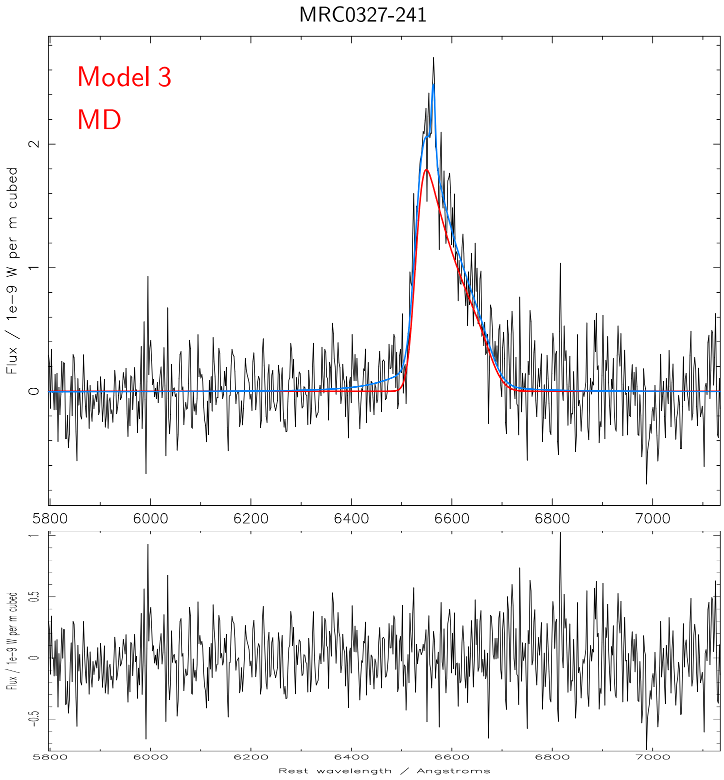
MRC0327-241
Model 3
MD
Flux / 1e−9 W per m cubed
0
1
2
5800
6000
6200
6400
6600
6800
7000
−0.5
0.5
1
Rest wavelength / Angstroms

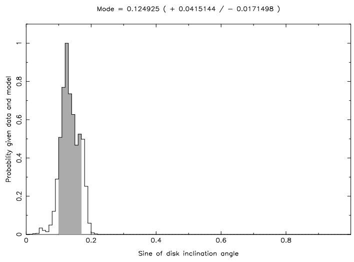
Mode = 0.124925 (+ 0.0415144 / − 0.0171498)
Probability given data and model
0
0.2
0.4
0.6
0.8
1
Sine of disk inclination angle

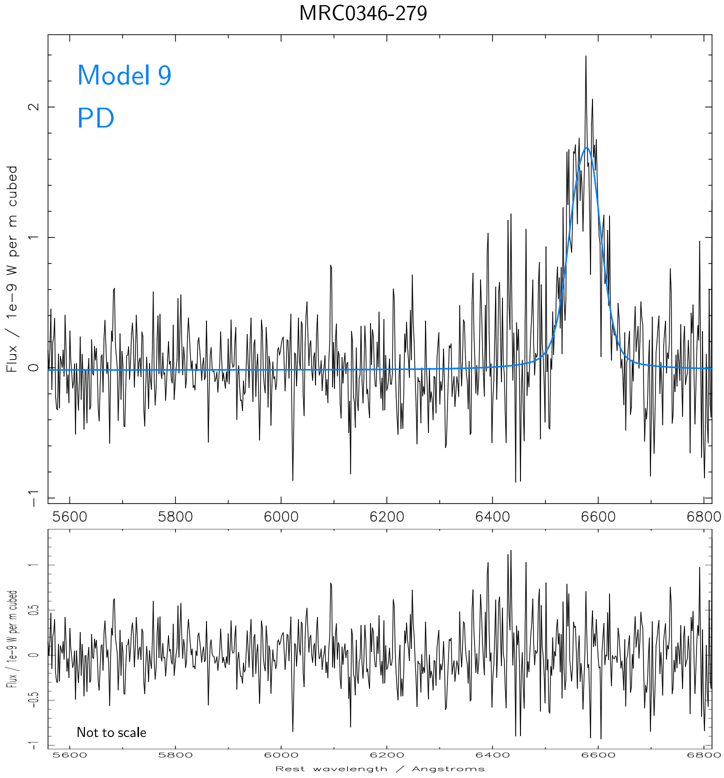
MRC0346-279
Model 9
PD
Flux / 1e−9 W per m cubed
−1
0
1
2
5600
5800
6000
6200
6400
6600
6800
−0.5
0.5
Not to scale
Rest wavelength / Angstroms

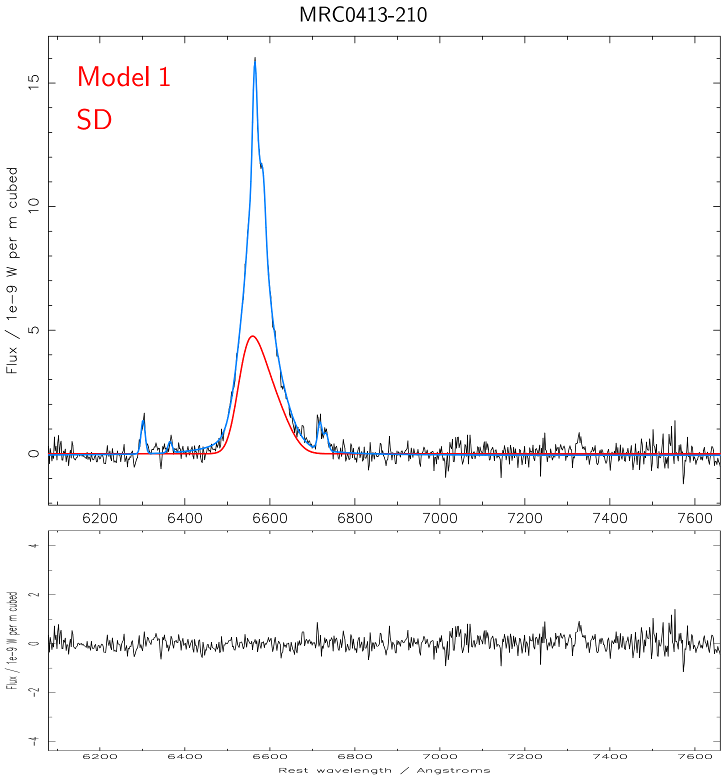
MRC0413-210
Model 1
SD
Flux / 1e−9 W per m cubed
0
5
10
15
6200
6400
6600
6800
7000
7200
7400
7600
Flux / 1e-9 W per m cubed
−4
−2
0
2
4
Rest wavelength / Angstroms

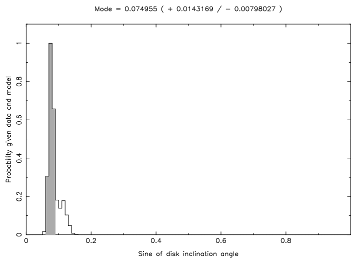
Mode = 0.074955 (+ 0.0143169 / − 0.00798027)
Probability given data and model
0
0.2
0.4
0.6
0.8
1
Sine of disk inclination angle

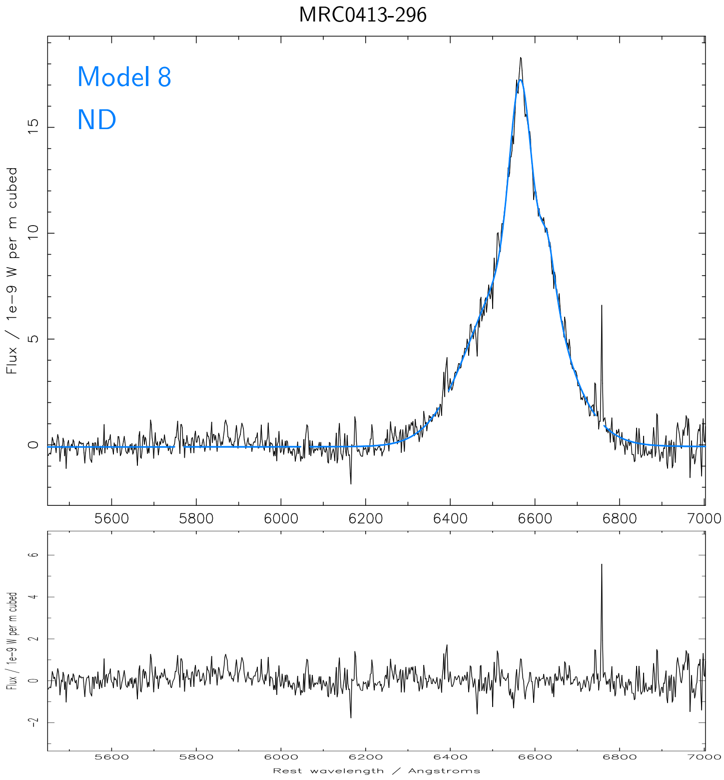
MRC0413-296
Model 8
ND
Flux / 1e−9 W per m cubed
0
5
10
15
5600
5800
6000
6200
6400
6600
6800
7000
Flux / 1e-9 W per m cubed
−2
0
2
4
6
Rest wavelength / Angstroms

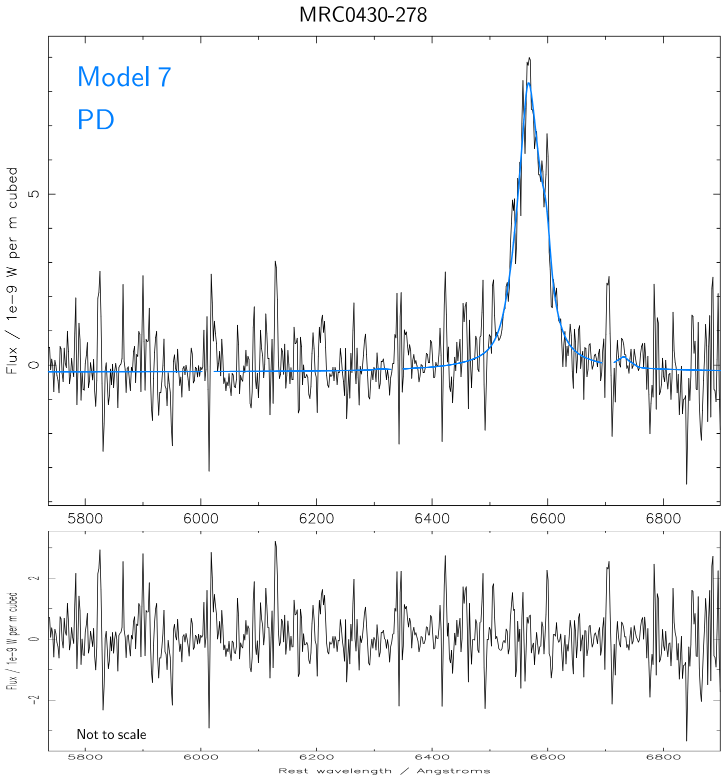
MRC0430-278
Model 7
PD
Flux / 1e−9 W per m cubed
0
5
5800
6000
6200
6400
6600
6800
Flux / 1e−9 W per m cubed
−2
0
2
Not to scale
Rest wavelength / Angstroms

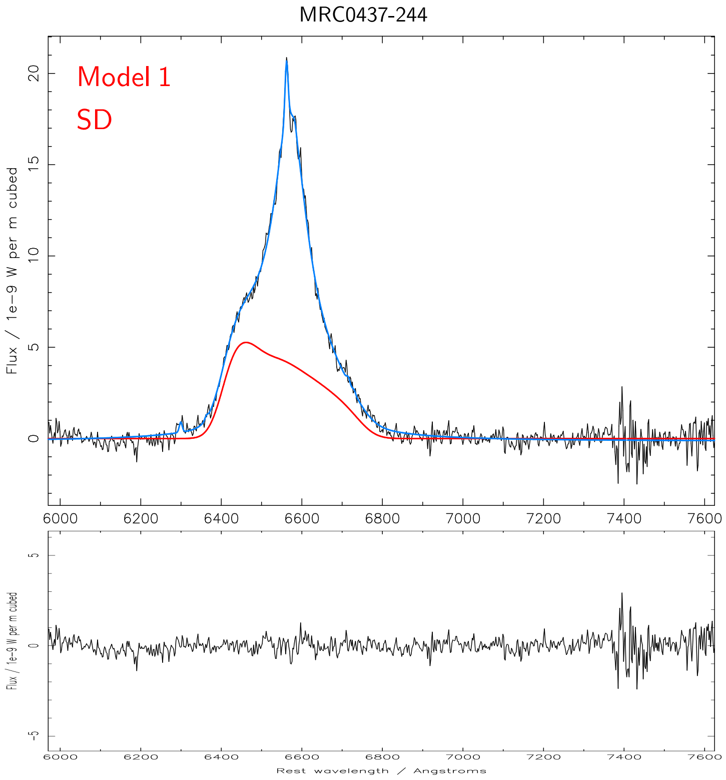
MRC0437-244
Model 1
SD
Flux / 1e−9 W per m cubed
0
5
10
15
20
6000
6200
6400
6600
6800
7000
7200
7400
7600
Flux / 1e−9 W per m cubed
−5
0
5
Rest wavelength / Angstroms

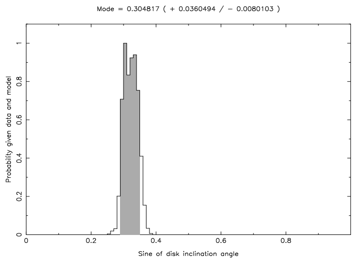
Mode = 0.304817 (+ 0.0360494 / − 0.0080103)
Probability given data and model
0
0.2
0.4
0.6
0.8
1
0
0.2
0.4
0.6
0.8
Sine of disk inclination angle

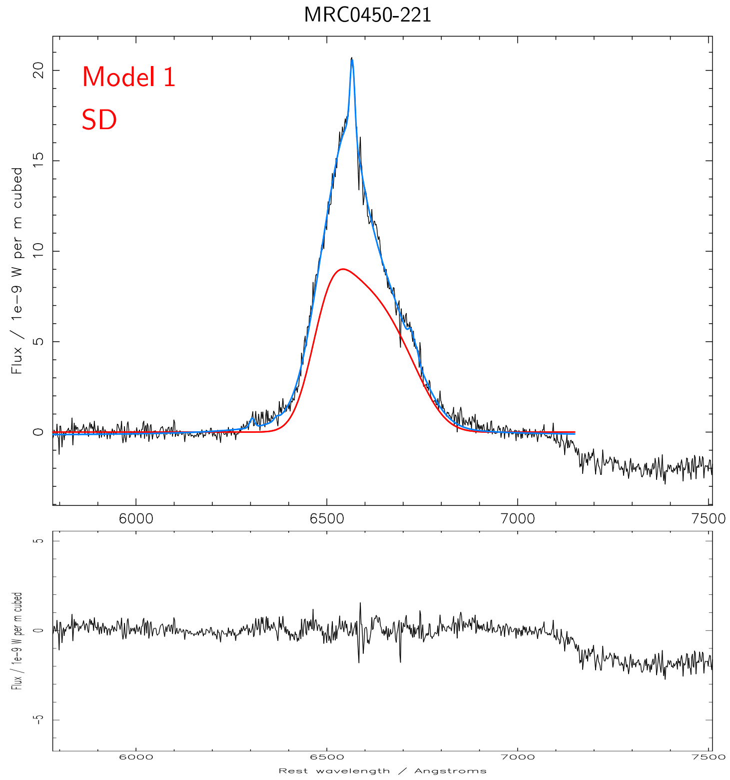
MRC0450-221
Model 1
SD
Flux / 1e−9 W per m cubed
0
5
10
15
20
6000
6500
7000
7500
Flux / 1e−9 W per m cubed
−5
0
5
Rest wavelength / Angstroms

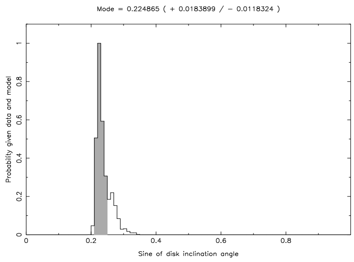
Mode = 0.224865 (+ 0.0183899 / − 0.0118324)
Probability given data and model
0
0.2
0.4
0.6
0.8
1
Sine of disk inclination angle

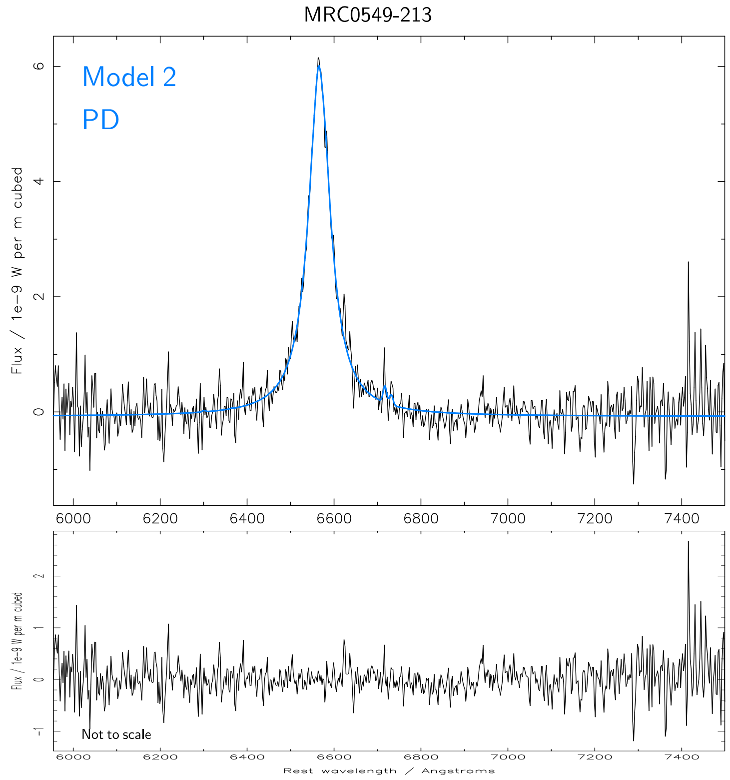
MRC0549-213
Model 2
PD
Flux / 1e−9 W per m cubed
0
2
4
6
6000
6200
6400
6600
6800
7000
7200
7400
Flux / 1e−9 W per m cubed
−1
0
1
2
Not to scale
Rest wavelength / Angstroms

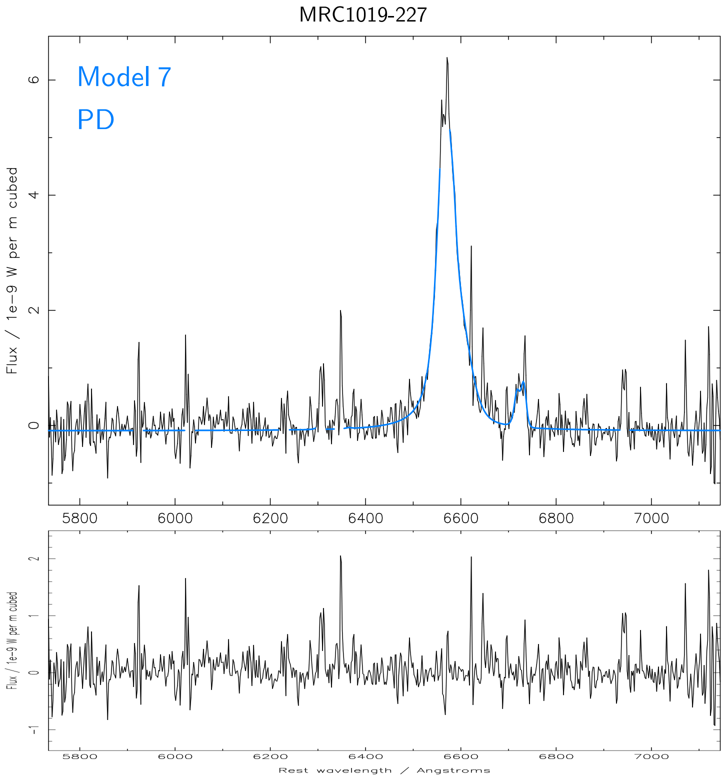
MRC1019-227
Model 7
PD
Flux / 1e−9 W per m cubed
Rest wavelength / Angstroms
5800
6000
6200
6400
6600
6800
7000

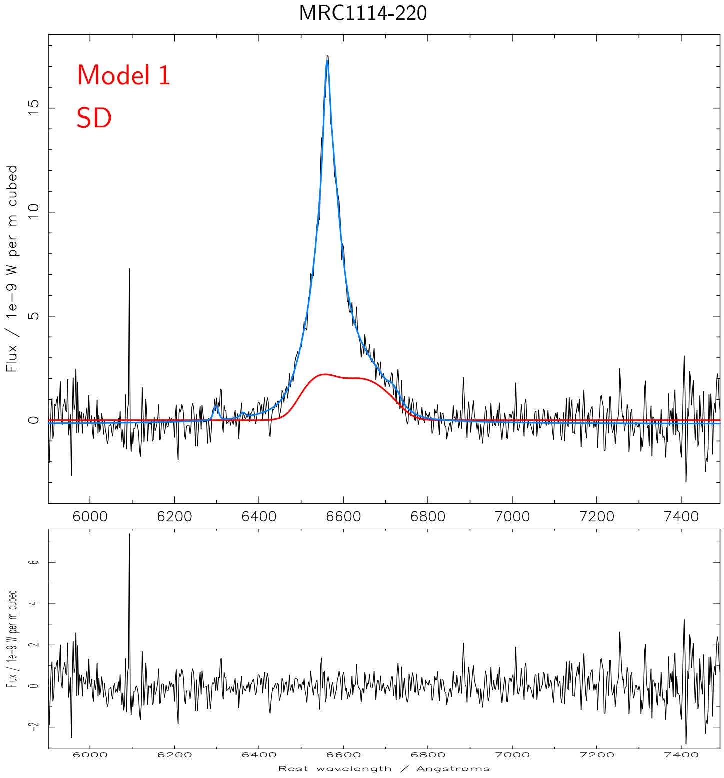
MRC1114-220
Model 1
SD
Flux / 1e−9 W per m cubed
Rest wavelength / Angstroms
6000
6200
6400
6600
6800
7000
7200
7400

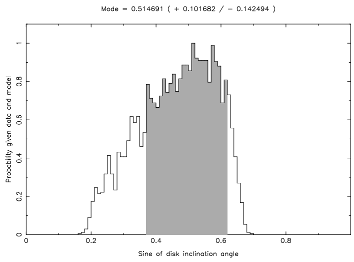
Mode = 0.514691 (+ 0.101682 / − 0.142494)
Probability given data and model
Sine of disk inclination angle
0
0.2
0.4
0.6
0.8
1

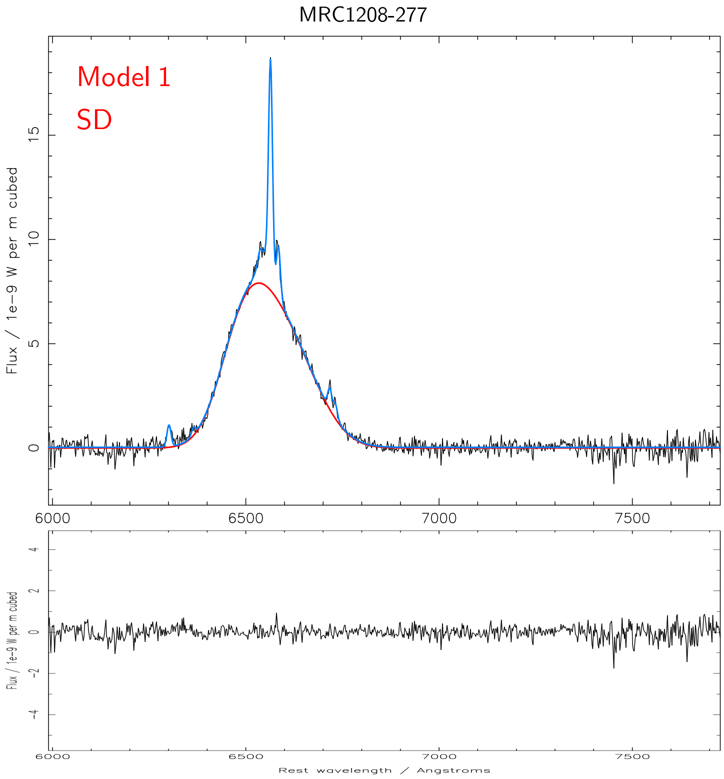
MRC1208-277
Model 1
SD
Flux / 1e−9 W per m cubed
0
5
10
15
6000
6500
7000
7500
Flux / 1e−9 W per m cubed
−4
−2
0
2
4
Rest wavelength / Angstroms

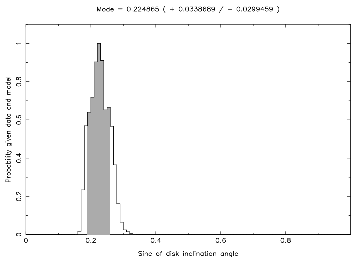
Mode = 0.224865 (+ 0.0338689 / − 0.0299459)
Probability given data and model
0
0.2
0.4
0.6
0.8
1
Sine of disk inclination angle

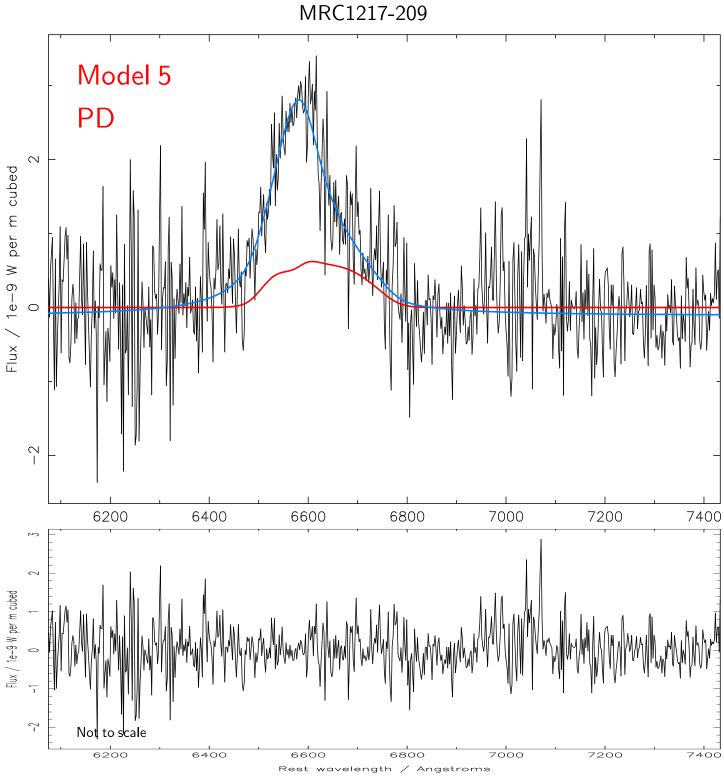
MRC1217-209
Model 5
PD
Flux / 1e−9 W per m cubed
−2
0
2
6200
6400
6600
6800
7000
7200
7400
Flux / 1e−9 W per m cubed
−2
−1
0
1
2
3
Not to scale
Rest wavelength / Angstroms

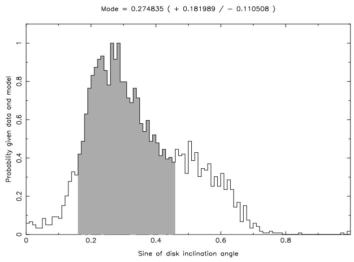
Mode = 0.274835 (+ 0.181989 / − 0.110508)
Probability given data and model
0
0.2
0.4
0.6
0.8
1
Sine of disk inclination angle

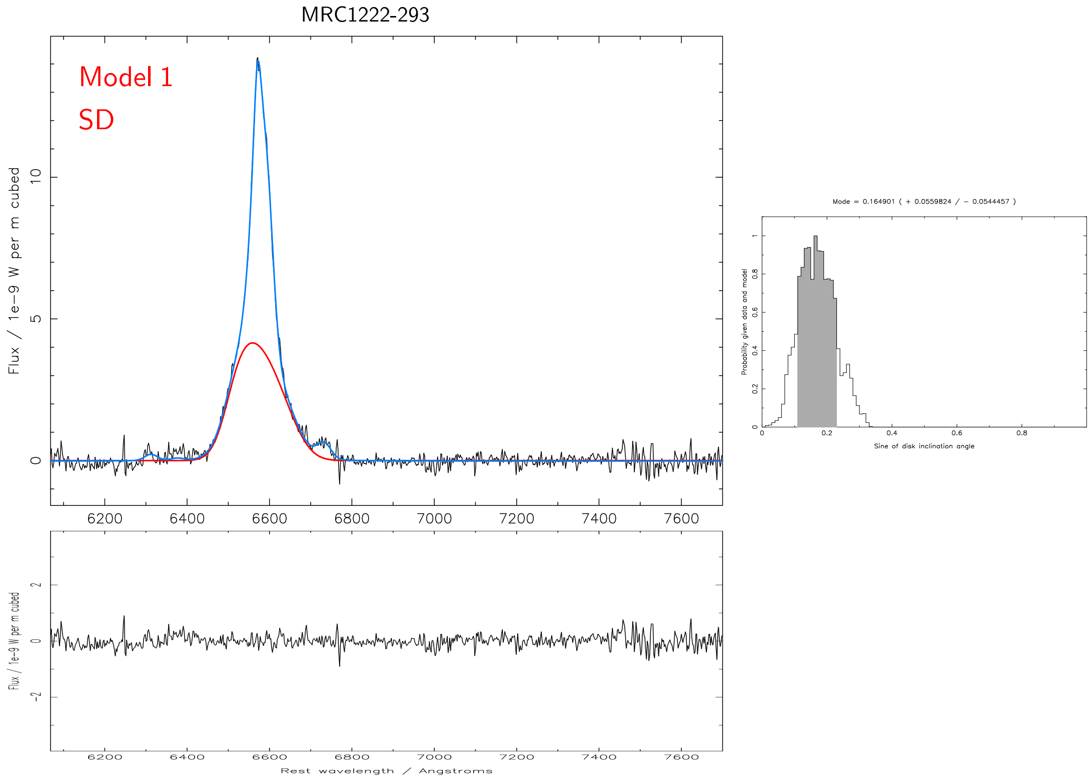
MRC1222-293
Model 1
SD
Flux / 1e−9 W per m cubed
0
5
10
6200
6400
6600
6800
7000
7200
7400
7600
−2
0
2
Rest wavelength / Angstroms
Mode = 0.164901 (+ 0.0559824 / − 0.0544457)
Probability given data and model
0
0.2
0.4
0.6
0.8
1
Sine of disk inclination angle

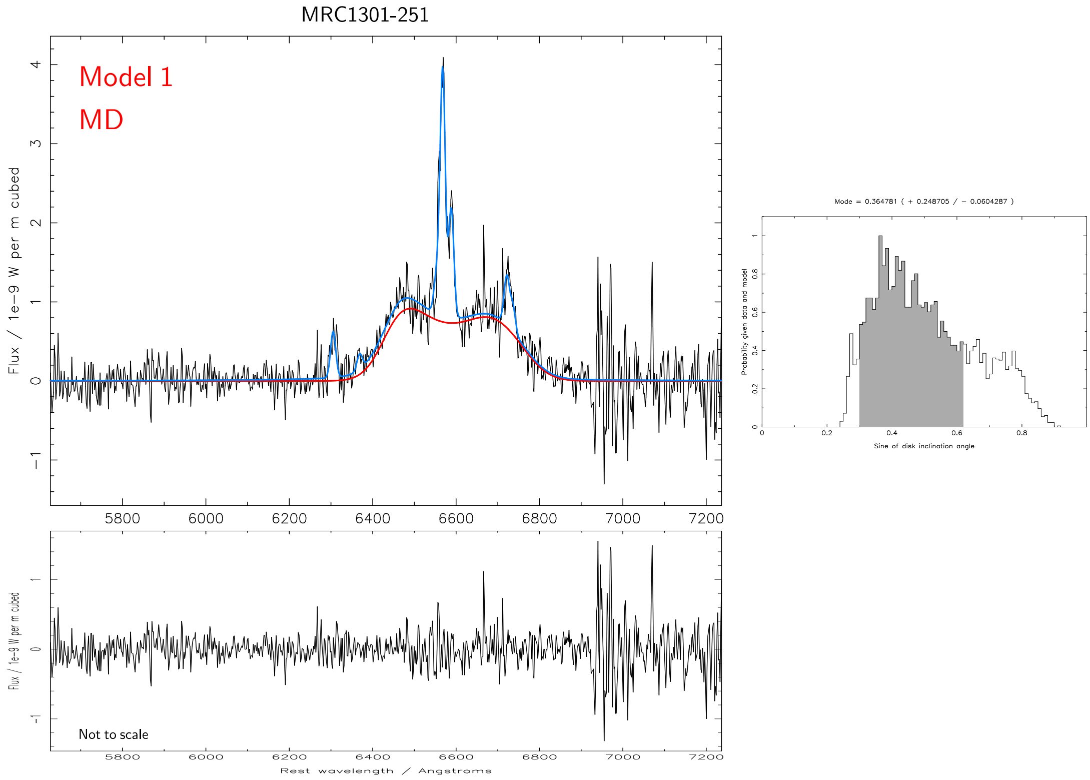
MRC1301-251
Model 1
MD
Flux / 1e−9 W per m cubed
−1
0
1
2
3
4
5800
6000
6200
6400
6600
6800
7000
7200
Not to scale
Rest wavelength / Angstroms
Mode = 0.364781 (+ 0.248705 / − 0.0604287)
Probability given data and model
0
0.2
0.4
0.6
0.8
1
Sine of disk inclination angle

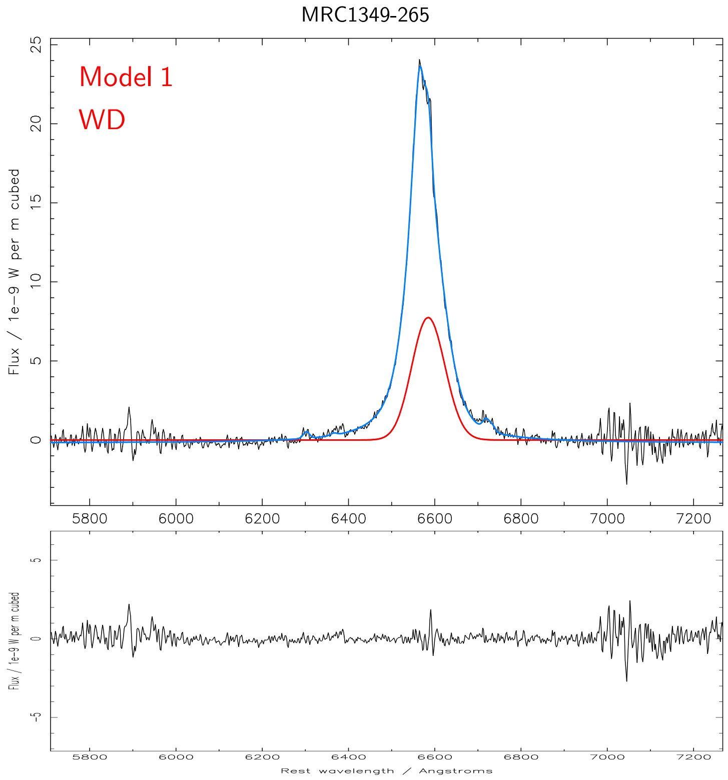
MRC1349-265
Model 1
WD
Flux / 1e−9 W per m cubed
0
5
10
15
20
25
5800
6000
6200
6400
6600
6800
7000
7200
Flux / 1e−9 W per m cubed
−5
0
5
Rest wavelength / Angstroms

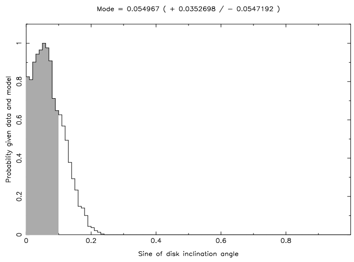
Mode = 0.054967 (+ 0.0352698 / − 0.0547192)
Probability given data and model
0
0.2
0.4
0.6
0.8
1
0
0.2
0.4
0.6
0.8
Sine of disk inclination angle

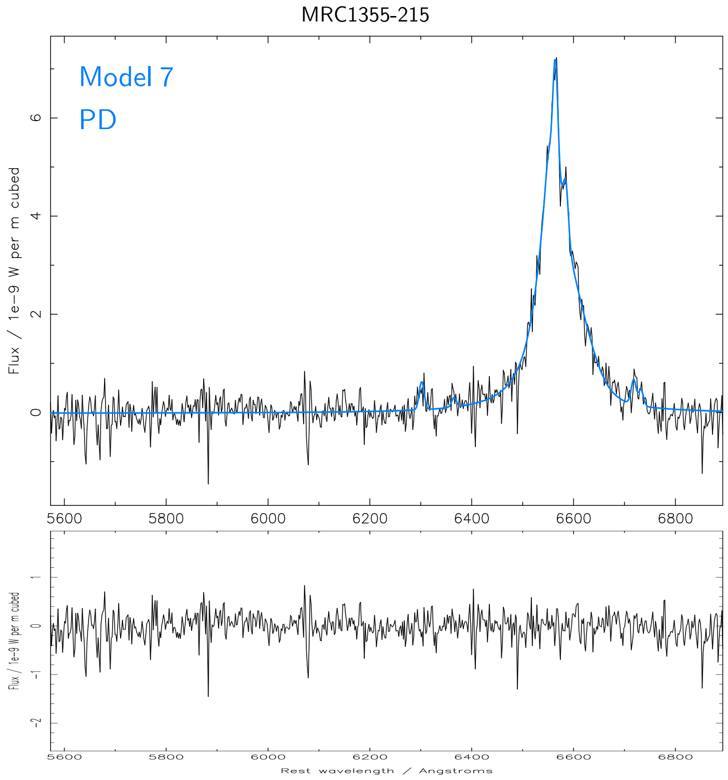
MRC1355-215
Model 7
PD
Flux / 1e−9 W per m cubed
0
2
4
6
5600
5800
6000
6200
6400
6600
6800
Flux / 1e−9 W per m cubed
−2
−1
0
1
Rest wavelength / Angstroms

MRC1355-236

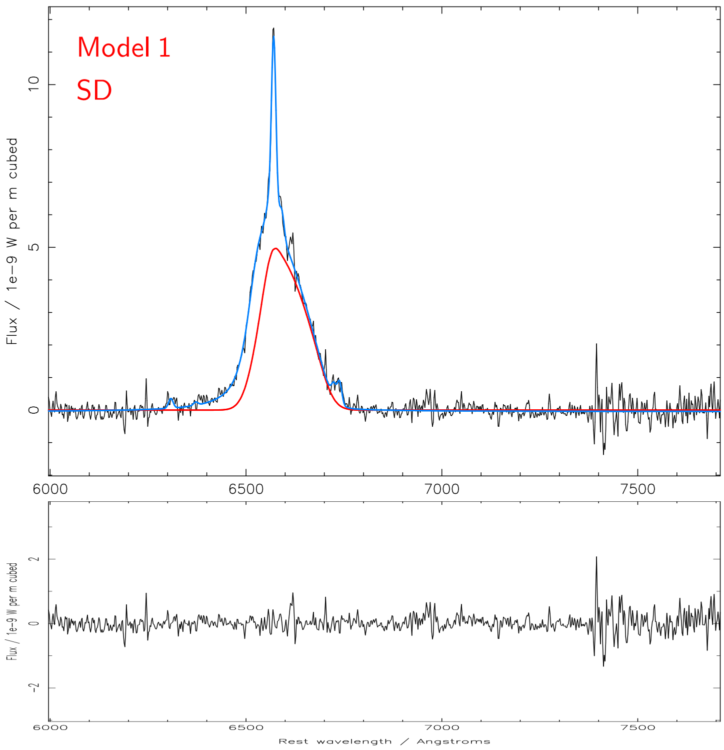

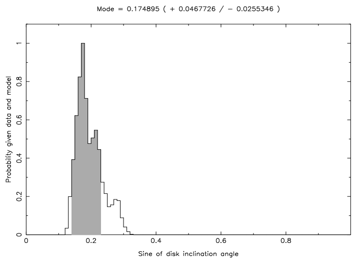

MRC1359-281

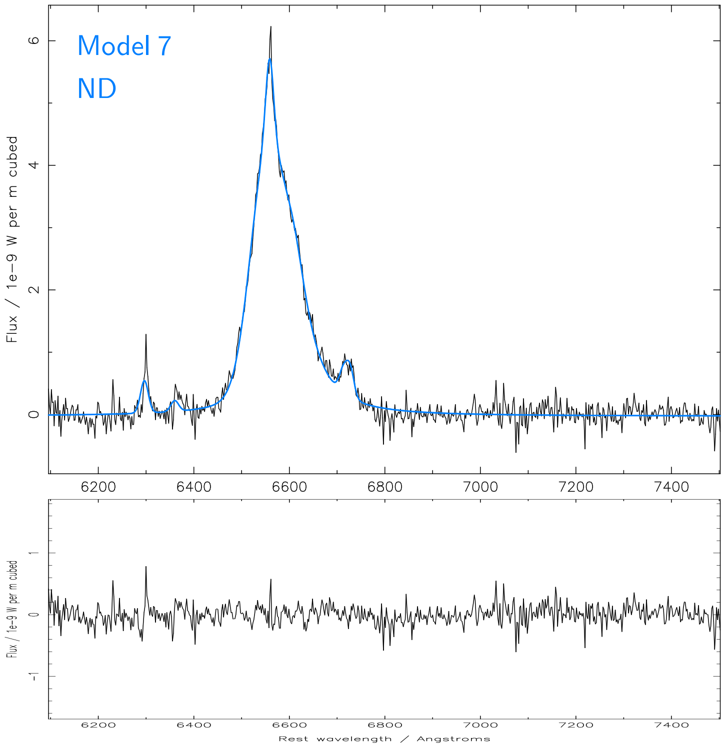

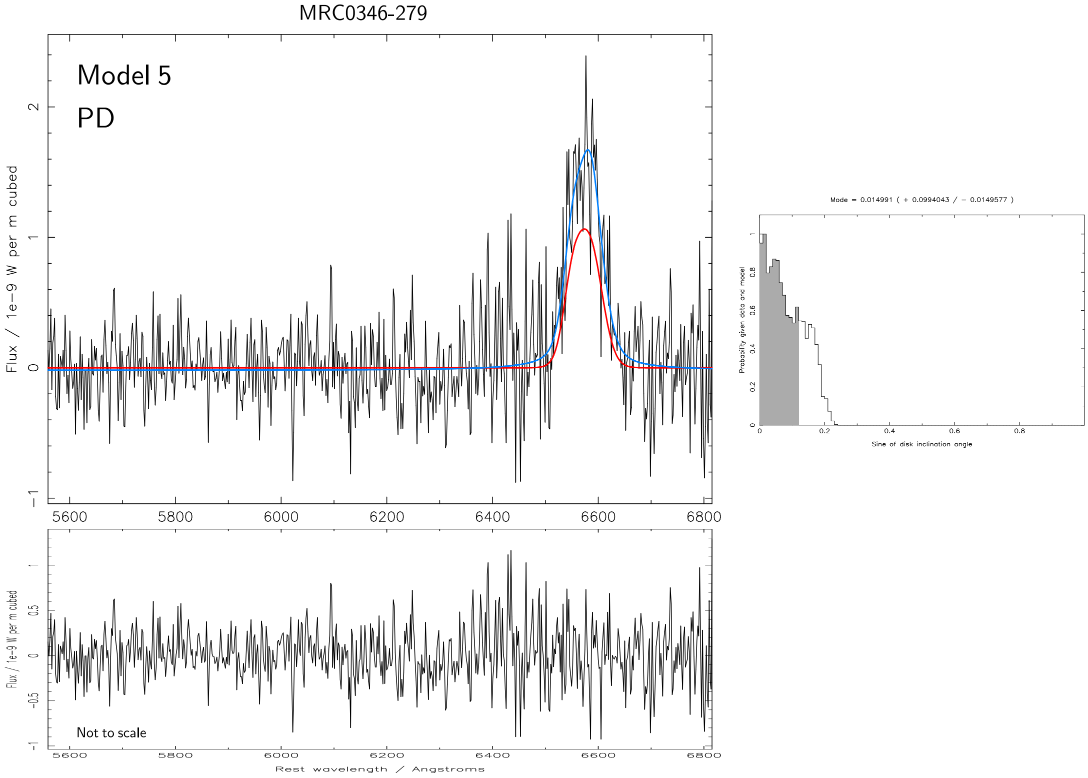

Figure 3.14: The best Bayesian fits including an accretion disk for each quasar, for the cases in which the highest evidence fit did not include a disk. Residuals are plotted below each spectrum. The flux scale of the residuals is the same as for the spectrum, except in cases specifically marked "Not to scale" in the lower left corner. Wavelengths are rest frame.
The best fit is shown with the blue line. The disk component is shown with a red line, and the posterior distribution of the sine of the disk axis angle (normalised to unity) is shown plotted against the sine of the disk axis angle (axis from 0 to 1) in a small plot to the right of the spectrum. The shaded area of this plot shows the 1-σ error bounds.
Each plot is labelled with the index of the model with which it was fit. It is also labelled with a code according to whether there is evidence for a disk: SD = strong evidence for a disk; MD = moderate evidence for a disk; WD = weak evidence for a disk; PD = a possible disk, i.e. the best fit is a non-disk model, but there is only weak or inconclusive evidence for this; ND = strong evidence against the presence of a disk.

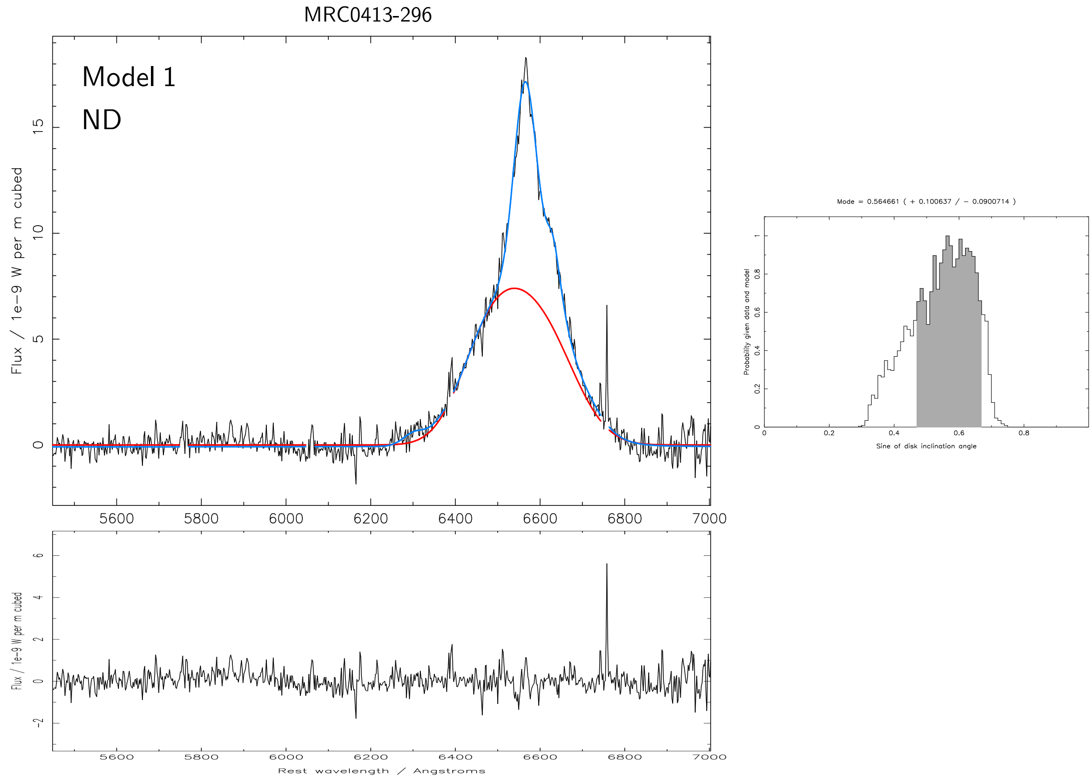
MRC0413-296
Model 1
ND
Flux / 1e−9 W per m cubed
0
5
10
15
5600
5800
6000
6200
6400
6600
6800
7000
Flux / 1e−9 W per m cubed
−2
0
2
4
6
Rest wavelength / Angstroms
Mode = 0.564661 (+ 0.100637 / − 0.0900714)
Probability given data and model
0
0.2
0.4
0.6
0.8
1
Sine of disk inclination angle

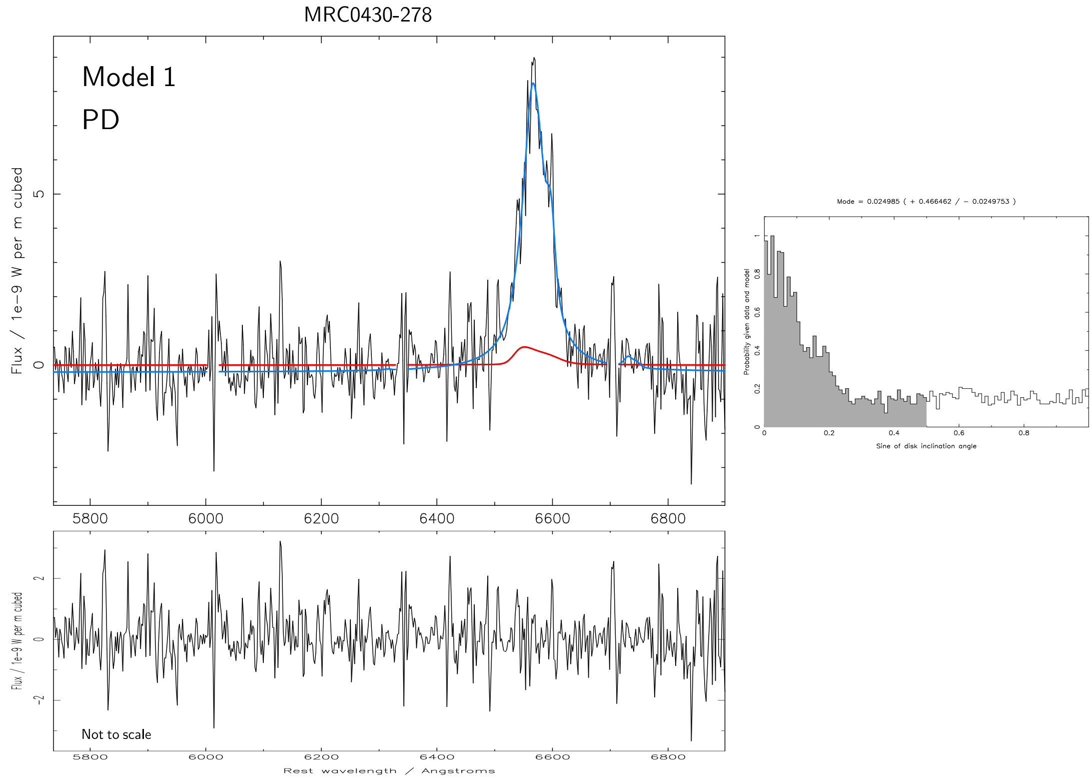
MRC0430-278
Model 1
PD
Flux / 1e−9 W per m cubed
0
5
5800
6000
6200
6400
6600
6800
Flux / 1e−9 W per m cubed
−2
0
2
Not to scale
Rest wavelength / Angstroms
Mode = 0.024985 (+ 0.466462 / − 0.0249753)
Probability given data and model
0
0.2
0.4
0.6
0.8
1
Sine of disk inclination angle

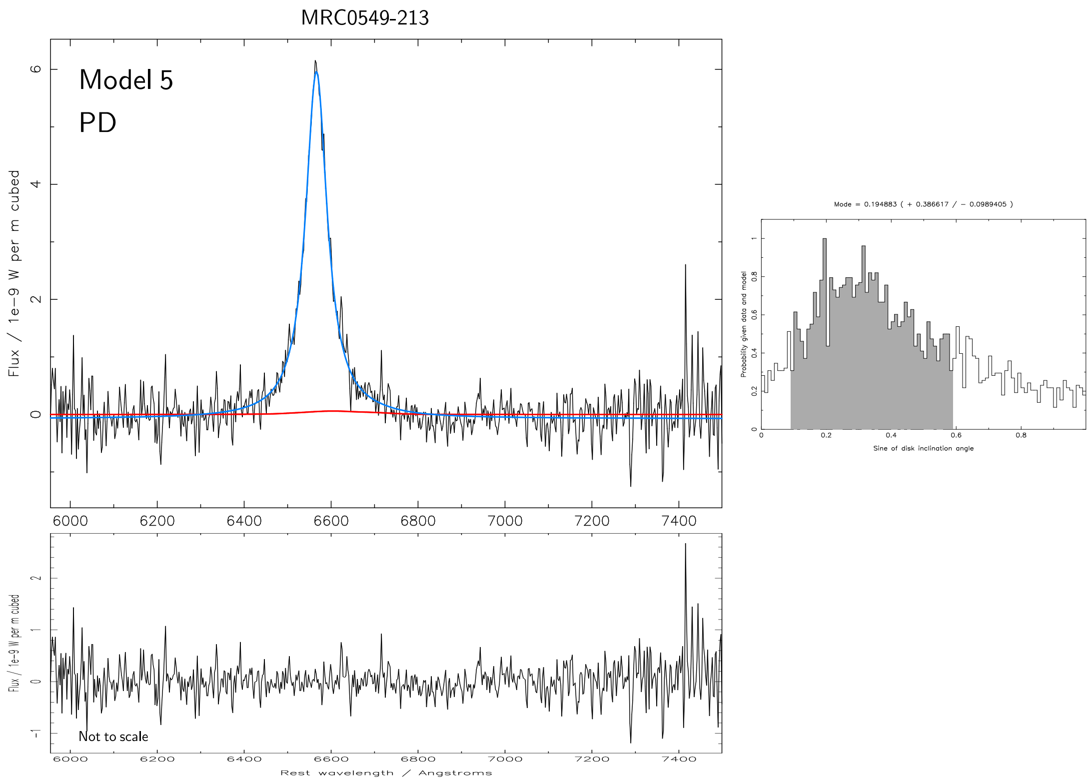
MRC0549-213
Model 5
PD
Flux / 1e−9 W per m cubed
6000
6200
6400
6600
6800
7000
7200
7400
Not to scale
Rest wavelength / Angstroms
Mode = 0.194883 (+ 0.386617 / − 0.0989405)
Probability given data and model
Sine of disk inclination angle

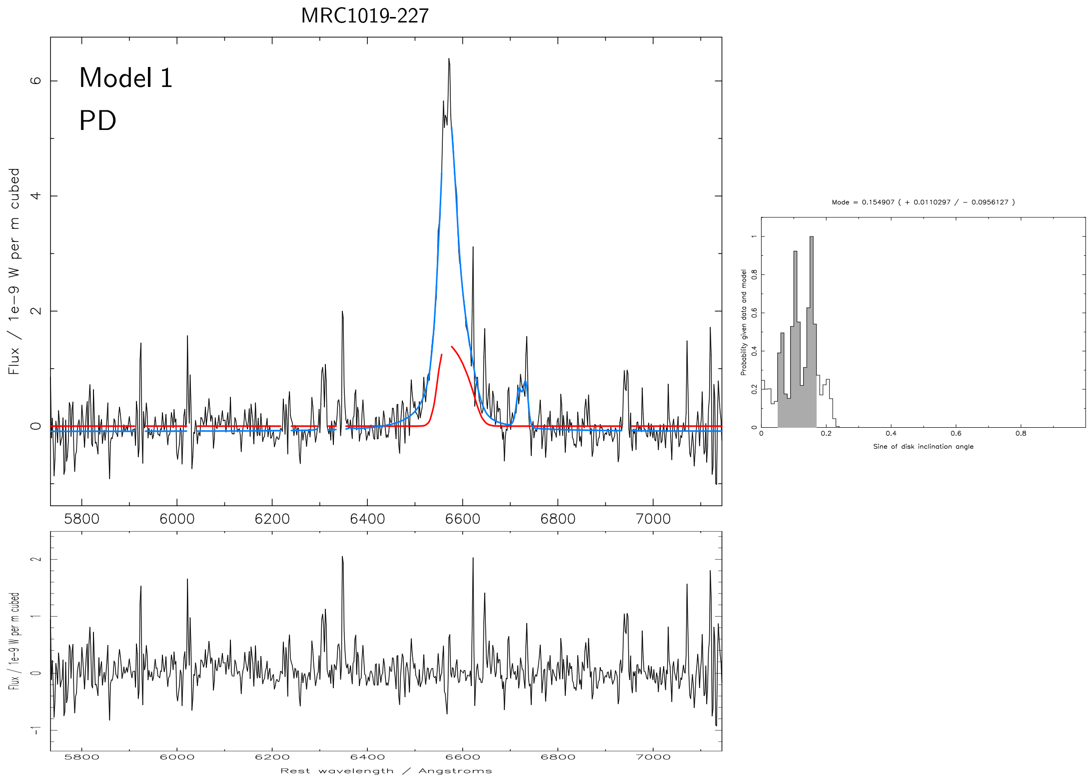
MRC1019-227
Model 1
PD
Flux / 1e−9 W per m cubed
5800
6000
6200
6400
6600
6800
7000
Rest wavelength / Angstroms
Mode = 0.154907 (+ 0.0110297 / − 0.0956127)
Probability given data and model
Sine of disk inclination angle

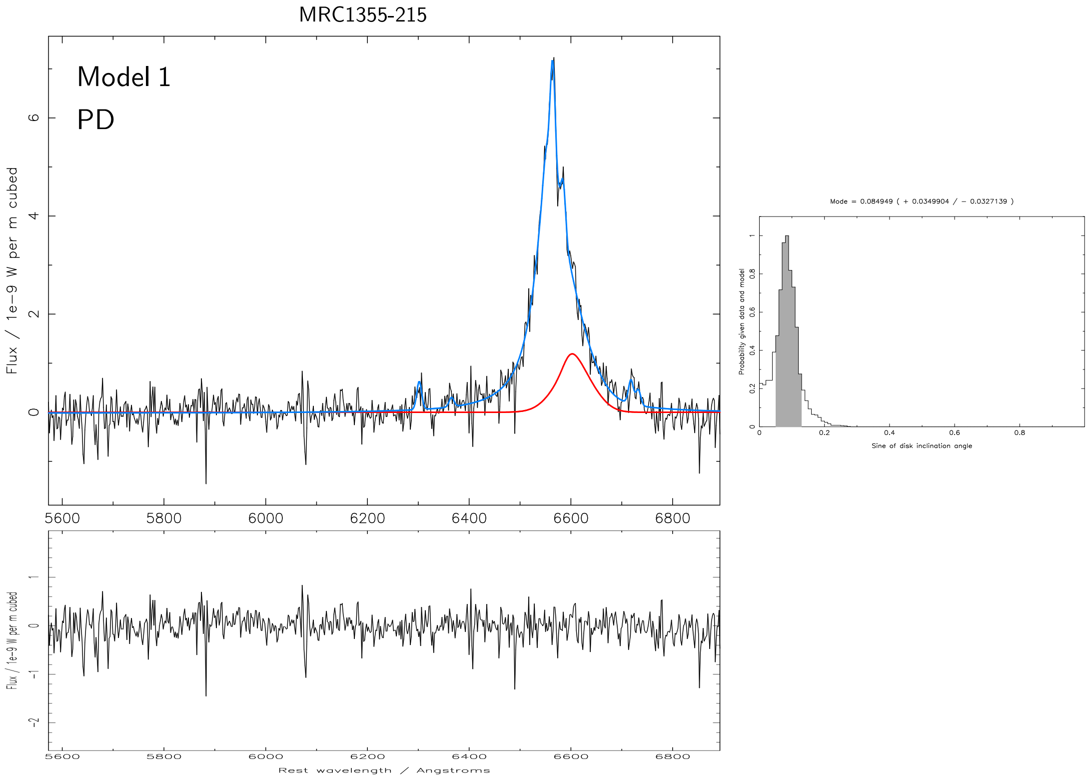
MRC1355-215
Model 1
PD
Flux / 1e−9 W per m cubed
0
2
4
6
5600
5800
6000
6200
6400
6600
6800
Flux / 1e−9 W per m cubed
−2
−1
0
1
5600
5800
6000
6200
6400
6600
6800
Rest wavelength / Angstroms
Mode = 0.084949 (+ 0.0349904 / − 0.0327139)
Probability given data and model
0
0.2
0.4
0.6
0.8
1
0
0.2
0.4
0.6
0.8
Sine of disk inclination angle

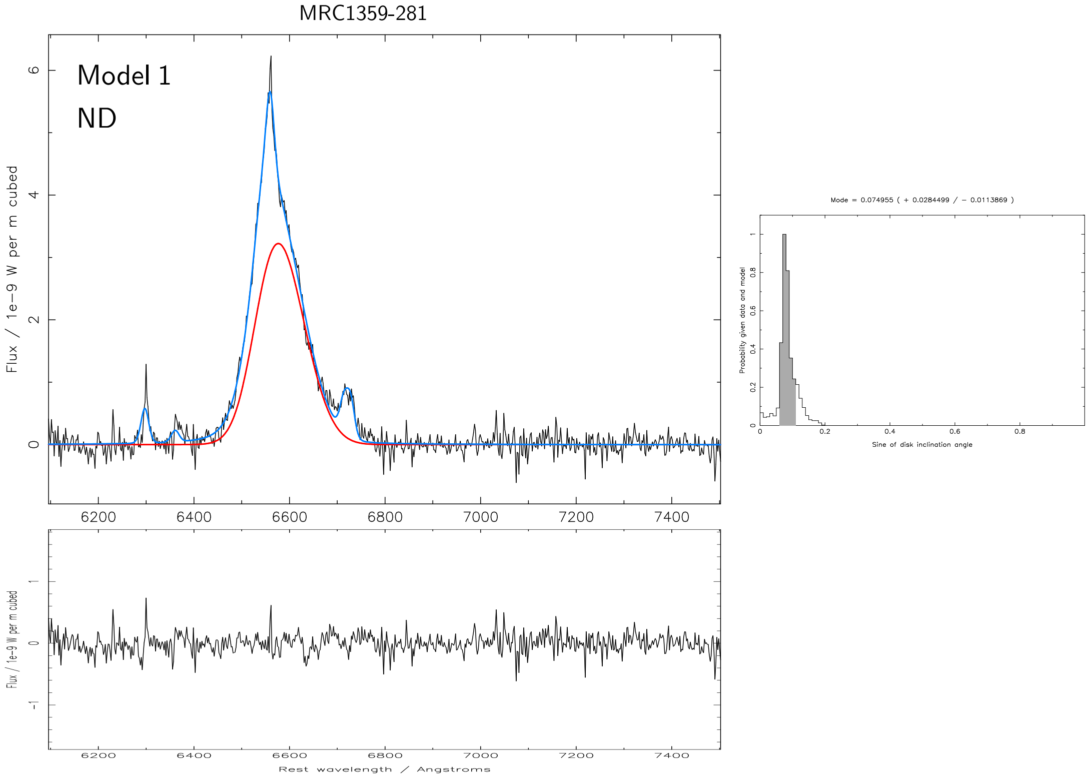
MRC1359-281
Model 1
ND
Flux / 1e−9 W per m cubed
0
2
4
6
6200
6400
6600
6800
7000
7200
7400
Flux / 1e−9 W per m cubed
−1
0
1
6200
6400
6600
6800
7000
7200
7400
Rest wavelength / Angstroms
Mode = 0.074955 (+ 0.0284499 / − 0.0113869)
Probability given data and model
0
0.2
0.4
0.6
0.8
1
0
0.2
0.4
0.6
0.8
Sine of disk inclination angle

3.6.2 *Correlations between the parameters*

Plots 3.5, 3.8, 3.9, 3.10, 3.11 and 3.12 show the correlations between the disk fitting parameters for two randomly-selected quasars, MRC0437-244 and MRC0450-221. There are no strong correlations of any other parameters with the local velocity dispersion of the disk material or the outer disk radius. There is a correlation such that when the sine of the disk axis angle increases, the inner radius increases and the wavelength shift of the disk component with respect to 6564.61 Å increases.

In the model of Chen & Halpern (1989) for an optically-emitting accretion disk, the emission line widths increase with decreasing inner disk radius. The inner disk radius, which is defined as a dimensionless quantity in units of the gravitational radius R_{G}, anticorrelates with the black hole mass. In the model for double-peaked lines, the line width therefore correlates positively with the black hole mass. Observationally, the widths of broad, low-ionisation emission lines are known to correlate with black hole mass (Vestergaard (2002), McLure & Jarvis (2002)), which is postulated to be due to virialisation of the emitting material.

An increase in the disk axis angle causes the two peaks of the disk emission to move further apart, as the rotating material in the disk has a higher velocity component along the line of sight. This effect has been observed observationally by Jarvis & McLure (2006), who found that using radio spectral indices as a proxy for source orientation, the sources at greater angles to the line of sight have larger broad-line widths.

The correlation between the disk axis inclination angle and the inner radius of the disk can therefore be interpreted in terms of the observed width of the broad emission; these two parameters act upon the emission line width in opposing senses, and so the fitted model is a trade-off between the two. The correlation with the shift of the disk component is caused by the stronger (blueward) line peak aligning with the strongest component in the spectrum, whereas the weaker (redward) peak of the line does not impose such a strong constraint on the fitting; the degree of wavelength shift required to fit the line profile depends on the separation between the two peaks, which is most strongly dependent on the angle of the accretion disk to the line of sight.

The disk axis angle has by far the largest effect on the profile of the emission, and therefore this parameter constrains more strongly than any of the others. The double-peaked emission therefore provides a robust method for measuring orientation.

3.6.3 *Discussion*

Table 3.7 summarises the results of the model selection process. Of the nineteen objects, eight have strong evidence for disks according to Jeffreys' criterion; two have moderate evidence for a disk; one has weak evidence for a disk; six have possible disks, which means that either the results were inconclusive, or that there was weak evidence against a disk; and in only two cases is there strong evidence against the presence of a disk.

It is very notable that the fits for all but two sources, MRC0413-296 and MRC1359-281, prefer models which include a complex broad-line region of more than one component. The traditional model of a single emitting region is not sufficient to describe the complex profiles of these lines. In most of the cases, the preferred fits were the ones with all the narrow lines and either the Lorentzian broad line plus the disk, or the Lorentzian line plus the Gaussian. In only five fits were models with less than the full complement of narrow lines preferred, and of these, four were the spectra with the lowest signal-to-noise ratio.

Another interesting result is that in no cases were models with the disk emission as the only broad emission selected; Figure 3.3 shows that in most cases, these models have extremely low evidence. It therefore seems implausible that the broad-line emission from quasars could result solely from accretion disks; there is certainly a classical broad-line region, or similar, present.

The distributions for the sine of the disk axis angles, shown in Figures 3.13 and 3.14, are on the whole reasonably Gaussian, though in some cases, these are cut off by the zero-angle boundary. There is one notable exception: MRC0549-213 has high probability in the low-angle end of the distribution, though shows some probability over the entire range. This source appears to have weak disk emission, as it is well-fit by a Lorentzian line, and is classed as a "possible disk" source, with no strong evidence either for or against a disk.

Quasar		Best fit Model	Evidence For Disk	For best-fit with disk		For best-fit without disk		Disk angle
				$\Delta \ln E_{1d}^{2}$	$\Delta \ln E_{1d}^{n}$	$\Delta \ln E_{1n}^{2}$	$\Delta \ln E_{1n}^{d}$	
1	MRC0222-224	1	SD	3.85	10.13			$40\,^\circ \pm^{5}_{11}$
2	MRC0327-241	3	MD	1.57	3.90			$7\,^\circ \pm^{3}_{2}$
3	MRC0346-279	9 (5)	PD			1.09	2.44	$0\,^\circ \pm^{5}_{0}$
4	MRC0413-210	1	SD	5.54	–			$4\,^\circ \pm^{1}_{1}$
5	MRC0413-296	8 (1)	ND			5.73	–	$34\,^\circ \pm^{6}_{7}$
6	MRC0430-278	7 (1)	PD			0.10	0.52	$1\,^\circ \pm^{28}_{1}$
7	MRC0437-244	1	SD	4.72	93.55			$18\,^\circ \pm^{2}_{1}$
8	MRC0450-221	1	SD	10.57	34.96			$13\,^\circ \pm^{1}_{1}$
9	MRC0549-213	2 (5)	PD			0.01	1.23	$11\,^\circ \pm^{24}_{6}$
10	MRC1019-227	7 (1)	PD			0.35	–	$9\,^\circ \pm^{1}_{6}$
11	MRC1114-220	1	SD	2.40	5.48			$31\,^\circ \pm^{7}_{9}$
12	MRC1208-277	1	SD	33.36	–			$13\,^\circ \pm^{2}_{2}$
13	MRC1217-209	5	PD	1.03	–			$16\,^\circ \pm^{11}_{7}$
14	MRC1222-293	1	SD	6.13	–			$9\,^\circ \pm^{3}_{3}$
15	MRC1301-251	1	MD	1.43	2.52			$21\,^\circ \pm^{9}_{6}$
16	MRC1349-265	1	WD	2.02	–			$3\,^\circ \pm^{2}_{3}$
17	MRC1355-215	7 (1)	PD			0.57	–	$5\,^\circ \pm^{2}_{2}$
18	MRC1355-236	1	SD	6.40	–			$10\,^\circ \pm^{3}_{2}$
19	MRC1359-281	7 (1)	ND			8.43	–	$4\,^\circ \pm^{2}_{0}$

Table 3.7: Summary of the model fitting results:
Columns 1 and 2: Index and name of the quasars.
Column 3: Index of the best-fit model. If this model does not include an accretion disk, the index of the best-fit model including an accretion disk is given in brackets.
Column 4: Code to show whether there is evidence for a disk according to the odds ratio: SD = strong evidence for a disk; MD = moderate evidence for a disk; WD = weak evidence for a disk; PD = a possible disk, i.e. the best fit is a non-disk model, but there is only weak or inconclusive evidence for this; ND = strong evidence against the presence of a disk.
Columns 5 and 6: Natural logarithmic evidence difference between the best-fit model, which is a disk, and the second best model (Column 5, $\Delta \ln E_{1d}^{2}$), and in cases where the second best fit is also a disk, between the best fit model and the best-fit model without a disk (Column 6, $\Delta \ln E_{1d}^{n}$).
Columns 7 and 8: Natural logarithmic evidence difference between the best-fit model, which is not a disk, and the second best model (Column 7, $\Delta \ln E_{1n}^{2}$), and in cases where the second best fit is also not a disk, between the best fit model and the best-fit model with a disk (Column 8, $\Delta \ln E_{1n}^{d}$).
Column 9: Best-fit angle of the disk axis and the error in degrees.

The disks have fitted axis angles between 0° and 40°; this range is consistent with the definition of quasars as being objects viewed within the opening angle of a dusty torus, which has a range dependent on source luminosity, but is generally supposed to be roughly 45° for radio luminous AGN (Lawrence 1991).

As expected, those sources with disk axis angles close to the line of sight in general have less strong evidence for a disk. The reason for this is that when the angles of the disk axis to the line of sight are small, the disk emission is not distinctive and double-peaked, but instead, rather similar to a Gaussian profile, and in these cases, there is little to distinguish the broad Lorentzian plus accretion disk fit from the broad Lorentzian plus broad Gaussian fit, except that the fit with the Gaussian has fewer parameters, and is therefore favoured by Occam's Razor. It is only those fits with greater disk axis angles to the line of sight, or those with a very high signal-to-noise ratio in the spectra, that make it possible to detect an emission disk with high probability.

Figure 3.15 shows the disk axis angles from all model fits for each quasar. In most cases, the angles are extremely stable. In cases where there is some disagreement between the various models, all disk axis angles from models within one Jeffreys' criterion of the best fit are consistent with each other.

3.7 *Conclusions*

There is strong evidence for the presence of an accretion disk in eight out of nineteen of the quasars in this sub-sample, with the majority of the rest exhibiting strong evidence for a two-component broad-line region, but showing no preference between a classical broad line region plus a disk, and either two broad-line regions or a broad line region and an outflow. In only two sources was there evidence against the presence of a disk, and for one, the disk axis angle is predicted to be low. The other case appears to be unusual, in that is has a very complex structure, possibly arising from three separate broad-line emitting regions.

The fact that we expect not to find strong evidence for an accretion disk when the disk axis of the source is at a low angle to the line of sight makes it quite plausible that all these sources do in fact have disks, although a much larger sample would be needed to make this more than speculation.

What is clear is that a single region of broad emission is not sufficient to model the

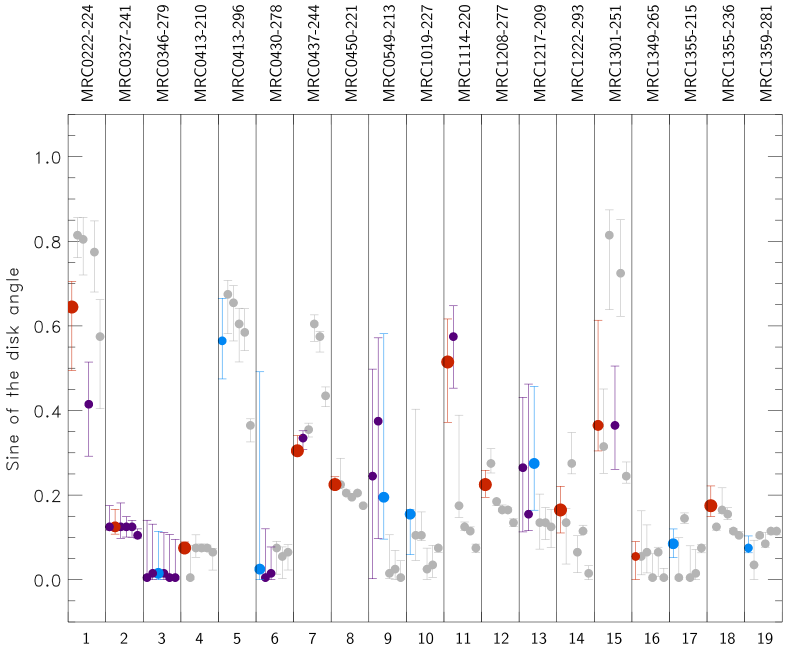

Figure 3.15: Disk axis angles for every model fit with a disk. A large red point indicates strong evidence for a disk, a medium-sized red point indicates moderate evidence for a disk, and a small red point indicates weak evidence for a disk. A medium-sized blue point indicates a possible disk, which means either the evidence was inconclusive or that there was weak evidence against a disk. A small blue point indicates there is strong evidence against the presence of a disk. Purple points are those of fits which fall within one Jeffreys' criterion of the best fit, and these can be seen in all cases to be consistent with the best-fit disk. All other angles are plotted in grey.

processes which occur within the dusty-torus zone of fast-moving clouds near the centre of quasars, and that there are either accretion disks, multiple zones of emitting clouds, outflows, or some other phenomenon giving rise to complex emission lines.

Chapter 4 Radio Properties

4.1 *Introduction*

Radio spectral energy distributions of quasars from the Molonglo sub-sample are used as diagnostics to measure the orientation of the jets to the line of sight in Chapter 5. For this sub-sample, total flux densities covering a wide range of frequencies were available, but five of the six Compact Steep Spectrum (CSS) sources did not have radio maps of high enough resolution to measure the core flux densities.

High resolution L-band radio maps were obtained with MERLIN for these five sources with small projected sizes. The cores of the quasars were identified with reference to the optical position, and the core flux densities obtained. The largest angular sizes and projected sizes of these quasars were measured.

4.2 *Observations and Data Reduction*

L-band (1408 MHz or 1420 MHz) observations of the five CSS sources were taken using the MERLIN array with the Mk II, Cambridge, Darnhall, Defford, Knockin and Tabley antennae; the Lovell Telescope was not included. Each source was observed for roughly twelve hours, split over several days. Details of the sources are given in Table 4.1 and observational information for these targets is given in Table 4.2, including the phase reference sources, observations of which were interleaved with the target observations. All polarisations were observed; the maps have been created in Stokes I.

Quasar (1)	 (2)	R.A. J(2000) (3)	Dec. J(2000) (4)	z (5)	$S_{408\mathrm{MHz}}$ (Jy) (6)	$\alpha_{408\mathrm{MHz}}^{4.86\mathrm{GHz}}$ (7)
1	MRC0222-224	02 25 16.6	-22 15 22	1.603	2.36	0.95
6	MRC0430-278	04 32 17.7	-27 46 24	1.633	0.95	0.76
10	MRC1019-227	10 21 27.6	-23 01 54	1.542	0.96	0.98
16	MRC1349-265	13 52 10.3	-26 49 28	0.924	3.59	0.63
19	MRC1359-281	14 02 02.4	-28 22 25	0.802	2.30	0.52

Table 4.1: Quasar information:
Columns 1 and 2: Index and name of the quasar.
Columns 3 and 4: J(2000) Right Ascension (in hours, minutes and seconds) and Declination (in degrees, minutes and seconds).
Column 5: Redshift of the quasar.
Column 6: 408 MHz flux ($S_{408\mathrm{MHz}}$) of the quasar in Jy (Kapahi et al. 1998a)
Column 7: 408 MHz to 4.86 GHz spectral index of the quasar ($\alpha_{408\mathrm{MHz}}^{4.86\mathrm{GHz}}$), from Kapahi et al. (1998a).

Quasar (1)	(2)	Date obs. (3)	Frequency (MHz) (4)	Bandwidth (MHz) (5)	Calibrators (6)
1	MRC0222-224	2008-01-05, 2008-01-06, 2008-01-09, 2008-01-10	1408	13	0218-220, 0552+398, OQ208, 3C286
6	MRC0430-278	2007-12-28, 2007-12-29, 2007-12-30, 2007-12-31, 2008-01-01, 2008-01-03, 2008-01-14, 2008-01-15, 2008-01-16, 2008-01-17, 2008-01-18, 2008-01-19, 2008-01-20, 2008-01-21, 2008-01-22, 2008-01-23, 2008-01-24, 2008-01-25, 2008-01-26, 2008-01-28, 2008-01-29, 2008-01-30, 2008-02-06	1420	13	0435-283, OQ208, 3C286
10	MRC1019-227	2008-01-06, 2008-01-07	1408	13	1017-220, 0552+398, 3C286
16	MRC1349-265	2008-01-23, 2008-01-26	1420.5	14	1336-260A, OQ208, 3C286
19	MRC1359-281	2008-01-29, 2008-01-30, 2008-02-06	1420	13	1358-298, 0552+398, 3C286

Table 4.2: Observational details:
Columns 1 and 2: Index and name of the quasar.
Column 3: Date of the observations.
Column 4: Frequency of the observation in MHz.
Column 5: Bandwidth of the observation in MHz.
Column 6: Calibrators used. The first entry in the list is the phase reference source; observations of this source were interleaved with the target observations. The other sources are pointing calibrators. In each case, 3C286 was the primary flux calibrator, used to calibrate the flux density scale on the shortest baselines.

The data were reduced using standard *AIPS* procedures, with extensive help from Tom Muxlow and Anita Roberts at Jodrell Bank. The target and calibrator data were carefully flagged, to remove bad visibilities from amplitude drop-offs or radio frequency interference, either as individual points or for a whole baseline if the anomalous points were found to be systematic. The *MERLIN AIPS* script* was used to perform the basic processing. The highest and lowest channels were removed from the data set, and 13 channels of the 15 were averaged together, to give an effective bandwidth of 13 MHz. The bandpass calibration was then applied.

Flux density calibrations were made using the calibrators shown in Table 4.2. Self-calibration was then performed with combinations of *SCMAP* and *IMAGR* in *AIPS* and *DIFMAP*. The self-calibration techniques used for each source are summarised in Table 4.3. The general procedure was to perform several rounds of phase-only self-calibration with a solution interval of 1 minute, followed by one round of phase and amplitude self-calibration with a solution interval of 10 minutes.

Quasar		Frequency (MHz)	Self-calibration techniques
1	MRC0222-224	1408	*SCMAP* and *IMAGR*
6	MRC0430-278	1420	*SCMAP* and *IMAGR*
10	MRC1019-227	1408	*SCMAP* and *IMAGR*
16	MRC1349-265	1420	*SCMAP*, *IMAGR* and *DIFMAP*
19	MRC1359-281	1420	*SCMAP*, *IMAGR* and *DIFMAP*

Table 4.3: The observation frequencies and self-calibration techniques used to create the radio maps.

4.2.1 *Optical positions*

The best optical images available for MRC02222-224, MRC1019-227, MRC1349-265 and MRC135-281 are DSS2 images (McLean et al. 2000). *SkyView* was used to retrieve 1 degree square red DSS2 images centred on the quasar, and the positions of all Tycho/Hipparcos stars within this field of view ($\sim$ 20 for each source) were measured using *imexamine* in *IRAF*. The positions of the stars were compared to their Tycho Catalogue (Høg et al. 2000) positions to determine an average shift in Right Ascension and Declination, and a standard

---

**MERLIN* is a script of *AIPS* procedures written by Anita Richards.

deviation on this value, for each quasar. The quasar position was then measured using *imexamine* and corrected by this shift.

The error on this procedure is the combined error from the error in the shift between the measured positions on the DSS image of the Tycho stars and their catalogue values (typically 0.5 arcsecond), the absolute error in the positions of the Tycho stars (taken as 0.05 arcsec, as this was a relatively consistent value) and the *imexamine* error from the measurement on the DSS plate (also ∼0.05 arcsec).

The optical position of MRC0430-278 was measured using an EFOSC2 focus image from the ESO 3.6 m telescope. Using the package *KARMA KOORDS*, the astrometry of the EFOSC2 focus image was corrected with the relative astrometry of a DSS2 image. The absolute astrometry was then calibrated using Tycho/Hipparcos stars, as before.

Quasar		Optical position	Error in arcseconds
1	MRC0222-224	02:25:16.597 -22:15:21.46	0.662 0.414
6	MRC0430-278	04:32:17.673 -27:46:24.93	0.071 0.071
10	MRC1019-227	10:21:27.587 -23:01:55.53	0.514 0.812
16	MRC1349-265	13:52:10.301 -26:49:28.74	0.698 0.636
19	MRC1359-281	14:02:02.466 -28:22:25.13	0.871 0.567

Table 4.4: Table of CSS optical positions measured either from DSS images or from an EFOSC2 focus image in the case of MRC0430-278, and corrected using the positions of Tycho/Hipparcos stars.

4.3 *Radio Maps*

Presented in Figure 4.1 are the new radio maps of the CSS sources observed with MERLIN. The crosses show the optical positions of the quasars and the errors on these positions. Contour levels and peak flux densities are marked on the plots, and synthesised beams are shown in the bottom right corner. Since these sources were visible to MERLIN only at low elevations, the synthesised beam sizes are elongated. For MRC1359-281, the three possible core components have been labelled.

Two of the sources, MRC1349-265 and MRC1359-281, had their synthesised beams circularised with *IMAGR* in *AIPS*. These maps are shown in Figure 4.2. In the case of these two sources, the flux density and source size measurements were made from these maps with the circularised beams. The flux density and peak flux density of MRC1349-265 vary by less than 1% between the two maps. For MRC1359-281, there is a 3% difference between the integrated flux density of the two maps, and a 10% change in the peak flux density.

Figure 4.3 shows maps of CSS sources in the Molonglo sub-sample from the literature, from Kapahi et al. (1998a) and from de Silva et al. (in preparation, b). MRC1114-220 was not re-observed with MERLIN, as the L-band and C-band maps observed by de Silva et al. (in preparation, b) are high resolution, clearly identify the core, and give a reliable core flux density measurement for this source.

Figure 4.4 shows radio maps of the sources with projected sizes larger than 25 kpc, observed in VLA snapshot mode by Kapahi et al. (1998a) at 4860 MHz (C-band).

4.3.1 *Notes on CSS maps*

MRC0222-224 : A source with clear twin lobes, and a possible core between them; however, this feature includes only the same level of flux density as two other artifacts in the image, so this is not a strong core detection.

MRC0430-278 : A triple source, with two lobes and a central core. The precise optical position fixes the core as the central component.

MRC1019-227 : A clearly resolved triple source, with two lobes and a core between them.

MRC1114-220 : the map of de Silva et al. (in preparation, b) shows two clear components with spectral indices of $\alpha_{1658\mathrm{MHz}-4994\mathrm{MHz}} = 0.04$ (Eastern component) and $\alpha_{1658\mathrm{MHz}-4994\mathrm{MHz}} \sim 0.9$ (Western component), so the Eastern component is identified as the core, in agreement with the optical position of 11:14:26.08 -22:00:29.4 (in B1950 coordinates).

MRC1349-265 : This source is very compact, and the error bars on the optical position enclose a large proportion of the source. However, comparing the 4994 MHz radio map from de Silva et al. (in preparation, b) (Figure 4.3) to the circularised-beam 1420 MHz map (Figure 4.2), and also noting the largest angular size is 2.4 arcseconds in the 4994 MHz map as compared to 3.6 arcseconds in the 1420 MHz map (Table 4.7), it is very likely that the core is the Southern component in the 4994 MHz map, with a radio lobe as the Northern component. The other lobe is not seen. In the 1420 MHz map, the core is then the small

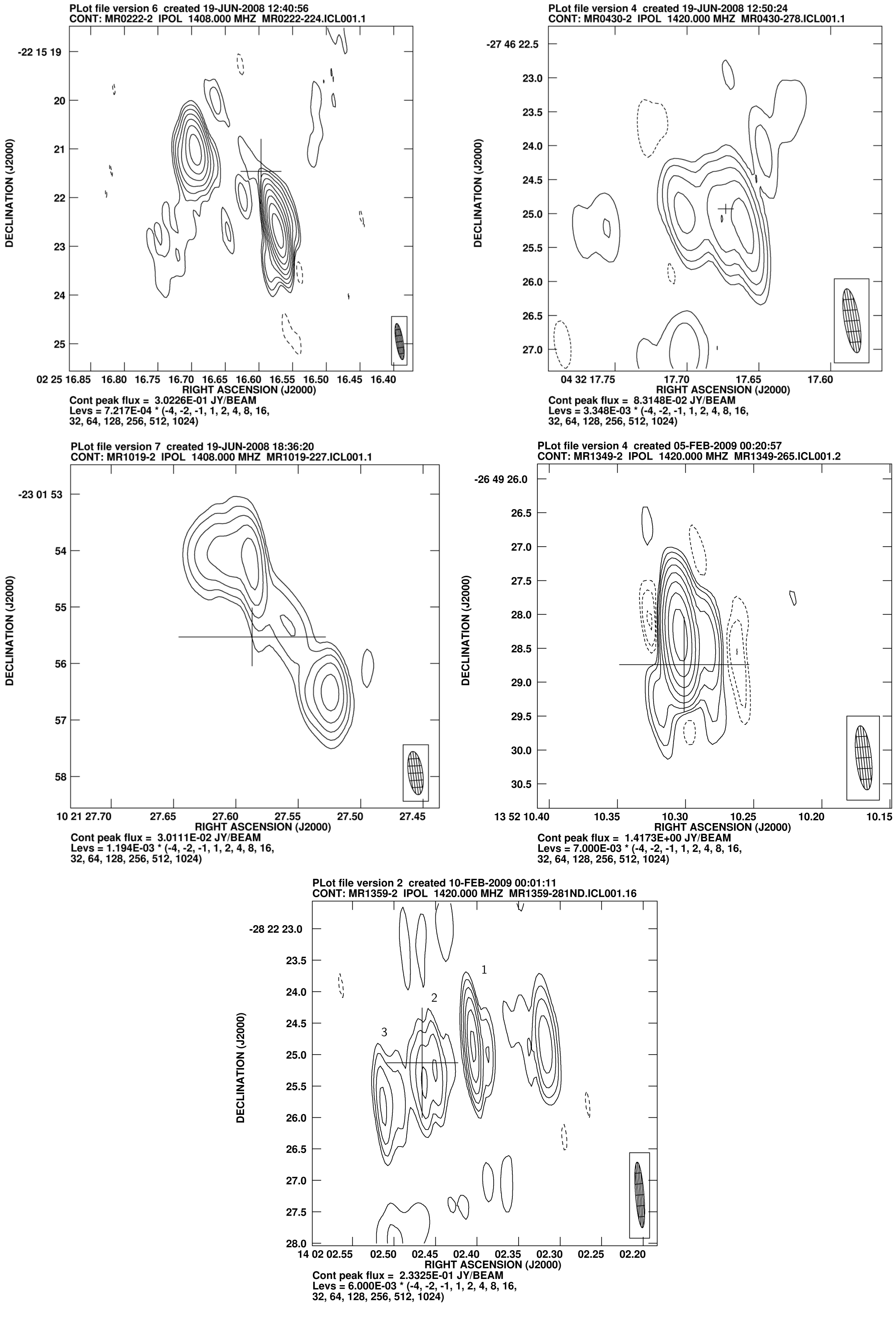

Figure 4.1: New L-band radio maps from MERLIN for five of the Molonglo CSS radio sources. Synthesised beam sizes are shown in the lower right of each figure. Contour levels are given with each figure. Crosses show optical positions and errors.

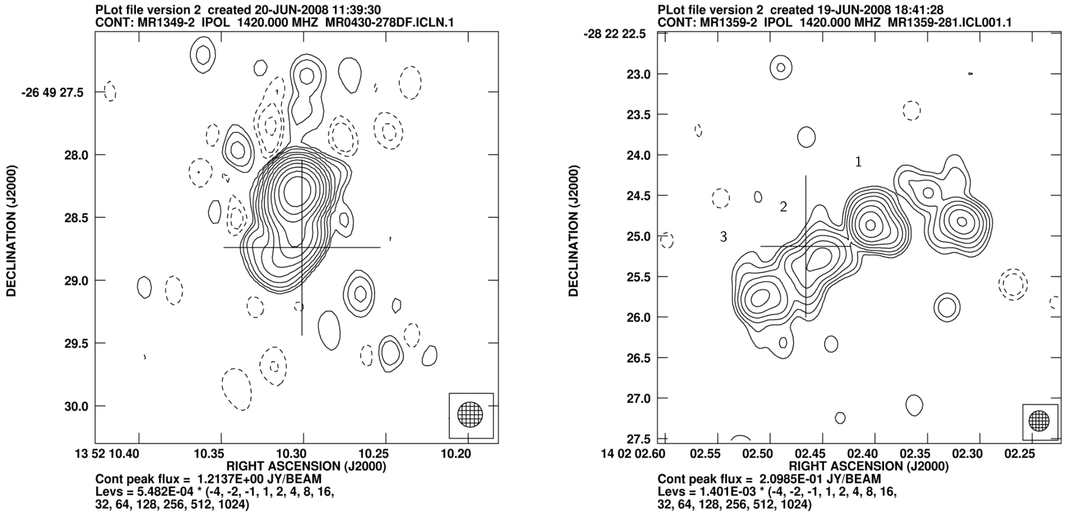

Figure 4.2: New L-band radio maps from MERLIN for two of the Molonglo CSS radio sources, which were created with circularised synthesised beams (beam sizes are shown in the lower right of each figure). Contour levels are given with each figure. Crosses show optical positions and errors.

protrusion below the region with the most flux, between a strong approaching jet to the North, and a weaker receding jet located to the South.

MRC1359-281 : This source has at least four components. The optical position coincides well with the second most Easterly feature (2), though the one-sigma error bars do not rule out the core being the most Easterly feature (3), with this source having only a one-sided jet, or the second most Westerly blob (1). The C-band map of this source, reduced from archival VLA data by de Silva et al. (in preparation, b) at 4.86 GHz shows a single component source located at 14:02:02.4±0.02 -28:22:25.8±0.2 with a size of greater than 1 arcsecond. This does not coincide exactly with any of the features in the L-band map, but it is likely that this feature includes core emission from the quasar.

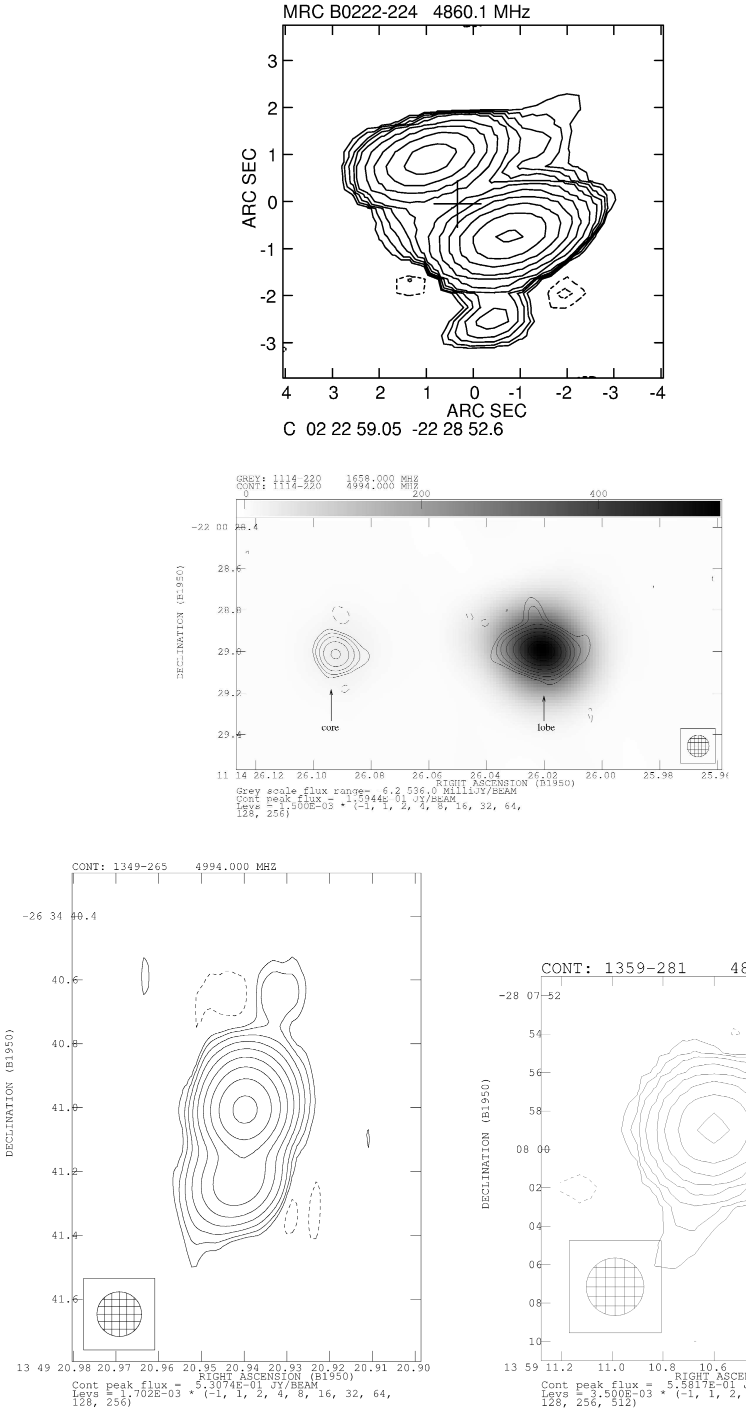

Figure 4.3: Other CSS radio maps for the Molonglo Sample: MRC0222-224 in C-band from Kapahi et al. (1998a), observed in snapshot mode at the VLA; MRC1114-220 in L-band (greyscale) and C-band (contours) from de Silva et al. (in preparation, b) (Note: the optical position of this source is 11:14:26.08 -22:00:29.4 in B1950 coordinates), observed with MERLIN; MRC1349-265 and MRC1359-281 in C-band from de Silva et al. (in preparation, b), MRC1349-265 was observed with MERLIN, and the MRC1359-281 map was re-reduced from archival VLA data.

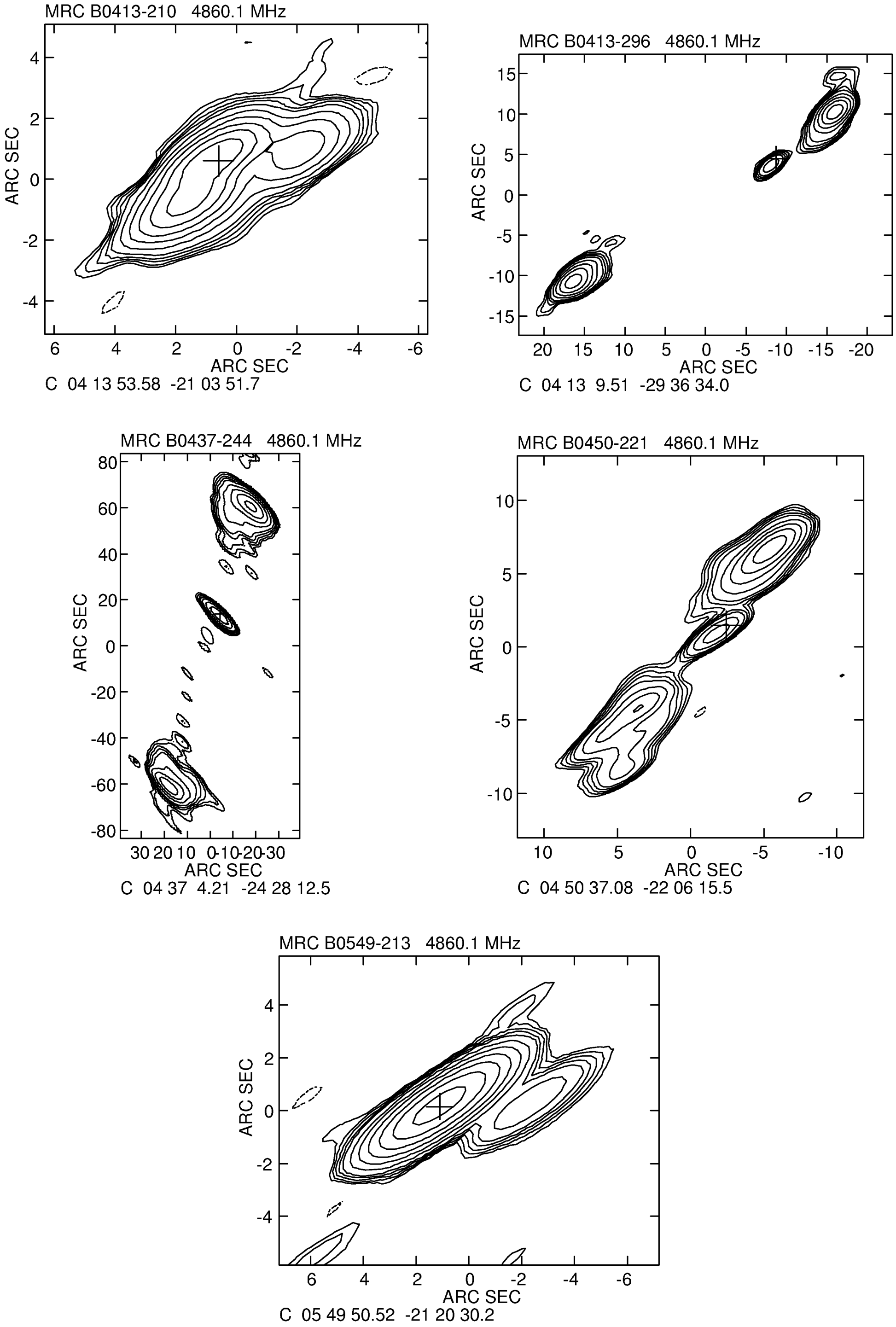

Figure 4.4: Maps of the sub-sample of quasars from Kapahi et al. (1998a). All maps are C-band VLA snapshots.

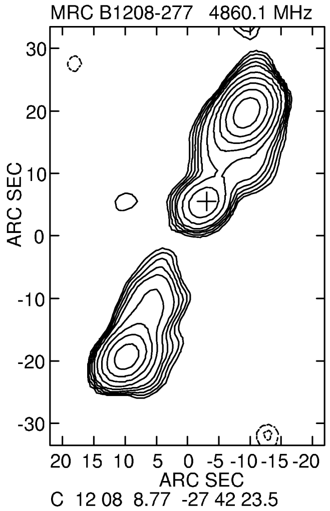
MRC B1208-277 4860.1 MHz
ARC SEC
30
20
10
0
-10
-20
-30
20 15 10 5 0 -5 -10 -15 -20
ARC SEC
C 12 08 8.77 -27 42 23.5

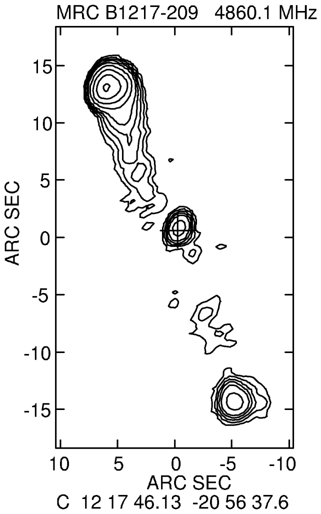
MRC B1217-209 4860.1 MHz
ARC SEC
15
10
5
0
-5
-10
-15
10 5 0 -5 -10
ARC SEC
C 12 17 46.13 -20 56 37.6

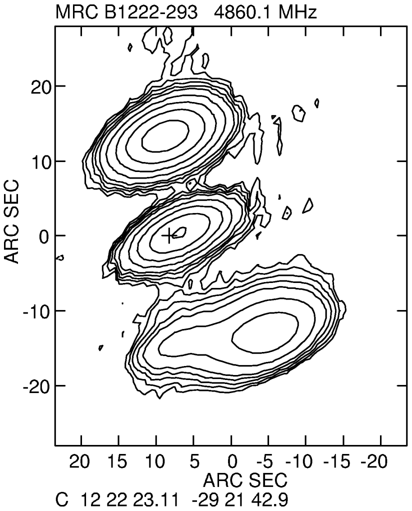
MRC B1222-293 4860.1 MHz
ARC SEC
20
10
0
-10
-20
20 15 10 5 0 -5 -10 -15 -20
ARC SEC
C 12 22 23.11 -29 21 42.9

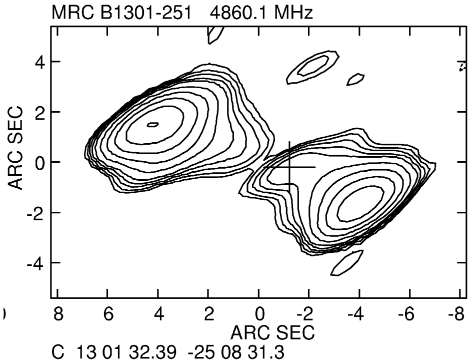
MRC B1301-251 4860.1 MHz
ARC SEC
4
2
0
-2
-4
8 6 4 2 0 -2 -4 -6 -8
ARC SEC
C 13 01 32.39 -25 08 31.3

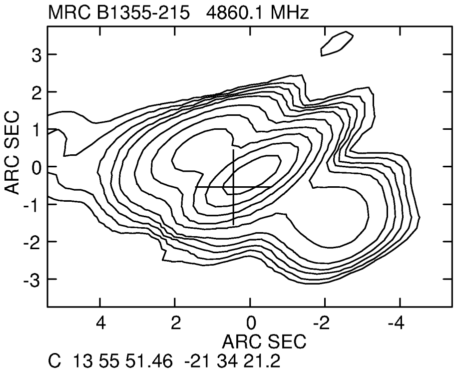
MRC B1355-215 4860.1 MHz
ARC SEC
3
2
1
0
-1
-2
-3
4 2 0 -2 -4
ARC SEC
C 13 55 51.46 -21 34 21.2

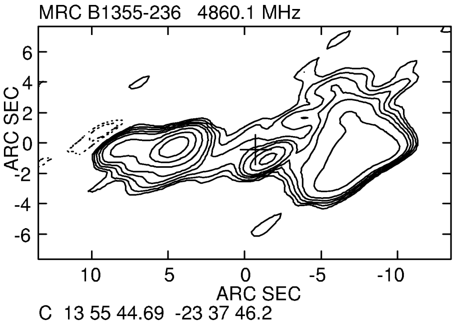
MRC B1355-236 4860.1 MHz
ARC SEC
6
4
2
0
-2
-4
-6
10 5 0 -5 -10
ARC SEC
C 13 55 44.69 -23 37 46.2

4.4 *Analysis*

4.4.1 *Integrated flux density*

The total flux densities of the CSS sources were measured in *AIPS*, and are shown in Table 4.5. For the cases of MRC1349-265 and MRC1359-281, these flux densities were measured from the radio maps with the circularised beams. The 1.4 GHz flux densities from MERLIN are consistently lower than the NVSS fluxes (Condon et al. 1998) which are shown for comparison. This is not unexpected: the NVSS survey has resolution $\sim$ 45 arcseconds, compared to $\sim$ 0.15 arcsecond for MERLIN. The source sizes for these CSS objects are approximately 2 arcseconds (see Table 4.7), and therefore these will be unresolved in the NVSS survey and the NVSS flux densities will not be missing any flux. For L-band observations with the MERLIN array used for these observations, the maximum angular size of a source which can be mapped is 2.5 arcseconds, and so it is unsurprising that some of the flux from the most extended structure of these sources is missing. These total flux densities were therefore not used in the spectral energy distribution fitting procedure in Chapter 5.

The thermal noise expected in the L-band for MERLIN with this array set-up in $\sim$ 12 hours is $\sim$ 60μJy. The rms noise values calculated from the maps range from $\sim$ 200 – 1200μJy, and so these observations are typically not thermal noise limited, which is unsurprising at these low elevations.

4.4.2 *Core flux densities*

Core flux densities were found for most sources by fitting single elliptical Gaussians to the core components with *IMFIT* in *AIPS*. For the two sources MRC1349-265 and MRC1359-281, these flux densities were measured from the maps with the circularised beams. MRC1349-265 has overlapping components, and so this was fit with three Gaussians, the central one being taken as the core. MRC1359-281 has three possibilities for the core (see Figure 4.2 for labels), with component 2 being the closest to the optical position. This component is taken as the core during the rest of this thesis, although tests were carried out using component 1 as the core for the SED fitting in Chapter 5, and this made negligible difference

Quasar (1)	(2)	Flux density (mJy) (3)	Peak flux density (mJy beam^{-1}) (4)	rms noise (mJy beam^{-1}) (5)	Dynamic range (6)	NVSS flux density (mJy) (7)
1	MRC0222-224	700 ± 2.3	300	0.200	3500	828
6	MRC0430-278	287 ± 5.4	83	0.719	400	398
10	MRC1019-227	171 ± 5.2	30	0.399	430	261
16	MRC1349-265	1720 ±11.9	1420	1.294	1300	1900
19	MRC1359-281	783 ± 2.0	210	0.129	6000	1100

Table 4.5: Total flux densities at 1.4 GHz for Molonglo CSS sources: Columns 1 and 2: Index and name of the quasar.
Column 3: Total flux density of the source in mJy, with rms errors.
Column 4: Peak flux density of the source in mJy beam^{-1}.
Column 5: rms noise measurement in mJy beam^{-1}.
Column 6: Dynamic range of the radio map.
Column 7: 1.4 GHz NVSS total flux density for comparison (Condon et al. 1998).

to the analysis.

The measured fluxes with *IMFIT* errors are summarised in table 4.6. The integrated fluxes of the core components almost certainly include extended emission, since the cores are very likely to be unresolved (beam sizes for MERLIN are approximately 0.15 arcsecond). The peak flux densities are therefore taken for the core flux densities in Chapter 5. The errors on the core flux densities are taken to be ±20% to allow for core variability (e.g. Lister et al. 1994).

Quasar		Peak flux density of core (mJy beam^{-1})	Integrated flux density of core (mJy)
1	MRC0222-224	1.969 ± 0.249	3.869 ± 0.694
6	MRC0430-278	57.16 ± 0.410	176.0 ± 1.62
10	MRC1019-227	5.069 ± 0.521	17.82 ± 2.29
16	MRC1349-265	167.2 ± 0.388	211.8 ± 0.788
19	MRC1359-281 (1)	198.0 ± 0.085	277.7 ± 0.186
19	MRC1359-281 (2)	61.86 ± 0.081	177.2 ± 0.303
19	MRC1359-281 (3)	57.99 ± 0.082	116.2 ± 0.235

Table 4.6: Table of CSS core fluxes measured with *IMFIT* in *AIPS*, and the formal errors. There are three possibilities for the core in MRC1359-281. Component 2 is closest to the optical position, component 1 is west of the optical position, and component 3 is east of the optical position. Component 2 is treated as the core in the rest of this thesis.

4.4.3 *Source sizes*

The largest angular sizes of the CSS sources are measured from the radio maps, taking the distance between the most separated components of the sources. For MRC1349-265 and MRC1359-281, these measurements are made from the radio maps with the circularised beams. The error on the angular size measurement is ∼0.1 arcsec. For MRC1349-265, the centres of the components are not easily differentiated from the radio map, and so the positions of the fitted components from *IMFIT* in *AIPS* are used to determine the separation.

The projected sizes of these sources were then calculated as

$$l = 2D_A \tan \frac{LAS}{2} \tag{4.1}$$

where l is the projected source size, D_A is the angular size distance, determined with Ned Wright's cosmology calculator[†], and LAS is the largest angular size in radians.

Quasar (1)	(2)	LAS (arcsec) (3)	Projected size (kpc) (4)	LAS (arcsec) from lit. (5)	Reference (6)
1	MRC0222-224	2.4	20.6	2.4	Kapahi et al. (1998a)
6	MRC0430-278	0.67	5.7	<2	Kapahi et al. (1998a)
10	MRC1019-227	2.5	21.2	2.2	Kapahi et al. (1998a)
16	MRC1349-265	0.36	4.5	0.24	de Silva et al. (in preparation, b)
19	MRC1359-281	3.1	2.8	<1.37	de Silva et al. (in preparation, b)

Table 4.7: The largest angular sizes and projected sizes of the CSS sources measured from the radio maps:
Columns 1 and 2: Index and name of the quasar.
Column 3: Largest angular size (arcsec).
Column 4: Projected source sizes (arcsec).
Columns 5 and 6: Latest measured largest angular source size from the literature (column 5) and the reference for this (column 6).

The largest angular sizes for MRC0222-224 and MRC1019-227 are comparable with those from recent literature, and the measurement for MRC0430-278 is a clear improvement on an estimate for the extent of an unresolved source. MRC1349-265 has a smaller extent in C-band, as the weaker lobe is not bright enough to be seen at this frequency, and

---

[†] Ned Wright's cosmology calculator: http://www.astro.ucla.edu/ wright/CosmoCalc.html

MRC1359-281 has only the core resolved in C-band, but has 4 separate blobs in the L-band map.

4.5 *Conclusions*

New L-band radio maps were obtained for five of the six CSS sources in the Molonglo subsample, and cores were identified using optical positions and comparison with C-band maps from the literature. Core fluxes of $\sim 2 - 200$ mJy were measured.

Chapter 5 | *Jet inclination angles*

5.1 *Introduction*

The radio spectral energy distributions (SEDs) of the Molonglo quasar sample are used to constrain the angles of the approaching radio jets to the line of sight, on the assumption that the compact core emission is Doppler boosted along the direction of the jet velocity. The extended emission of the radio lobe is thought to be, to a good approximation, equally luminous from all viewing angles; the core is most luminous at small jet angles, due to the effects of Doppler boosting. The core-to-lobe flux density ratio at high (10 GHz) frequency (R_{10GHz}) of these objects is often used as a means of probing the orientation of these sources (e.g. Jackson & Wall 1999).

In this chapter, a variation on the standard method of measuring the core-to-lobe flux density ratio from the SED is developed, which interpolates the low-frequency flux density to higher frequencies (Section 5.4). This model is used to fit the core and total flux densities of a sub-sample of 3CRR quasars and radio galaxies (Section 5.5), and in Section 5.6, the relation between this new interpolated core-to-lobe flux density ratio, R_{interp}, and the logarithmic luminosity of the source is determined for the 3CRR sample. This relation is modelled with a function comprising of two parts: an angle-dependent Doppler boosting term, and a lobe luminosity-dependent term, empirically constrained, and potentially arising from the fall in radio lobe luminosity compared to the jet power over time (e.g. Kaiser 2005; Blundell et al. 1999). The SEDs of the Molonglo sub-sample are then fitted, using this relation between logarithmic luminosity and R_{interp} to retrieve the probability distributions for the jet angles of these quasars (Section 5.7).

5.2 *Molonglo Quasar Sample Radio Data*

5.2.1 *Radio flux densities*

Spectral energy distributions for the Molonglo quasar sub-sample were compiled from the literature. Table 5.1 summarises the origins of the total radio flux densities, which cover frequencies from 74 MHz to beyond 20 GHz. The errors on the total flux densities are taken from the relevant papers. It is worth noting that these measurements span a large period of time, from the early 1970s until 2006, and so there is a possibility of time variability whenever, as in the core, compact regions contribute significantly to the luminosity.

Flux densities of the core components are summarised in Table 5.2. The core values are more uncertain than the overall values due to measurement errors, uncertainty in the core position or identification, and the fact that the core is the most time variable part of the quasar. In some cases, there are 4.86 GHz core flux densities from the VLA which differ significantly from the Parkes-Tidbinbilla interferometer (PTI) flux densities at 2.29 GHz for the same object (Baker, priv. comm.). This may be an indication of small scale structure, as the PTI has resolution of $\sim$ 0.1 arcsecond compared to $\sim$ 1 arcsecond for the VLA, or that the cores are variable on timescales of $\sim$ 1 year. Since the core flux densities are measured over a timescale of many years, all core errors with measured values of less than 20% are set to 20% to allow for variability. Lister et al. (1994) make a two-epoch study of 33 quasars, and find that 12 are variable: 5 at the 20% – 30% level, and 7 distributed between 30% – 100%; the lowest variation from this study was chosen to represent the errors on the core flux densities, as to have very high core errors would have been to weaken the constraints of the cores on the fitting significantly. Choosing this relatively low core error acts as a crude form of weighting, to balance the fact that far fewer core flux densities were available than total flux densities.

Frequency (GHz)	Source of total flux density
0.074	VLA Low-Frequency Sky Survey (VLSS), Cohen et al. (2007a)
0.080	Observed with the Culgoora Circular Array, Slee (1995); Slee & Higgins (1973, 1975); Slee (1977)
0.160	Observed with the Culgoora Circular Array, Slee (1995); Slee & Higgins (1973, 1975); Slee (1977)
0.365	from the Texas 365 MHz Survey, Douglas et al. (1996)
0.408	Molonglo Reference Catalogue, Large et al. (1981)
0.843	SUMMS Survey, Mauch et al. (2003), priv. comm. Mauch
1.4	NRAO VLA Sky Survey (NVSS), Condon et al. (1998)
1.658	MERLIN flux densities from de Silva et al. (in preparation, b)
2.7	Parkes Radio Sources Catalogue, Wright & Otrupcek (1990, 1996)
4.8	Australia Telescope 20 GHz Survey (Sadler (priv. comm.) & Massardi et al. 2008)
4.86	VLA flux densities, Kapahi et al. (1998a) and Parkes-MIT-NRAO catalogue, Griffith et al. (1994)
4.994	MERLIN flux densities from de Silva et al. (in preparation, b)
5	Parkes Radio Sources Catalogue, Wright & Otrupcek (1990, 1996)
8.44	VLA flux densities, Kapahi et al. (1998a)
8.6	Australia Telescope 20 GHz Survey (Sadler (priv. comm.) & Massardi et al. 2008)
18.5	ATCA flux densities, Ricci et al. (2006)
19.9	Australia Telescope 20 GHz Survey (Sadler (priv. comm.) & Massardi et al. 2008)
22	ATCA flux densities, Ricci et al. (2006)
23	WMAP flux densities, Bennett et al. (2003)
33	WMAP flux densities, Bennett et al. (2003)
41	WMAP flux densities, Bennett et al. (2003)
61	WMAP flux densities, Bennett et al. (2003)

Table 5.1: References for the total radio flux densities used in compiling the spectral energy distributions for the Molonglo Quasar Sample.

Frequency (GHz)	Source of core flux density
1.4	MERLIN flux densities, see Chapter 4
1.658	MERLIN flux densities from de Silva et al. (in preparation, b)
2.29	Parkes-MIT-NRAO catalogue, Griffith et al. (1994)
4.86	VLA flux densities, Kapahi et al. (1998a)
4.994	MERLIN flux densities from de Silva et al. (in preparation, b)
8.44	VLA flux densities, Kapahi et al. (1998a)

Table 5.2: This table shows the references for the core component radio flux densities for the Molonglo Quasar Sample.

5.3 *3CRR Sample Radio Data*

5.3.1 *Radio flux densities of the 3CRR sample*

A sub-sample of the 3CRR sample (Laing et al. 1983) was selected by first selecting only the FRII sources (to match the Molonglo Quasar Sample) and then discarding sources which do not have published SEDs in Laing & Peacock (1980), which removed 10 sources from the FRII sample. This resulted in a sample of 115 radio sources that should be effectively unbiased. The 3CRR sample itself contains two quasars boosted into the sample by their cores (Willott et al. 2000); these sources were both excluded from the sub-sample.

Core flux densities for these sources were then taken from Blundell et al. (in preparation), which includes core measurements from a number of origins spanning frequencies L-band (1.5 GHz) through to U-band (15 GHz).

The sources were divided into quasars and radio galaxies following Grimes et al. (2004), which classed the radio sources as radio galaxies, weak quasars or quasars. The weak quasars were then assigned either as quasars or radio galaxies as follows, to keep the analysis simple. The weak quasars are a mixed bag of different objects : some have moderate extinction ($A_V \sim 2$) and have broad H α lines but narrow H β lines; some show a high degree of extinction ($A_V \sim 10$) and have narrow H α, but broad Paα; some have broad emission lines but are not sufficiently intrinsically optically luminous to be classed as quasars; and some have no broad lines but a quasar nucleus that can be inferred from a far-IR bump in the SED.

The weak quasars which were insufficiently luminous to outshine the host galaxy, 3CRR382 and 3CRR390.3, were classified as quasars. If a radio source is seen to have extinction, it is difficult to be sure without spectropolarimetry whether the extinction is because the emission lines are viewed through the torus, or whether they consist of scattered light; in the absence of spectropolarimetry, most of these sources were classed as galaxies, with two exceptions. 3CRR109 is similar to 3CRR382 in that they are both dominated by a bright point-like optical nucleus and exhibit polarisation which can be explained by localised polarised emission, broadened by seeing and diluted by host galaxy starlight and by spatial averaging, rather than resulting from scattering (Cohen et al. 1999). 3CRR303, like 3CRR109, also appears to be a lightly veiled quasar and has very broad H α similar to those of 3CRR109 (Eracleous & Halpern 1994), this was also classified as a quasar. This 3CRR sub-sample consists of 30 quasars and 85 radio galaxies.

5.4 *Measuring $R_{\rm interp}$ from the SEDs*

5.4.1 *Definition of R and $R_{\rm 10GHz}$*

The definition of R was first established by Hine & Scheuer (1974) as

$$R = \frac{\text{Flux density of beamed core components}}{\text{Flux density of unbeamed components}} \; . \tag{5.1}$$

The point of this value is to provide a simple measure of the orientation of a radio source based upon a comparison of the core and extended flux densities. The extended parts of a radio source are, to a first approximation, equally luminous from all angles, whereas the radiation from the core of the source is strongly concentrated in a cone of narrow opening angle, due to Doppler boosting at small jet angles to the line of sight. The core flux density is often the limiting factor in this method, since in many objects it is not clearly resolved, and in these cases only a limit can be found for R. In some other objects, it is not possible to identify every region of emission definitively as a core or radio lobe. R is usually measured at a fiducial frequency of rest-frame 10 GHz, and is then referred to as $R_{\rm 10GHz}$.

5.4.2 *Definition of $R_{\rm interp}$*

A variation on the classical $R_{\rm 10GHz}$ value is now defined which follows the same principles as the original, but accounts for the observation that most radio sources do not follow a single power law spectrum (e.g. Heavens & Meisenheimer 1987). This variation is distinguished from the classical $R_{\rm 10GHz}$ with the symbol $R_{\rm interp}$, and it should be noted that $R_{\rm interp}$ is defined at rest-frame 10 GHz, in the same way as $R_{\rm 10GHz}$. According to synchrotron theory, at low enough frequencies, the SED will be a good approximation to a power law of spectral index 0.5, where $S = \nu^{-\alpha}$, the power-law index arising from first-order Fermi acceleration (Drury 1983; Heavens & Drury 1988). Using this information, a double power law is fitted to the extended component, with the low-frequency spectral index fixed at $\alpha_{\rm low} = 0.5$, and the high-frequency spectral index ($\alpha_{\rm high}$), break frequency ($\nu_{\rm break}$) and flux density at the break frequency ($S_{\rm norm}$) as free parameters:

$$S_{\rm lobe} = \frac{2S_{\rm norm}(\frac{\nu}{\nu_{\rm break}})^{\alpha_{\rm low}}}{1 + (\frac{\nu}{\nu_{\rm break}})^{\alpha_{\rm low}-\alpha_{\rm high}}}. \tag{5.2}$$

This equation tends towards

$$\begin{aligned} S_{\rm lobe} &= 2S_{\rm norm}(\frac{\nu}{\nu_{\rm break}})^{\alpha_{\rm low}} \quad \text{at} \quad \nu \ll \nu_{\rm break} \\ &= 2S_{\rm norm}(\frac{\nu}{\nu_{\rm break}})^{\alpha_{\rm high}} \quad \text{at} \quad \nu \gg \nu_{\rm break} \end{aligned} \tag{5.3}$$

in the limit of low or high frequencies respectively.

The total flux density of the SED is given by

$$S_{\rm tot} = S_{\rm lobe} + S_{\rm core} \tag{5.4}$$

where $S_{\rm core}$ is a constant, left as a free parameter in the fitting process.

$R_{\rm interp}$ is now defined on the basis of the low-frequency part of the double power law fit, so the part of the spectral energy distribution with spectral index $\alpha_{\rm low} = 0.5$ is extrapolated to a rest frequency of 10 GHz, and $R_{\rm interp}$ is the ratio of the core flux density to this extrapolated value.

$$R_{\rm interp} = \frac{S_{\rm core}}{2S_{\rm norm}(\frac{\nu}{\nu_{\rm break}})^{\alpha_{\rm high}}} \tag{5.5}$$

This shown in graphically in Figure 5.1. The low-frequency part of the SED is used, as the low-frequency emission is thought to be reasonably independent of viewing angle, and depends less on radio source age than the high frequency emission. The low-frequency emission is insensitive to synchrotron and inverse Compton losses, but falls off over time due to adiabatic losses (e.g. Blundell et al. 1999).

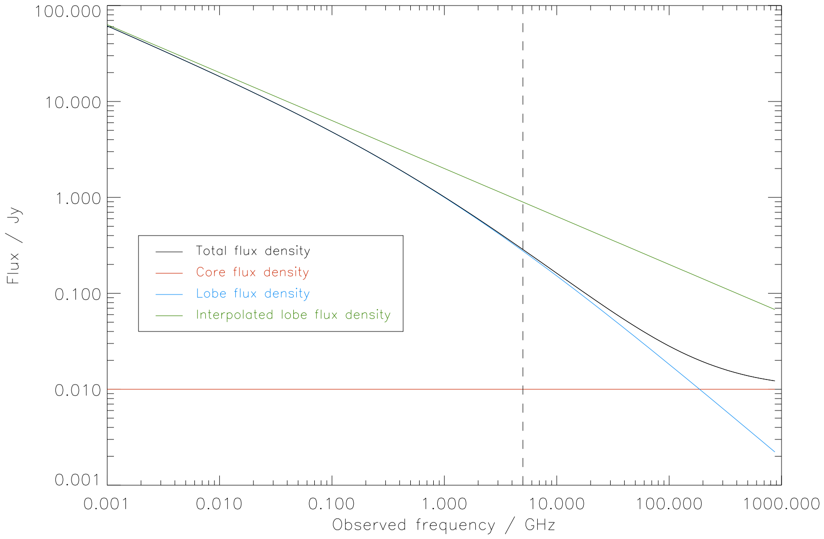

Figure 5.1: A diagram to show how R_{interp} is calculated for a source with $z = 1$, $S_{\mathrm{norm}} = 1$ Jy, $\alpha_{\mathrm{high}} = 1$, $\nu_{\mathrm{break}} = 1$ GHz and $S_{\mathrm{core}} = 0.01$. The blue line shows the lobe flux density calculated from Equation 5.2, and the green line shows the interpolation of the low frequency part of the lobe emission. The red line shows the core flux density, assuming $\alpha_{\mathrm{core}} = 0$, and the black line shows the total source flux density. The dotted vertical line shows the rest-frame 10 GHz frequency for a redshift of $z = 1$. R_{interp} is equal to the ratio of the core flux density (red line) to the interpolated lobe flux density (green line) at a frequency of 10 GHz in the rest frame of the source; in this example, $R_{\mathrm{interp}}= 0.011$ and $R_{\mathrm{10GHz}}= 0.036$.

5.5 *Fitting the 3CRR Sub-sample*

The integrated flux densities from the various surveys were treated as total flux densities, since these include the core components in addition to the extended emission. The core flux density was treated as a constant, since with only one or two measured core flux densities for each quasar, the model could only sensibly have one degree of freedom. The assumption of a constant flux density is reasonable since the core radio emission usually has a power-law index close to zero, arising from the self-absorbed bases of the jets (Cawthorne 1991). In addition, this component of emission is often a variable quantity, so any more complex model would be unjustifiable.

The free parameters of this model were fitted using the Bayesian Monte Carlo routine, *BayeSys3* by Skilling (2004)*, called with a wrapper written by D. Sivia (priv. comm.). The total flux densities and the core flux densities were simultaneously fitted, with the core values additionally treated as lower limits to the total flux density.

The likelihood function was calculated using the χ^2, which was modified by the number of 1-σ limits violated by the model, a simple way of dealing with limits which essentially treats them as a step function in probability:

$$\ln \mathscr{L} = -\frac{1}{2}\chi^2 - P \times N_L \tag{5.6}$$

where $\ln \mathscr{L}$ is the natural logarithmic likelihood, P is a constant representing a penalty placed on the fit, and N_L is the number of limits exceeded in the model. $P = 5$ was used in the following analysis, though $P = 10$ was also tested and found not to have any measurably different effect; this parameter is not expected to have significant influence, since it has been set to a high value which makes breaking any limits very unlikely.

There are two cases in which the Bayesian fit did not fully constrain. The first was when the core flux density for the radio source was an upper limit rather than a detection, and with a lack of strong curvature in the total flux density to constrain the core, there was only a limit to R_{interp}. Since this only affected eight objects of the 115 in the sample, the limits to the core flux density were treated as detections in the fitting process for these cases. A second analysis was run which set the core flux densities as detections at 50 percent of the limit value, and this was found to make no difference at all to the analysis, so these cases did not result in any significant bias.

The second case was that the break frequency was not constrained, which occurred in cases where the break frequency appeared to be lower than the minimum frequency of the SED. In these cases, the break frequency was set to 10 MHz in the rest frame of the object, so for a source in this sample at z $\sim$ 1, this corresponded to $\sim$ 5 MHz in the observed frame. The observed SEDs have flux densities down to $\sim$10 MHz observed frame, which allowed the break frequency to constrain to somewhat below this value, hence 10 MHz rest frame was roughly the highest break frequency the source could possess which was not constrained by the fit. If the break frequency was lower than this, then R_{interp} would

---

* *BayeSys* website: http://www.inference.phy.cam.ac.uk/bayesys/

be smaller, and higher jet angles would be found. The break frequency was unconstrained for 15 of the 115 3CRR radio sources.

5.5.1 *Correlations with* $R_{\rm interp}$

Figure 5.2 shows the $R_{\rm interp}$ values for the 3CRR sample plotted against logarithmic 178 MHz luminosity. Considering just the radio galaxies, where the effect of Doppler boosting is small, an anticorrelation is seen between $\log R_{\rm 10GHz}$ and $\log L_{\rm 178MHz}$, with a probability of $> 99.9\%$ measured using both Spearman's Rho test and Kendell's Tau, with *ASURV* (Lavalley et al. 1992) embedded in *IRAF* (Tody 1986, 1993). Following Scheuer (1980) and others, Blundell & Rawlings (1999) theorise that after a rapid increase of lobe luminosity in a radio source, the luminosity of the lobes, $L_{\rm lobe}$, will thereafter decrease slowly with time for a constant jet power, Q, due to adiabatic losses. For an increase in age of a factor of ten, a decrease of $\sim \frac{1}{3}$ is expected in low-frequency lobe luminosity for a constant jet power. The core luminosity might remain a relatively faithful tracer of Q. Since $R_{\rm interp}$ is defined as the ratio of the flux densities or luminosities of the radio core to the radio lobes, then as the source ages, the $L_{\rm lobe}$ decreases and $R_{\rm interp}$ increases.

There is a large degree of scatter in the $\log R_{\rm 10GHz} - \log L_{\rm 178MHz}$ relation, presumably due to the scatter in ages of the sources and the scatter in the theorised relation $L_{\rm core} \propto L_{\rm lobe}$ for a fixed age. The relation is quantified by Blundell & Rawlings (1999) as

$$L_{\rm lobe} = AQ^{31/28} n^{9/14} t^{-5/28} \tag{5.7}$$

where Q is the jet power, n is the electron number density at a radius of 100 kpc from the source, t is the age of the source and A is a constant.

Ignoring the evolution with age and the variation with gaseous environment, then with the assumption that $L_{\rm core} \propto Q^P$, where P is a constant power (following Miller et al. (1993)) then Equation 5.7 becomes

$$L_{\rm lobe} = K {L_{\rm core}}^x \tag{5.8}$$

where K and $x = \frac{31}{28P}$ are constants.

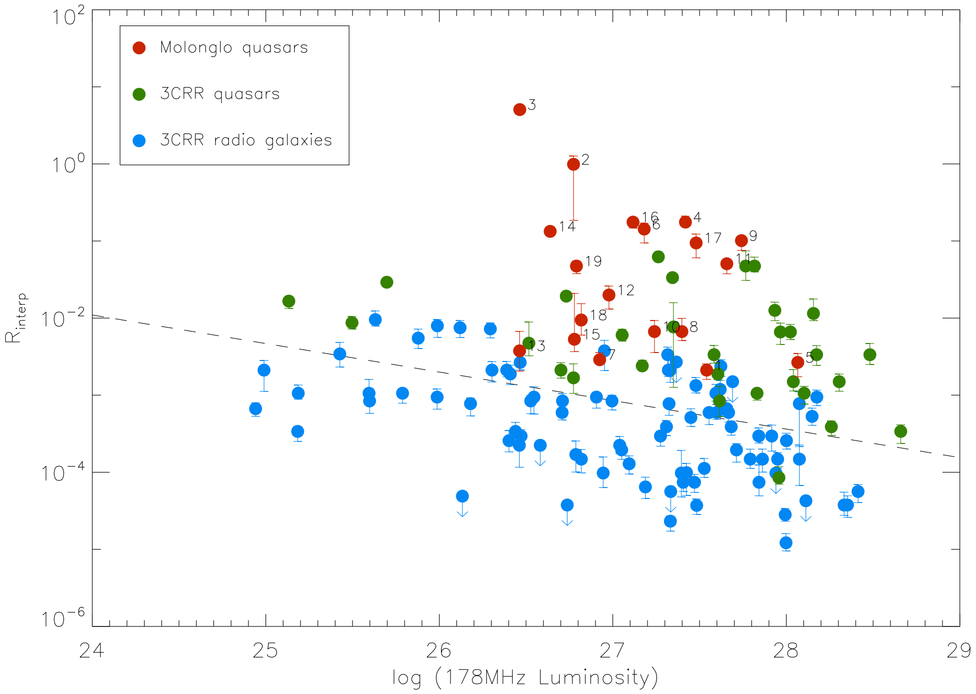

Figure 5.2: Core-to-lobe flux density ratio $R_{\rm interp}$ (fitted for the Molonglo sub-sample in Section 5.7) plotted against logarithmic 178 MHz rest-frame luminosity for the 3CRR sub-sample radio galaxies (blue points) and quasars (green points). The Molonglo quasar sub-sample is plotted in red. The dotted line shows a linear fit to the anticorrelation between $\log R_{\rm interp}$ and $\log L_{\rm 178MHz}$ for the 3CRR radio galaxies; the slope is -0.37 and the intercept at $\log L_{\rm 178MHz}= 24$ is $\log R_{\rm interp}= -1.96$. At 178 MHz, $L_{\rm 178MHz}\simeq L_{\rm lobe}$.

Combining Equation 5.8 with the definition of $R_{\rm interp}$, then

$$R_{\rm interp} = \frac{L_{\rm core}}{L_{\rm lobe}} = K^{-\frac{1}{x}} L_{\rm lobe}{}^{\frac{1-x}{x}}. \tag{5.9}$$

From the measured slope of $\log R_{\rm interp} \propto -0.37 \log L_{\rm lobe}$, then $P \simeq 0.7$. This is reasonably consistent with the value of $P \sim 1$ found by Miller et al. (1993) observationally and from theoretical arguments.

Taking the logarithm of this equation and simplifying, then

$$\log R_{\rm interp} = A \log L_{\rm lobe} + B \tag{5.10}$$

where A and B are constants, and $A = \frac{1-x}{x} = \frac{28P}{31} - 1$. The slope is found to be $A \sim -0.1$ for $P \sim 1$. This calculated value for A is not used in the following analysis, but is left as a free parameter.

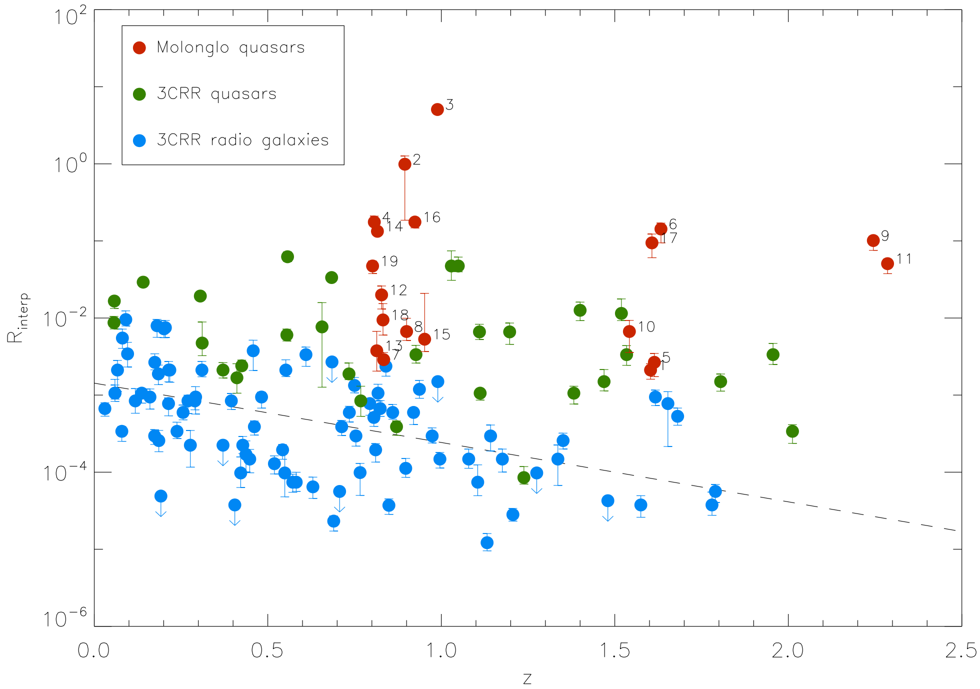

Figure 5.3: Core-to-lobe flux density ratio $R_{\rm interp}$ (fitted for the Molonglo sub-sample in Section 5.7) plotted against redshift z for the 3CRR sub-sample radio galaxies (blue points) and quasars (green points). The Molonglo quasar sub-sample is plotted in red. The dotted line shows a linear fit to the anticorrelation between $\log R_{\rm interp}$ and z for the 3CRR radio galaxies; the slope is -0.77 and the intercept at $z = 0$ is $\log R_{\rm interp} = -2.85$.

The plot of $\log R_{\rm 10GHz}$ versus z for 3CRR radio galaxies shows an anticorrelation with a probability of $> 99.9\%$ measured using both Spearman's Rho test and Kendell's Tau, with *ASURV* (Lavalley et al. 1992) embedded in *IRAF*. A modest anticorrelation is expected to arise when a low-frequency flux density limit is used to select a sample of radio sources from a population which declines in luminosity as it ages, with the effect that the more distant sources from the sample are more luminous (this effect is known as the Malmquist bias), and hence have higher jet power. As the lobe luminosity declines, the core luminosity also decreases, but not as quickly, and therefore the sources at high redshift have smaller $R_{\rm interp}$ values.

The young quasars (CSS sources) are preferentially found at high redshift and are more luminous, but the aging effect in this sample is not expected to be strong, as the flux limit excludes the majority of sources with jets consisting mostly of aged plasma. The $\log R_{10\mathrm{GHz}} - z$ anticorrelation is not expected to be as strong as the anticorrelation between $\log R_{\mathrm{interp}}$ and $\log L_{178\mathrm{MHz}}$. In this analysis, we assume that the primary link is between $\log R_{\mathrm{interp}}$ and $\log L_{178\mathrm{MHz}}$, as explained physically by models in which the core luminosity is proportional to the jet power, and $L_{178\mathrm{MHz}}$ drops with age.

5.6 *Modelling the Relation between R_{interp}, $L_{178\mathrm{MHz}}$ and θ_{jet}*

5.6.1 *Overview of the method*

The 3CRR sub-sample of radio sources is generally supposed to have jets randomly orientated in space (Cawthorne et al. 1986), without significant selection effects due to Doppler boosting. Blundell & Rawlings (1999) states that there are three other mechanisms which may cause biases in low-frequency selected samples: synchrotron self-absorption (reabsorption of synchrotron radiation by the emitting electrons); free-free absorption (absorption of synchrotron radiation by material lying outside the radio source); and a possible low-energy cut-off of the synchrotron-emitting particles. However, these effects are relatively minor compared to the biases potentially introduced by Doppler boosting.

The relationship between R_{interp} and 178 MHz luminosity is modelled for the 3CRR population of quasars and radio galaxies, and this relation and fitted parameters are applied to the Molonglo sub-sample of quasars, assuming that for a given rest-frame lobe luminosity, these sources are the same. The relation between $\log L_{178\mathrm{MHz}}$, $\log R_{\mathrm{interp}}$ and θ is used in conjunction with Equation 5.5, which fits R_{interp} from the SED, and the relation between flux density and luminosity, to directly model the jet angles in the Molonglo Quasar sub-sample from the SED.

5.6.2 *Luminosity distribution*

In order to account for the distribution of the radio sources in logarithmic luminosity, and thereby deconvolve this from the relation between $\log L_{178\mathrm{MHz}}$ and $\log R_{\mathrm{interp}}$, a function was fitted to the luminosity distribution of all objects in the 3CRR subsample, binned as

$\Delta \log L_{178\mathrm{MHz}} = 0.5$. A range of functional forms was tried, including $(\log L_{178\mathrm{MHz}})^2$ times a Gaussian, a sum of two Gaussians, a double power law and a log-normal curve. The log-normal curve was selected as this has the lowest χ^2 and a sensible behaviour at the boundaries of the region enclosing all sources (see Figure 5.4).

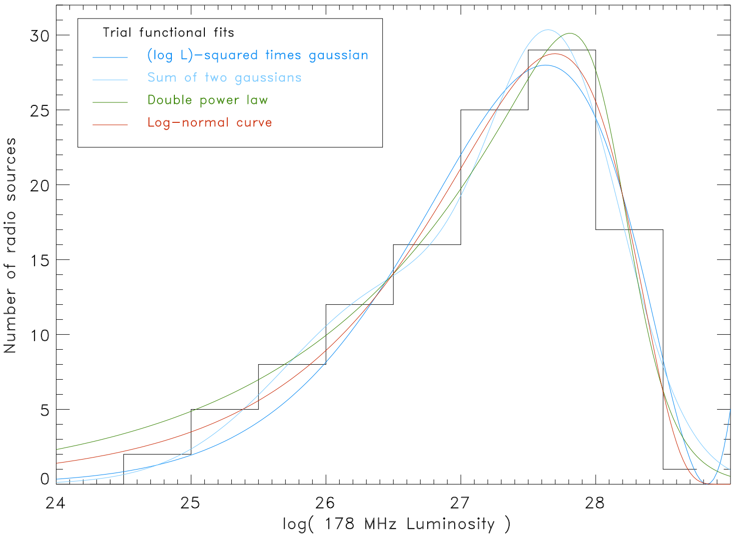

Figure 5.4: A comparison of functional fits to the distribution of logarithmic luminosities for the 3CRR sample of radio sources. The log normal curve, plotted in red, was found to have the lowest χ^2 fit (reduced $\chi^2 = 0.11$), and was therefore selected.

5.6.3 *Calculating* θ_{crit}

The critical angle is the average angle at which the division is made between radio galaxies and quasars due to the opening angle of the obscuring torus; if the radio source is viewed within a cone that is unobscured by the torus then a quasar is seen, at larger viewing angles, radio galaxies are observed.

For a sample of sources whose jets are randomly oriented, the distribution expected in θ is $\mathrm{Prob}(\theta)\mathrm{d}\theta = \sin\theta\mathrm{d}\theta$. The probability of the source being observed as a quasar, referred to as the quasar fraction, is then

$$\mathrm{P(quasar)} = \int_0^{\theta_{\mathrm{crit}}} \sin\theta\mathrm{d}\theta = 1 - \cos\theta_{\mathrm{crit}} \; . \tag{5.11}$$

Similarly, the probability of the source being seen as a radio galaxy is

$$\mathrm{P(galaxy)} = \int_{\theta_{\mathrm{crit}}}^{\frac{\pi}{2}} \sin\theta \mathrm{d}\theta = \cos\theta_{\mathrm{crit}} \ . \tag{5.12}$$

The critical angle may depend on the ionising luminosity of the source, because such luminosity sublimates any dust close to the radio source, the so-called "receding-torus" model (Lawrence 1991). A proxy for the ionising luminosity is the narrow line luminosity, since these lines are cooling radiation from clouds heated by the quasar nucleus. The narrow line luminosity is in turn related to the radio luminosity via an empirical relation (e.g. Willott et al. 1999).

The critical angle is related to the source luminosity by the relation $\tan\theta = r/h$, where r is the inner radius of the dusty torus and follows $r \propto L_{[\mathrm{OII}]}^{0.5}$ (Willott et al. 2000), and h is the luminosity-independent height of the dusty torus. Normalising this relation to remove the torus height

$$\tan\theta_{\mathrm{crit}} = \tan\theta_{\mathrm{norm}} (L_{[\mathrm{OII}]}/L_{[\mathrm{OII}]\mathrm{norm}})^{0.5} \ . \tag{5.13}$$

Willott et al. (1999) relate $L_{[\mathrm{OII}]}$ to $L_{151\mathrm{MHz}}$ for FRII sources from the 3CRR and the 7C radio surveys with an empirical relation. Since this relation is not expected to vary significantly with redshift, this relation can sensibly by applied to the 3CRR sources alone. Willott et al. (1999) find

$$L_{[\mathrm{OII}]} \propto L_{151\mathrm{MHz}}{}^{\alpha_{\mathrm{NLR-radio}}} \tag{5.14}$$

with $\alpha_{\mathrm{NLR-radio}} = 0.81 \pm 0.04$. The exponent of this relation is independent of the exact frequency of the radio luminosity, so $L_{151\mathrm{MHz}}$ can be replaced by L_{radio}.

Substituting 5.14 into 5.13

$$\tan\theta_{\mathrm{crit}} = \tan\theta_{\mathrm{norm}} (L_{\mathrm{radio}}/L_{\mathrm{radio\,norm}})^{0.405} \ . \tag{5.15}$$

This equation for critical angle works well at luminosities greater than about $L_{\mathrm{radio}} = 10^{27}\mathrm{WHz}^{-1}\mathrm{sr}^{-1}$, but at lower luminosities, this model predicts a much lower fraction of quasars than is actually observed. The quasar fraction is therefore fixed at 10% for luminosities $L_{178\mathrm{MHz}} < 8 \times 10^{26}\mathrm{WHz}^{-1}\mathrm{sr}^{-1}$, which agrees with the available data (Vardoulaki et al. (2008), Mauch, priv. comm.).

The quasar fraction is therefore modelled by the receding torus model at high luminosities, with the normalisation angle, θ_{norm}, fixed at $L_{\mathrm{radio\,norm}} = 10^{27}\mathrm{WHz}^{-1}\mathrm{sr}^{-1}$, and a constant quasar fraction of 10% for $L_{178\mathrm{MHz}} < 8 \times 10^{26}\mathrm{WHz}^{-1}\mathrm{sr}^{-1}$. The range specified by 0.5 magnitudes in luminosity above and below $L_{178\mathrm{MHz}} < 8 \times 10^{26}\mathrm{WHz}^{-1}\mathrm{sr}^{-1}$ is fit by a cubic function which matches the values and partial differentials of these functions. Figure 5.5 shows the difference between the fitted quasar fraction and that of Willott et al. (2000).

The radio galaxy and quasar luminosity distributions are individually fit by the overall luminosity function modified by the radio galaxy and quasar fractions respectively; the χ^2 from these two fits are added and minimised (Figures 5.6 and 5.7). The critical angle at $L_{\mathrm{radio\,norm}} = 10^{27}\mathrm{WHz}^{-1}\mathrm{sr}^{-1}$ was found to be $\theta_{\mathrm{norm}} = 28.1°$. Figure 5.8 shows the overall luminosity distribution with the radio galaxy and quasar distributions.

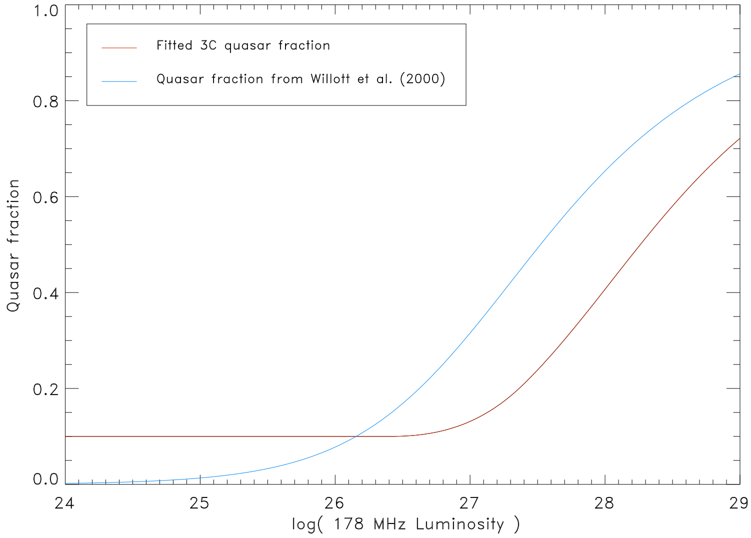

Figure 5.5: A comparison of the quasar fraction fitted for the 3CRR sample to that fitted to the 3CRR, 6C and 7C combined sample in Willott et al. (2000), with all cosmology corrected to $H_0 = 70\,\mathrm{kms}^{-1}\mathrm{Mpc}^{-1}$, $\Omega_{\mathrm{M}} = 0.3$ and $\Omega_{\Lambda} = 0.7$. The fraction differs from that of Willott et al. (2000) in that the 3CRR sample has a lower critical angle, and tends towards a constant quasar fraction at low luminosities.

The difference between the Willott et al. (2000) model of quasar fraction and the model used in this thesis at luminosities $L_{\rm radio} < 10^{27}{\rm WHz}^{-1}{\rm sr}^{-1}$ may reflect different definitions of "quasar". Willott et al. (2000) required an optical nucleus with $M_B > -23$; this requirement was excluded from the selection of the 3CRR sub-sample used here.

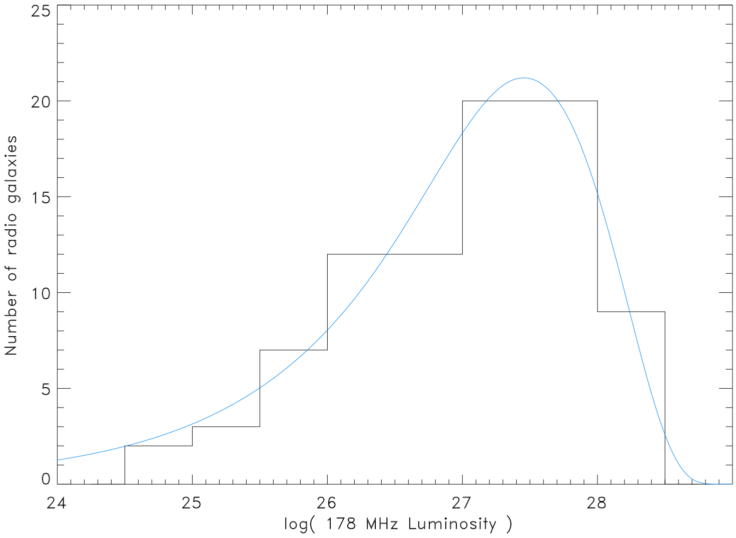

Figure 5.6: The fit to the logarithmic luminosity distribution of radio galaxies in the 3CRR sub-sample found by multiplying the overall luminosity distribution of the 3CRR sub-sample (Figure 5.8) with the fitted radio galaxy fraction. The reduced $\chi^2$for this fit is 0.23.

5.6.4 *Modelling the* $\log R_{\rm interp} - \log L_{\rm 178MHz}$ *relation*

5.6.4.1 *Likelihood for a general set of radio sources*

Following the method of Marshall et al. (1983), a likelihood function for source density in the $\log R_{\rm interp} - \log L_{178}$ plane is determined. For a general population of radio sources, the distribution in the $\log R_{\rm interp} - \log L_{178}$ plane is given by $\rho(\log R_{\rm interp}, \log L_{178})$ where $\rho(\log R_{\rm interp}, \log L_{178}) {\rm d}\log R_{\rm interp}\, {\rm d}\log L_{178}$ is the expected number of radio sources in the differential element ${\rm d}\log R_{\rm interp}\, {\rm d}\log L_{178}$ at $\log R_{\rm interp}$ $\log L_{178}$.

$\Omega(\log R_{\rm interp}, \log L_{178})$ is the fractional volume of the sky in which sources are detected if they are present, which depends on the selection effects. This means that the expected number of observed sources in the differential element ${\rm d}\log R_{\rm interp}\, {\rm d}\log L_{178}$ at

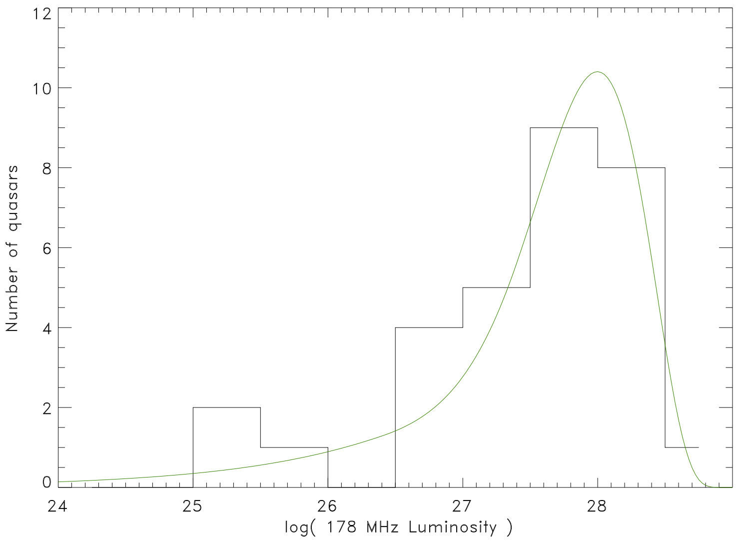

Figure 5.7: The fit to the logarithmic luminosity distribution of quasars in the 3CRR sub-sample found by multiplying the overall luminosity distribution of the 3CRR sub-sample (Figure 5.8) with the fitted quasar fraction. The reduced $\chi^2$for this fit is 0.46.

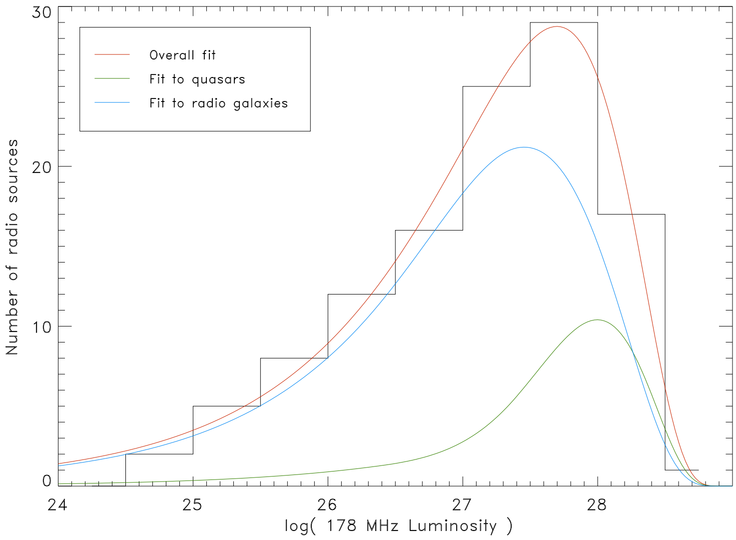

Figure 5.8: The fit to the logarithmic luminosity distribution of all radio sources in the 3CRR sub-sample (red line), with the fits to the logarithmic luminosity distribution of the radio galaxies (blue line) and the quasars (green line) shown.

$\log R_{\text{interp}}$ $\log L_{178}$ is

$$\rho(\log R_{\text{interp}}, \log L_{178})\Omega(\log R_{\text{interp}}, \log L_{178})\mathrm{d}\log R_{\text{interp}}\,\mathrm{d}\log L_{178}\ . \tag{5.16}$$

The likelihood function, $\mathscr{L}$, is defined as the product of the probabilities of observing exactly one quasar in the element $\mathrm{d}\log R_{\text{interp}}\,\mathrm{d}\log L_{178}$ at each $(\log R_{\text{interp}_i}, \log L_{178i})$ for the N sources in the data set, and the probabilities of observing zero sources in all other elements in the accessible regions of the plane. Poisson probabilities are used.

$$\begin{aligned}\mathscr{L} \;=\; & \prod_i^N \rho(\log R_{\text{interp}_i}, \log L_{178\,i})\Omega(\log R_{\text{interp}_i}, \log L_{178\,i})\mathrm{d}\log R_{\text{interp}}\,\mathrm{d}\log L_{178} \\ & e^{-\rho(\log R_{\text{interp}_i},\log L_{178\,i})\Omega(\log R_{\text{interp}_i},\log L_{178\,i})\mathrm{d}\log R_{\text{interp}}\,\mathrm{d}\log L_{178}} \\ & \prod_j e^{-\rho(\log R_{\text{interp}_j},\log L_{178\,j})\Omega(\log R_{\text{interp}_j},\log L_{178\,j})\mathrm{d}\log R_{\text{interp}}\,\mathrm{d}\log L_{178}}\end{aligned} \tag{5.17}$$

where the index j runs over all differential elements in which no sources were observed.

Defining the entropy, $S = -2\ln(\mathscr{L})$ then

$$\begin{aligned}S \;=\; & -2\ln\prod_i^N \rho(\log R_{\text{interp}_i}, \log L_{178\,i})\Omega(\log R_{\text{interp}_i}, \log L_{178\,i})\mathrm{d}\log R_{\text{interp}}\,\mathrm{d}\log L_{178} \\ & e^{-\rho(\log R_{\text{interp}_i},\log L_{178\,i})\Omega(\log R_{\text{interp}_i},\log L_{178\,i})\mathrm{d}\log R_{\text{interp}}\,\mathrm{d}\log L_{178}} \\ & \prod_j e^{-\rho(\log R_{\text{interp}_j},\log L_{178\,j})\Omega(\log R_{\text{interp}_j},\log L_{178\,j})\mathrm{d}\log R_{\text{interp}}\,\mathrm{d}\log L_{178}}\ .\end{aligned} \tag{5.18}$$

Now, the terms which sum $\rho(\log R_{\text{interp}}, \log L_{178})\Omega(\log R_{\text{interp}}, \log L_{178})$ over all space are replaced with an integral over the full range of $\log R_{\text{interp}}$ and $\log L_{178}$:

$$\begin{aligned}S \;=\; & -2\sum_i^N \ln\rho(\log R_{\text{interp}_i}, \log L_{178\,i}) - 2\sum_i^N \ln\Omega(\log R_{\text{interp}_i}, \log L_{178\,i}) \\ & -2\sum_i^N \ln\mathrm{d}\log R_{\text{interp}} - 2\sum_i^N \ln\mathrm{d}\log L_{178} \\ & +2\int_{\log R_{\text{interp}_{\min}}}^{\log R_{\text{interp}_{\max}}}\int_{\log L_{178\,\min}}^{\log L_{178\,\max}} \rho(\log R_{\text{interp}}, \log L_{178})\end{aligned}$$

$$\Omega(\log R_{\mathrm{interp}}, \log L_{178}) \mathrm{d} \log R_{\mathrm{interp}} \, \mathrm{d} \log L_{178} \ . \tag{5.19}$$

Dropping the terms which are independent of the model parameters, including $\Omega(\log R_{\mathrm{interp}}, \log L_{178})$ which does not depend on the parameters so long as the parameter space encloses all objects, and the density of the sources falls off at the edges of the box:

$$\begin{aligned} S &= -2 \sum_{i}^{N} \ln \rho(\log R_{\mathrm{interp}_i}, \log L_{178\,i}) \\ &\quad +2 \int_{\log R_{\mathrm{interp}_{\min}}}^{\log R_{\mathrm{interp}_{\max}}} \int_{\log L_{178\,\min}}^{\log L_{178\,\max}} \rho(\log R_{\mathrm{interp}}, \log L_{178}) \\ &\qquad \Omega(\log R_{\mathrm{interp}}, \log L_{178}) \mathrm{d} \log R_{\mathrm{interp}} \, \mathrm{d} \log L_{178} \end{aligned} \tag{5.20}$$

The entropy S is minimised to find the best fit.

5.6.4.2 *Extension to a 2-population set of sources*

Grimes et al. (2004) have described how to formulate this overall likelihood for a sample which contains two types of source, radio galaxies and quasars. The method is to essentially add two likelihoods together, one for each type of source:

$$\begin{aligned} S &= -2 \sum_{i}^{N_{\mathrm{rg}}} \ln \rho(\log R_{\mathrm{interp}_i}, \log L_{178\,i})_{\mathrm{rg}} \\ &\quad +2 \int_{\log R_{\mathrm{interp}_{\min}}}^{\log R_{\mathrm{interp}_{\max}}} \int_{\log L_{178\,\min}}^{\log L_{178\,\max}} \rho(\log R_{\mathrm{interp}}, \log L_{178})_{\mathrm{rg}} \\ &\qquad \Omega(\log R_{\mathrm{interp}}, \log L_{178})_{\mathrm{rg}} \mathrm{d} \log R_{\mathrm{interp}} \, \mathrm{d} \log L_{178} \\ &\quad -2 \sum_{i}^{N_{\mathrm{qso}}} \ln \rho(\log R_{\mathrm{interp}_i}, \log L_{178\,i})_{\mathrm{qso}} \\ &\quad +2 \int_{\log R_{\mathrm{interp}_{\min}}}^{\log R_{\mathrm{interp}_{\max}}} \int_{\log L_{178\,\min}}^{\log L_{178\,\max}} \rho(\log R_{\mathrm{interp}}, \log L_{178})_{\mathrm{qso}} \\ &\qquad \Omega(\log R_{\mathrm{interp}}, \log L_{178})_{\mathrm{qso}} \mathrm{d} \log R_{\mathrm{interp}} \, \mathrm{d} \log L_{178} \end{aligned} \tag{5.21}$$

where N_{rg} is the number of radio galaxies and N_{qso} is the number of quasars.

5.6.4.3 *Calculating the differential number density*

The model for the R_{interp} value is formed from a relation with a dependence on radio luminosity that is linear in log space, and the Doppler boosting factor, $f(\theta, \gamma)$, where θ is the angle of the jet to the line of sight and γ is the Lorentz factor. The mean value of R_{interp} is then

$$\langle R_{\mathrm{interp}} \rangle = B {L_{178}}^{A} f(\theta, \gamma) \tag{5.22}$$

where

$$f(\theta, \gamma) = \frac{1}{\gamma^2} \left(\frac{1}{(1 + \beta \cos\theta)^2} + \frac{1}{(1 - \beta \cos\theta)^2} \right) . \tag{5.23}$$

The Doppler boosting function given in Equation 5.23 is plotted in Figure 5.9. In log space, this becomes

$$\langle \log R \rangle = (A \log L_{178} + B) + \log f(\theta, \gamma) \tag{5.24}$$

where A and B are constants. This term accounts for the overall trend in the $\log R_{\mathrm{interp}} - \log L_{178}$ plane, and is modified with a Gaussian scatter of dispersion C.

The term $g(\log L_{178})$ is the fitted luminosity distribution for the population of radio sources, which is the luminosity distribution for all sources modified by the quasar fraction to account for the type of source.

For a general population of radio sources, the distribution in the $\log R_{\mathrm{interp}} - \log L_{178}$ plane is hence given by $\rho(\log R_{\mathrm{interp}}, \log L_{178})$ where

$$\begin{aligned} \rho(\log R_{\mathrm{interp}}, \log L_{178}) &= \int_{\theta_{\mathrm{low}}}^{\theta_{\mathrm{high}}} \frac{1}{\sqrt{2\pi}C} e^{-\frac{(\log R_{\mathrm{interp}} - ((A \log L_{178} + B) + \log f(\theta,\gamma)))^2}{2C^2}} \\ &\qquad g(\log L_{178}) \sin\theta \mathrm{d}\theta \end{aligned} \tag{5.25}$$

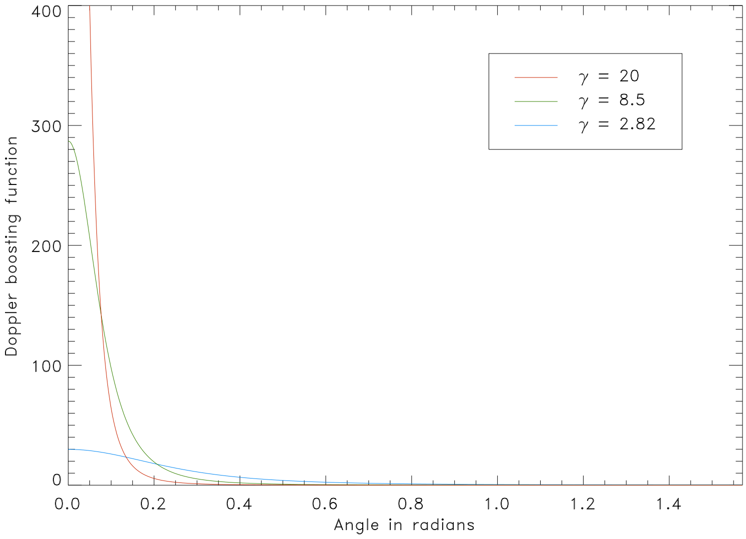

Figure 5.9: The Doppler boosting function, $f(\theta,\gamma)$, given in Equation 5.23, for different values of γ, versus jet angle in radians.

in which $\rho(\log R_{\mathrm{interp}}, \log L_{178})\mathrm{d}\log R_{\mathrm{interp}}\,\mathrm{d}\log L_{178}$ is the expected number of radio sources in the differential element $\mathrm{d}\log R_{\mathrm{interp}}\,\mathrm{d}\log L_{178}$.

The entire expression is integrated over $\sin\theta\mathrm{d}\theta$ to account for the random distribution of the objects in space.

5.6.4.4 *The specific case*

A radio galaxy is seen when a radio source is viewed at jet angles between θ_{crit} and $\frac{\pi}{2}$. A quasar is seen when a radio source is viewed at angles between 0 and θ_{crit}.

The entropy of a set of radio sources including both radio galaxies and quasars is

$$\begin{aligned} S &= -2\sum_{i}^{N_{\mathrm{rg}}} \ln\left(\int_{\theta_{\mathrm{crit}}}^{\frac{\pi}{2}} \frac{1}{\sqrt{2\pi}C} e^{-\frac{(\log R_{\mathrm{interp}}-((A\log L_{178}+B)+\log f(\theta,\gamma)))^2}{2C^2}} g(\log L_{178})\sin\theta\mathrm{d}\theta\right) \\ &\quad +2\int_{\log L_{178\,\mathrm{min}}}^{\log L_{178\,\mathrm{max}}}\int_{\theta_{\mathrm{crit}}}^{\frac{\pi}{2}}\int_{\log R_{\mathrm{interp}_{\mathrm{min}}}}^{\log R_{\mathrm{interp}_{\mathrm{max}}}} \frac{1}{\sqrt{2\pi}C} e^{-\frac{(\log R_{\mathrm{interp}}-((A\log L_{178}+B)+\log f(\theta,\gamma)))^2}{2C^2}} g(\log L_{178}) \\ &\quad \Omega(\log R_{\mathrm{interp}}, \log L_{178})_{\mathrm{rg}}\mathrm{d}\log L_{178}\sin\theta\mathrm{d}\theta\mathrm{d}\log R_{\mathrm{interp}} \end{aligned}$$

$$
\begin{aligned}
&-2\sum_{i}^{N_{\mathrm{qso}}}\ln\left(\int_{0}^{\theta_{\mathrm{crit}}}\frac{1}{\sqrt{2\pi}C}e^{-\frac{(\log R_{\mathrm{interp}}-((A\log L_{178}+B)+\log f(\theta,\gamma)))^{2}}{2C^{2}}}g(\log L_{178})\sin\theta\mathrm{d}\theta\right)\\
&+2\int_{\log L_{178\,\mathrm{min}}}^{\log L_{178\,\mathrm{max}}}\int_{0}^{\theta_{\mathrm{crit}}}\int_{\log R_{\mathrm{interp}_{\mathrm{min}}}}^{\log R_{\mathrm{interp}_{\mathrm{max}}}}\frac{1}{\sqrt{2\pi}C}e^{-\frac{(\log R_{\mathrm{interp}}-((A\log L_{178}+B)+\log f(\theta,\gamma)))^{2}}{2C^{2}}}g(\log L_{178})\\
&\Omega(\log R_{\mathrm{interp}},\log L_{178})_{\mathrm{rg}}\mathrm{d}\log L_{178}\sin\theta\mathrm{d}\theta\mathrm{d}\log R_{\mathrm{interp}} \qquad (5.26)
\end{aligned}
$$

In this equation, the integral over angle must be calculated before the integral over luminosity, as θ_{crit} depends on luminosity. The integration over $\log R_{\mathrm{interp}}$ is calculated analytically, as follows:

$$
\begin{aligned}
S \;=\; &-2\sum_{i}^{N_{\mathrm{rg}}}\ln\left(\int_{\theta_{\mathrm{crit}}}^{\frac{\pi}{2}}\frac{1}{\sqrt{2\pi}C}e^{-\frac{(\log R_{\mathrm{interp}}-((A\log L_{178}+B)+\log f(\theta,\gamma)))^{2}}{2C^{2}}}g(\log L_{178})\sin\theta\mathrm{d}\theta\right)\\
&+2\Omega_{\mathrm{rg}}\int_{\log L_{178\,\mathrm{min}}}^{\log L_{178\,\mathrm{max}}}\int_{\theta_{\mathrm{crit}}}^{\frac{\pi}{2}}\frac{1}{2}\left(\mathrm{erf}\left(\frac{(\log R_{\mathrm{interp}_{\mathrm{min}}}-((A\log L_{178}+B))+\log f(\theta,\gamma))}{\sqrt{2}C}\right)-\right.\\
&\left.\mathrm{erf}\left(\frac{(\log R_{\mathrm{interp}_{\mathrm{max}}}-((A\log L_{178}+B))+\log f(\theta,\gamma))}{\sqrt{2}C}\right)\right)\\
&g(\log L_{178})\mathrm{d}\log L_{178}\sin\theta\mathrm{d}\theta\\
&-2\sum_{i}^{N_{\mathrm{qso}}}\ln\left(\int_{0}^{\theta_{\mathrm{crit}}}\frac{1}{\sqrt{2\pi}C}e^{-\frac{(\log R_{\mathrm{interp}}-((A\log L_{178}+B)+\log f(\theta,\gamma)))^{2}}{2C^{2}}}g(\log L_{178})\sin\theta\mathrm{d}\theta\right)\\
&+2\Omega_{\mathrm{qso}}\int_{\log L_{178\,\mathrm{min}}}^{\log L_{178\,\mathrm{max}}}\int_{0}^{\theta_{\mathrm{crit}}}\frac{1}{2}\left(\mathrm{erf}\left(\frac{(\log R_{\mathrm{interp}_{\mathrm{min}}}-((A\log L_{178}+B))+\log f(\theta,\gamma))}{\sqrt{2}C}\right)-\right.\\
&\left.\mathrm{erf}\left(\frac{(\log R_{\mathrm{interp}_{\mathrm{max}}}-((A\log L_{178}+B))+\log f(\theta,\gamma))}{\sqrt{2}C}\right)\right)\\
&g(\log L_{178})\mathrm{d}\log L_{178}\sin\theta\mathrm{d}\theta \qquad (5.27)
\end{aligned}
$$

where Ω_{ng} and Ω_{qso} are numbers that are independent of $\log R_{\mathrm{interp}}$ and $\log L_{178}$.

5.6.4.5 *Fitting the R_{interp}– $L_{178\mathrm{MHz}}$ model*

The likelihood function given in Equation 5.27 is used in the Bayesian Monte Carlo routine *BayeSys3* to fit the parameters A, B and γ of Equation 5.22, and the scatter on this relation, C, to the 3CRR sub-sample. Random numbers were required to create the scatter on the R_{interp}– $L_{178\mathrm{MHz}}$ relation. These were generated with a Mersenne Twister code (Matsumoto

& Nishimura 1998), which produces a long sequence of highly random numbers very fast and reproducibly.

As is the nature of Monte Carlo optimisation, the probability distributions for the parameter values have some small scatter due the the random seed of the fitting. Five models with different seeds were therefore run, and the average of the posterior parameter distributions from these models were found. The slope and constant of the R_{interp}– L_{178MHz} relation produced posterior distributions which were Gaussian-like, and so the average of Gaussians fit to these posteriors were taken. The scatter on the R_{interp}– L_{178MHz} relation had a slightly asymmetric posterior, and the Lorentz factor γ had a very asymmetric distribution (Figure 5.10), and so for these, the average of the maxima of the distributions were found instead. The values of the fitted parameters and their errors are given in Table 5.3.

Parameter	Description	Fitted value	Error
A	Constant of the R_{interp}– L_{178MHz} relation	2.718	0.065
B	Slope of the R_{interp}– L_{178MHz} relation	-0.2109	0.0026
C	Scatter on the R_{interp}– L_{178MHz} relation	0.5233	0.0130
γ	Lorentz factor	2.822	0.084

Table 5.3: The fitted values of the parameters of Equation 5.22, with all four parameters allowed to vary freely.

The likelihood distribution of Equation 5.27 with parameter values from Table 5.3 is shown in Figure 5.11, with the 3CRR radio galaxies and quasars plotted over the likelihood contours. The likelihood function is in general a good fit to the distribution of sources. There are three outlying quasars, fainter than $\log L_{\mathrm{178MHz}} = 26$: these are 3CRR303, 3CRR382 and 3CRR390.3, which are all weak quasars (see Section 5.3). These sources lie near the radio galaxy/quasar divide, and therefore it is not unreasonable that they should lie outside the region of high quasar likelihood.

The fitted slope of the R_{interp}– L_{178MHz} relation, given in Table 5.3, is ~ -0.21. This is a steeper slope than the estimated slope of ~ -0.1, found from Equations 5.9 and 5.10 with the Miller et al. (1993) assumption that core luminosity scales directly with jet power. This is broadly consistent, as factors such as jet power and gas density have been ignored.

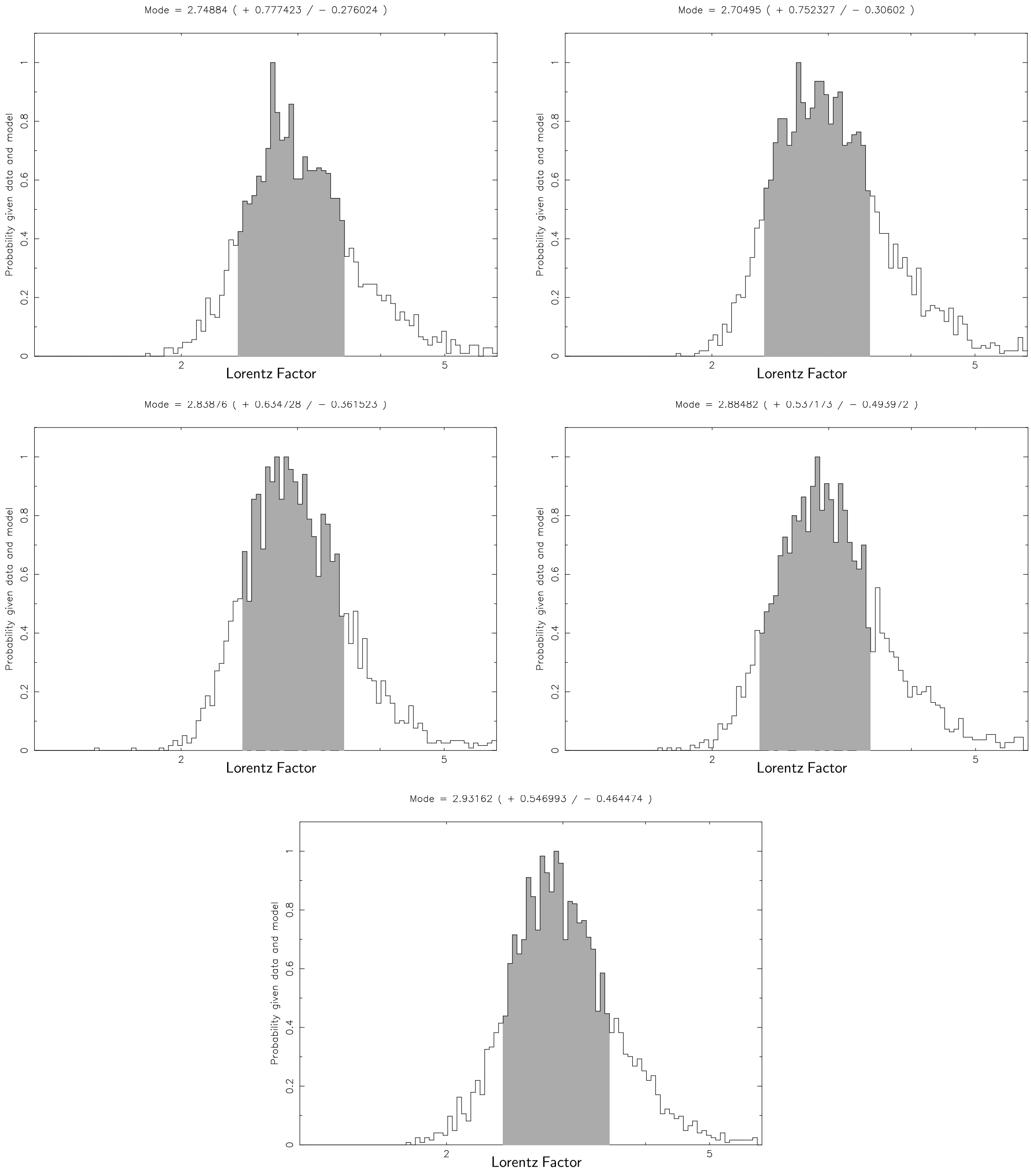

Figure 5.10: Posterior probability distributions of the Lorentz factor, γ, found for five different random seeds. These probability distributions are asymmetric. The value of γ used was the average of the modes of the distributions.

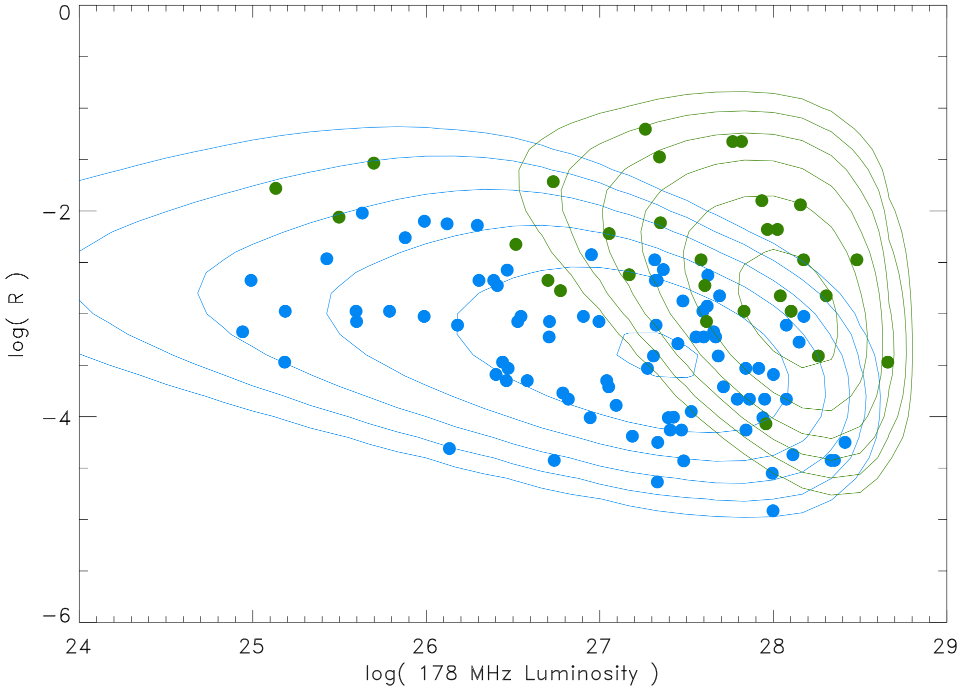

Figure 5.11: Core-to-lobe flux density ratio, R_{interp}, plotted against logarithmic 178 MHz rest-frame luminosity for the 3CRR radio galaxies (blue points) and quasars (green points). The blue and green contours show the maximum likelihood regions of the plot according to Equation 5.27 for radio galaxies and quasars respectively. The contour levels are $K\times$ [1, 2, 4, 8, 16, 32], where K is a constant normalised by the number of sources for each class.

The Lorentz factor is measured as $\gamma = 2.82$, which is significantly lower than the values given in the majority of the literature; Jackson & Wall (1999) use a value of $\gamma = 8.5$, while Cohen et al. (2007b) and Kellermann et al. (2008) find from proper motion studies that while most Lorentz factors are lower, values of up to $\gamma \sim 30$ are seen. To investigate the effect of a significantly higher Lorentz factor on the distribution of jet angles for the Molonglo sample, a second set of fitting was carried out (Section 5.8.2) with γ fixed at 20; the free parameters fit to the 3C sub-sample are shown in Table 5.4. The slope of the R_{interp}– $L_{178\mathrm{MHz}}$ relation with the Lorentz factor fixed is -0.18, which is slightly closer to the value of Blundell et al. (1999). The values of $\gamma = 2.82$ and $\gamma = 20$ are expected to be approximately the higher and lower bounds of expected values.

Parameter	Description	Fitted value	Error
A	Constant of the R_{interp}– $L_{178\mathrm{MHz}}$ relation	3.394	0.053
B	Slope of the R_{interp}– $L_{178\mathrm{MHz}}$ relation	-0.1818	0.0019
C	Scatter on the R_{interp}– $L_{178\mathrm{MHz}}$ relation	0.5093	0.0144
γ	Lorentz factor	Fixed at 20	

Table 5.4: The fitted values of the parameters of Equation 5.22, with γ fixed at a value of 20.

5.7 *Fitting the Jet Angles of the Molonglo Sub-sample*

The radio SEDs of the Molonglo sub-sample of quasars are fitted with a two-component model of a flat-spectrum core and an extended lobe given by the double power law of Equation 5.2. In this case, the R_{interp}– $L_{178\mathrm{MHz}}$ relation of Equation 5.22 is used within the Bayesian model to directly output a jet angle. Rather than the previous set of free parameters, which consisted of the high-frequency spectral index (α_{high}), break frequency (ν_{break}), flux density at the break frequency (S_{norm}) and core flux density (S_{core}) as free parameters, this model replaces the core flux density with the jet angle, θ. Within the Bayesian model, θ is used to calculate the core flux density, which is then fit to the observed SED, together with the total flux density.

The overall chi-squared of the fit to the SED is

$$\chi_{\mathrm{tot}}{}^2 = \sum_i \frac{S_{\mathrm{tot}\,i}{}^2 - S_{\mathrm{model}\,i}{}^2}{\mathrm{E}_i{}^2} \tag{5.28}$$

where $S_{\mathrm{tot}\,i}$ is the total measured flux density at each frequency i, with error $\mathrm{E_i}$ and

$$S_{\mathrm{model}\,i} = S_{\mathrm{core}\,i} + S_{\mathrm{lobe}\,i} \ . \tag{5.29}$$

If there were a single fitted value of R_{interp}, then

$$S_{\mathrm{core}} = R_{\mathrm{interp}} S_{\mathrm{interp}} \ . \tag{5.30}$$

where S_{interp} is the interpolated flux density at rest frame 10 GHz, assuming a low-frequency spectral index of 0.5.

Modifying this equation to account for the probability distribution in $R_{\rm interp}$ rather than a single value

$$S_{\rm core} = \int_{R_{{\rm interp}_{\rm min}}}^{R_{{\rm interp}_{\rm max}}} R_{\rm interp} \frac{{\rm dP}}{{\rm d}R_{\rm interp}} S_{\rm interp} {\rm d}R_{\rm interp} \tag{5.31}$$

where

$$\frac{{\rm dP}}{{\rm d}R_{\rm interp}} = \frac{{\rm dP}}{{\rm d}\log R_{\rm interp}} \frac{{\rm d}\log R_{\rm interp}}{{\rm d}R_{\rm interp}} \ . \tag{5.32}$$

For this sample of Molonglo quasars

$$\frac{{\rm dP}}{{\rm d}\log R_{\rm interp}} = \frac{1}{\sqrt{2\pi}C} e^{-\frac{(\log R_{\rm interp} - ((A \log L_{178} + B) + \log f(\theta,\gamma)))^2}{2C^2}} \tag{5.33}$$

and therefore

$$\frac{{\rm dP}}{{\rm d}R_{\rm interp}} = \frac{1}{\sqrt{2\pi}C} e^{-\frac{(\log R_{\rm interp} - ((A \log L_{178} + B) + \log f(\theta,\gamma)))^2}{2C^2}} \times \frac{1}{R_{\rm interp} \ln 10} \ . \tag{5.34}$$

Now the core flux density is given by

$$S_{\rm core} = \int_{R_{{\rm interp}_{\rm min}}}^{R_{{\rm interp}_{\rm max}}} \frac{1}{\ln 10} \frac{1}{\sqrt{2\pi}C} e^{-\frac{(\log R_{\rm interp} - ((A \log L_{178} + B) + \log f(\theta,\gamma)))^2}{2C^2}} S_{\rm interp} {\rm d}R_{\rm interp} \ . \tag{5.35}$$

Equation 5.35 was integrated computationally within *BayeSys3*.

$\log L_{178}$ is calculated from $S_{\rm lobe\,178}$ using the relation between flux density and luminosity from Peacock (1999) (Equation 5.36), noting that $S_{\rm lobe\,178}$ is very close to $S_{\rm tot\,178}$ as the core flux density is negligible at these frequencies. The observed flux density is linked to the emitted luminosity of a source by an equation which takes into account not only the luminosity distance of the source, but also that the waveband is a factor of $(1+z)$ narrower in the observed frame than in the emitted frame:

$$S_{178} = \frac{L_{178(1+z)}(1+z)}{D_{\rm lum}^2} \ . \tag{5.36}$$

The K-correction accounts for that fact that the flux density varies with frequency, and so for quasars with spectral indices $\alpha < 0$ then the flux density at the observed frequency is less than that at the emitted frequency, and so

$$L_{178} = L_{178(1+z)} \frac{S_{178}}{S_{178(1+z)}} \ . \tag{5.37}$$

Substituting Equation 5.36 into Equation 5.37 then

$$L_{178} = \frac{S_{178}^{2}}{S_{178(1+z)}} \frac{D_{\mathrm{lum}}^{2}}{(1+z)} \; . \tag{5.38}$$

The luminosity distance is calculated within the Bayesian fitting routine using the equations of Pen (1999).

5.7.1 *Stability of the fits*

Figure 5.12 shows the stability of the Bayesian fitting process of the SEDs of two random quasars with a change of Bayesian seed; these fits are extremely stable.

There is a very close linear correlation between the break frequency of the source and the normalisation factor, which is expected as the normalisation factor is defined to be simply the flux density of the source at the break frequency.

The sine of the jet angle correlates with all other parameters for MRC0450-221 (Figure 5.12(top)): as the spectral index of the high frequency part of the power law becomes steeper, the break frequency moves to lower frequencies (the SED fit becoming more rounded) and so the normalisation factor increases. This gives a larger lobe flux density, and hence a smaller R_{interp} value and a greater jet angle to the line of sight. MRC1114-220 does not show any significant correlations between the sine of the jet angle and any of the other parameters, possibly as there appears to be greater scatter in the total flux points, and so the lobe flux component is less well fixed.

Figure 5.13 shows the variation in the fitted sine jet angle parameter with ten different random seeds for the same quasars. The difference between the dispersion of the posterior angles and the average dispersion of the angle for each seed individually was used to determine an error on the output jet angle due to the random seed. This error was added in quadrature to the individual errors on the sine of the jet angle fit to each source.

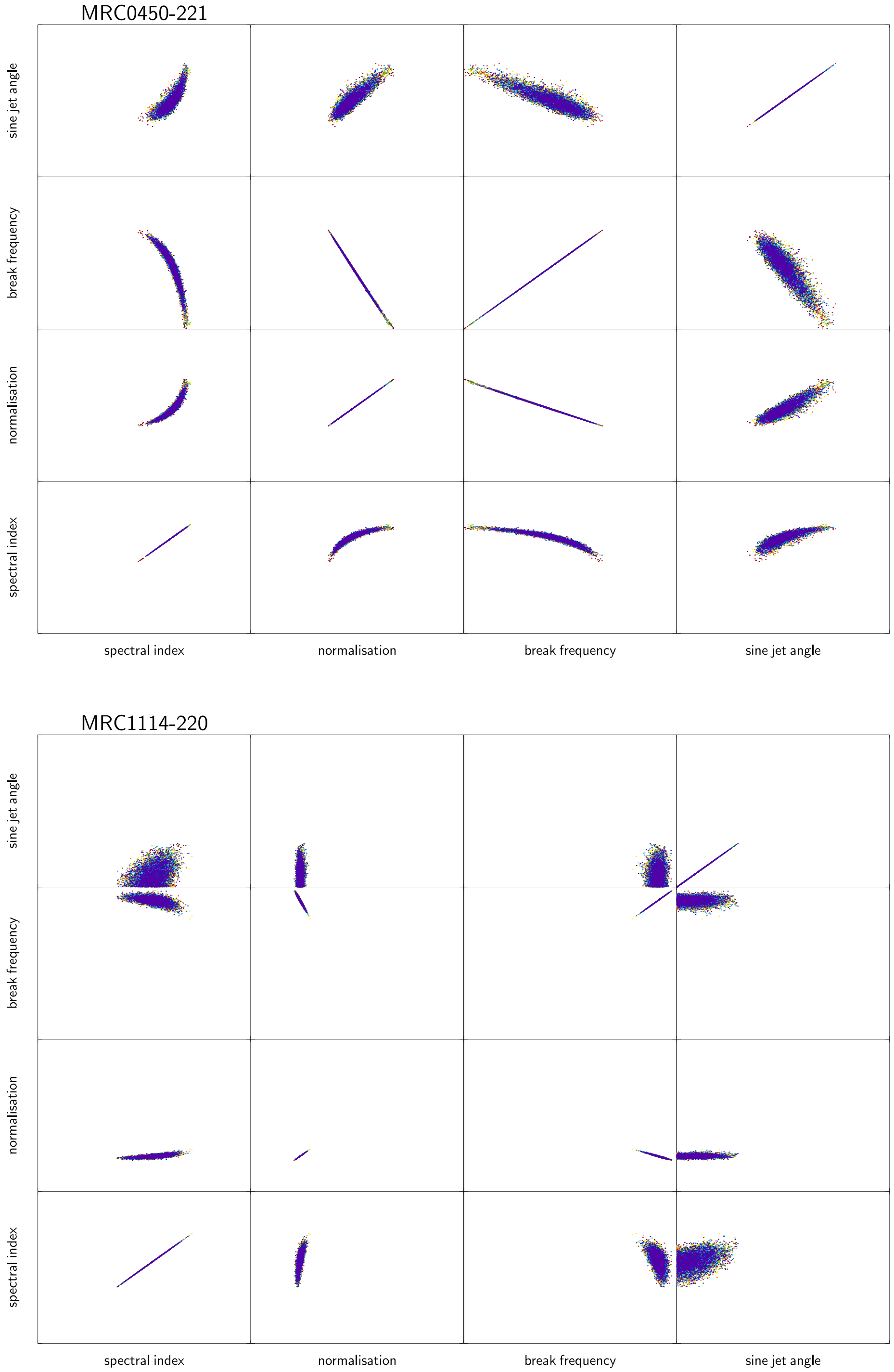

Figure 5.12: A plot of the correlations between all parameters for MRC0450-221 (top) and MRC1114-220 (bottom) for ten different random seeds in the Bayesian fit, plotted in different colours. The parameters are the high-frequency spectral index, the normalisation factor, the break frequency and the sine of the jet inclination angle. In all cases, the probability distributions converge on the same regions. Correlations between derived parameters are more prevalent in the top example as the flux densities of the SED fluctuate less from a smooth fit for MRC0450-221.

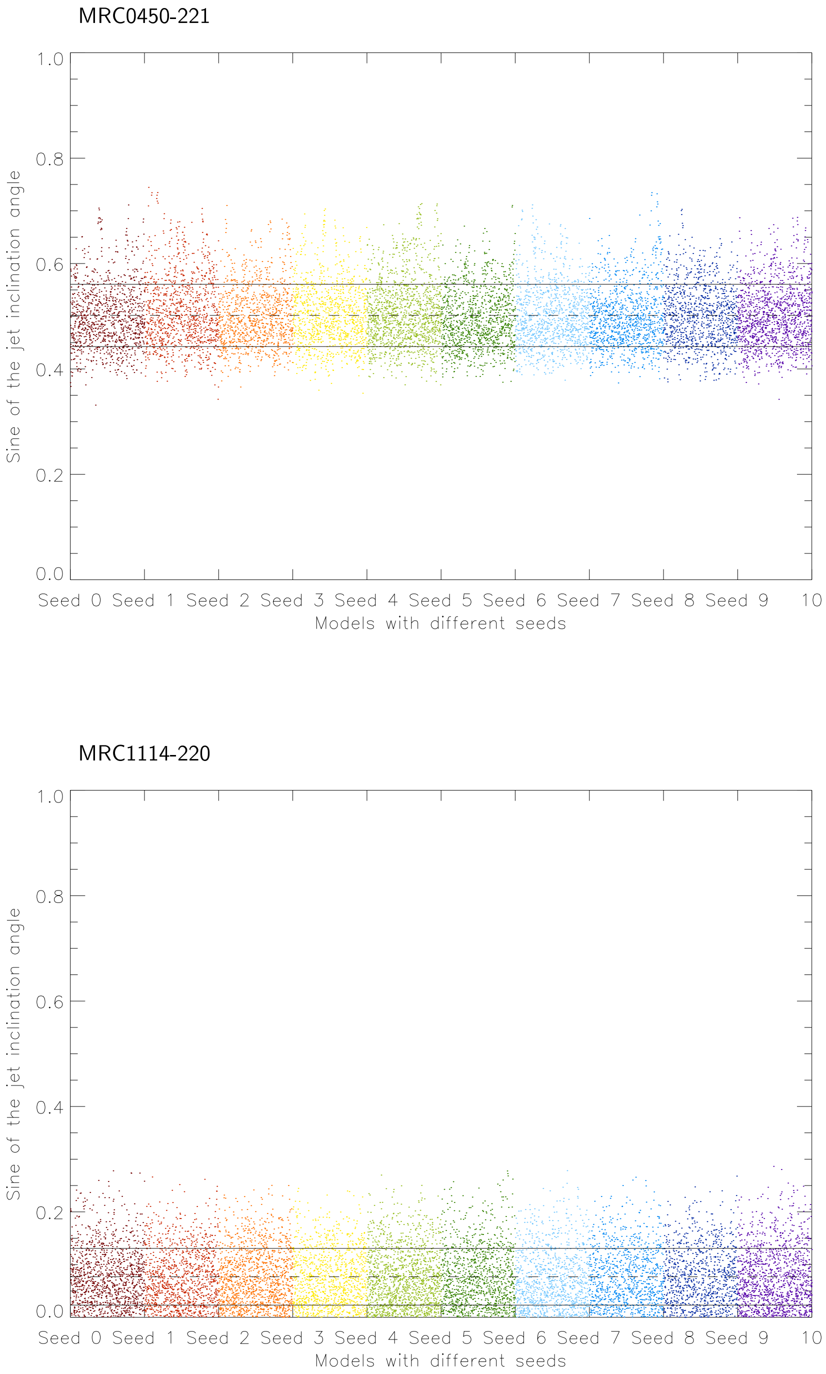

Figure 5.13: A plot to show the scatter in jet inclination angles found for ten different Bayesian random seeds for two sample quasars. The error on jet angle due to the choice of seed in the Bayesian fitting was found by calculating the overall standard deviation for all ten random seeds, and subtracting the average standard deviation for one random seed. This error was added in quadrature with the error from each Bayesian fit.

5.8 *Results of the SED Fitting*

5.8.1 *SED fits with* $\gamma = 2.8$

The fitted SEDs and the posterior distributions for the sine of the jet inclination angles, with a Lorentz factor of $\gamma = 2.8$, are presented in Figure 5.14.

5.8.1.1 *Notes on individual SEDs*

MRC0327-241: Above approximately 100 MHz, the core component dominates the total flux density of this object. The spread in flux densities over this region is likely to be governed by time variability of the core component.

The break frequency appears to be lower than observed 74 MHz, though this may be simply that the lobe flux is weak and not well fit. The break frequency was assumed to be at 10 MHz in the quasar rest-frame, in the same way as for the 3CRR quasars which did not have constrained break frequencies.

The lobe flux density is less than 0.95 Jy at observed 408 MHz, and so this quasar is included in the sample as a result of the core.

MRC0346-279: All flux densities for this object from 74 MHz to 41 GHz lie in a narrow band which covers only a factor of 2 in flux density. The lobe component is very weak for this quasar. The break frequency appears to be lower than observed 74 MHz, and so the break frequency was assumed to be at 10 MHz in the quasar rest-frame.

The lobe flux density is less than 0.95 Jy at observed 408 MHz, and so this quasar is included in the sample as a result of the core.

MRC0413-210: The break frequency appears to be lower than observed 74 MHz, and so the break frequency was assumed to be at 10 MHz in the quasar rest-frame.

MRC0430-278: The core flux density is not well fitted; the measured core flux density is proscribed by the fitting of the total flux density. It is likely that the core flux density measurement was contaminated by lobe flux, as this source is a very close triple (see Chapter 4). This discrepancy in the fitting process leads to a wide spread on the posterior probabil-

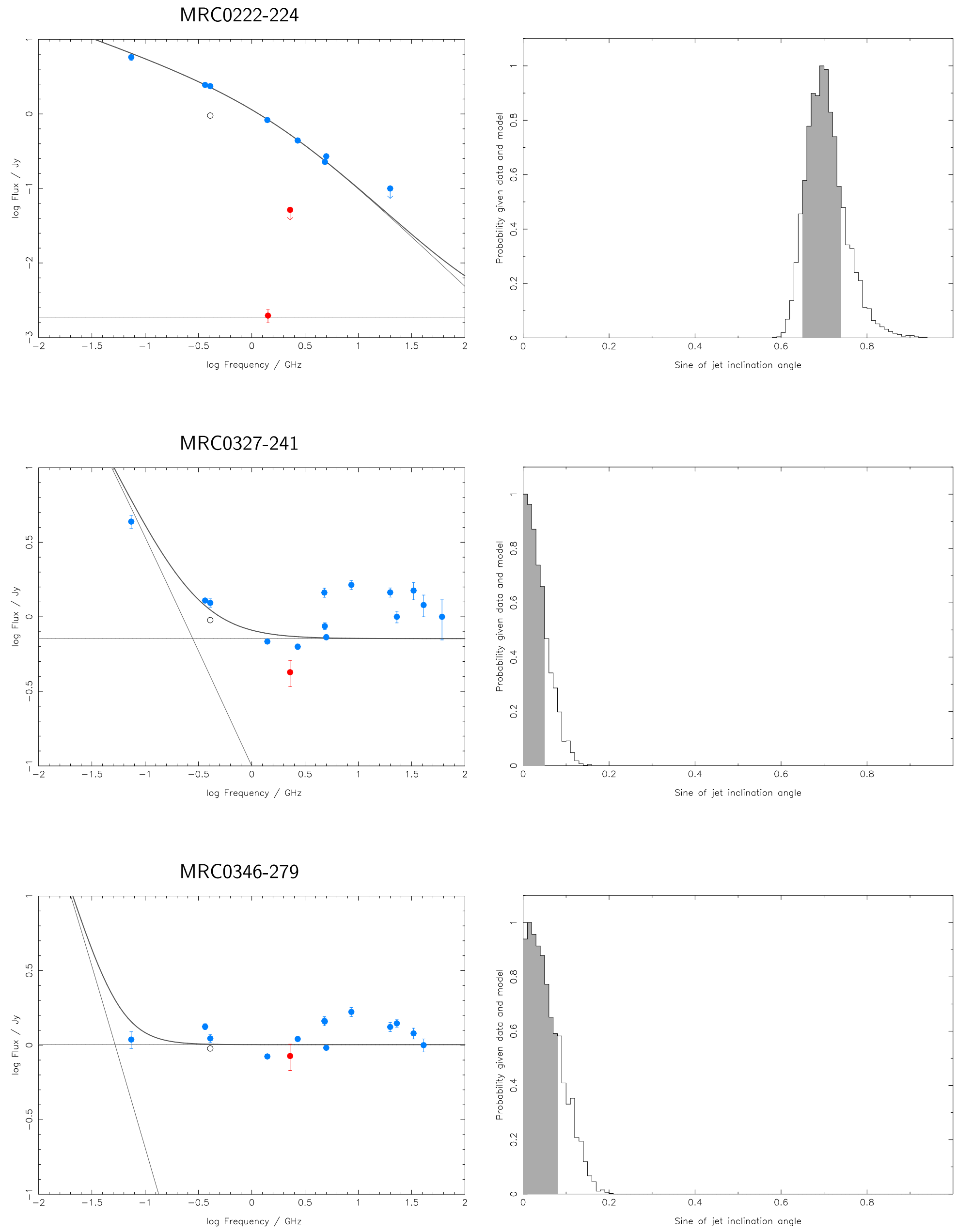

Figure 5.14: Fitted radio spectral energy distributions for the Molonglo quasar sub-sample, assuming a Lorentz factor $\gamma = 2.82$, as fitted to the 3C sample. The blue points are integrated flux densities, and the red points are core flux densities. The bold line is the overall fit to the integrated flux density SED, the upper narrow line gives the lobe emission component, and the lower narrow line is the fitted constant core component. The small white-filled circle shows the selection flux density and frequency of the Molonglo sample of radio sources. The probability distribution for the jet angle is shown in the right-hand plots, with shaded area marking 1-σ errors.

MRC0413-210

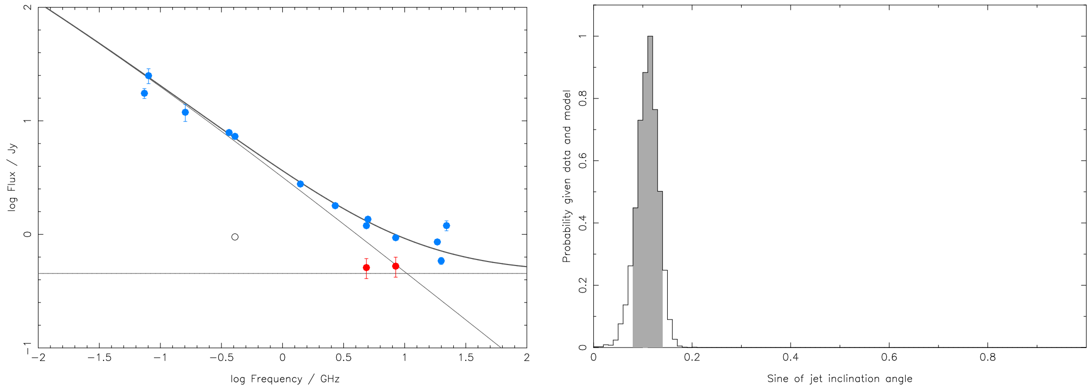

MRC0413-296

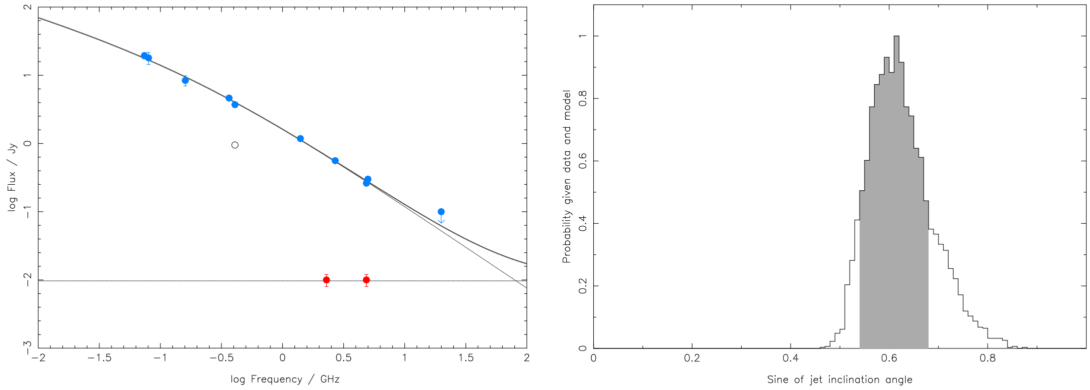

MRC0430-278

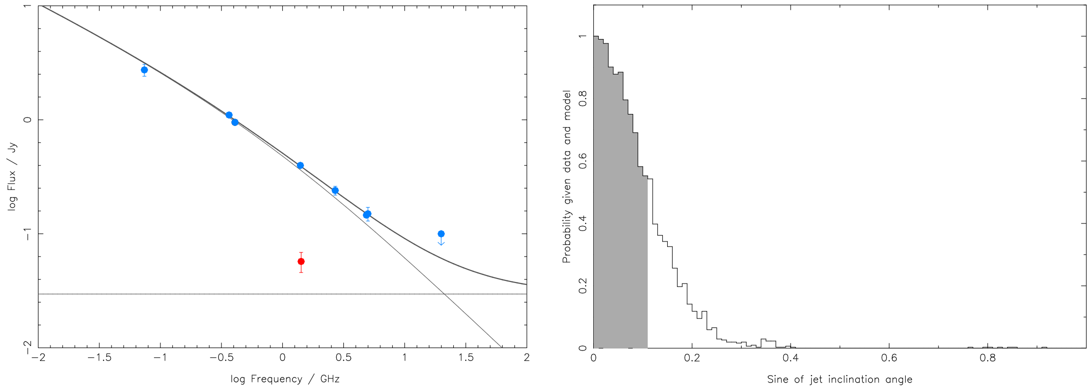

MRC0437-244

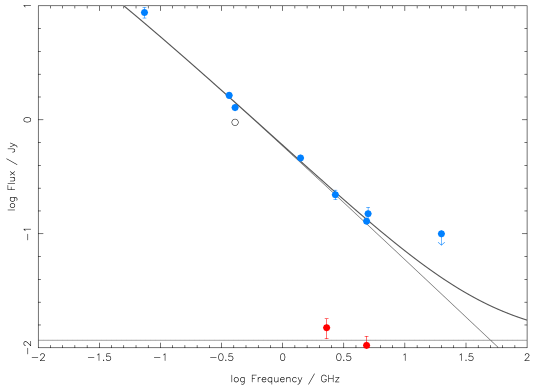

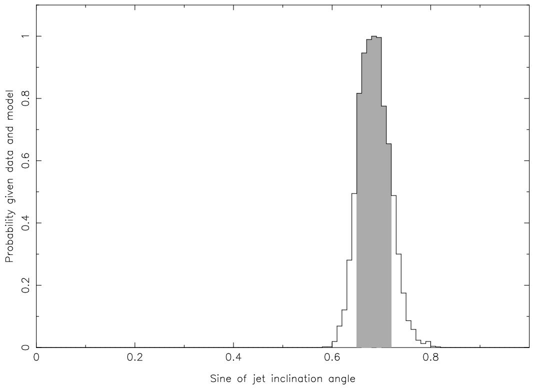

MRC0450-221

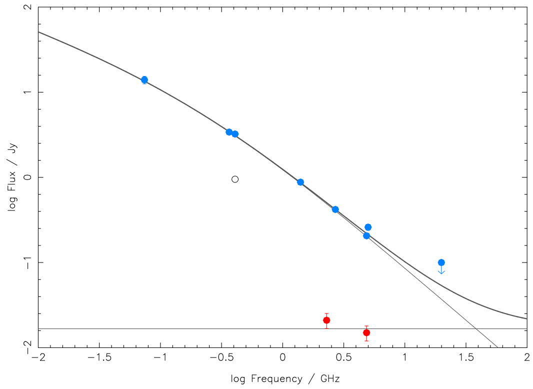

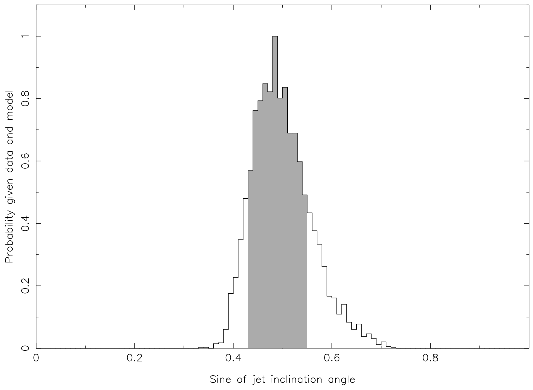

MRC0549-213

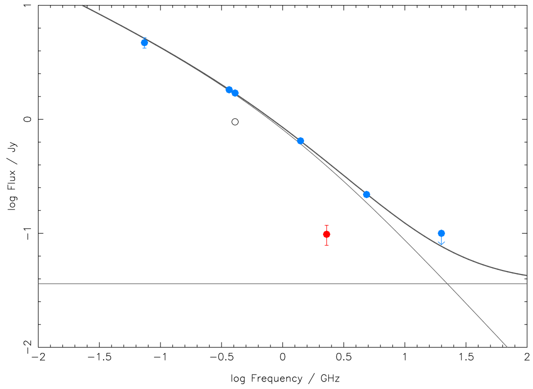

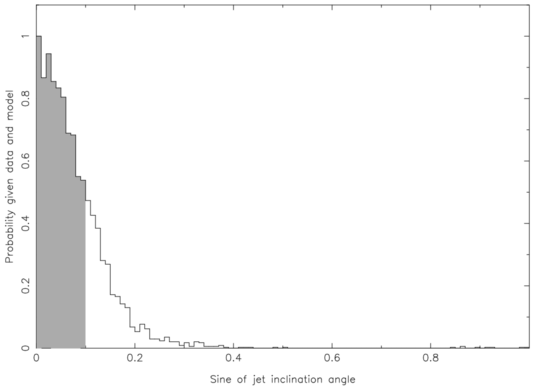

MRC1019-227

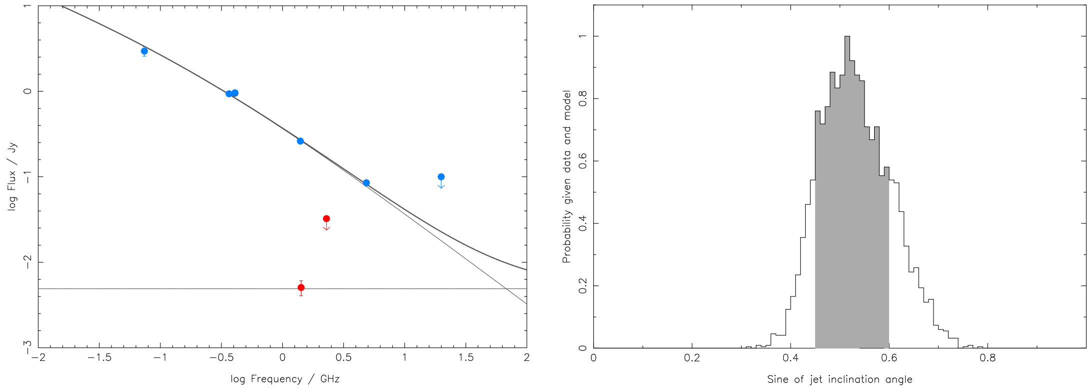

MRC1114-220

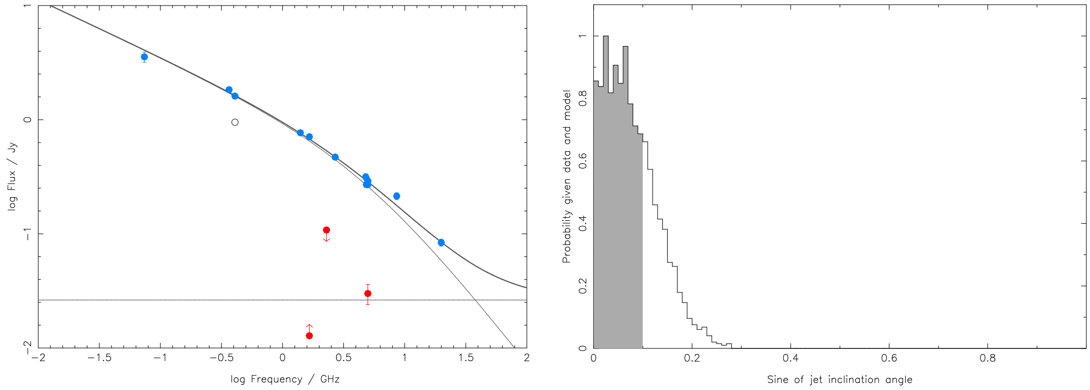

MRC1208-277

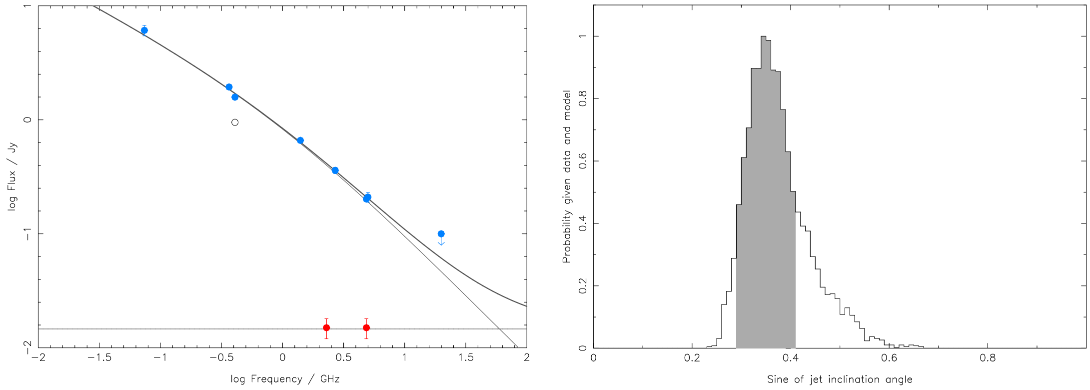

MRC1217-209

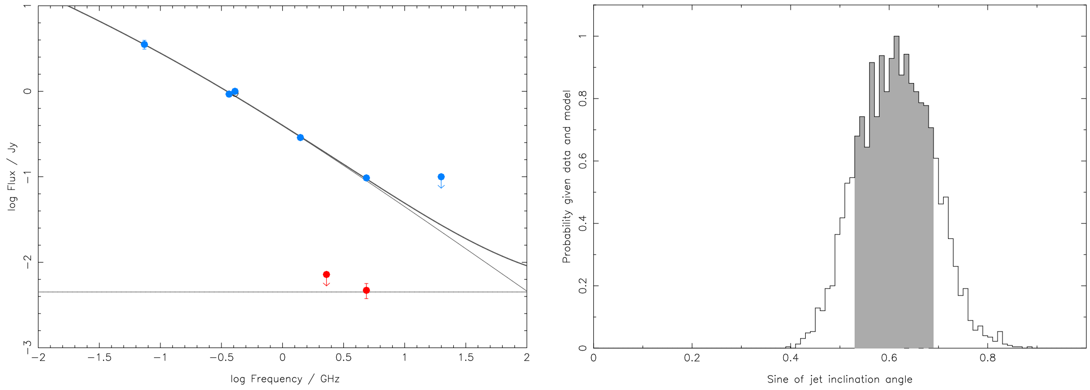

MRC1222-293

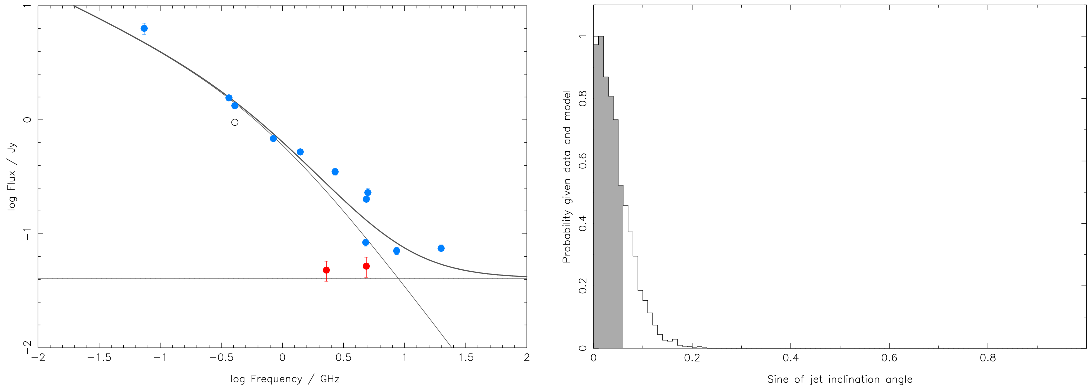

MRC1301-251

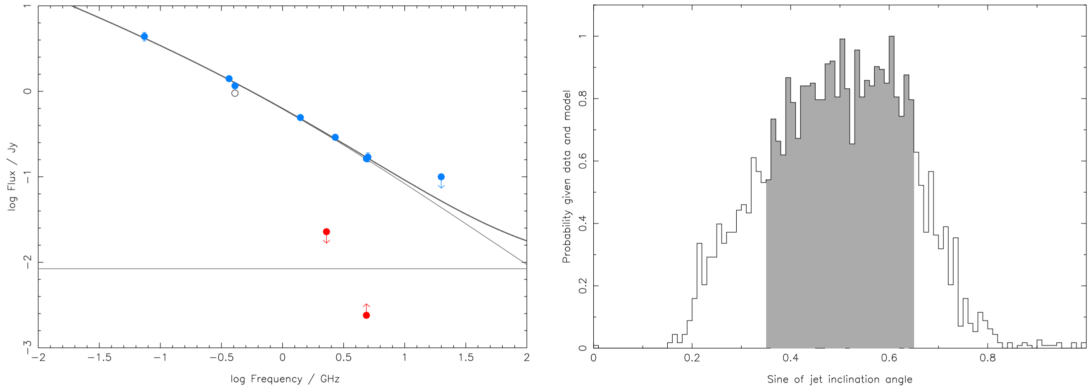

MRC1349-265

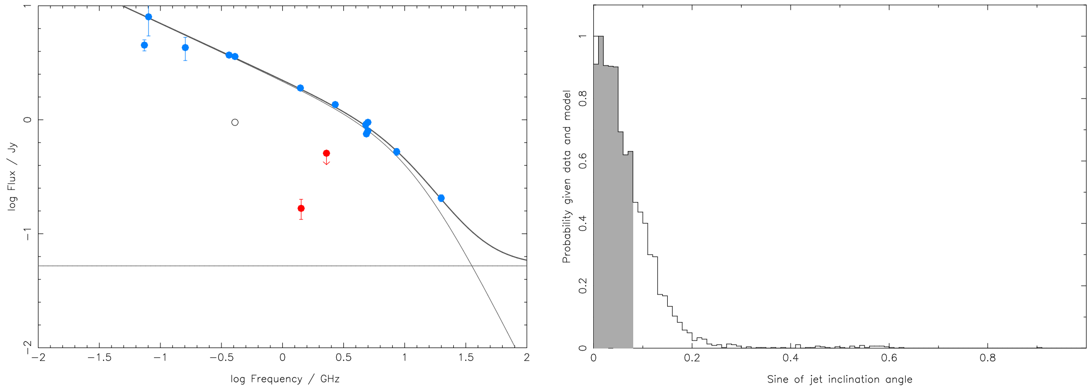

MRC1355-215

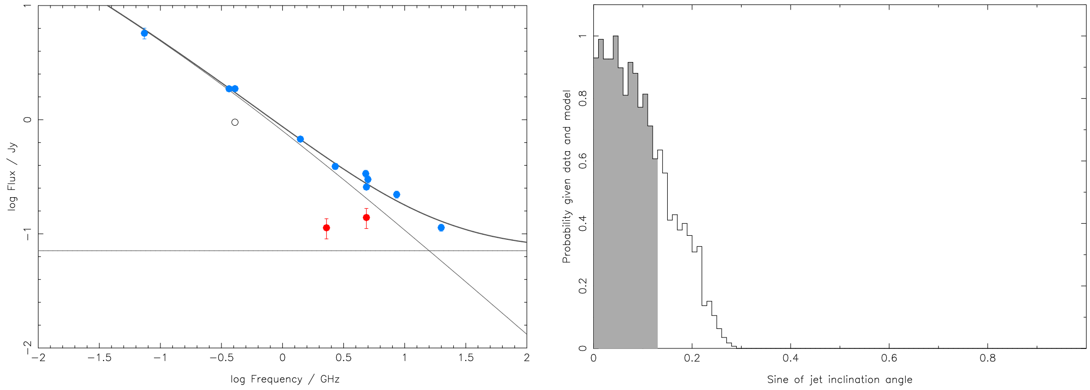

MRC1355-236

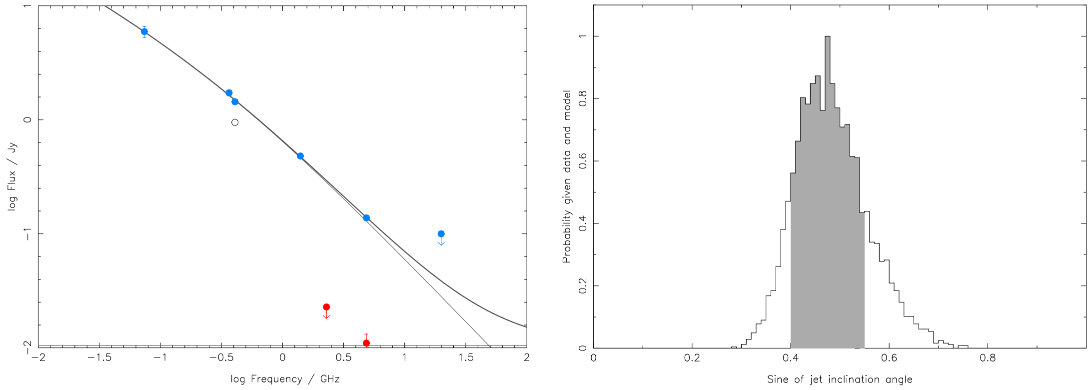

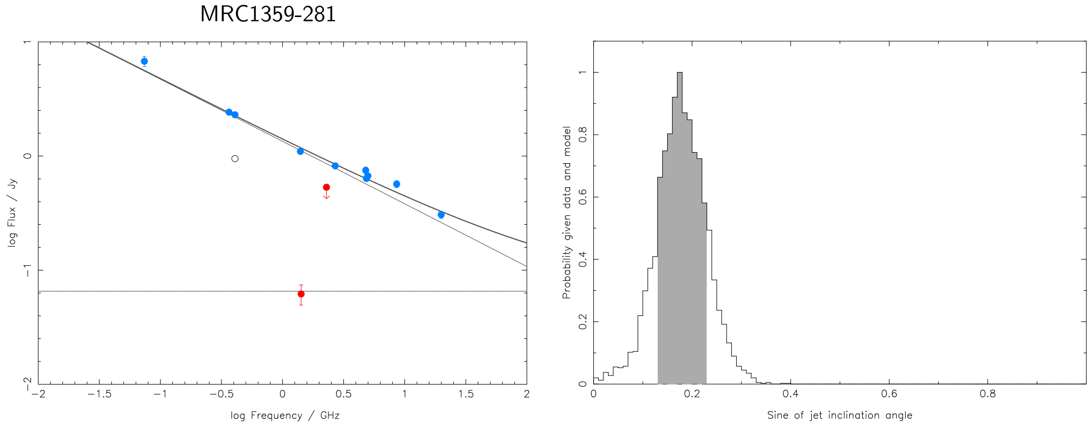

ity distribution of the sine of the jet angle.

MRC0437-244: The break frequency appears to be lower than observed 74 MHz, and so the break frequency was assumed to be at 10 MHz in the quasar rest-frame.

MRC0549-213: In a similar way to MRC0430-278, the measured core flux density of this quasar is not well fitted; it is likely that this flux density measurement was contaminated by lobe flux.

MRC1019-227: The 0.95 Jy at 408 MHz point indicating the selection flux density of the Molonglo sample is obscured in Figure 5.14 by the total flux density point. This source is on the edge of the selection flux density for the Molonglo sample, and considering the errors on the fitted lobe and core flux densities, it cannot be ruled out that this source was boosted into the sample by the core flux density.

MRC1217-209: This source has a break frequency which is just constrained at $\sim$ 18 MHz. The 0.95 Jy at 408 MHz point indicating the selection flux density of the Molonglo sample is partially obscured in Figure 5.14 by the total flux density point. This source is on the edge of the selection flux density for the Molonglo sample, and considering the errors on the fitted lobe and core flux densities, it cannot be ruled out that this source was boosted into the sample by the core flux density.

MRC1349-265: The measured core flux densities are not well fitted, and are inconsistent with the total flux densities. The core flux density at 2.29 GHz is an upper limit; the core flux density at 1.4 GHz was measured in Chapter 4, and it is likely that this value is contaminated by lobe flux, as this source is so close as to not have distinct radio components.

MRC1359-281: The break frequency appears to be lower than observed 74 MHz, and so the break frequency was assumed to be at 10 MHz in the quasar rest-frame.

5.8.1.2 *Discussion*

The fitted jet angles with their errors and R_{interp} values are presented in Table 5.5. These vary between 2° and 44°, which is consistent with the opening angle expected of powerful FRII sources (e.g. Lawrence 1991). This critical angle of $\sim 45^\circ$ for the Molonglo sample can be compared to the critical angle of 28° fitted to the 3CRR sample, reflecting the lower jet powers of the 3CRR sample; this is consistent with the receding torus model.

Examining the SED plots, there are two quasars which clearly do not have lobe flux densities larger than the flux limit of the survey, 0.95 Jy at 408 MHz, and have therefore been boosted into the Molonglo sample of radio sources by virtue of their strong cores; these are MRC0327-241 and MRC0346-279. Additionally, there are two sources (MRC1019-227 and MRC1217-209) whose cores, while 2 – 3 orders of magnitude weaker than the lobe emission at the sample selection frequency, may have been vital in their selection; however, the errors on the core and lobe fluxes are too large to determine with certainty whether this is the case.

It is worrying that while only two sources have been found to be boosted into this sub-sample of quasars, there are eight sources with fitted jet angles less than 5°. This effect is probably caused in part by the probability distributions "piling up" against the 0° constraint; however, this effect should not cause such a large bunching of angles. This overdensity at low angles is an indication that the method of calibrating the jet angles using the 3CRR sample may be afflicted with biases which have not been properly considered.

The fitted R_{interp} values for the Molonglo sub-sample are compared to values from the literature in Figure 5.15. There is a good correlation, as expected, though the R_{10GHz} values from the literature are larger than the fitted R_{interp} values by a factor of ~ 10 (see Fig-

Quasar		z	$\log L_{178\mathrm{MHz}}$	Jet angles	R_{interp}	R_{lit}	Type
1	MRC0222-224	1.603	27.54	$44\,^{\circ} \pm^{4}_{5}$	0.0020	<0.37	CSS
2	MRC0327-241	0.895	26.77	$2\,^{\circ} \pm^{2}_{2}$	0.068	>1.0	
3	MRC0346-279	0.989	26.46	$3\,^{\circ} \pm^{2}_{3}$	0.10	>5.0	
4	MRC0413-210	0.807	27.42	$6\,^{\circ} \pm^{3}_{2}$	0.043	0.71	
5	MRC0413-296	1.614	28.07	$38\,^{\circ} \pm^{5}_{5}$	0.0024	0.031	
6	MRC0430-278	1.633	27.18	$4\,^{\circ} \pm^{2}_{4}$	0.055		CSS
7	MRC0437-244	0.834	26.92	$43\,^{\circ} \pm^{4}_{4}$	0.0031	0.098	
8	MRC0450-221	0.900	27.40	$29\,^{\circ} \pm^{4}_{5}$	0.0072	0.086	
9	MRC0549-213	2.245	27.74	$4\,^{\circ} \pm^{2}_{4}$	0.042	<0.55	
10	MRC1019-227	1.542	27.24	$32\,^{\circ} \pm^{6}_{6}$	0.0062		CSS
11	MRC1114-220	2.286	27.66	$4\,^{\circ} \pm^{2}_{4}$	0.045		CSS
12	MRC1208-277	0.828	26.98	$21\,^{\circ} \pm^{3}_{5}$	0.019	0.088	
13	MRC1217-209	0.814	26.46	$38\,^{\circ} \pm^{6}_{6}$	0.0051	0.057	
14	MRC1222-293	0.816	26.64	$2\,^{\circ} \pm^{2}_{2}$	0.068	0.38	
15	MRC1301-251	0.952	26.78	$30\,^{\circ} \pm^{12}_{9}$	0.0046	0.020	
16	MRC1349-265	0.924	27.12	$3\,^{\circ} \pm^{2}_{3}$	0.060		CSS
17	MRC1355-215	1.607	27.48	$5\,^{\circ} \pm^{3}_{5}$	0.047	0.84	
18	MRC1355-236	0.832	26.82	$29\,^{\circ} \pm^{5}_{6}$	0.0094	0.098	
19	MRC1359-281	0.802	26.79	$10\,^{\circ} \pm^{4}_{3}$	0.047		CSS

Table 5.5: Median jet angles with errors and R_{interp} values for all Molonglo quasars in the sub-sample, fitted with the $\gamma = 2.8$ model.
Columns 1 and 2: Index and name of the quasars.
Column 3: Redshift.
Column 4: Logarithmic 178 MHz luminosity.
Column 5: Fitted jet angle and errors for the $\gamma = 2.8$ model.
Column 6: Fitted R_{interp} value for the $\gamma = 2.8$ model.
Column 7: The classical values of $R_{10\mathrm{GHz}}$ from the literature (Kapahi et al. 1998a)
Column 8: Note on whether the source is a CSS.

ure 5.1). This is reasonable, as using the total flux density rather than the interpolated low-frequency lobe flux density gives a much smaller lobe flux density in the high-frequency part of the spectrum at which R_{interp} is measured. The smaller lobe flux density leads to a larger overall R_{interp} value.

Figure 5.16 shows the correlation between the fitted R_{interp} values and sines of the jet angles. The linearity of this plot demonstrates that the substitution of the core flux density with the jet angle as a free parameter in the fitting model is reasonable. Some degree of clustering of sources at low jet angles is expected: the density of sources falling in this region is enhanced by the Doppler boosting effect which causes preferential selection of

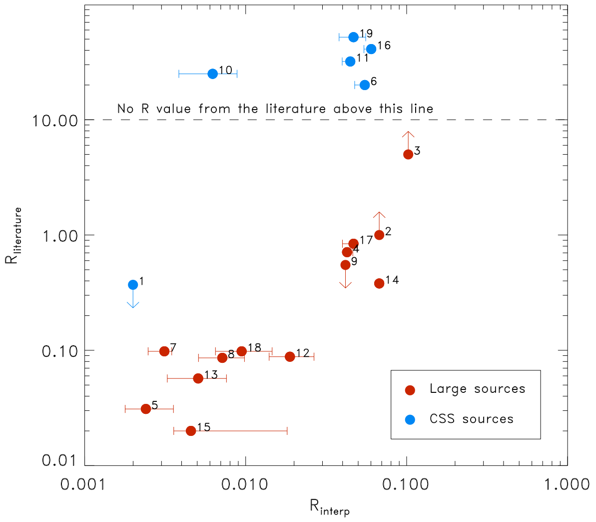

Figure 5.15: $R_{\rm lit}$ from Kapahi et al. (1998a) plotted against the fitted $R_{\rm interp}$ value from the Bayesian analysis with $\gamma = 2.8$, for the Molonglo quasar sub-sample. CSS sources (projected size < 25 kpc) are plotted in blue, and the sources with projected sizes > 25 kpc are plotted in red (note that the name "large sources" refers to projected size). Sources with no measured values in Kapahi et al. (1998a) (these are all CSS sources) are plotted above the dotted line.

low jet angle objects. However, only two sources have clearly been boosted into this sub-sample by their cores, and so the over-density in this region demonstrates that the method of calibrating the jet angles may be unreliable at low angles to the line of sight.

5.8.2 *SED fits with* $\gamma = 20$

The fitted SEDs and the posterior distributions for the sines of the jet angles, with a Lorentz factor fixed at $\gamma = 20$ but otherwise calibrated against the 3CRR sub-sample, are presented in Figure 5.17.

The posterior probability distributions for the $R_{\rm interp}$ values and the core flux densities are well-constrained with single peaks for these fits; however, the posteriors for the sines of the jet angles are in many cases double-peaked, except in cases where the lobe flux is overwhelmingly strong. This small zone of non-zero probability at low disk axis angles comes from a small degeneracy in the high-frequency spectral index and normali-

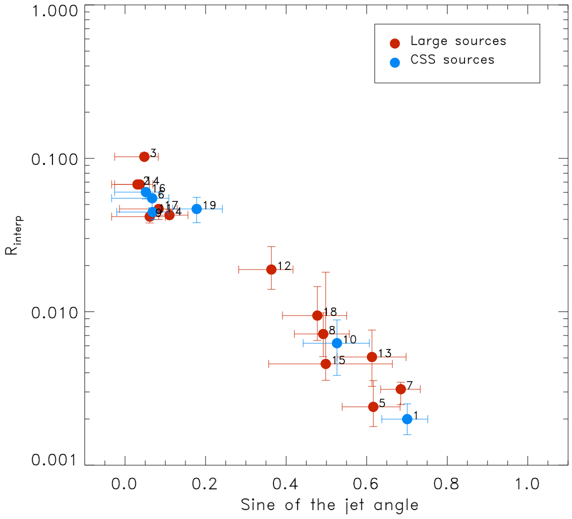

Figure 5.16: Fitted R_{interp} value plotted against the fitted sine of the jet angle for the Molonglo quasar sub-sample, from the analysis with $\gamma = 2.8$. Note that the name "large sources" refers to projected size; these sources have projected sizes > 25 kpc, whilst CSS sources have smaller projected sizes.

sation factor which describe the part of the SED arising from the radio lobe. In most cases, this low-jet-angle possibility represents only a very small fraction of the probability distribution, and is excluded by selecting the median jet angle, and finding the 1-σ errors by selecting the smallest region of parameter space which includes 68% of the probability.

5.8.2.1 *Notes on individual SEDs*

MRC0327-241: The break frequency appears to be lower than observed 74 MHz, and as before, the break frequency was fixed at 10 MHz in the quasar rest-frame.

MRC0346-279: The break frequency does not constrain within the observed range, and so the break frequency was assumed to be at 10 MHz in the quasar rest-frame, as before.

MRC0413-210: The break frequency appears to be lower than observed 74 MHz, and so the break frequency was assumed to be at 10 MHz in the quasar rest-frame.

MRC0430-278: The core flux density is much better fitted with $\gamma = 20$ than in the $\gamma = 2.8$ case.

MRC0222-224

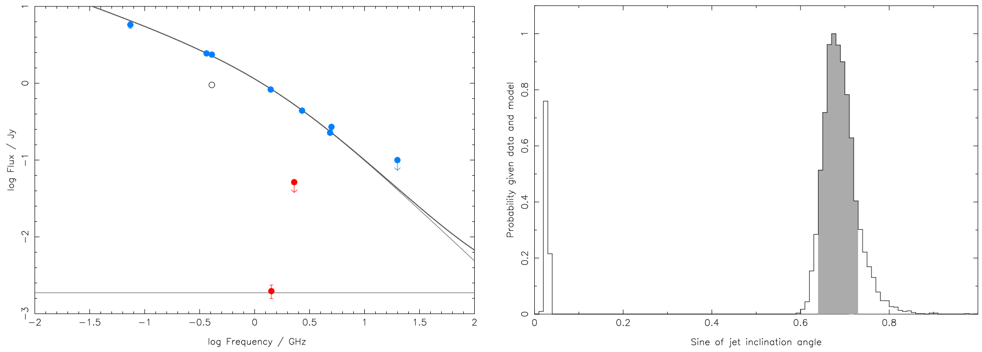

MRC0327-241

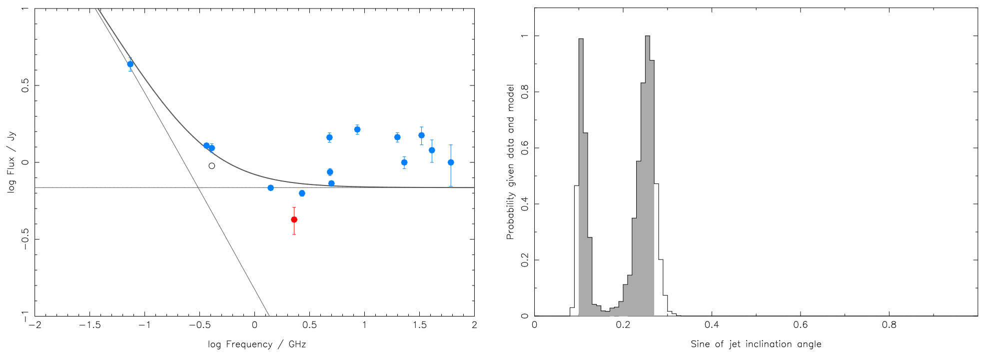

MRC0346-279

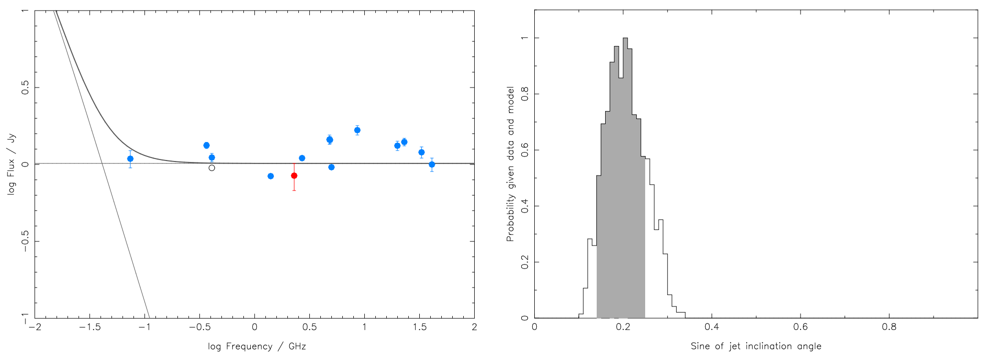

Figure 5.17: Fitted radio spectral energy distributions for the Molonglo quasar sub-sample, assuming a Lorentz factor $\gamma = 20$. The blue points are integrated flux densities, and the red points are core flux densities. The bold line is the overall fit to the integrated flux density SED, the upper narrow line gives the lobe emission, and the lower narrow line is the fitted constant core component. The small white circle shows the selection flux density and frequency of the Molonglo sample of radio sources.The probability distribution for the jet angle is shown in the right-hand plots, with shaded area marking 1-σ errors.

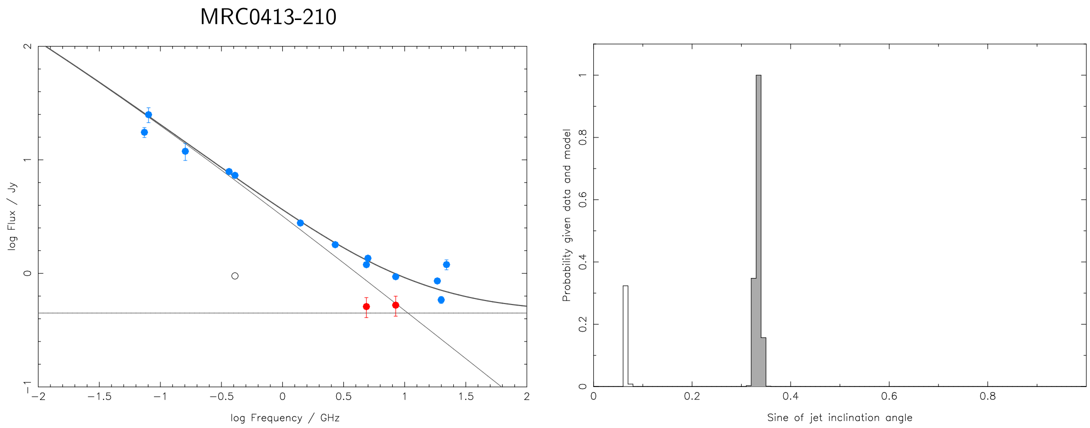

MRC0413-210

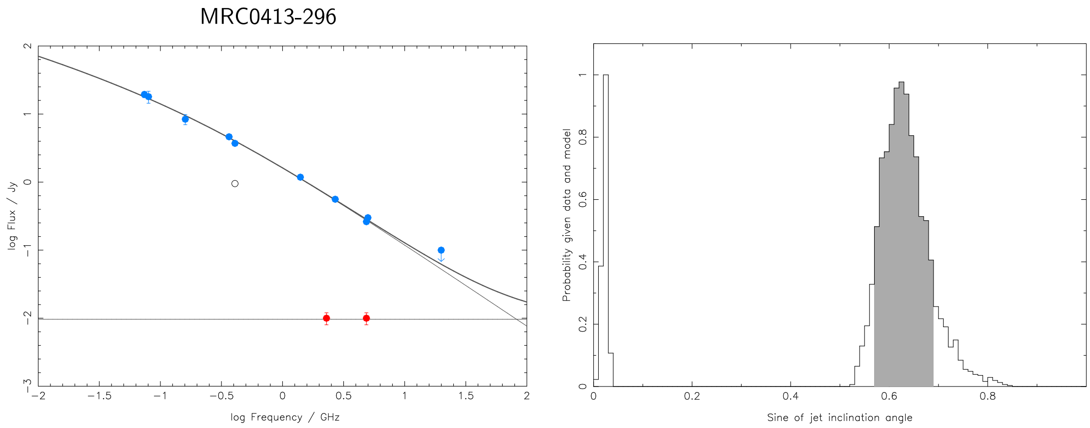

MRC0413-296

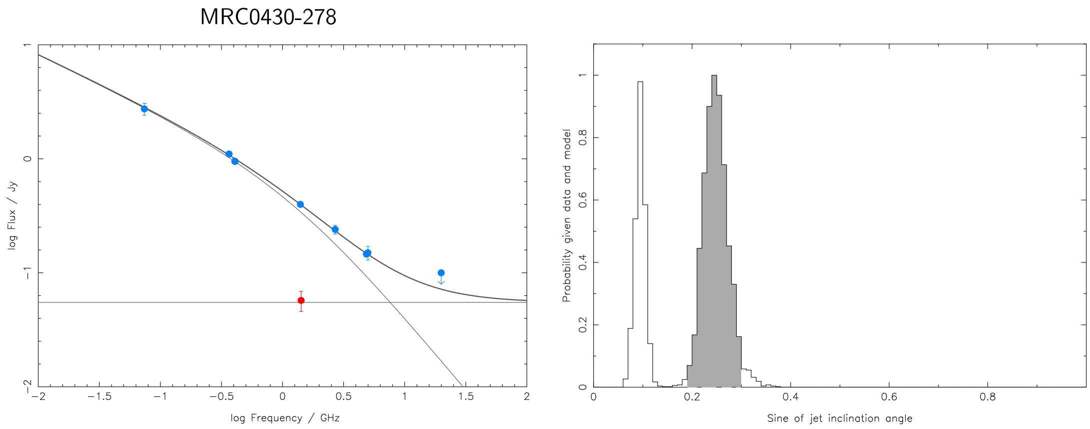

MRC0430-278

MRC0437-244

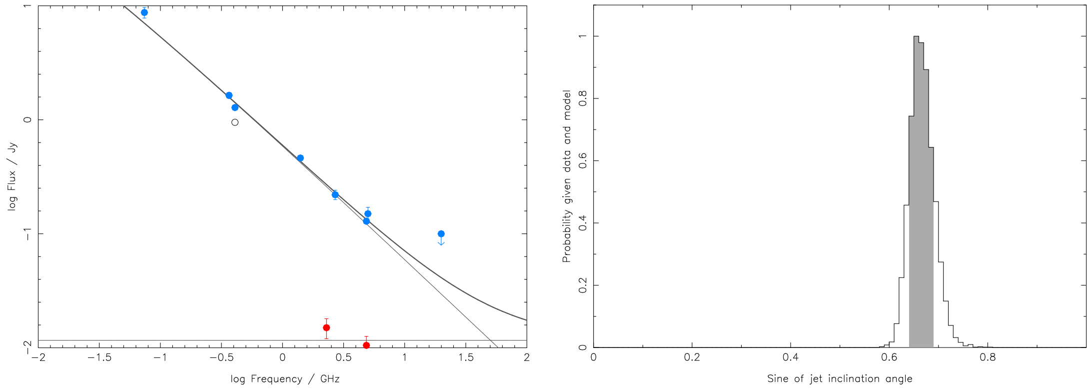

MRC0450-221

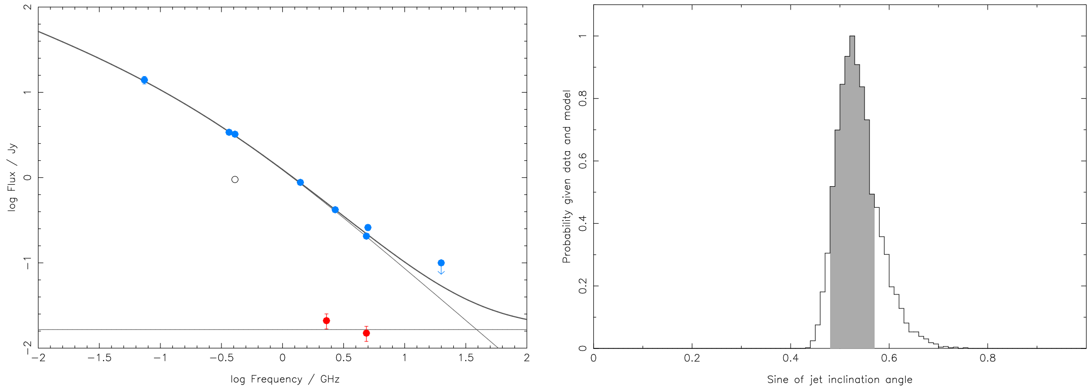

MRC0549-213

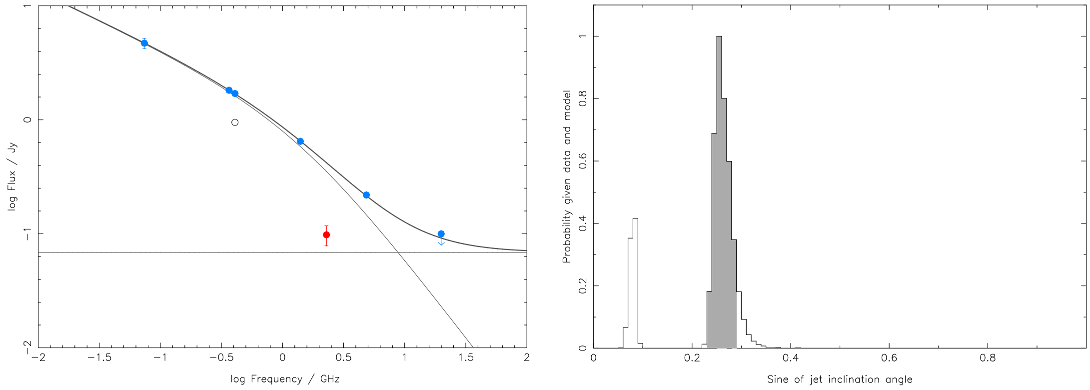

MRC1019-227

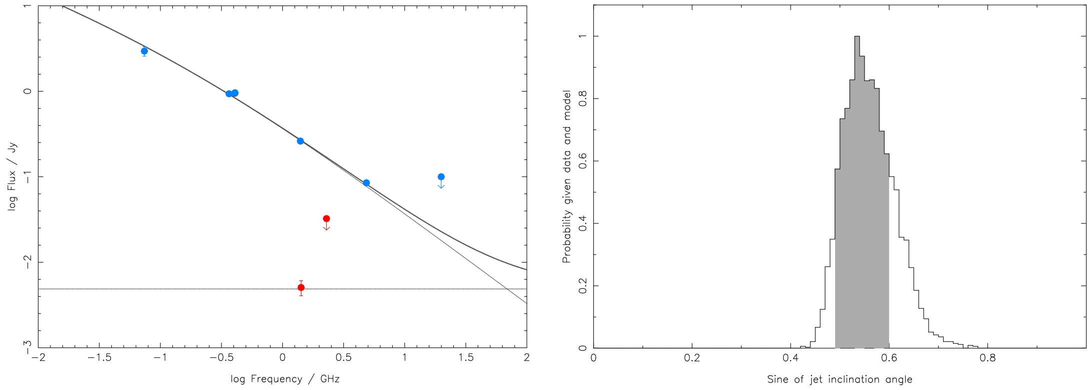

MRC1114-220

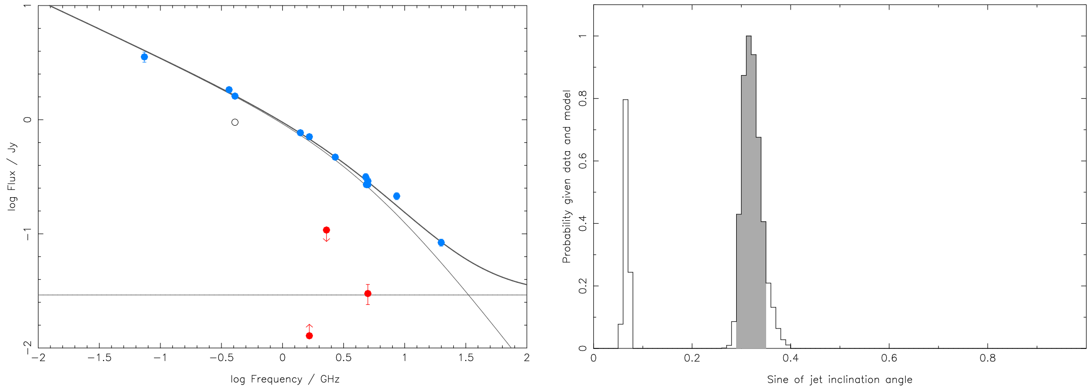

MRC1208-277

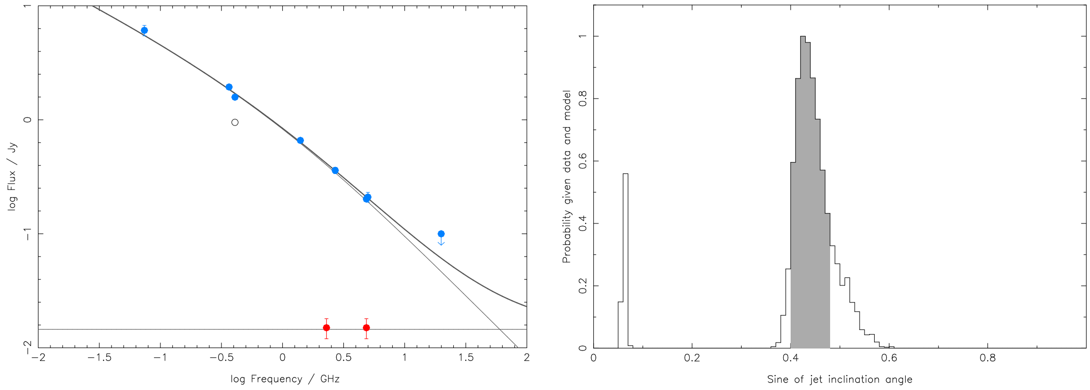

MRC1217-209

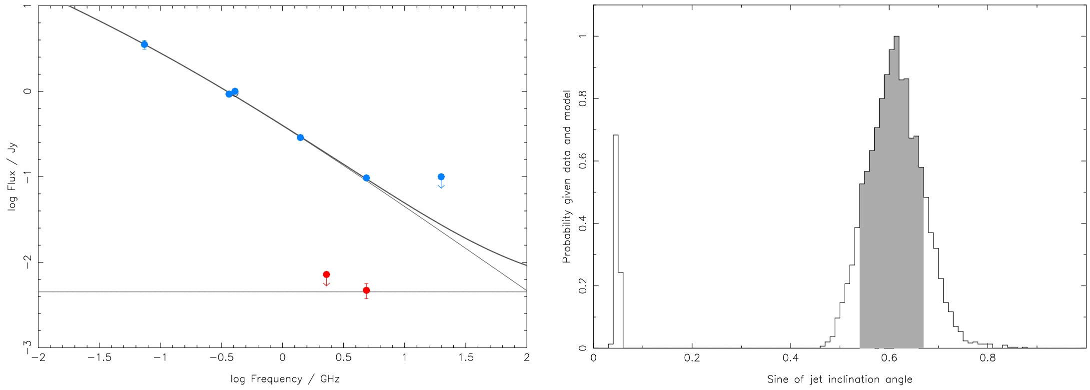

MRC1222-293

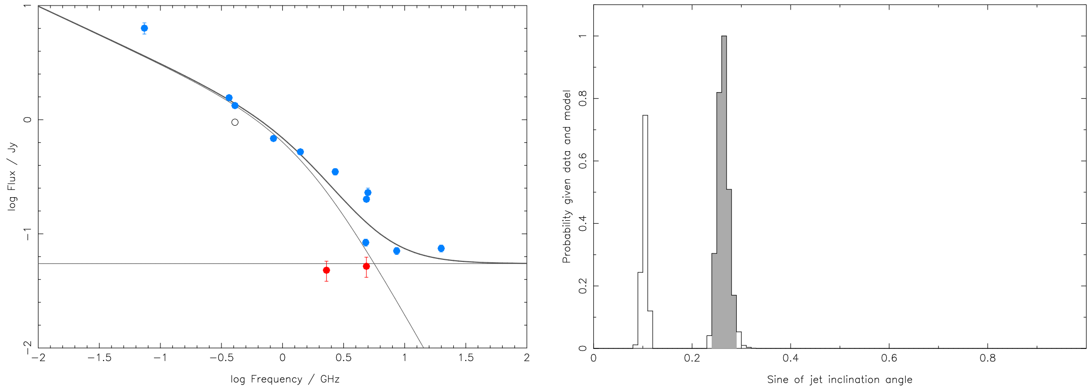

MRC1301-251

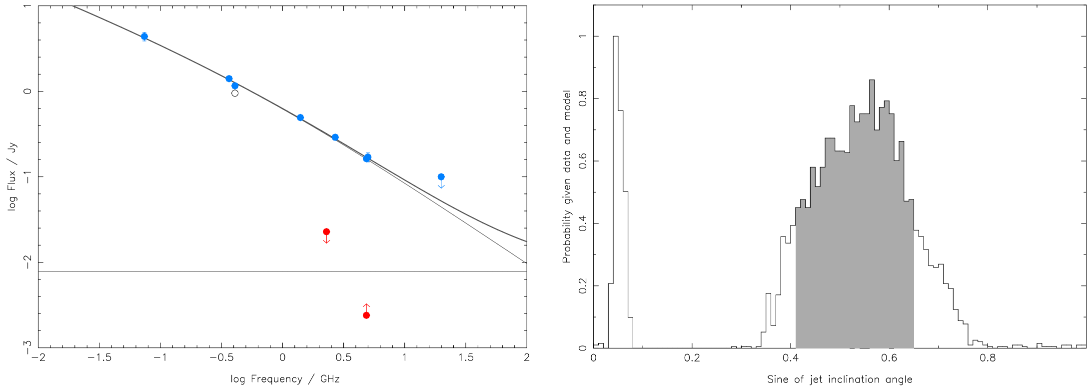

MRC1349-265

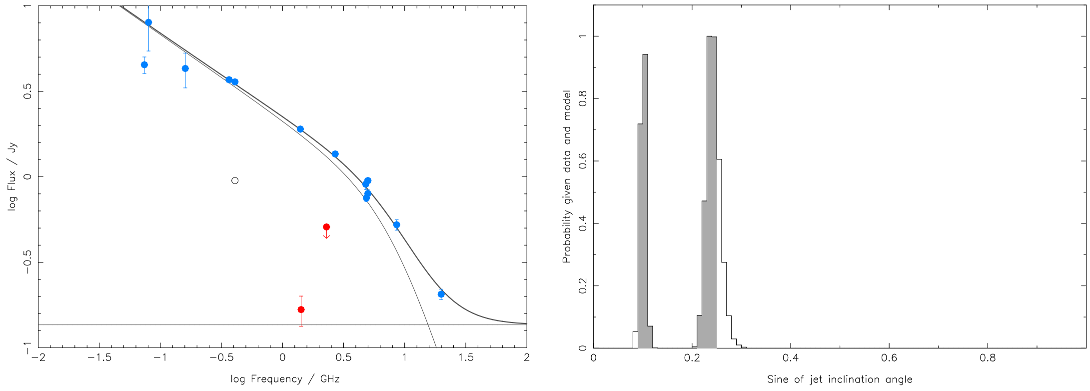

MRC1355-215

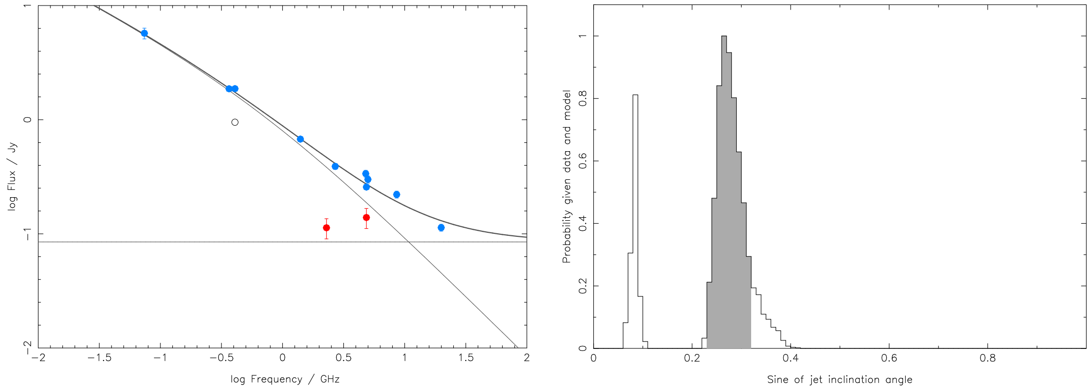

MRC1355-236

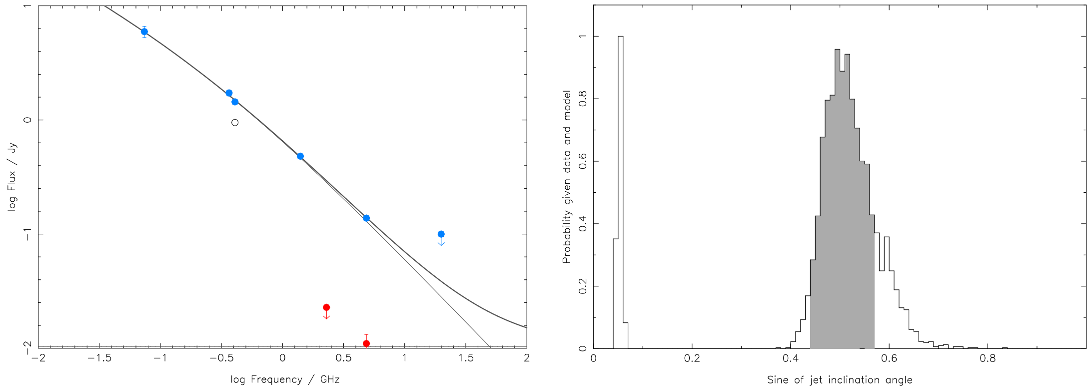

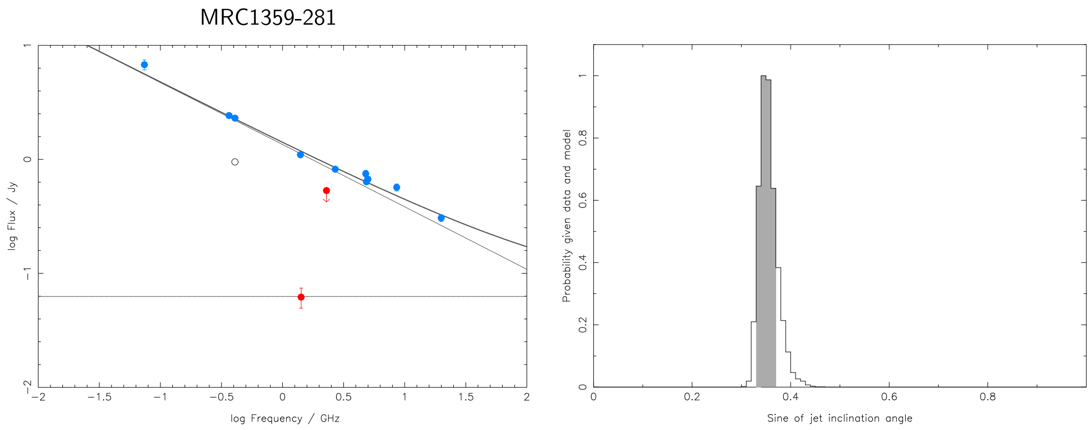

MRC0437-244: The break frequency appears to be lower than observed 74 MHz, and so the break frequency was assumed to be at 10 MHz in the quasar rest-frame.

MRC0549-213: The core flux density is much better fitted with $\gamma = 20$ than in the $\gamma = 2.8$ case.

MRC1359-281: The break frequency appears to be lower than observed 74 MHz, and so the break frequency was assumed to be at 10 MHz in the quasar rest-frame.

5.8.2.2 *Discussion*

The fitted jet angles with their errors and R_{interp} values are presented in Table 5.6. These vary between 12° and 43°, which as in the $\gamma = 2.8$ case, is consistent with the predicted opening angle for powerful radio sources of $\sim 45°$ (Lawrence 1991, as before). The fitted SEDs have not changed shape significantly between the $\gamma = 2.8$ and $\gamma = 20$ fits, and the same two sources (MRC0327-241 and MRC0346-279) are seen to have been clearly boosted into the sample by their cores. The sources MRC1019-227 and MRC1217-209 are still on the borderline of the sample selection flux density by their lobe emission alone, with the magnitude of the errors on the flux densities making it impossible to determine whether these sources were boosted into the sample by their comparatively weak cores.

Figure 5.18 shows the same close correlation between the fitted R_{interp} values and

Quasar		z	$\log L_{178\mathrm{MHz}}$	Jet angles	R_{interp}	R_{lit}	Type
1	MRC0222-224	1.603	27.54	$43\,^{\circ} \pm^{3}_{3}$	0.0022	<0.37	CSS
2	MRC0327-241	0.895	26.77	$14\,^{\circ} \pm^{1}_{8}$	0.14	>1.0	
3	MRC0346-279	0.989	26.46	$12\,^{\circ} \pm^{2}_{3}$	0.27	>5.0	
4	MRC0413-210	0.807	27.42	$19\,^{\circ} \pm^{1}_{1}$	0.043	0.71	
5	MRC0413-296	1.614	28.07	$38\,^{\circ} \pm^{5}_{4}$	0.0024	0.031	
6	MRC0430-278	1.633	27.18	$14\,^{\circ} \pm^{4}_{2}$	0.14		CSS
7	MRC0437-244	0.834	26.92	$42\,^{\circ} \pm^{2}_{2}$	0.0031	0.098	
8	MRC0450-221	0.900	27.40	$32\,^{\circ} \pm^{2}_{3}$	0.0067	0.086	
9	MRC0549-213	2.245	27.74	$15\,^{\circ} \pm^{2}_{1}$	0.10	<0.55	
10	MRC1019-227	1.542	27.24	$34\,^{\circ} \pm^{3}_{4}$	0.0062		CSS
11	MRC1114-220	2.286	27.66	$18\,^{\circ} \pm^{2}_{1}$	0.045		CSS
12	MRC1208-277	0.828	26.98	$26\,^{\circ} \pm^{3}_{2}$	0.020	0.088	
13	MRC1217-209	0.814	26.46	$37\,^{\circ} \pm^{4}_{5}$	0.0050	0.057	
14	MRC1222-293	0.816	26.64	$15\,^{\circ} \pm^{2}_{1}$	0.13	0.38	
15	MRC1301-251	0.952	26.78	$32\,^{\circ} \pm^{8}_{8}$	0.0055	0.020	
16	MRC1349-265	0.924	27.12	$14\,^{\circ} \pm^{1}_{8}$	0.15		CSS
17	MRC1355-215	1.607	27.48	$16\,^{\circ} \pm^{3}_{2}$	0.10	0.84	
18	MRC1355-236	0.832	26.82	$30\,^{\circ} \pm^{4}_{4}$	0.0094	0.098	
19	MRC1359-281	0.802	26.79	$21\,^{\circ} \pm^{1}_{1}$	0.047		CSS

Table 5.6: Median jet angles with errors and R_{interp} values for all Molonglo quasars in the sub-sample, fitted with the $\gamma = 20$ model.
Columns 1 and 2: Index and name of the quasars.
Column 3: Redshift.
Column 4: Logarithmic 178 MHz luminosity.
Column 5: Fitted jet angle and errors for the $\gamma = 20$ model.
Column 6: Fitted R_{interp} value for the $\gamma = 20$ model.
Column 7: The classical values of $R_{10\mathrm{GHz}}$ from the literature (Kapahi et al. 1998a)
Column 8: Note on whether the source is a CSS.

sines of the jet angles as in 5.16, for the $\gamma = 2.8$ fits.

5.9 *Conclusions*

The orientation of the radio jets to the line of light was modelled for the Molonglo quasar sub-sample, calibrating against the 3CRR sub-sample. Two different cases were modelled: the case in which the Lorentz factor, γ, was as modelled from the 3CRR sample ($\gamma = 2.8$), and the case in which this parameter as fixed at $\gamma = 20$. This high value is shown by the literature to be towards the high end of possible Lorentz factors.

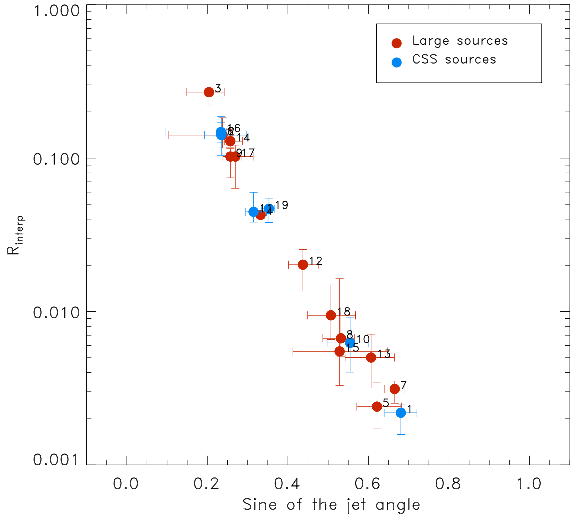

Figure 5.18: Fitted $R_{\rm interp}$ value plotted against the fitted sine of the jet angle for the Molonglo quasar sub-sample, from the analysis with $\gamma = 20$. Note that the name "large sources" refers to projected size; these sources have projected sizes > 25 kpc, whilst CSS sources have smaller projected sizes.

In both cases, the high jet angles were found to be consistent with a torus opening angle of $\sim 45°$, the approximate torus opening angle expected for a sample of high radio luminosity quasars. The $\gamma = 2.8$ range of jet angles were heavily clustered towards the low-angle end of the distribution, much more so than expected from the modest fraction of sources in the sub-sample by virtue of their Doppler-boosted cores (two out of nineteen). This problem is ameliorated by using a higher value of $\gamma = 20$ (compare Table 5.5 and Table 5.6).

Chapter 6 Analysis

The connections between the jet and disk axis angles and the source sizes are investigated in Section 6.1, and the correlation of these angles and the radio luminosity is investigated in Section 6.2. The distributions of the fitted jet and disk axis angles are investigated to check whether they are consistent with the predicted distribution for a randomly-oriented sample in Section 6.3.

The angles of the accretion disk axis and of the radio jet to the line of sight, measured by entirely independent methods, are compared in Section 6.4, to determine whether the results are consistent with a model of AGN in which the jets are launched orthogonally to the plane of the accretion disk.

6.1 *Correlations with Projected Source Size*

Using the results of Chapter 5, the fitted jet angles for the model with a Lorentz factor of $\gamma = 2.8$ are plotted against the projected quasar sizes in Figure 6.1, and the analogous plot for the jet angle model with $\gamma = 20$ is shown in Figure 6.2. The positive correlations between jet angle and projected size of the sources with linear size greater than 25 kpc are at 96% confidence and 98% confidence for the $\gamma = 2.8$ and $\gamma = 20$ models respectively, using Kendall's Tau test in *ASURV* (Lavalley et al. 1992) (see Table 6.1). Including the CSS sources in the correlation decreases these confidence levels marginally, as there is more scatter seen in the distribution of CSS sources.

These correlations are expected statistically, as the sources at smaller jet angles to the line of sight appear foreshortened. The scatter on the relation arises from the real scatter in sizes, as well as from measurement errors. Many CSS sources are expected to be intrinsically small due to their youth (e.g. Fanti et al. 1995), and therefore it is interesting

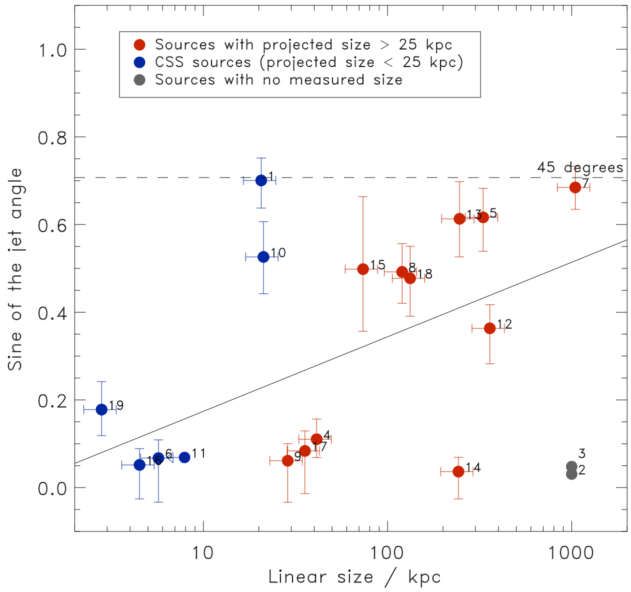

Figure 6.1: Best-fit jet angles for the $\gamma = 2.8$ model versus the projected linear size of the quasar in kpc. The errors on the jet angles are the Bayesian errors and the random seed errors added in quadrature. The red points indicate sources with projected sizes greater than 25 kpc, blue points indicate CSS sources, and the grey points are core-dominated sources without measured linear sizes. To match index numbers to source names, see Table 6.2 for example. The black line shows the best linear fit (minimising χ^2) to all sources excluding the core-dominated sources (grey points). There is a correlation at 92% confidence by Kendall's Tau between the same sub-set of sources, and between the 11 sources with projected linear sizes greater than 25 kpc at 96% confidence (see Table 6.1).

to consider these in isolation from the non-CSS sources. There are four CSS sources at low jet angle which appear to be part of the same population as the sources larger than 25 kpc, and two (MRC0222-224 and MRC1019-227) which have larger fitted jet angles, greater than 30°.

The best-fit disk axis angles for the Molonglo quasars are plotted against the projected linear size of the source in Figure 6.3. There is a weak correlation at 88% confidence by Kendall's Tau test (see Table 6.1) that for the lobe-dominated sources, the sources of largest projected size have greater disk axis angles to the line of sight, as expected statistically from foreshortening if the accretion disks are perpendicular to the radio jets. This correlation is strengthened slightly to 91% confidence if the CSS sources are included in

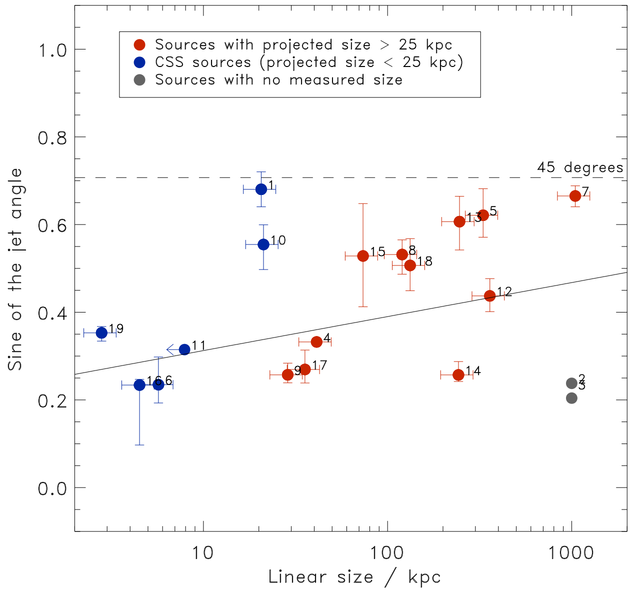

Figure 6.2: Best-fit jet angles for the $\gamma = 20$ model versus the projected linear size of the quasar in kpc. The errors on the jet angles are the Bayesian errors and the random seed errors added in quadrature. The red points indicate sources with projected sizes greater than 25 kpc, blue points indicate CSS sources, and the grey points are core-dominated sources without measured linear sizes. To match index numbers to source names, see Table 6.2 for example. The black line shows the best linear fit (minimising χ^2) to all sources excluding the core-dominated sources (grey points). There is a correlation at 96% confidence by Kendall's Tau between this same sub-set of sources, and between the 11 sources with projected linear sizes greater than 25 kpc at 98% confidence (see Table 6.1).

the sample.

There are four CSS sources with disk axis angles less than 12° that appear to fall on the same relation as the non-CSS sources. It is likely that some or all of these are actually part of the same population as the non-CSS sources, the only difference being projected size (the CSS definition having an arbitrary projected size limit at 25 kpc). The remaining two CSS sources, MRC0222-224 and MRC1114-220, have strong evidence for disks inclined at greater than 30° to the line of sight, and it is possible that these are part of an intrinsically different CSS population.

Of the two CSS outliers in terms of disk axis angle, only one of these sources is an outlier in terms of the jet angle as well. This source, MRC0222-224, is therefore by all measures intrinsically small. This source merits further investigation; it has a measured Balmer decrement H α / H $\beta \sim 23$, a factor of 2 higher than any of the other sources in this Molonglo sub-sample (Down et al., in preparation), and is therefore likely to be a young AGN shrouded in a cocoon of dust.

MRC1114-220, which is the other outlier on the sine disk axis angle – projected size plot, has a fitted disk axis angle of $\sim 30^\circ$, but a jet angle of 4° in the $\gamma = 2.8$ model, and 4° in the $\gamma = 20$ model. The radio map (see Chapter 4) clearly shows a core and what may be an approaching jet with no receding jet visible. This implies a small jet angle to the line of sight, consistent with the values measured here. It is possible that this is a genuinely young source whose jet and disk axis angles are misaligned in the wake of a merger which triggered the activity, or perhaps the jet is precessing.

MRC1019-227, which is the second outlier on the sine jet angle – projected size plot, has a fitted disk axis angle of $\sim 9^\circ$, but a jet angle of 32° in the $\gamma = 2.8$ model, and 34° in the $\gamma = 20$ model. The radio map (see Chapter 4) shows a clear triple source, consistent with the high jet angle to the line of sight. It is possible that in this small source, the disk is highly inclined, but buried inside a shell of shielding material which absorbs the disk emission and re-emits it as broad, featureless emission; otherwise, it may be precessing, or be a genuine outlier.

Parameter correlated with source size	All lobe-dominated sources		CSS sources excluded	
	Kendall's τ	Prob	Kendall's τ	Prob
Jet angle ($\gamma = 2.8$)	0.632	92%	0.982	96%
Jet angle ($\gamma = 20$)	0.721	96%	1.055	98%
Disk axis angle	0.603	91%	0.727	88%

Table 6.1: Kendall's Tau values and probabilities that there is a correlation between the various fitted angles and the projected source sizes, both including and excluding the CSS sources from the fit.

The source sizes were deprojected by simply dividing the apparent source sizes by the sine of the fitted angle, to compensate for simple geometric projection. This does not take into account the expansion of the source, but since the hotspots of jets are only expected to advance at a maximum speed of $\sim 0.1c$ (Scheuer 1995), this effect is small and is not considered. The deprojected sizes are given in Table 6.2, and are plotted in Figure 6.4.

Quasar		Projected size (kpc)	Deprojected source size (kpc)		
			Jet angle ($\gamma = 2.8$)	Jet angle ($\gamma = 20$)	Disk axis angle
1	MRC0222-224	20.6	$29\pm^{3}_{2}$	$30\pm^{2}_{2}$	$32\pm^{10}_{3}$
2	MRC0327-241	-	-	-	-
3	MRC0346-279	-	-	-	-
4	MRC0413-210	41.2	$370\pm^{230}_{110}$	$120\pm^{2}_{3}$	$550\pm^{80}_{90}$
5	MRC0413-296	330.4	$540\pm^{80}_{50}$	$530\pm^{50}_{20}$	$590\pm^{110}_{90}$
6	MRC0430-278	5.7	$85\pm^{260}_{30}$	$24\pm^{5}_{5}$	$230\pm^{8400}_{220}$
7	MRC0437-244	1045.9	$1500\pm^{120}_{100}$	$1570\pm^{60}_{50}$	$3430\pm^{120}_{370}$
8	MRC0450-221	120.0	$240\pm^{40}_{30}$	$230\pm^{20}_{10}$	$530\pm^{30}_{40}$
9	MRC0549-213	28.7	$470\pm^{1331}_{180}$	$110\pm^{10}_{10}$	$150\pm^{150}_{100}$
10	MRC1019-227	21.2	$40\pm^{8}_{5}$	$38\pm^{4}_{3}$	$140\pm^{220}_{10}$
11	MRC1114-220	<7.9	$120\pm^{500}_{40}$	$25\pm^{2}_{2}$	$15\pm^{6}_{3}$
12	MRC1208-277	359.3	$990\pm^{280}_{130}$	$820\pm^{70}_{70}$	$1600\pm^{250}_{210}$
13	MRC1217-209	245.9	$400\pm^{70}_{50}$	$410\pm^{50}_{40}$	$900\pm^{600}_{360}$
14	MRC1222-293	242.7	$6670\pm^{16060}_{3150}$	$940\pm^{60}_{100}$	$1470\pm^{730}_{380}$
15	MRC1301-251	73.6	$150\pm^{60}_{40}$	$140\pm^{40}_{30}$	$200\pm^{80}_{60}$
16	MRC1349-265	4.5	$87\pm^{260}_{36}$	$19\pm^{27}_{1}$	$82\pm^{56000}_{32}$
17	MRC1355-215	35.6	$430\pm^{3000}_{150}$	$130\pm^{20}_{20}$	$420\pm^{270}_{120}$
18	MRC1355-236	132.6	$280\pm^{60}_{40}$	$260\pm^{30}_{30}$	$760\pm^{130}_{160}$
19	MRC1359-281	2.8	$16\pm^{8}_{4}$	$8\pm^{1}_{1}$	$37\pm^{8}_{10}$

Table 6.2: Projected and deprojected source sizes.
Columns 1 and 2: Index and name of the quasars.
Column 3: Projected source sizes.
Column 4: Deprojected source sizes calculated using the fitted jet angles from the $\gamma = 2.8$ model.
Column 5: Deprojected source sizes calculated using the fitted jet angles from the $\gamma = 20$ model.
Column 6: Deprojected source sizes calculated using the fitted disk axis angles.

The distributions of deprojected source sizes found using the jet angles with $\gamma = 2.8$ and the disk axis angles are similar, single-peaked distributions, with the majority of the sources in the range 100 kpc – 1 Mpc. The $\gamma = 20$ model for measuring jet angles gives larger angles, and therefore smaller deprojected sizes, and this has two peaks in the distribution, possibly due to scatter. In this model, all CSS sources are deprojected to sizes $<$ 100 kpc. The $\gamma = 2.8$ model has all bar one CSS source deprojected to less than 100 kpc; the other CSS source, MRC1114-220, has a deprojected size of $\sim$ 120 kpc. Deprojecting the source sizes with the disk axis angles, four of the CSS sources have deprojected sizes of less than 100 kpc (MRC0222-224, MRC1114-220, MRC1349-265 and MRC1359-281). It is worth bearing in mind that the projected source size is defined as the distance between the centres of the furthest separated visible components, so in the case of MRC1114-220, this is only the distance between the core and one lobe; the size may therefore be underestimated by a factor of around 2. It is likely that MRC0222-224 and MRC1359-281 are genuinely small sources, as they have deprojected sizes of less than 50 kpc by all measures of deprojection. Some of the rest of the sources labelled as CSS may actually be part of the non-CSS population which happen to be at relatively small jet angles to the line of sight, but whose cores are not strongly Doppler-boosted.

The cumulative distributions of the deprojected source sizes for each of the fitted angles are shown in Figure 6.5. Note that there are two sources missing from these distributions, which have no measured linear size. The expected distributions of linear sizes, assuming that the hotspots of the lobes are expanding at a constant rate, are also shown. The calculated deprojected sizes are broadly consistent with a constant expansion of the heads of the jets, up to $\sim$ 1 Mpc, although there is a suggestion of an excess of small sources. The drop off of the distribution at sizes greater than $\sim$ 1 Mpc is likely to be due to the duty cycle of the quasars, which will deplete the number of sources larger than a certain cut-off value as they become quiescent. The distribution tails off gradually, which can be explained by some sources having an unusually long duty cycle, by the largest sources being in unusually low-density environments or by the intrinsic variation in jet speeds between quasars.

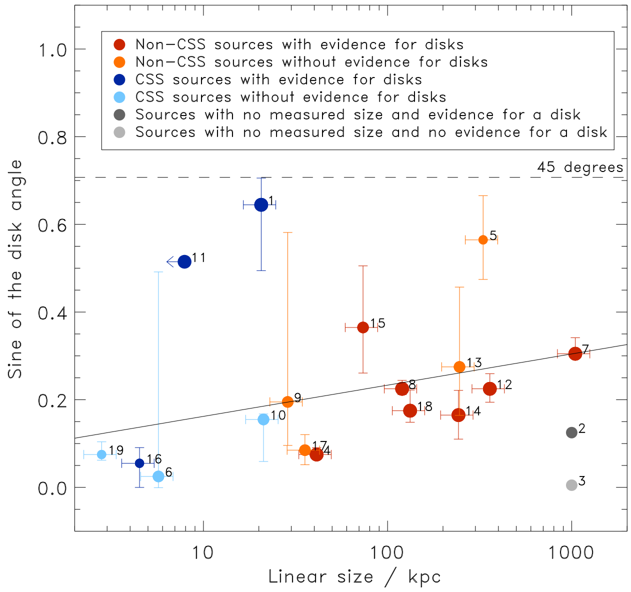

Figure 6.3: Best-fit disk axis angles versus the projected linear size of the quasar in kpc. The disk axis angle error bars include both the error returned from the individual fits and a systematic error from the variation introduced by the random seed added in quadrature, but do not take into account any error due to model selection. The sources with linear sizes greater then 25 kpc are plotted in red and orange, and CSS sources are plotted in blue and turquoise. The two sources plotted in grey are core-dominated sources without measured sizes. The large red, blue or dark grey points have strong evidence for a disk, medium-sized red/blue/dark grey points have moderate evidence, and small red/blue/dark grey points have weak evidence. The medium-sized orange/turquoise/light grey points have possible disks (there is weak evidence against a disk or inconclusive evidence) and the small orange/turquoise/light grey points have evidence against a disk. To match index numbers to source names, see Table 6.2 for example. The black line shows the best linear fit to all sources excluding the core-dominated sources (grey points). There is a correlation at 91% confidence by Kendall's Tau test between the same sub-set of sources, and between the 11 sources with projected linear sizes greater than 25 kpc at 88% confidence (see Table 6.1).

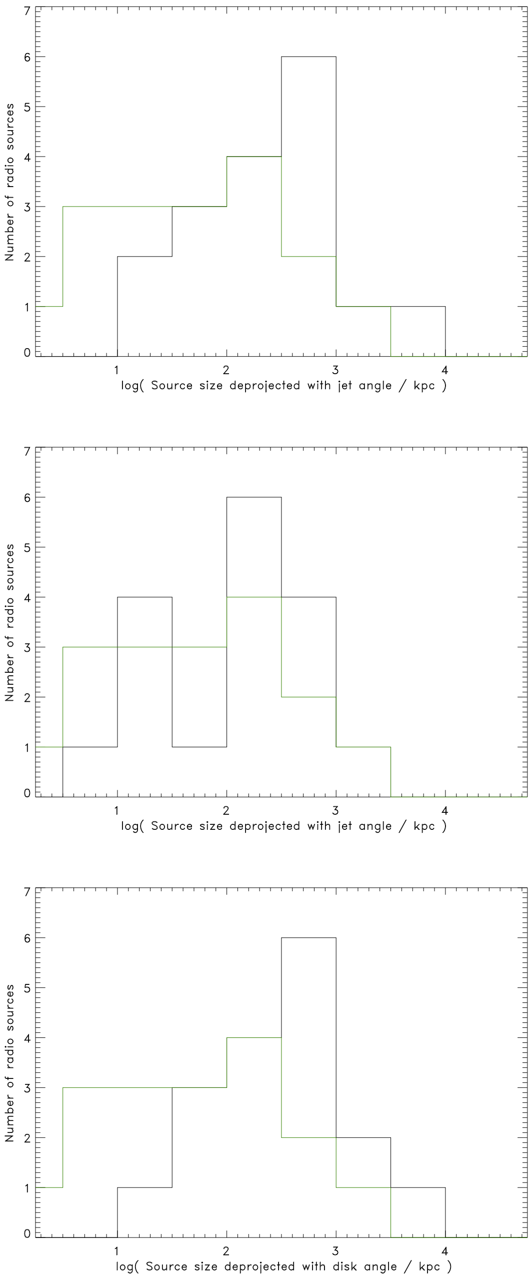

Figure 6.4: Histograms of source sizes deprojected using various fitted angles (black line). The top histogram shows the source sizes deprojected with the jet angles found from the $\gamma = 2.8$ model, the central histogram shows the source sizes deprojected with the jet angles found from the $\gamma = 20$ model, and the bottom histogram shows the source sizes deprojected with the fitted disk axis angles. In each case, the projected sizes are plotted in green.

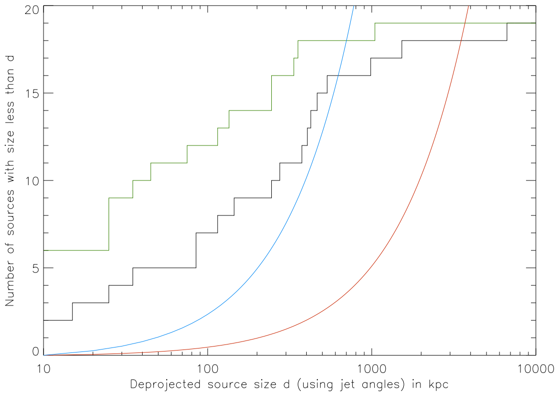

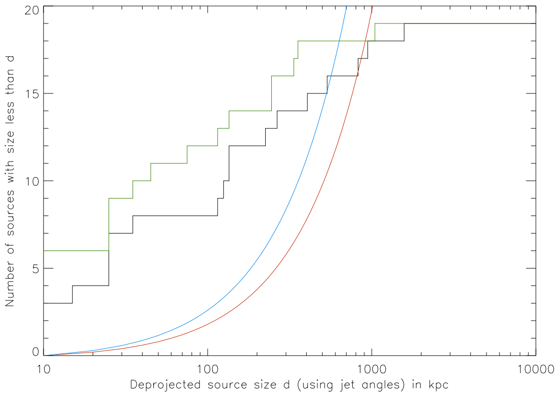

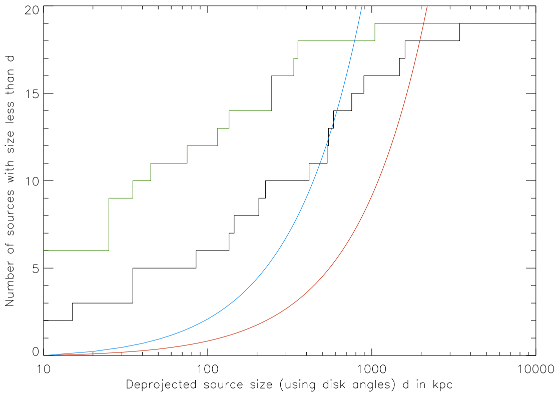

Figure 6.5: Cumulative distributions of source sizes deprojected using various fitted angles (black line). The top histogram shows the source sizes deprojected with the jet angles found from the $\gamma = 2.8$ model, the central histogram shows the source sizes deprojected with the jet angles found from the $\gamma = 20$ model, and the bottom histogram shows the source sizes deprojected with the fitted disk axis angles. The green line shows the distribution on projected source sizes for comparison. The red and blue lines show the predicted distribution if the heads of the jets are expanding at a constant rate; the red line is normalised at the deprojected size of the largest source in the sample, the blue line is normalised at 1 Mpc.

6.2 *Correlations with Radio Luminosity*

The sine of the best-fit jet angles for the quasars (the $\gamma = 2.8$ model) are plotted against the radio luminosity in Figure 6.6. Figure 6.7 is the analogous plot for the $\gamma = 20$ model. There is no obvious correlation in this plot, and the Kendall's Tau probability that there is a correlation is only 49% (see Table 6.3), or 54% in the case of the $\gamma = 20$ model. The correlation is so weak that the fitted lines (minimising the χ^2) slope in different directions for each of these plots.

The critical angle is also plotted on each of the angle versus $\log L_{178\mathrm{MHz}}$ plots, calculated from the model calculated in Section 5.6.3 of Chapter 5. The lower line is normalised by an opening angle of 28° at $\log L_{178\mathrm{MHz}}= 27$, and the upper line by an opening angle of 45° at $\log L_{178\mathrm{MHz}}= 27$. Both models have a minimum quasar fraction of 10% which dominates the curves at low radio luminosities. From the distribution of fitted jet angles, it can be concluded that the fiducial angle of 28°, measured from the 3CRR sample, is too low for the Molonglo sample. A fiducial opening angle of 45° at $\log L_{178\mathrm{MHz}}= 27$ is in agreement with all fitted jet angles except for that of one of the lowest luminosity sources, MRC1301-251.

Figure 6.8 shows the sine of the best-fit disk axis angles plotted against the 178 MHz radio luminosity. There is a weak correlation between these quantities, at a probability of 78% according to Kendall's Tau test (see Table 6.3). The measurement of disk axis angle is entirely independent of the radio luminosity, so the fact that these parameters are correlated provides direct, albeit weak, evidence for the receding torus model (Lawrence 1991). Sources with high radio luminosity have larger torus opening angles, and therefore these sources appear as quasars when viewed at disk axis angles up to this opening angle, if the disk axis is aligned with the radio jets. A larger sample size is needed to confirm this result, but it is important to do so as it would yield the first direct test of this model.

The envelopes showing the luminosity-dependent opening angles for a critical angle of 27° at $\log L_{178\mathrm{MHz}}= 27$ and 45° at $\log L_{178\mathrm{MHz}}= 27$ on Figure 6.8 show that the fitted disk axis inclination angles are in agreement with either of these models.

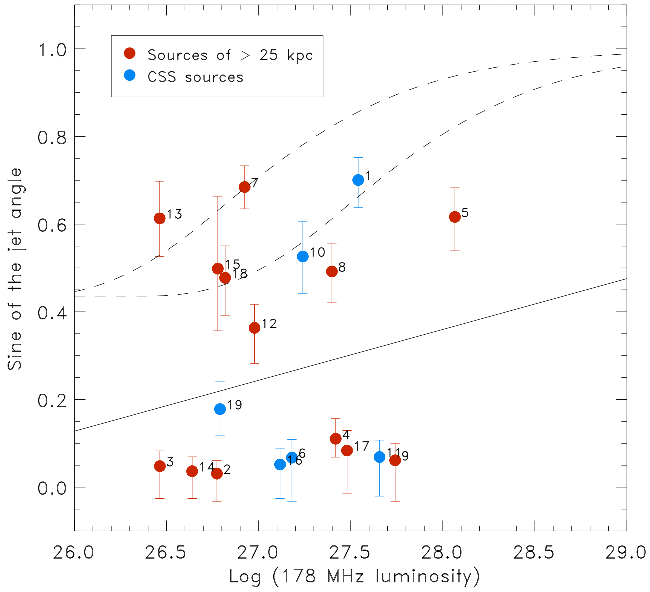

Figure 6.6: Best-fit jet angles for the model with $\gamma = 2.8$ versus the logarithmic 178 MHz luminosity. The errors on the jet angles are the Bayesian errors and the random seed errors added in quadrature. The red points indicate sources with projected sizes greater than 25 kpc and blue points indicate CSS sources. The best-fit line (minimising χ^2) is shown in black. The lower dashed line shows the luminosity-dependent critical angle with fiducial angle 28° at $\log L_{178\mathrm{MHz}} = 27$, and minimum quasar fraction 10% (see Section 5.6.3 of Chapter 5). The upper dashed line shows the radio luminosity-dependent critical angle calculated from the same model, with a fiducial angle of 45° at $\log L_{178\mathrm{MHz}} = 27$.

Parameter correlated with $\log L_{178\mathrm{MHz}}$	Kendall's τ	Prob
Jet angle ($\gamma = 2.8$)	0.222	49 %
Jet angle ($\gamma = 20$)	0.246	54 %
Disk axis angle	0.409	78 %

Table 6.3: Kendall's Tau values and probabilities that there is a correlation between the various fitted angles and the logarithmic 178 MHz radio luminosity.

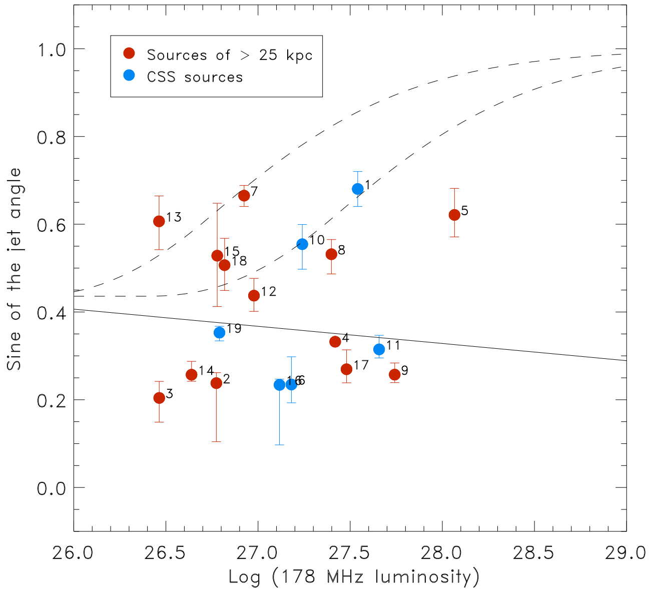

Figure 6.7: Best-fit jet angles for the model with $\gamma = 20$ versus the logarithmic 178 MHz luminosity. The errors on the jet angles are the Bayesian errors and the random seed errors added in quadrature. The red points indicate sources with projected sizes greater than 25 kpc and blue points indicate CSS sources. The best-fit line (minimising χ^2) is shown in black. The lower dashed line shows the luminosity-dependent critical angle with fiducial angle 28° at log $L_{178\text{MHz}}$= 27, and minimum quasar fraction 10% (see Section 5.6.3 of Chapter 5). The upper dashed line shows the radio luminosity-dependent critical angle calculated from the same model, with a fiducial angle of 45° at log $L_{178\text{MHz}}$= 27.

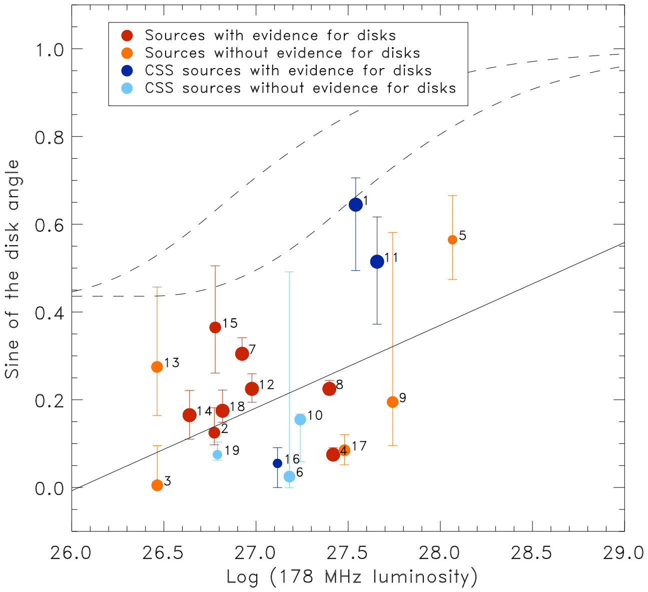

Figure 6.8: Best-fit disk axis angles versus the logarithmic 178 MHz luminosity. The disk axis angle error bars include both the error returned from the individual fits, and a systematic error from the variation introduced by the random seed, added in quadrature, but do not take into account any error due to model selection. The sources with projected linear sizes greater then 25 kpc are plotted in red and orange, and CSS sources are plotted in blue and turquoise. The large red or blue points have strong evidence for a disk, medium-sized red or blue points have moderate evidence, and small red or blue points have weak evidence. The medium-sized orange or turquoise points have possible disks (there is weak evidence against a disk or inconclusive evidence) and the small orange or turquoise points have evidence against a disk. The best-fit line (minimising χ^2) is shown in black. The lower dashed line shows the radio luminosity-dependent critical angle with fiducial angle 28° at log $L_{178\mathrm{MHz}}$= 27, and minimum quasar fraction 10% (see Section 5.6.3 of Chapter 5). The upper dashed line shows the luminosity-dependent critical angle calculated from the same model, with a fiducial angle of 45° at log $L_{178\mathrm{MHz}}$= 27.

6.3 *Distribution of Angles*

The expected distribution of jet angles can be modelled for the Molonglo quasar sample, including a Doppler-boosted core component. From Bayes' Theorem

$$\mathrm{Prob}(\theta|L_{\mathrm{tot}} > L_{\mathrm{min}}) \propto \mathrm{Prob}(L_{\mathrm{tot}} > L_{\mathrm{min}}|\theta) \times \mathrm{Prob}(\theta) \tag{6.1}$$

where

$$\mathrm{Prob}(\theta) = \sin\theta \mathrm{d}\theta \tag{6.2}$$

and the proportionality is required because there is no good information about the overall number of sources where $L_{\mathrm{tot}} > L_{\mathrm{min}}$.

Marginalising the lobe luminosity, then

$$\mathrm{Prob}(L_{\mathrm{tot}} > L_{\mathrm{min}}|\theta) = \int_0^\infty \mathrm{Prob}(L_{\mathrm{tot}} > L_{\mathrm{min}}|\theta, L_{\mathrm{lobe}})\mathrm{Prob}(L_{\mathrm{lobe}})\mathrm{d}L_{\mathrm{lobe}} \ . \tag{6.3}$$

From Willott et al. (2001), the radio luminosity function of high luminosity AGN is

$$\rho(L) = \rho_{\mathrm{norm}}(\frac{L}{L_{\mathrm{norm}}})^{-\alpha} \tag{6.4}$$

where ρ is the comoving space density in logarithmic luminosity space and $\alpha \sim 2.3$. Since this relation was found for 151 MHz and 178 MHz, then this total luminosity is low enough in frequency to be approximated as the lobe luminosity. Then

$$\mathrm{Prob}(L_{\mathrm{lobe}}) \propto L_{\mathrm{lobe}}^{-\alpha} \times \frac{\mathrm{d}\log L_{\mathrm{lobe}}}{L_{\mathrm{lobe}}} \propto L_{\mathrm{lobe}}^{-\alpha-1} \tag{6.5}$$

Defining $R_{10\mathrm{GHz}}$ in the same way as Jackson & Wall (1999),

$$R_{10\mathrm{GHz}} = R_c \frac{1}{\gamma^2}\left(\frac{1}{(1+\beta\cos\theta)^2} + \frac{1}{(1-\beta\cos\theta)^2}\right) \tag{6.6}$$

where R_c is some fiducial $R_{10\mathrm{GHz}}$-value, and is found by Jackson & Wall (1999) to be $R_c \sim 0.01$ for FRII sources. The total flux density is then defined as

$$S_{\mathrm{tot}} = S_{\mathrm{lobe}}(1 + R_{10\mathrm{GHz}}) \ , \tag{6.7}$$

and since $S \propto L$ then

$$L_{\mathrm{tot}} = L_{\mathrm{lobe}}(1 + R_{\mathrm{10GHz}}) \ . \tag{6.8}$$

Now for each L_{lobe} and θ, the total luminosity is uniquely defined, and $\mathrm{Prob}(L_{\mathrm{tot}} > L_{\mathrm{min}}|\theta, L_{\mathrm{lobe}})$ becomes simply 0 or 1. The upshot of this is that for a given θ, there is one limiting lobe flux $L_{\mathrm{lim}}(\theta)$ above which this probability is 1, and below which it is zero, and this simply changes the limits on the integration so that, substituting equations 6.3, 6.5 and 6.2 into 6.1:

$$\mathrm{Prob}(\theta|L_{\mathrm{tot}} > L_{\mathrm{min}}) \propto \int_{L_{\mathrm{lim}}(\theta)}^{\infty} L_{\mathrm{lobe}}^{-\alpha-1} \mathrm{d}L_{\mathrm{lobe}} \times \sin\theta \mathrm{d}\theta \ . \tag{6.9}$$

This integrates to

$$\begin{aligned} \mathrm{Prob}(\theta|L_{\mathrm{tot}} > L_{\mathrm{min}}) &\propto [-L_{\mathrm{lobe}}^{-\alpha}]_{L_{\mathrm{lim}}(\theta)}^{\infty} \times \sin\theta \\ &\propto L_{\mathrm{lim}}(\theta)^{-\alpha} \times \sin\theta \end{aligned} \tag{6.10}$$

The normalised cumulative distributions of fitted jet angles for the $\gamma = 2.8$ and $\gamma = 20$ models are shown in Figure 6.9, with the theoretical model calculated in Equation 6.10 for different values of the Lorentz factor γ overplotted. Note that the median redshift of the Molonglo sub-sample, $z \sim 1$, was used to calculate this theoretical distribution, though this parameter was found to make little difference. It can be seen that the $\gamma = 2.8$ theoretical model does not match the fitted distribution of jet angles well. The best fitting theoretical models are the $\gamma = 8.5$ or $\gamma = 20$ models.

The reason behind this discrepancy is likely to be that a single value of γ was used in the modelling process, with no scatter. This is a thorny issue, since the mode of the γ distribution was used, and the actual probability distribution was asymmetric, with a long tail towards higher values of γ. It is highly probable that the Lorentz factor is not a constant for a population of quasars, but has some scatter. It is also possible that a single quasar can have a different value of the Lorentz factor depending on the viewing angle, such that when it is viewed in a narrow cone close to the jet axis, a very high value of γ close to 20 is seen, whilst when viewed from larger angles, the outer sheath of the jet is visible, with γ closer to 8.5 (e.g. Hardcastle 2006).

There is another issue at work, which is that one quasar was excluded from this subsample of quasars on the basis of optical faintness. This source has a higher probability of having a large jet angle to the line of sight, since it may well be a reddened source in which the dusty torus is blocking some sight lines to the optically bright nucleus. The other excluded quasar was a core-dominated source, with a small angle to the line of sight. An extra quasars added to each end of the angle distribution function would make it more in agreement with a two-component jet with high γ at small angles to the line of sight, and a smaller Lorentz factor at large angles.

The fact that the distribution of fitted jet angles can be reproduced by a model in which the number of objects viewed at small angles is enhanced by Doppler boosting provides supporting evidence that Doppler boosting is genuinely the reason behind the sample selection effect in which excess sources with small angles to the line of sight are selected.

Figure 6.11 shows the cumulative probability distribution for the disk axis angles, with the theoretical distributions for different values of the Lorentz factor γ shown for comparison. As with the jet angles, the true distribution is consistent with a value of the Lorentz factor between $\gamma = 8.5$ and $\gamma = 20$. It is likely that the Lorentz factor is dependent on angle, such that the distribution is modelled by $\gamma \sim 20$ close to the line of sight, when viewing the sources down the axis of their jets, and $\gamma \sim 8.5$ when viewed at larger angles; the luminosity – disk axis angle relation would then have some scatter in γ due to intrinsic differences in the sources.

The distribution in fitted disk axis angle levels off at just below 45°, and all fitted disk axis angles are below this value. This is consistent with the opening angle which might be expected for a sample of powerful FRII sources. The fact that no quasars are observed with disk axis angles larger than this adds weight to the unification scheme which suggests radio galaxies and quasars are the same objects viewed at different angles to the line of sight.

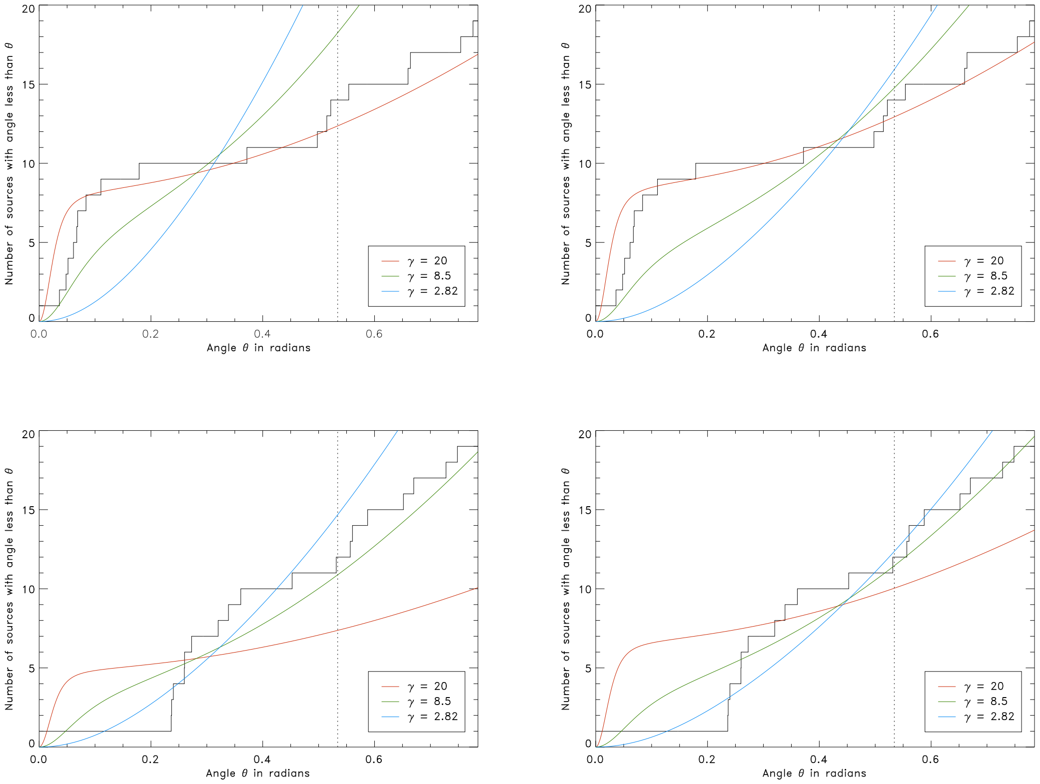

Figure 6.9: The top panels show the cumulative distribution of the fitted jet angles of the sources in the Molonglo sub-sample (from the model with $\gamma = 2.82$). The coloured lines show the theoretical distributions of jet angle, normalised in area up to an angle of 28° (left hand plot) and 45° (right hand plot); the dotted line marks an angle of 28°. The blue line shows the expected cumulative distribution of angles for $\gamma = 2.82$ modelled from the Jackson & Wall (1999) relation, the green line shows the distribution for $\gamma = 8.5$, and the red line shows the distribution for $\gamma = 20$. The bottom panels show the analogous plots for the model with $\gamma = 20$.

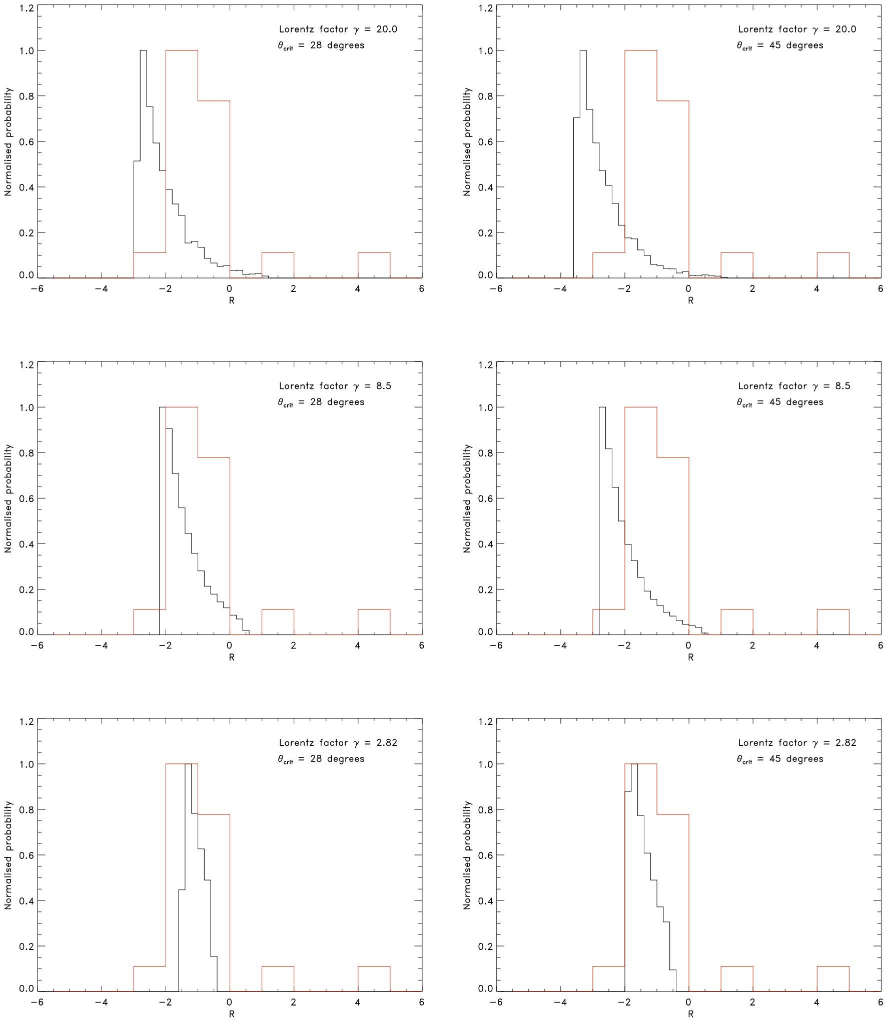

Figure 6.10: The black histograms show the modelled probability distribution of the original core-to-lobe flux density ratio $R_{10\text{GHz}}$ for the Molonglo sub-sample, calculated from the equation of Jackson & Wall (1999) and normalised to unity. These are calculated for three different values of the Lorentz factor, $\gamma = 2.82$, $\gamma = 8.5$ and $\gamma = 20$, and two different values of the critical angle at $\log L_{178\text{MHz}} = 27$, $\theta_{\text{crit}} = 28^\circ$ and $\theta_{\text{crit}} = 45^\circ$. The red histogram shows the fitted $R_{10\text{GHz}}$ values of the Molonglo sub-sample, from the jet model with Lorentz factor $\gamma = 2.82$. The measured $R_{10\text{GHz}}$ values from the $\gamma = 20$ model are slightly different, as the fitted cores vary, but the differences are very small.

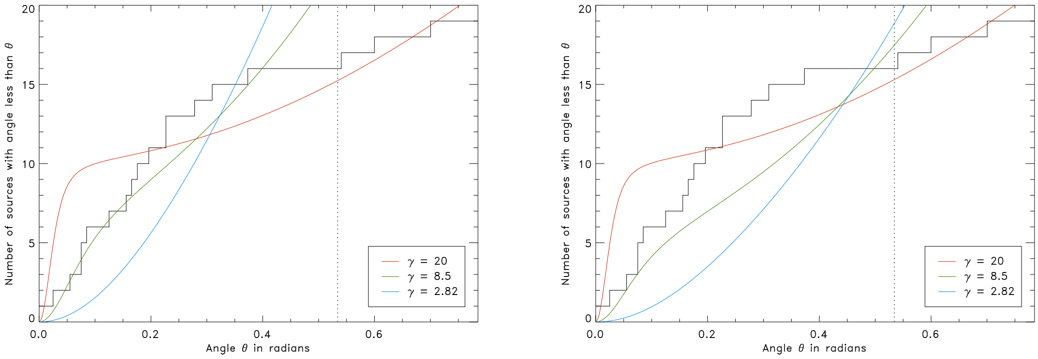

Figure 6.11: These plots show the cumulative distribution of the fitted disk angles of the sources in the Molonglo sub-sample. The coloured lines show the theoretical distributions of jet angle, normalised in area up to an angle of 28° (left hand plot) and 45° (right hand plot); the dotted line marks an angle of 28°. The blue line shows the expected cumulative distribution of angles for $\gamma = 2.82$ modelled from the Jackson & Wall (1999) relation, the green line shows the distribution for $\gamma = 8.5$, and the red line shows the distribution for $\gamma = 20$.

6.4 *Correlation between Disk Axis Angle and Jet Angle*

The jet angles and disk axis angles have been fitted by entirely independent methods. All fitted angles are given in Table 6.4. The sines of these angles have been plotted against each other in Figure 6.12 (for the jet model with $\gamma = 2.8$) and Figure 6.13 (for the jet model with $\gamma = 20$). The Kendall's Tau probabilities for a correlation being present are given in Table 6.5 for the cases that the CSS sources are included in the statistical analysis, and that only non-CSS sources are included. In all cases, the probability of a correlation is greater than 99.5%.

Quasar		z	log $L_{178\text{MHz}}$	Disk axis angle	Jet angle ($\gamma = 2.8$)	Jet angle ($\gamma = 20$)	Type
1	MRC0222-224	1.603	27.54	$40\,^\circ \pm^{5}_{11}$	$44\,^\circ \pm^{4}_{5}$	$43\,^\circ \pm^{3}_{3}$	CSS
2	MRC0327-241	0.895	26.77	$7\,^\circ \pm^{3}_{2}$	$2\,^\circ \pm^{2}_{2}$	$14\,^\circ \pm^{1}_{8}$	
3	MRC0346-279	0.989	26.46	$0\,^\circ \pm^{5}_{0}$	$3\,^\circ \pm^{2}_{3}$	$12\,^\circ \pm^{2}_{3}$	
4	MRC0413-210	0.807	27.42	$4\,^\circ \pm^{1}_{1}$	$6\,^\circ \pm^{3}_{2}$	$19\,^\circ \pm^{1}_{1}$	
5	MRC0413-296	1.614	28.07	$34\,^\circ \pm^{6}_{7}$	$38\,^\circ \pm^{5}_{5}$	$38\,^\circ \pm^{5}_{4}$	
6	MRC0430-278	1.633	27.18	$1\,^\circ \pm^{28}_{1}$	$4\,^\circ \pm^{2}_{4}$	$14\,^\circ \pm^{4}_{2}$	CSS
7	MRC0437-244	0.834	26.92	$18\,^\circ \pm^{2}_{1}$	$43\,^\circ \pm^{4}_{4}$	$42\,^\circ \pm^{2}_{2}$	
8	MRC0450-221	0.900	27.40	$13\,^\circ \pm^{1}_{1}$	$29\,^\circ \pm^{4}_{5}$	$32\,^\circ \pm^{2}_{3}$	
9	MRC0549-213	2.245	27.74	$11\,^\circ \pm^{24}_{6}$	$4\,^\circ \pm^{2}_{4}$	$15\,^\circ \pm^{2}_{1}$	
10	MRC1019-227	1.542	27.24	$9\,^\circ \pm^{1}_{6}$	$32\,^\circ \pm^{6}_{6}$	$34\,^\circ \pm^{3}_{4}$	CSS
11	MRC1114-220	2.286	27.66	$31\,^\circ \pm^{7}_{9}$	$4\,^\circ \pm^{2}_{4}$	$18\,^\circ \pm^{2}_{1}$	CSS
12	MRC1208-277	0.828	26.98	$13\,^\circ \pm^{2}_{2}$	$21\,^\circ \pm^{3}_{5}$	$26\,^\circ \pm^{3}_{2}$	
13	MRC1217-209	0.814	26.46	$16\,^\circ \pm^{11}_{7}$	$38\,^\circ \pm^{6}_{6}$	$37\,^\circ \pm^{4}_{5}$	
14	MRC1222-293	0.816	26.64	$9\,^\circ \pm^{3}_{3}$	$2\,^\circ \pm^{2}_{2}$	$15\,^\circ \pm^{2}_{1}$	
15	MRC1301-251	0.952	26.78	$21\,^\circ \pm^{9}_{6}$	$30\,^\circ \pm^{12}_{9}$	$32\,^\circ \pm^{8}_{8}$	
16	MRC1349-265	0.924	27.12	$3\,^\circ \pm^{2}_{3}$	$3\,^\circ \pm^{2}_{3}$	$14\,^\circ \pm^{1}_{8}$	CSS
17	MRC1355-215	1.607	27.48	$5\,^\circ \pm^{2}_{2}$	$5\,^\circ \pm^{3}_{5}$	$16\,^\circ \pm^{3}_{2}$	
18	MRC1355-236	0.832	26.82	$10\,^\circ \pm^{3}_{2}$	$29\,^\circ \pm^{5}_{6}$	$30\,^\circ \pm^{4}_{4}$	
19	MRC1359-281	0.802	26.79	$4\,^\circ \pm^{2}_{0}$	$10\,^\circ \pm^{4}_{3}$	$21\,^\circ \pm^{1}_{1}$	CSS

Table 6.4: Table of all fitted angles:
Columns 1 and 2: Index and name of the quasars.
Column 3: Redshift of the quasar.
Column 4: Logarithm of the 178 MHz quasar luminosity.
Column 5: Fitted disk axis angles and errors.
Columns 6 and 7: Fitted jet angles and errors for the $\gamma = 2.8$ and $\gamma = 20$ models respectively.
Column 8: Indication of whether the source is classed as CSS.

These plots are consistent with the disks and jets in these objects being orthogonal

Parameter correlated with disk axis angle	All lobe-dominated sources		CSS sources excluded	
	Kendall's τ	Prob.	Kendall's τ	Prob.
Jet angle ($\gamma = 2.8$)	1.041	99.8%	1.256	99.7%
Jet angle ($\gamma = 20$)	1.205	99.9%	1.308	99.8%

Table 6.5: Kendall's Tau values and probabilities that there is a correlation between the fitted jet angle and the fitted disk axis angle, both including and excluding the CSS sources from the fit.

in the majority of cases. The offset of the cluster of sources around $\theta_{\text{jet}} \sim 0.4 - 0.6$ and $\theta_{\text{disk}} \sim 0.2 - 0.4$ from the $\theta_{\text{disk}} = \theta_{\text{jet}}$ line seems likely to be due to imperfections in the method of using the 3CRR sub-sample to constrain parameters (specifically γ) used in the jet fitting of the Molonglo sub-sample.

The reduced χ^2 for the $\theta_{\text{disk}} - \theta_{\text{jet}}$ plot using the $\gamma = 2.8$ jet model (6.12) is 1.29, and for the plot using the $\gamma = 20$ jet model (6.13), the reduced χ^2 is 2.27. The fact that the χ^2 values are close to unity indicates that the scatter on the relation is not much larger than the error bars. In Figure 6.12, MRC1114-220 is the outlier, and is roughly 2-σ away from the best-fit line. In a population of 20 objects, it is reasonable to expect one outlier of 2-σ arising from Poisson errors, so this source can be explained by the scatter.

It is interesting, however, that the outlying quasar is a CSS source, and worth speculating on other possible reasons that this source may not lie on the $\theta_{\text{disk}} - \theta_{\text{jet}}$ relation. It is possible that this CSS source is a recently-triggered source in which the disk has been disrupted by the activating galaxy merger, and is misaligned from the jet. Such large offsets between disk axis angles and jet angles are not seen in any of the older sources, in which the disks and jets would have had time to realign following any disruption during their birth.

The other possibility is that the jet is precessing in this small source. The jet angle from the $\gamma = 2.8$ model is 4° and the disk axis angle is fitted as 31°. High precession angles of this order of magnitude have been seen in microquasars, such as SS433 with a precession angle of $\sim 20°$ (e.g. Blundell & Bowler 2004); the accretion disk and jet are perpendicular and both precess with a period of 164 days in this source, with a phase lag of ~ 16 days between the two (Crampton & Hutchings 1981). The accretion disks of quasars are much larger, and so it is possible either that there is a correspondingly long time lag between the disk and the jets, or that there is a time delay between the inner disk beginning to precess, and the precession propagating to the outer disk, resulting in a warped disk with the double-peaked lines arising from the non-precessing outer part. The absence of a large number of outliers in this plot shows that it is unlikely that the most powerful sources are precessing with similarly large angles to the line of sight.

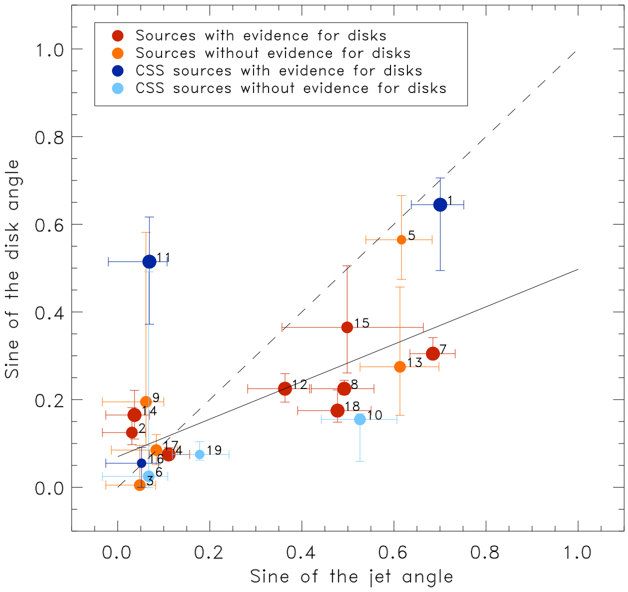

Figure 6.12: The disk axis angles measured from the IR spectra (see Chapter 3) plotted against the jet inclination angles measured from the radio spectral energy distributions for the case that $\gamma = 2.8$ (Chapter 5). The disk axis angle error bars include both the error returned from the individual fits, and a systematic error from the variation introduced by the random seed added in quadrature, but do not take into account the error due to model selection. The errors on the jet angles are the Bayesian errors and the random seed errors added in quadrature. The sources with projected linear sizes greater then 25 kpc are plotted in red and orange, and CSS sources are plotted in blue and turquoise. The large red or blue points have strong evidence for a disk, medium-sized red/blue points have moderate evidence, and small red/blue points have weak evidence. The medium-sized orange/turquoise points have possible disks (there is weak evidence against a disk or inconclusive evidence) and the small orange/turquoise points have evidence against a disk. The best-fit line is plotted as a solid line, and has slope of 0.427 and an intercept of 0.070. The reduced χ^2 of this fit is 1.29. $\theta_{\text{disk}} = \theta_{\text{jet}}$ is shown as a dashed line.

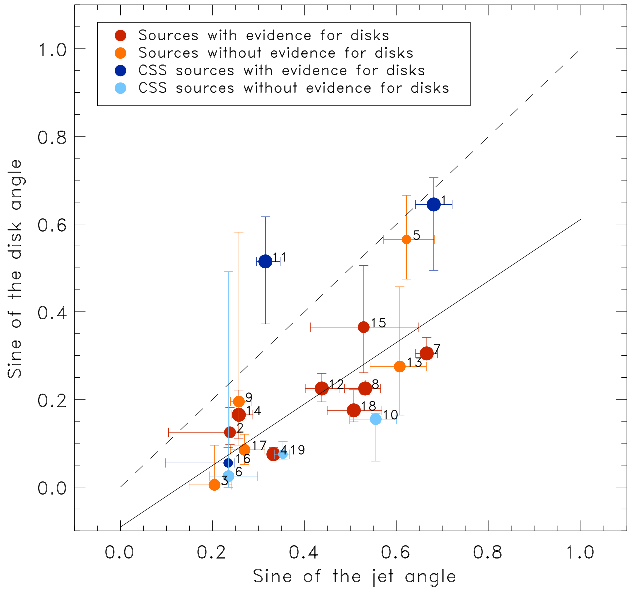

Figure 6.13: The disk axis angles measured from the IR spectra (see Chapter 3) plotted against the jet inclination angles measured from the radio spectral energy distributions for the case that $\gamma = 20$ (Chapter 5). The disk axis angle error bars include both the error returned from the individual fits, and a systematic error from the variation introduced by the random seed added in quadrature, but do not take into account the error due to model selection. The errors on the jet angles are the Bayesian errors and the random seed errors added in quadrature. The sources with projected linear sizes greater then 25 kpc are plotted in red and orange, and CSS sources are plotted in blue and turquoise. The large red or blue points have strong evidence for a disk, medium-sized red/blue points have moderate evidence, and small red/blue points have weak evidence. The medium-sized orange/turquoise points have possible disks (there is weak evidence against a disk or inconclusive evidence) and the small orange/turquoise points have evidence against a disk. The best-fit line is plotted as a solid line, and has slope of 0.702 and an intercept of -0.091. The reduced χ^2 of this fit is 2.27. $\theta_{\rm disk} = \theta_{\rm jet}$ is shown as a dashed line.

6.5 *Conclusions*

The disk axis angles and jet angles measured in this thesis have been shown to be consistent with a model in which these radio luminous quasars are drawn from a parent population of powerful radio sources, and viewed at an angle within $\sim 45^\circ$ to the line of sight. The sources viewed at larger angles than this are expected to appear as radio galaxies, in accordance with this unification theory. Furthermore, there is weak but direct evidence, through a correlation of the fitted disk axis angles with the radio luminosity, that the receding torus model is correct. In this model, more luminous sources have larger torus opening angles and are therefore seen as quasars up to higher angles to the line of sight.

The measured distributions of disk axis angles and jet angles show an excess of sources at small angles to the line of sight. The distributions are shown to agree with the theory that an excess of low-angle sources is shifted into samples selected at moderate radio luminosities by Doppler boosting of the cores.

The distributions of source sizes deprojected using the disk axis angles and the jet angles are in agreement with a model in which the heads of the jets advance at a constant rate up to ~ 1 Mpc, after which the numbers drop off quickly, perhaps because the median duty cycle for this type of source causes them to become quiescent. The plot of disk axis angles versus jet angles furthermore shows that the jets of the larger sources are not in general prone to precessing at large angles.

The disk axis angle – jet angle correlation is strong, and taking into account the discrepancies between the sub-sample of Molonglo quasars and the 3CRR sample of radio sources used for normalisation, the results are consistent with the disk axis angles and jet angles being orthogonal, with the possible exception of the CSS source MRC1114-220.

There are several reasons that the accretion disk and the jet may be misaligned in radio sources. The source may have been recently triggered by a galaxy merger, which would disrupt the central black hole such that its spin would no longer align with the accretion disk, and re-alignment takes $\sim$ a few times 10^7 years (Scheuer & Feiler 1996). The jet, launched along the spin axis, would then be misaligned with the disk. Another possibility is that the jets of the quasars are precessing at angles of up to $\sim 30^\circ$, as seen in some microquasars. It is also possible that some of the intrinsically small CSS sources are in dense environments, and have jets which are frustrated by dense material lying outside the central region.

Chapter 7 | *Conclusions*

A very brief summary of the results is presented in Section 7.1, followed by a discussion of the ways in which these methods could be improved upon and extended in Section 7.2.

7.1 *Summary of Results*

Infrared spectroscopy of the H α emission lines of a sub-sample of high-redshift Molonglo quasars ($0.8 < z < 2.3$) was fitted with a composite model of broad and narrow emission, including theoretical emission from an optically thick, flattened, rotating outer accretion disk. All bar two of the nineteen sources was found to have emission consistent with that predicted from an accretion disk, whilst eight of the sources had strong Bayesian evidence for the more complex disk emission over a model which included two broad lines. It can be concluded that the best explanation for the complexity required to fit these broad H α lines is optical emission from an accretion disk in the heart of these quasars in addition to the H α emission from the classical broad-line region of fast-moving gas clouds outside the nucleus. It may be that accretion disk emission has been seen in so few AGN because the classical broad emission lines have a tendency to swamp the disk emission, requiring a complex model in order to retrieve the accretion disk contribution to the line. This result requires a larger quasar sample for confirmation.

Angles of the radio jets to the line of sight were modelled for the same quasar sub-sample, by fitting a double power law representing the radio lobe emission and a constant core flux density component to the total spectral energy distributions of these quasars. By modelling the ratio of the core flux density to the radio lobe flux density as a function of the low-frequency radio luminosity and the angle of the quasar to the line of sight, using the 3CRR radio source sample as a training sample which was thought to have an unbiased distribution of jet angles, the jet angles for the Molonglo sample were directly retrieved from the spectral energy distributions. The distribution of jet angles produced by this method, in which the Doppler factor was fitted as $\gamma = 2.8$, appeared to overpredict the number of sources at small angles to the line of sight; if these angles were correct, then more than two sources would appear as core-dominated quasars. Fitting the jet angles with a model in which γ was fixed at the higher value of $\gamma = 20$ produced a range of jet angles more evenly dispersed, with fewer at low angles to the line of sight. Although it is clear that a more complex model is required in which γ is allowed to vary, the two calculated models ($\gamma = 2.8$ and $\gamma = 20$) bracket uncertainties induced by this effect. There is likely to be an intrinsic variation in γ between sources, in addition to a variation in γ with angle to the line of sight, such that lower values of γ are observed away from the jet axis.

The recovered disk axis angles and jet angles for the Molonglo sub-sample have been found to be consistent with a sample selection process in which sources at low angles to the line of sight are over-represented by being Doppler-boosted into the sample.

Using the disk axis angles and the jet angles to deproject the observed sizes of the quasars, the deprojected size distribution was found to be consistent with a scenario in which the heads of the sources are expanding into the surrounding medium at a roughly constant speed, up to a size of $\sim$ 1 Mpc. A few sources have sizes larger than this, which can be explained by a scatter in jet expansion speeds, caused by intrinsic differences between the jets or variations in the density of the intergalactic medium into which the jet is expanding; or by a scatter in jet lifetimes.

A weak correlation was found between the sine of the accretion disk axis angle and the logarithm of the low-frequency radio luminosity. This is direct, albeit tenuous, evidence for the receding torus model first suggested by Lawrence (1991) in which the opening angle of the torus widens with increasing radio luminosity. The highest angles measured by all models for disk axis angles and jet angles are 40 – 45 °, consistent with the opening angle predicted for radio luminous sources.

The disk axis angles and jet angles correlate strongly, and are consistent with the radio jets launching orthogonally to the accretion disk, as is expected if the power for the radio jets is extracted from the spin of the black hole, as in the Blandford & Znajek (1977) mechanism. It is interesting to note that the outlier quasar on the jet angle – disk axis angle plot is a compact steep spectrum source, and may therefore be intrinsically young and small. This may be a statistical outlier caused by the scatter in the relation, but a larger sample of sources may show that CSS sources are less likely to have jets orthogonal to the accretion disk, if the theory in which these sources are born in galaxy mergers is true, and if powerful jets emerge faster than the time needed for the accretion disk and the spin axis of the black hole to align.

7.2 *Future Work*

7.2.1 *Improvements to the method*

There are a number of ways in which the Bayesian disk-fitting method used in this thesis could be improved upon. Ideally, with more computing time and resources, the models would all be re-run, keeping the priors totally uniform. However, the results for the fitted disk axis angles have proven to be extremely stable, and so there is good reason to believe that this would not have a significant effect on the majority of the results. Calculating in advance the highest velocities expected from outflows, it would then be possible to use the priors to discriminate between fits which comprise physically possible shifts between two separate broad line regions, or a broad line region and an outflow, and those which do not.

Although the stability of the fits has been shown to be good in general, it would be better to run several seeds for every model, in order to check for each spectrum fitted that the results are truly stable, and that no false minima are found.

The disk model used in this thesis was necessarily a simple one, in order to avoid over-fitting the variable-quality data and to keep the number of parameters low enough for the available computing resources. It would be interesting to explore more complex models, possibly only using a few clean spectra; in particular, the effects of varying the radial exponent of the disk emissivity, which was fixed in this model, and the effects of disk ellipticity should be investigated. Non-circular disks can give rise to a much wider range of emission line shapes, including double peaked profiles with a blue peak of higher intensity than the red peak.

The results of the jet angle fitting process have shown that a single-γ model is imperfect. A more appropriate model for the Doppler factor would include both a jet angle and a jet-power dependent term, as well as an intrinsic object-to-object scatter on the bulk motions of the jets. It may be possible to marginalise the scatter on the Doppler factor, and hence create a vastly improved model with the addition of only one or two extra parameters.

7.2.2 *Extension to a large sample*

The obvious next step is to apply this method to a much larger sample of radio sources. The Sloan Digital Sky Survey (SDSS) is an obvious candidate. Strateva et al. (2003) searched for double-peaked lines in $\sim$ 3200 AGN from this survey by fitting multiple Gaussians to each emission line region, having first subtracted the narrow lines. They considered that any spectrum requiring more than one broad Gaussian to fit included disk emission, and found $\sim$ 120 such AGN, a fraction of only 4%. This fraction is so much lower than the fraction of 58% found in the Molonglo quasar sub-sample presented here partly because Strateva et al. (2003) only classed sources as double-peaked when there were two distinct, separable broad components, which is not always the case for disk emission. The sample of Strateva et al. (2003) also included radio galaxies, in which the disk emission is likely to be obscured by a dusty torus; this torus may only have a small opening angle due to the low power of SDSS sources.

If there are insufficiently large samples of luminous quasars at low redshift that are not badly affected by starlight contamination, then a high-redshift sample observed in the near-infrared might prove a better alternative. The recently developed FMOS instrument might be ideal to efficiently obtain a large sample of near-infrared spectra.

The treatment of a larger sample size would allow interesting results to be tested and confirmed, in particular the disk axis angle – low frequency radio luminosity correlation which provides direct evidence for the receding torus model, and the disk axis angle – jet angle relation which shows that the disks and jets are orthogonal. In order to deal with a sample of $\gtrsim$ 100 sources, it would certainly be desirable to automate the model selection procedures for fitting the H α emission lines.

7.2.3 *Further work*

The Chen & Halpern (1989) equation used to fit the accretion disks includes the black hole mass, and so this value can be retrieved from the normalisation constant of the fitted disk. This circumvents the problem raised by Jarvis & McLure (2006), in which the correlation of broad line widths with source orientation in quasars (Wills & Browne 1986), explained by the accretion disk model, prevent these lines being used as indicators of black hole mass (e.g. McLure & Dunlop 2004). The relation between black hole mass and deprojected source size can then be investigated.

The
Bibliography

Alexander, P. & Leahy, J. P. 1987, MNRAS, 225, 1

Amico, P., Cuby, J., Devillard, N., Jung, Y., & Lidman, C. 2002, ISAAC Data Reduction Guide 1.5

Antonucci, R. 1993, ARA&A, 31, 473

Antonucci, R. R. J. & Miller, J. S. 1985, ApJ, 297, 621

Archibald, E. N., Dunlop, J. S., Jiminez, R., et al. 2002, MNRAS, 336, 353

Bahcall, J. N. & Soneira, R. M. 1980, ApJS, 44, 73

Baker, J. C., Hunstead, R. W., Athreya, R. M., et al. 2002, ApJ, 568, 592

Baker, J. C., Hunstead, R. W., Kapahi, V. K., & Subrahmanya, C. R. 1999, ApJS, 122, 29

Baldwin, J. A. 1977, ApJ, 214, 679

Barnes, J. E. & Hernquist, L. E. 1991, ApJ, 370, L65

Barthel, P. D. 1989, ApJ, 336, 606

Begelman, M. C., Blandford, R. D., & Rees, M. J. 1984, Review of Modern Physics, 56, 255

Bennett, C. L., Hill, R. S., Hinshaw, G., et al. 2003, The WMAP First Year Source Catalog (WMAP1) (VizieR On-line Data Catalog)

Blandford, R. D. 1979, American Institute of Physics Conference Proceedings, 56, 333

Blandford, R. D. & Znajek, R. L. 1977, MNRAS, 179, 433

Blundell, K. M. & Bowler, M. G. 2004, ApJ, 616, L159

Blundell, K. M. & Rawlings, S. 1999, Nat, 339, 330

Blundell, K. M., Rawlings, S., & Willott, C. J. 1999, AJ, 117, 677

Bon, E. 2005, Mem. S.A.It., 7, 34

Bridle, A. H., Hough, D. H., Lonsdale, C. J., Burns, J. O., & Laing, R. A. 1994, AJ, 108, 766

Bridle, A. H. & Perley, R. A. 1984, ARAA, 22, 319

Brown, L. M. J., Robson, E. I., Gear, W. K., et al. 1989, ApJ, 340, 129

Cawthorne, T. V. 1991, Beams and Jets in Astrophysics, , ed. P. A. Hughes, Cambridge Astrophysics Series, 19, 187

Cawthorne, T. V., Scheuer, P. A. G., Morison, I., & Muxlow, T. W. B. 1986, MNRAS, 219, 883

Chen, K. & Halpern, J. P. 1989, ApJ, 344, 115

Chen, K., Halpern, J. P., & Filippenko, A. V. 1989, ApJ, 339, 742

Cohen, A. S., Lane, W. M., Cotton, W. D., et al. 2007a, AJ, 134, 1245

Cohen, M. H., Barthel, P. D., Pearson, T. J., & Zensus, J. A. 1988, ApJ, 329, 1

Cohen, M. H., Cannon, W., Purcell, G. H., et al. 1971, ApJ, 170, 207

Cohen, M. H., Lister, M. L., Homan, D. C., et al. 2007b, ApJ, 658, 232

Cohen, M. H., Ogle, P. M., Tran, H. D., Goodrich, R. W., & Miller, J. S. 1999, ApJ, 118, 1963

Collin-Souffrin, S. 1987, AA, 179, 60

Collin-Souffrin, S., Dumont, S., Heidmann, N., & Joly, M. 1980, AA, 83, 190

Condon, J. J., Cotton, W. D., Greison, E. W., et al. 1998, AJ, 115, 1693

Crampton, D. & Hutchings, J. B. 1981, ApJ, 251, 604

Daly, R. A. 1992, ApJ, 399, 426

de Silva, E., Baker, J. C., Hunstead, R. W., & Saunders, R. D. E. in preparation, a

de Silva, E., Baker, J. C., Saunders, R. D. E., & Hunstead, R. W. in preparation, b

De Young, D. S. 1998, ApJ, 507, 161

Dennett-Thorpe, J., Barthel, P., & van Bemmel, I. 2000, AA, 364, 501

Devillard, N. 1997, Messenger, 87, 19

Douglas, J. N., Bash, F. N., Bozyan, F. A., Torrence, G. W., & Wolfe, C. 1996, AJ, 111, 1945

Drury, L. 1983, Space Science Reviews, 36, 57

Eales, S. A. 1992, ApJ, 397, 49

Eracelous, M. & Halpern, J. P. 2003, ApJ, 599, 886

Eracleous, M. & Halpern, J. P. 1994, ApJS, 90, 1

Fabian, A. C. 1999, MNRAS, 308, L39

Falcke, H., Körding, E., & Markoff, S. 2004, A&A, 414, 895

Fanaroff, B. L. & Riley, J. M. 1974, MNRAS, 167, 31P

Fanti, C., Fanti, R., Dallacasa, D., et al. 1995, AA, 302, 317

Fender, R. 2004, New Astronomy Reviews, 48, 1399

Filippenko, A. V. 1988, Adv. Space Res., 8, 5

Garrington, S. t., Leahy, J. P., Conway, R. G., & Laing, R. A. 1988, Nature, 331, 147

Gaskell, C. M. 2008, The Nuclear Region, Host Galaxy and Environment of Active Galaxies, eds. Erika Benítez, Irene Cruz-González, & Yair Krongold, Revista Mexicana de Astronomìa y Astrofísica (Serie de Conferencias), 32, 1

Griffith, M. R., Wright, A. E., Burke, B. F., & Ekers, R. D. 1994, ApJS, 90, 179

Grimes, J. A., Rawlings, S., & Willott, C. J. 2004, MNRAS, 349, 503

Halpern, J. P. & Chen, K. 1989, Active Galactic Nuclei: Proceedings of the 134th Symposium of the International Astronomical Union, held in Santa Cruz, California, August 15 – 19, 1988. Edited by D. E. Osterbrock and J. S. Miller, 134, 245

Hardcastle, M. J. 2006, MNRAS, 366, 1465

Hardcastle, M. J., Alexander, P., Pooley, G. G., & Riley, J. M. 1999, MNRAS, 304, 135

Heavens, A. F. & Drury, L. O. 1988, MNRAS, 235, 997

Heavens, A. F. & Meisenheimer, K. 1987, MNRAS, 225, 335

Hine, R. G. & Scheuer, P. A. G. 1974, MNRAS, 166, 513

Høg, E., Fabricius, C., Makarov, V. V., et al. 2000, AA, 355, L27

Hutchings, J. B., Janson, T., & Neff, S. G. 1989, ApJ, 342, 660

Jackson, C. A. & Wall, J. V. 1999, MNRAS, 304, 160

Jarvis, M. J. & McLure, R. J. 2006, MNRAS, 369, 182

Jeffreys, H. 1939, Theory of probability, 3rd edn. (OUP)

Jester, S., Körding, E., & Fender, R. 2006, Proceedings of the VI Microquasar workshop: Microquasars and beyond, 26

Jeyakumar, S. & Saikia, D. J. 2000, MNRAS, 311, 397

Kaiser, C. R. 2005, MNRAS, 360, 176

Kaiser, C. R. 2006, MNRAS, 367, 1083

Kapahi, V. K., Athreya, R. M., Subrahmanya, C. R., et al. 1998a, ApJS, 118, 327

Kapahi, V. K., Athreya, R. M., van Breugel, W., McCarthy, P. J., & Subrahmanya, C. R. 1998b, ApJS, 118, 275

Kellermann, K. I., Lister, M. L., Homan, D. C., et al. 2008, Approaching Micro-Arcsecond Resolution with VSOP-2: Astrophysics and Technology ASP Conference Series

Kellermann, K. I., Sramek, R., Schmidt, M., Shaffer, D. B., & Green, R. 1989, AJ, 98, 1195

Körding, E., Jester, S., & Fender, R. 2006, MNRAS, 372, 1366

Koski, A. T. 1978, ApJ, 223, 56

Krolik, J. H. & Begelman, M. C. 1986, ApJ, 308, L55

Lacy, M., Laurent-Muehleisen, S. A., Ridgway, S. E., Becker, R. H., & White, R. L. 2001, ApJ, 551, L17

Laing, R. A. 1988, Nature, 331, 149

Laing, R. A. & Peacock, J. A. 1980, MNRAS, 190, 903

Laing, R. A., Riley, J. M., & Longair, M. S. 1983, MNRAS, 204, 151

Landsman, W. B. 1993, Astronomical Data Analysis Software and Systems II, A.S.P. Conference Series, edited by R. J. Hanisch, R. J. V. Brissenden, and J. Barne, 52, 246

Large, M. I., Mills, B. Y., Little, A. G., Crawford, D. F., & Sutton, J. M. 1981, MNRAS, 194, 693

Lavalley, M., Isobe, T., & Feigelson, E. 1992, Astronomical Data Analysis Software and Systems I, A.S.P. Conference Series, 25, 245

Lawrence, A. 1991, MNRAS, 252, 586

Lister, M. L., Gower, A. C., & Hutchings, J. B. 1994, AJ, 108, 821

Longair, M. S. & Riley, J. M. 1979, MNRAS, 188, 625

Magorrian, J., Tremaine, S., Richstone, D., et al. 1998, AJ, 115, 2285

Malkan, M. A. & Sargent, W. L. W. 1982, ApJ, 254, 22

Marshall, H. L., Avni, Y., Tananbaum, H., & Zamorani, G. 1983, ApJ, 269, 35

Martínez-Sansigre, A., Rawlings, S., Lacy, M., et al. 2005, Nature, 436, 666

Massardi, M., Ekers, R. D., Murphy, T., et al. 2008, MNRAS, 384, 775

Matsumoto, M. & Nishimura, T. 1998, ACM Transactions on Modeling and Computer Simulations: Special Issue on Uniform Random Number Generation

Mauch, T., Murphy, T., Buttery, H. J., et al. 2003, MNRAS, 342, 1117

McCarthy, P. J., Kapahi, V. K., van Breugel, W., et al. 1996, ApJS, 107, 19

McCarthy, P. J., van Breugel, W., Spinrad, H., & Djorgovski, S. 1987, ApJ, 321, L29

McLean, B. J., Greene, G. R., Lattanzi, M. G., & Pirenne, B. 2000, Astronomical Data Analysis Software and Systems IX, A.S.P. Conference proceedings, 216, 145

McLure, R. J. & Dunlop, J. S. 2004, MNRAS, 352, 1390

McLure, R. J. & Jarvis, M. J. 2002, MNRAS, 337, 109

McLure, R. J., Kukula, M. J., Dunlop, J. S., et al. 1999, MNRAS, 308, 377

Miller, P., Rawlings, S., & Saunders, R. 1993, MNRAS, 263, 425

Moorwood, A., Cuby, J.-G., Biereichel, P., et al. 1998, Messenger, 94, 7

Netzer, H. 1985, MNRAS, 216, 63

Nipoti, C., Blundell, K. M., & Binney, J. 2006, Proceedings of the VI Microquasar woskshop: Microquasars and beyond., 87

O'Dea, C. P. 1998, PASP, 110, 493

Orr, M. J. L. & Browne, I. W. A. 1982, MNRAS, 200, 1067

Owsianik, I. & Conway, J. E. 1998, AA, 337, 69

Peacock, J. A. 1981, MNRAS, 196, 135

Peacock, J. A. 1999, Cosmological Physics (Cambridge University Press)

Pen, U. 1999, ApJS, 120, 49

Pérez, E., Penston, M. V., Tadhunter, C., Mediavilla, E., & Moles, M. 1988, MNRAS, 230, 353

Peterson, B. M. 1997, Active Galactic Nuclei, 1st edn. (Cambridge University Press)

Pickles, A. J. 1998, PASP, 110, 863

Pier, E. A. & Krolik, J. H. 1992, ApJ, 401, 99

Pier, E. A. & Krolik, J. H. 1993, ApJ, 418, 673

Pounds, K., Reeves, J., O'Brien, P., et al. 2001, ApJ, 559, 181

Press, W. H., Teukolsky, S. A., Vetterling, W. T., & Flannery, B. P. 1992, Numerical recipes in C. The art of scientific computing, 2nd edn. (CUP)

Rawlings, S. & Saunders, R. 1991, Nature, 349, 138

Rees, M. J., Begelman, M. C., Blandford, R. D., & Phinney, E. S. 1982, Nature, 295, 17

Reeves, J. N., Turner, M. J. L., Pounds, K. A., et al. 2001, AA, 365, L134

Ricci, R., Prandoni, I., Gruppioni, C., Sault, R. J., & de Zotti, G. 2006, AA, 445, 465

Rousselot, P., Lidman, C., Cuby, J.-G., Moreels, G., & Monnet, G. 2000, AA, 354, 1134

Scheuer, P. A. G. 1980, MNRAS, 193, 285

Scheuer, P. A. G. 1982, Extragalactic radio sources; proceedings of the symposium, Albequrque, NM, August 3 – 7, 1981, 163

Scheuer, P. A. G. 1992, What does it take to make a radio galaxy? In Extragalactic Radio Sources: From Beams to Jets: Proceedings of the 7th I.A.P. meeting, held at the Institut d'Astrophysique de Paris, Paris, France, July 2 – 5, 1991. Editors J. Roland, H. Sol, G. Pelletier, 1st edn. (Cambridge University Press)

Scheuer, P. A. G. 1995, MNRAS, 277, 331

Scheuer, P. A. G. & Feiler, R. 1996, MNRAS, 282, 291

Scheuer, P. A. G. & Readhead, A. C. S. 1979, Nature, 277, 182

Schlegel, D. J., Finkbeiner, D. P., & Davis, M. 1998, ApJ, 500, 525

Schmitt, H. R., Pringle, J. E., Clarke, C. J., & Kinney, A. L. 2002, ApJ, 575, 150

Shakura, N. I. & Sunyaev, R. A. 1973, AA, 24, 337

Silk, J. & Rees, M. J. 1998, AA, 331, L1

Simpson, C. 1998, MNRAS, 297, L39

Simpson, C., Rawlings, S., & Lacy, M. 1999, MNRAS, 306, 828

Sivia, D. 1996, Data Analysis. A Bayesian Tutorial, 2nd edn. (OUP)

Skilling, J. 2004, BayeSys and MassInf (Maximum Entropy Data Consultants Ltd (est. 1981))

Slee, O. B. 1977, Australian Journal of Physics, Astrophysics Supplement, 43, 1

Slee, O. B. 1995, Australian Journal of Physics, 48, 143

Slee, O. B. & Higgins, C. S. 1973, Australian Journal of Physics, Astrophysics Supplement, 27, 1

Slee, O. B. & Higgins, C. S. 1975, Australian Journal of Physics, Astrophysics Supplement, 36, 1

Steenbrugge, K. C. & Blundell, K. M. 2008, MNRAS, 388, 1457

Strateva, I. V., Strauss, M. A., Hao, L., et al. 2003, AJ, 126, 1720

Tody, D. 1986, Proc. SPIE Instrumentation in Astronomy VI, ed. D.L. Crawford, 627, 733

Tody, D. 1993, Astronomical Data Analysis Software and Systems II, A.S.P. Conference Series, eds. R.J. Hanisch, R.J.V. Brissenden, and J. Barnes, 52, 173

Tristram, K. R. W., Meisenheimer, K., Jaffe, W., et al. 2007, AA, 474, 837

Trotta, R. 2008, Contemporary Physics, 49, 71

Urry, C. M. & Padovani, P. 1995, PASP, 107, 803

van Bemmel, I. & Barthel, P. 2001, AA, 379, L21

Vardoulaki, E., Rawlings, S., Simpson, C., et al. 2008, MNRAS, 387, 505

Veilleux, S. & Osterbrock, D. E. 1987, ApJS, 63, 295

Vermeulen, R. C. & Cohen, M. H. 1994, ApJ, 430, 467

Vestergaard, M. 2002, ApJ, 571, 733

Wardle, J. F. C. & Aaron, S. E. 1997, MNRAS, 286, 425

Webb, G. M., Drury, L. O., & Biermann, P. 1984, AA, 137, 185

Willott, C. J., Rawlings, S., Archibald, E. N., & Dunlop, J. S. 2002, MNRAS, 331, 435

Willott, C. J., Rawlings, S., Blundell, K. M., & Lacy, M. 1998, MNRAS, 300, 625

Willott, C. J., Rawlings, S., Blundell, K. M., & Lacy, M. 1999, MNRAS, 309, 1017

Willott, C. J., Rawlings, S., Blundell, K. M., & Lacy, M. 2000, MNRAS, 316, 449

Willott, C. J., Rawlings, S., Blundell, K. M., Lacy, M., & Eales, S. A. 2001, MNRAS, 322, 536

Wills, B. J. & Browne, I. W. A. 1986, ApJ, 302, 56

Wright, A. & Otrupcek, R. 1990, PKS Catalog (SIMBAD)

Wright, A. & Otrupcek, R. 1996, Parkes Radio Sources Catalogue (PKSCAT90) (VizieR Online Data Calalog: VIII/15)

Wright, C. O., Egan, M. P., Kraemer, K. E., & Price, S. D. 2003, AJ, 125, 359

Zombeck, M. V. 1990, Handbook of Space Astronomy and Astrophysics, 2nd edn. (Cambridge University Press)